

## 7. SITE 953<sup>1</sup>

### Shipboard Scientific Party<sup>2</sup>

#### HOLE 953A

**Date occupied:** 22 August 1994  
**Date departed:** 23 August 1994  
**Time on hole:** 1 day, 3 hr, 10 min  
**Position:** 28°39.023'N, 15°8.681'W  
**Bottom felt (drill-pipe measurement from rig floor, m):** 3588.9  
**Distance between rig floor and sea level (m):** 11.10  
**Water depth (drill-pipe measurement from sea level, m):** 3577.8  
**Total depth (from rig floor, m):** 3781.50  
**Penetration (m):** 192.60  
**Number of cores (including cores having no recovery):** 21  
**Total length of cored section (m):** 192.60  
**Total core recovered (m):** 197.69  
**Core recovery (%):** 102.6  
**Oldest sediment cored:**  
Depth (mbsf): 192.60  
Nature: clayey nannofossil ooze  
Earliest age: late Pliocene

#### HOLE 953B

**Date occupied:** 23 August 1994  
**Date departed:** 24 August 1994  
**Time on hole:** 17 hr, 30 min  
**Position:** 28°39.015'N, 15°8.680'W  
**Bottom felt (drill-pipe measurement from rig floor, m):** 3588.9  
**Distance between rig floor and sea level (m):** 11.10  
**Water depth (drill-pipe measurement from sea level, m):** 3577.8  
**Total depth (from rig floor, m):** 3786.60  
**Penetration (m):** 197.70  
**Number of cores (including cores having no recovery):** 1  
**Total length of cored section (m):** 9.60  
**Total core recovered (m):** 7.46  
**Core recovery (%):** 77.7  
**Oldest sediment cored:**  
Depth (mbsf): 197.70  
Nature: clayey nannofossil ooze  
Earliest age: late Pliocene

#### HOLE 953C

**Date occupied:** 24 August 1994  
**Date departed:** 4 September 1994  
**Time on hole:** 11 days, 2 hr, 35 min  
**Position:** 28°39.014'N, 15°8.671'E  
**Bottom felt (drill-pipe measurement from rig floor, m):** 3588.9  
**Distance between rig floor and sea level (m):** 11.10  
**Water depth (drill-pipe measurement from sea level, m):** 3577.8  
**Total depth (from rig floor, m):** 4747.60  
**Penetration (m):** 1158.70  
**Number of cores (including cores having no recovery):** 103  
**Total length of cored section (m):** 971.70  
**Total core recovered (m):** 556.24  
**Core recovery (%):** 57.2  
**Oldest sediment cored:**  
Depth (mbsf): 1158.70  
Nature: hyaloclastite lapillistone  
Earliest age: early late Miocene

**Principal results:** Site 953, the first of four sites to be drilled into the volcanic apron, is located 68 km northeast of Gran Canaria, 90 km west of Fuerteventura, and 98 km east of Tenerife at a water depth of 3577.8 m. As no structural or other complications were indicated on the high-resolution pre-site survey data, no additional reflection seismic data was acquired on our approach to Site 953. The pre-site survey profiles show a sequence, about 1 s thick, with an almost parallel layering and with a gentle dip (~1°) north.

The objective for drilling Site 953 was to study the evolution of the complex ~16 m.y. history of Gran Canaria as reflected in the volcanoclastic sediment deposited in the sedimentary basin north of the island. Drilling at Site 953 penetrated a practically complete Quaternary to middle Miocene 1159-m-thick section, according to calcareous nannofossil and planktonic foraminifer biostratigraphies. These nonvolcanic and volcanoclastic sediments were divided into seven major units and three subunits that correspond closely to the lithostratigraphic subdivision of the volcanic rocks on Gran Canaria.

Unit I (0–197 mbsf), late Pliocene to Holocene (0–3 Ma), predominantly consists of pelagic clayey nannofossil ooze and graded nannofossil clay-silt, with lesser amounts of foraminifer sands, lithic crystal sands, and silts. The remarkable coarse sands rich in neritic biogenic material recovered in the upper 100 m are interpreted as beach sands, redeposited as turbidites possibly related to glacially controlled changes in sea level. The minor thin fallout tephra layers probably represent Plinian eruptions on Tenerife.

Unit II (197–264 mbsf), early to late Pliocene (3–4.3 Ma), consists of clayey nannofossil ooze with foraminifers and graded nannofossil clay-silt, foraminifer lithic silts and sands, and basaltic lapillistones. This unit coincides closely in time and mineralogical composition of the sands with

<sup>1</sup>Schmincke, H.-U., Weaver, P.P.E., Firth, J.V., et al., 1995. *Proc. ODP, Init. Repts.*, 157: College Station, TX (Ocean Drilling Program).

<sup>2</sup>Shipboard Scientific Party is given in the list preceding the Table of Contents.

the Roque Nublo volcanic phase on Gran Canaria. It is also a period of high sedimentation rates.

The sediments in the interval of Unit III (264–398 mbsf), early Pliocene to late Miocene (4.3–8.3 Ma) contrast in physical and chemical properties from the intervals corresponding to volcanically active periods and coincide with the major hiatus in volcanic activity on Gran Canaria. The sediments recovered are dominantly gray to brownish gray, clayey nanofossil ooze; coarse volcanoclastic material is almost absent.

Unit IV (398–850 mbsf), late to middle Miocene (8.3–14 Ma), was subdivided into three subunits based on the frequency and composition of volcanoclastic mass flow deposits. Subunit IVa (398–504 mbsf) consists of interbedded nanofossil mixed sedimentary rock, nanofossil chalk, slump deposits, graded green nanofossil clay-siltstones, foraminifer sandstones, and green lithic-crystal sandstones and siltstones. Rock fragments in the volcanoclastic sediments are characteristically clasts of trachyphonolitic lava flows and ignimbrites.

Subunit IVb (504–754 mbsf), coinciding with the middle and early Fataga phases, shows a marked increase in abundance and thickness of volcanoclastic sandstones and some pumiceous units that could represent the distal submarine equivalents of ash flows. Subunit IVc (754–850 m) consists of nanofossil mixed sedimentary rock, crystal vitric siltstones and sandstones, vitric tuffs, and lapillistones and slump deposits. Influx of volcanoclastic material in this unit is correlated to the Mogan phase on Gran Canaria (13.4–14.0 Ma), which was dominated by major ash flow eruptions. Most striking are pumice-rich massive units, tentatively correlated to ash flows entering the sea, and thick tuffs consisting entirely of glass shards. A notable discovery at this site is the identification of the marine facies of cooling Unit P1, a 14 Ma ignimbrite that forms the most important stratigraphic marker on the island and separates the basaltic shield from the overlying felsic volcanics.

A major goal of Site 953 was to drill through the feather edge of the shield volcano that was expected to be composed of basaltic debris flows on account of the low slopes of the flanks apparent in the seismic records and the large distance from the island. The deepest target reflectors, assumed to image the distant very thin flank of Gran Canaria, are found at 900 ms twt and below. This thin outermost flank of the shield volcano is now believed, based on both drilling and more detailed interpretation of the seismic reflectors, to be represented by Unit VI. But the sediments representing the subaerial part of the shield are believed to begin with Unit V.

Unit V (850–889 mbsf), middle Miocene (10.4–13 Ma), is composed of nanofossil mixed sedimentary rock, nanofossil claystone, claystone, lithic crystal siltstones and sandstones, and basaltic lapillistone. Hundreds of small turbidite units of volcanic sand and silt, many only a few centimeters thick, occur in the interval from Section 157-953C-70R-3 to at least Section 157-953C-75R-1. These turbidites apparently record the growth of the subaerial shield prior to covering of the shield volcano by the Mogan ash flows. The sediments of Unit V occur *above* the main reflector, interpreted prior to drilling as the thin submarine flank of Gran Canaria.

Volcanoclastic rocks between Cores 157-953C-76R and 157-953C-83R (Unit VI, 889–969 mbsf, middle Miocene) are more complex and variable. They consist largely of basaltic sandstone, lapillistone, and breccia, interbedded with minor calcareous claystone and nanofossil mixed sediments. Recovery in this interval was extremely low, probably because of the abundance of coarse mixed breccias containing both shallow submarine and subaerially derived basaltic material. The sequence is interpreted to reflect the change from subaerial to emergent and shallow submarine volcanism.

The only major fossil bearing pelagic interval (Sections 157-953C-83R-1 to 157-953C-83R-2) encountered between 850 and 1159 mbsf separates Unit VI from Unit VII (969–1158.7 mbsf, late-early Miocene). Unit VII consists almost entirely of green hyaloclastite tuffs, lapillistones, and breccias that are interpreted as debris flow deposits 10–50 m thick. They consist of moderately to highly vesiculated shards and contain 30–70 vol% basaltic fragments, including oxidized scoria. Most basalt clasts have quench textures and probably represent true submarine basalts. Clinopyroxene, often in clots, dominates throughout, and some units are almost picritic with strongly altered and rarely fresh olivine. A 0.5-cm-thick

nanofossil-bearing chalk occurs in the lowermost core (157-953C-103R) and indicates an age no younger than 15.8 and no older than 17.4 Ma. Unit VII may be older than Gran Canaria because it is separated from Unit VI both seismically and by the only thick nonvolcanic sediment bed in the lower 300 m of the hole, and because they differ lithologically.

Mafic and evolved rocks and Miocene and Pliocene rock suites can be clearly distinguished by major and trace element abundances. More subtle differences between Mogan peralkaline trachytes and low silica rhyolites and early and late Fataga trachyphonolites can be clearly recognized. Major changes in sediment (phenocryst) mineralogy throughout the hole reflect known and dated compositional changes on land.

A reliable magnetostratigraphy was determined to a depth of 800 m (~14 Ma) but not in the thick underlying hyaloclastites. The intensity of magnetization and susceptibility records vary as a function of depth that appear to correlate with volcanic deposits, so that they may eventually serve as useful proxies for volcanic input.

An accumulation rate based on an integrated biostratigraphy and magnetostratigraphy sedimentation rate curve reflects the major contrast between volcanically active phases (shield, Mogan, Fataga, Roque Nublo, and post-Roque Nublo) and nonvolcanic periods, chiefly the time between approximately 8 and 5 Ma. Accumulation rates are as high as 112 m/m.y. during Mogan and early Fataga time, possibly 118 m/m.y. during accumulation of the basal hyaloclastite debris flows, and only 18m/m.y. during a major part of the volcanic hiatus between 6.2 and 8.2 Ma (360–390 mbsf).

This volcanic hiatus is also reflected in grain and bulk-density data. In Unit III, which corresponds to the ~5 m.y. nonvolcanic phase, the densities are remarkably constant, contrasting with major variations in sediment densities in other intervals that correspond to volcanically active periods.

The pore-water chemistry at Site 953 displays some of the most marked changes documented in the deep ocean and can be correlated with major chemical changes in the source rocks as well. Calcium and strontium are being liberated to pore waters in the upper few hundred meters. High sulfate concentrations around 500 mbsf are attributed to the dissolution of sulfur-rich volcanic glasses. High salinities, chlorinities, and alkali metal concentrations between 400 and 850 mbsf, combined with the precipitation of phillipsite, smectites, and analcime, indicate intense alteration of pyroclastic material. Alteration processes in the thick basaltic hyaloclastites below 890 mbsf act as a major source of pore-water calcium, strontium, and possibly potassium, and they provide a sink for most other pore-water constituents. Natrolite and other zeolites are being precipitated in vesicles, vugs, and veins in this interval. Variation in pore-water geochemistry is controlled principally by dissolution of volcanic glasses and the precipitation of smectites and zeolites.

Despite poor hole conditions, the quad combination tool string (sonic velocity, bulk density, resistivity, neutron porosity, and natural gamma-ray tools) was successfully deployed openhole from 980–375 mbsf. The quality of the geophysical logs is good. The components of potassium, uranium, and thorium derived from the total natural gamma-ray log are particularly diagnostic. The increase of potassium, uranium, and thorium downhole (~400 mbsf) reflects the increase in supply of volcanoclastics from the Fataga phase, relative the volcanic hiatus above. The preceding Mogan volcanic phase (~750–840 mbsf) is well distinguished by high uranium and thorium values that relate to highly evolved rhyolitic ash layers within this unit. Beneath this phase, the transition to the basaltic Gran Canaria shield phase (~840 mbsf) is reflected by a drastic decrease in the thorium log from the natural gamma-ray tool. The density, resistivity, and sonic velocity logs show an increasing lithification trend with depth through the Fataga phase and show less indurated lithologies with a higher degree of variance in the Mogan phase (750–840 mbsf). The transition downward into the shield phase (~840 mbsf) is characterized by a sharp increase in density, sonic velocity, and resistivity.

One of our objectives was to compare the predicted depth and stratigraphic correlation of reflectors obtained during the pre-cruise surveys. Sonic log data from 361 to 963 mbsf show that discrete velocity measurements from the cores are systematically too high in the deepest part of the hole, where sonic log velocities approximately fit the minimum values from the cores. The discrepancy is most likely a result of the sampling,

which tends to favor the more indurated rocks of the sediment sequence. Based on the sonic data, a new two-way traveltime/depth relation has been constructed, and a good correlation was found with the lithostratigraphic and volcanic event interpretations of the cored section. For example, the Mogan phase is seen as a characteristic group of concordant reflectors. The top of the Fataga phase seems to be represented by a high-amplitude reflector apparently well suited for regional mapping. The same is the case for the Roque Nublo phase, which appears as a narrow band of high-amplitude reflectors. A synthetic seismic profile calculated from the sonic log provides a precise correlation between cores and the seismic profiles.

All data available indicate that most volcanoclastic material was supplied to Site 953 from Gran Canaria. Notable exceptions include Pleistocene tephra layers presumably from Tenerife and the lower part of the basal hyaloclastites (Unit VII), which may have been supplied from islands to the east. Interestingly, the amount of quartz in the coarse fraction is very small, in contrast to DSDP Site 397 (Leg 47A). Stained quartz at Site 397 was interpreted to be of aeolian origin. The near-absence of quartz at Site 953 suggests that quartz found at Site 397 may have been transported by bottom currents rather than by wind. Site 953 is sheltered from Africa by the barrier of the older eastern Canary Islands. The only influx of sediments from Africa to Site 953 may be the green, slightly organic-rich turbidites in Subunits IVb and IVc, which also contain some quartz at their bases. The channel between Gran Canaria and Fuerteventura may have been much shallower at that time, allowing minor sediment mass flows to enter the sedimentary basin north of Gran Canaria.

In summary, the marine record at Site 953 shows an excellent first order correlation to the geological history of Gran Canaria. All major volcanic and nonvolcanic phases on this island are reflected in the ages, types and compositions of sediments, physical properties, and downhole logs. The lithostratigraphy has been controlled almost entirely by the mid-Miocene to Holocene subaerial and submarine volcanism of the island. The changes from submarine through emergent and subaerial shield and subsequent ash flow eruptions are especially well reflected in the sediments. Fundamental changes in composition of the dominant magma types, in the type of volcanic activity, and in the duration and volume of volcanic/magmatic phases as they evolved on land could be inferred from the marine record.

## BACKGROUND AND OBJECTIVES

### Location and Bathymetry

Site 953, the first of four sites to be drilled into the volcanic apron peripheral to Gran Canaria, is located in a semiclosed sedimentary basin 68 km northeast of the northern coast of Gran Canaria, 90 km west of Fuerteventura, 98 km east of the northern tip of Tenerife, and 180 km southeast of the Selvagens Islands. The basin is deeper by 500–1000 m than the South Canary Channel (Canary Passage) at the same longitude owing at least in part to the fact that sediments derived from the African continental margin were piled up between the barrier of the East Canary Ridge and Africa. The basin is bounded to the north by submarine ridges and seamounts south of the Dacia Seamount, to the northwest by the Selvagens Islands, and to the northeast by the Concepcion Seamount. The strait between Selvagens and an unnamed seamount 110 km to the east is ~3400 m deep.

Site 953 is located in the southeast of the deeper eastern part of the northern basin in a fairly flat area at a water depth of 3578 m. The basin fill above the Mesozoic ocean crust is believed to be made up of about 2000–3000 m of post-Jurassic and pre-Miocene sediments overlain by volcanoclastic sediments derived from the surrounding islands, principally Gran Canaria. These volcanoclastics are mixed and interlayered with hemipelagic nannofossil and foraminifer oozes and marls.

The evolution of Gran Canaria is characterized by several major distinct volcanic phases as discussed in detail in the VICAP Background and Objectives for Leg 157 (Chapter 2, this volume). Site 953 is expected to contain volcanoclastic deposits representing the most

complete record of the island's history within the basin facies of the apron.

## Objectives

The objectives of drilling Sites 953 and 954 are similar, with Site 953 representing the more distal and Site 954 the more proximal facies of the northern basin of the volcanoclastic apron. The basin sediments north of Gran Canaria are expected to differ significantly from those in the south on account of higher sedimentation rates and concentration of post-Miocene volcanic activity in the north of the island.

### *Temporal, Volcanic, and Compositional Evolution of the Shield Phases of Gran Canaria and Possibly Fuerteventura*

A major unsolved problem in understanding the evolution of oceanic intraplate volcanoes is the duration, lithology, and composition of the submarine shield phase. We aimed at drilling the distal edge of the seamount stage of Gran Canaria at Site 953 where it is approximately 50 m thick according to interpretation of seismic records. Volcanoclastic deposits from the shield phase of Fuerteventura are expected to be encountered below those of Gran Canaria. Can the different ages and therefore probable time gap of the submarine deposits of both shields be specified in time and composition more precisely than from the land record? Can a deeper submarine phase (i.e., eruption below the volatile fragmentation depth) be distinguished from the shallow water and emerging phase of a shield volcano?

### *How Well Are Volcanic and Nonvolcanic Periods on Gran Canaria Reflected in the Amount, Composition, and Type of Volcanoclastic Sediment Laid Down per Unit Time in the Basin North of the Island?*

We want to quantify the amount of volcanic detritus produced per unit time during nonvolcanic vs. constructive volcanic periods, many of which have been characterized on land in detail with respect to stratigraphy, volcanology, composition, and age. A comparison of the long erosional hiatus between ~9 and ~4 Ma and the large Roque Nublo stratocone built between ~4 and 3.5 Ma within the basin fill will be especially instructive in this regard. Better criteria are badly needed for distinguishing volcanoclastic rocks formed as a direct result of volcanic eruptions from those produced by erosion of volcanic rocks, and drilling Site 953 might provide suitable volcanoclastic sediments to study this problem in more detail.

### *History of the Sedimentary Basin North of the Central and Western Canaries*

By looking at the entire section drilled, we will monitor the change in sedimentation regime in the basin north of the island that began to form after the initial shield of Gran Canaria was constructed, marking the initial stage of the subdivision of the northern basin and South Canary Channel. The separation of the two basins proceeded with the growth of Tenerife. Only minor mass flows transported materials from Africa owing to the barrier of the eastern Canary Islands; this contribution should have become diminished as the channel between Fuerteventura and Gran Canaria became filled up after the shield building stage.

### *Event Detection and Characterization*

The growth and destruction history of Gran Canaria was punctuated by numerous events such as major explosive eruptions resulting in large ash flows and/or ash falls, and debris avalanches. We want to characterize the volcanic event deposits and hope to correlate some of them with prominent reflectors in the volcanic apron as well as

with major volcanic events on land. We also hope to correlate them with the drill sites south of the island and possibly also with some of the large volcanoclastic turbidites deposited on the Madeira Abyssal Plain.

### **Quantification of Sediment Budgets**

We have a rough idea of the type and accumulation rates of the hemipelagic background sedimentation in the area and suspect that the greater thickness of the sedimentary sequence from the seafloor to the top of the flank reflector results entirely from volcanoclastic sediments, largely from Gran Canaria but with minor contributions from the neighboring islands. This information will furnish crucial data needed for quantifying the total amount of volcanoclastics per unit time supplied to the sedimentary basin. The stratigraphic, sedimentological, volcanological, and compositional data will ultimately result in a more realistic calculation of sediment budgets for the submarine growth, subaerial evolution, and unroofing of Gran Canaria, Fuerteventura, and Tenerife, and ocean islands in general.

### **Alteration**

The large amount of glass of different composition that is expected, especially in the middle Miocene part of the hole, should allow a detailed study of the changes of types of secondary minerals and compositions of pore solutions with depth in a deep hole. The thermal effects of the core of the island on the diagenesis in a sequence of hemipelagic marly ooze and volcanoclastic sediments is probably less severe than at Site 954. We thus expect a larger number of unaltered glassy ash layers, although in smaller thicknesses than at Site 954.

## **OPERATIONS**

### **Site 952 (MAP 3) to Site 953 (VICAP 1A) Transit**

The *JOIDES Resolution* made the 506 nmi transit to Site 953 at an average speed of 11.2 kt. The vessel approached the position on a northerly heading and slowed as it neared the beacon-drop point. The thrusters and hydrophones were deployed as the vessel was offset to the GPS coordinates of the site. At 1053, local time, 22 August, the beacon was deployed on site.

### **Hole 953A**

An APC/XCB BHA was made up, and Core 157-953A-1H established the mud line depth at 3577.8 mbsl. APC coring proceeded routinely to 188.1 mbsf (Cores 1H to 20H; Table 1). Core 21H failed to achieve full stroke. The core barrel was drilled over and then pulled out with 175,000 lb overpull. Only half the core barrel was retrieved, leaving the other half stuck in the hole. The hole was terminated, and the pipe was pulled out of the hole with the bit clearing the mud line at 1355, 23 August. Cores 3H to 16H were oriented. Recovery was 102.6% of the 192.60 m cored interval.

### **Hole 953B**

The vessel was offset 20 m south of the first hole, Hole 953B was spudded and drilled ahead without a wash barrel to 188.1 m, and then XCB coring began. It was not possible to retrieve the first core barrel with wireline overpulls as high as 12,500 lb. Repeated attempts at freeing the barrel with the wireline jars also proved fruitless. The pipe was pulled out of the hole, ending Hole 953B. Investigation of the stuck core barrel showed that the POLYPAK material in the bit seal had apparently compressed on the landing of the XCB core barrel and jammed the POLYPAK material between the inner barrel spacer sub and the hard edge of the bit seal. When the bit cleared the mud line at

2309, 23 August, operations had to be suspended for 1.5 hr while 115 ft of drilling line were cut and slipped.

### **Hole 953C**

The vessel was offset 20 m east of Hole 953B, and an RCB BHA was run in and spudded Hole 953C at 1525, 24 August. The hole was drilled ahead with a wash barrel to a depth of 187 mbsf. RCB coring advanced rapidly through the upper portion of hole, which was composed of hard and soft interlayers of calcareous claystone and nanofossil mixed sediments. Recovery typically was below 50%. As the formation became more indurated with depth, recovery improved. Coring was concluded at 0915, 2 September, after coring a total of 971.70 m (1159 m TD) with a recovery of 57.2%. The rate of coring averaged 11.3 m/hr for the entire hole. There were no hole problems noted during coring operations. Regular preventive sweeps of sepiolite (30 bbl) were circulated. The chisel deplugger was deployed twice to unplug the bit after coring 157-953C-88R (1014 to 1017 mbsf). Methane was detected in trace amounts (maximum of 34 ppm) with no heavier hydrocarbons detected. A drift survey at 870 mbsf found the hole angle to be 4°.

Because of the extreme depth of the hole, an extensive wiper trip and hole conditioning exercise was performed, with three 50 bbl flushes of sepiolite and several washes to clear the bottom of fill. A tight spot at 598 mbsf required extra washing and reaming. The bit was released and the pipe was pulled up to logging depth. The bottom of the pipe was positioned at 372 mbsf. The first log was the quad combo, comprising the DIT, HTLD, CNT, NGT, LSS, and TLT, which logged down from 372–975 mbsf. An upgoing log was then recorded from 975 mbsf to the mud line (372 m inside pipe) during which 4000–5000 lb overpull was encountered between 975–911 mbsf and 535–499 mbsf. Having completed the upgoing log, the quad was run into the hole for a repeat section, but downward progress was stopped by an obstruction at 477 mbsf and the tool was pulled out of the hole. The logging equipment was rigged down and the pipe was run in the hole to clear bridges at 535 mbsf and deeper. While attempting to work past 533 mbsf, the pipe became stuck. During the attempts to free the drill string, the hole packed off and circulation, rotation, and vertical movement were lost. Efforts at freeing the pipe were fruitless, so the pipe was severed with explosives at the first joint of 5 in. pipe above the BHA. When the drill string was pulled out of the hole and the rig floor was secured at 1000, 4 September, the *JOIDES Resolution* was underway to the next site at full speed.

## **LITHOSTRATIGRAPHY**

The sedimentary succession recovered at Site 953 ranges in age from late early to middle Miocene to Holocene. It is 1158.7 m thick and consists of dominantly fine-grained pelagic sediments, coarser volcanoclastic material, and lesser amounts of neritic debris (Fig. 1). In the upper part of the sequence the principal lithologies include clayey nanofossil ooze with foraminifers, graded nanofossil clay-silt, foraminifer sand, and vitric sand. The middle part of the sequence is dominated by nanofossil chalk, nanofossil mixed sedimentary rocks, thick bedded lithic crystal siltstone and sandstone, and vitric tuffs and lapillistones of felsic compositions. Toward the base there is an abrupt transition to very coarse grained and thick bedded hyaloclastite tuffs, lapillistones, and breccias of mafic composition. The influx of coarse volcanoclastic material to Site 953 has played a fundamental role in controlling the lithostratigraphy. This influx is reflected in the percentage of sand size material per core as shown as a function of depth in Figure 2. Sand-size material has been broadly classified into three groups based on the abundance of volcanic vs. calcareous components. The type and abundance of volcani-

Table 1. Coring summary of Holes 953A, 953B, and 953C

Core	Date (1994)	Time (UTC)	Sub-bottom (m)		Cored (m)	Recovered (m)	Recovery (%)	Section	Length (m)	Depth (mbsf)		Samples
			Top	Bottom						Top	Bottom	
157-953A-1H Combined totals	Aug. 22	1805	0.0	7.6	7.6	7.60	100.0					
								1	1.50	0.00	1.50	
								2	1.50	1.50	3.00	
								3	1.50	3.00	4.50	
								4	1.50	4.50	6.00	IW 145-150
2H	Aug. 22	1900	7.6	17.1	9.5	9.66	101.0					
								5	1.45	6.00	7.45	HS 0-5
								CC	0.15	7.45	7.60	
								1	1.50	7.60	9.10	
								2	1.50	9.10	10.60	
3H	Aug. 22	2005	17.1	26.6	9.5	9.86	104.0					
								3	1.50	10.60	12.10	
								4	1.50	12.10	13.60	IW 145-150
								5	1.50	13.60	15.10	HS 0-5
								6	1.50	15.10	16.60	
4H	Aug. 22	2100	26.6	36.1	9.5	9.85	103.0					
								7	0.38	16.60	16.98	
								CC	0.28	16.98	17.26	
								1	1.50	17.10	18.60	
								2	1.50	18.60	20.10	
5H	Aug. 22	2155	36.1	45.6	9.5	8.43	88.7					
								3	1.50	20.10	21.60	IW 145-150
								4	1.50	21.60	23.10	HS 0-5
								5	1.50	23.10	24.60	
								6	1.50	24.60	26.10	
6H	Aug. 22	2250	45.6	55.1	9.5	9.78	103.0					
								7	0.74	26.10	26.84	
								CC	0.12	26.84	26.96	
								1	1.50	26.60	28.10	
								2	1.50	28.10	29.60	
7H	Aug. 22	2355	55.1	64.6	9.5	9.80	103.0					
								3	1.50	29.60	31.10	
								4	1.50	31.10	32.60	IW 145-150
								5	1.50	32.60	34.10	HS 0-5
								6	1.50	34.10	35.60	
8H	Aug. 22	2155	36.1	45.6	9.5	8.43	88.7					
								7	0.69	35.60	36.29	
								CC	0.16	36.29	36.45	
								1	1.50	36.10	37.60	
								2	1.50	37.60	39.10	
9H	Aug. 22	2355	55.1	64.6	9.5	9.80	103.0					
								3	1.50	39.10	40.60	IW 145-150
								4	1.50	40.60	42.10	HS 0-5
								5	1.50	42.10	43.60	
								6	0.75	43.60	44.35	
10H	Aug. 23	0040	64.6	74.1	9.5	9.66	101.0					
								6	0.18	44.35	44.53	
								1	1.50	45.60	47.10	
								2	1.50	47.10	48.60	
								3	1.50	48.60	50.10	
11H	Aug. 23	0125	74.1	83.6	9.5	9.90	104.0					
								4	1.50	50.10	51.60	IW 145-150
								5	1.50	51.60	53.10	HS 0-5
								6	1.50	53.10	54.60	
								7	0.52	54.60	55.12	
12H	Aug. 23	0230	83.6	93.1	9.5	10.13	106.6					
								CC	0.26	55.12	55.38	
								1	1.50	55.10	56.60	
								2	1.50	56.60	58.10	
								3	1.50	58.10	59.60	
13H	Aug. 23	0040	64.6	74.1	9.5	9.66	101.0					
								4	1.50	59.60	61.10	IW 145-150
								5	1.50	61.10	62.60	HS 0-5
								6	1.50	62.60	64.10	
								7	0.63	64.10	64.73	
14H	Aug. 23	0125	74.1	83.6	9.5	9.90	104.0					
								CC	0.17	64.73	64.90	
								1	1.50	64.60	66.10	
								2	1.50	66.10	67.60	
								3	1.50	67.60	69.10	
15H	Aug. 23	0230	83.6	93.1	9.5	10.13	106.6					
								4	1.50	69.10	70.60	
								5	1.50	70.60	72.10	IW 145-150
								6	1.50	72.10	73.60	HS 0-5
								7	0.52	73.60	74.12	
16H	Aug. 23	0125	74.1	83.6	9.5	9.90	104.0					
								CC	0.14	74.12	74.26	
								1	1.50	74.10	75.60	
								2	1.50	75.60	77.10	
								3	1.50	77.10	78.60	
17H	Aug. 23	0230	83.6	93.1	9.5	10.13	106.6					
								4	1.50	78.60	80.10	
								5	1.50	80.10	81.60	IW 143-150
								6	1.50	81.60	83.10	HS 0-5
								7	0.63	83.10	83.73	
18H	Aug. 23	0230	83.6	93.1	9.5	10.13	106.6					
								CC	0.27	83.73	84.00	
								1	1.50	83.60	85.10	
								2	1.50	85.10	86.60	
								3	1.50	86.60	88.10	
19H	Aug. 23	0230	83.6	93.1	9.5	10.13	106.6					
								4	1.50	88.10	89.60	
								5	1.50	89.60	91.10	IW 145-150
								6	1.50	91.10	92.60	HS 0-5
								7	0.84	92.60	93.44	
20H	Aug. 23	0230	83.6	93.1	9.5	10.13	106.6					
								CC	0.29	93.44	93.73	
								1	1.50	83.60	85.10	
								2	1.50	85.10	86.60	
								3	1.50	86.60	88.10	

Table 1 (continued).

Core	Date (1994)	Time (UTC)	Sub-bottom (m)		Cored (m)	Recovered (m)	Recovery (%)	Section	Length (m)	Depth (mbsf)		Samples
			Top	Bottom						Top	Bottom	
11H	Aug. 23	0330	93.1	102.6	9.5	9.17	96.5	1	1.50	93.10	94.60	HS 0-5
								2	1.50	94.60	96.10	
								3	1.50	96.10	97.60	
								4	1.50	97.60	99.10	
								5	1.50	99.10	100.60	
								6	0.81	100.60	101.41	
12H	Aug. 23	0430	102.6	112.1	9.5	9.90	104.0	CC	0.86	101.41	102.27	IW 145-150 HS 0-5
								1	1.50	102.60	104.10	
								2	1.50	104.10	105.60	
								3	1.50	105.60	107.10	
								4	1.50	107.10	108.60	
								5	1.50	108.60	110.10	
13H	Aug. 23	0525	112.1	121.6	9.5	9.65	101.0	6	1.50	110.10	111.60	HS 0-5
								7	0.68	111.60	112.28	
								CC	0.22	112.28	112.50	
								1	1.50	112.10	113.60	
								2	1.50	113.60	115.10	
								3	1.50	115.10	116.60	
14H	Aug. 23	0615	121.6	131.1	9.5	10.11	106.4	4	1.50	116.60	118.10	HS 0-5
								5	1.50	118.10	119.60	
								6	1.50	119.60	121.10	
								7	0.52	121.10	121.62	
								CC	0.13	121.62	121.75	
								1	1.50	121.60	123.10	
15H	Aug. 23	0710	131.1	140.6	9.5	9.66	101.0	2	1.50	123.10	124.60	IW 145-150 HS 0-5
								3	1.50	124.60	126.10	
								4	1.50	126.10	127.60	
								5	1.50	127.60	129.10	
								6	1.50	129.10	130.60	
								7	0.81	130.60	131.41	
16H	Aug. 23	0800	140.6	150.1	9.5	10.12	106.5	CC	0.30	131.41	131.71	HS 0-5
								1	1.50	131.10	132.60	
								2	1.50	132.60	134.10	
								3	1.50	134.10	135.60	
								4	1.50	135.60	137.10	
								5	1.50	137.10	138.60	
17H	Aug. 23	0850	150.1	159.6	9.5	9.82	103.0	6	1.20	138.60	139.80	HS 0-5
								7	0.76	139.80	140.56	
								CC	0.20	140.56	140.76	
								1	1.50	140.60	142.10	
								2	1.50	142.10	143.60	
								3	1.50	143.60	145.10	
18H	Aug. 23	0940	159.6	169.1	9.5	10.09	106.2	4	1.50	145.10	146.60	IW 145-150 HS 0-5
								5	1.50	146.60	148.10	
								6	1.50	148.10	149.60	
								7	0.84	149.60	150.44	
								CC	0.28	150.44	150.72	
								1	1.50	150.10	151.60	
19H	Aug. 23	1025	169.1	178.6	9.5	9.77	103.0	2	1.50	151.60	153.10	HS 0-5
								3	1.50	153.10	154.60	
								4	1.50	154.60	156.10	
								5	1.50	156.10	157.60	
								6	1.50	157.60	159.10	
								7	0.51	159.10	159.61	
20H	Aug. 23	1115	178.6	186.1	7.5	10.18	135.7	CC	0.31	159.61	159.92	IW 140-150 HS 0-5
								1	1.50	159.60	161.10	
								2	1.50	161.10	162.60	
								3	1.50	162.60	164.10	
								4	1.50	164.10	165.60	
								5	1.50	165.60	167.10	
19H	Aug. 23	1025	169.1	178.6	9.5	9.77	103.0	6	1.50	167.10	168.60	HS 0-5
								7	0.81	168.60	169.41	
								CC	0.28	169.41	169.69	
								1	1.50	169.10	170.60	
								2	1.50	170.60	172.10	
								3	1.50	172.10	173.60	
20H	Aug. 23	1115	178.6	186.1	7.5	10.18	135.7	4	1.50	173.60	175.10	HS 0-5
								5	1.50	175.10	176.60	
								6	1.40	176.60	178.00	
								7	0.70	178.00	178.70	
								CC	0.17	178.70	178.87	
								1	1.50	178.60	180.10	
20H	Aug. 23	1115	178.6	186.1	7.5	10.18	135.7	2	1.50	180.10	181.60	IW 140-150 HS 0-4
								3	1.50	181.60	183.10	
								4	1.50	183.10	184.60	
								5	1.50	184.60	186.10	
								6	1.50	186.10	187.60	
								7	0.85	187.60	188.45	

Table 1 (continued).

Core	Date (1994)	Time (UTC)	Sub-bottom (m)		Cored (m)	Recovered (m)	Recovery (%)	Section	Length (m)	Depth (mbsf)		Samples
			Top	Bottom						Top	Bottom	
21H	Aug. 23	1220	186.1	192.6	4.5	4.55	47.9	CC	0.33	188.45	188.78	
								1	1.50	186.10	187.60	
								2	1.50	187.60	189.10	
								3	1.50	189.10	190.60	
								CC	0.05	190.60	190.65	
Coring totals					192.6	197.69	102.6					
157-953B-1X	Aug. 24	0645	188.1	197.7	9.6	7.46	77.7					
								1	1.21	188.10	189.31	Disturbed
								2	1.50	189.31	190.81	Disturbed
								3	0.83	190.81	191.64	Disturbed
								4	1.50	191.64	193.14	Disturbed
								5	0.62	193.14	193.76	Disturbed
								6	1.50	193.76	195.26	Disturbed
								CC	0.30	195.26	195.56	
Coring totals					9.6	7.46	77.70					
157-953C-1W	Aug. 24	2020	0.0	187.0	187.0	0.29	wash core					
								1	0.29	0.00	0.29	
2R	Aug. 24	2120	187.0	196.5	9.5	1.96	20.6					
								1	1.50	187.00	188.50	HS 0-5
								2	0.46			
3R	Aug. 24	2225	196.5	206.1	9.6	3.74	38.9					
								1	1.50	196.50	198.00	
								2	1.50	198.00	199.50	IW 140-150
								3	0.74	199.50	200.24	HS 0-5
4R	Aug. 24	2335	206.1	215.8	9.7	1.86	19.2					
								1	1.50	206.10	207.60	
								2	0.36	207.60	207.96	HS 0-5
5R	Aug. 25	0040	215.8	225.5	9.7	3.00	30.9					
								1	1.50	215.80	217.30	
								2	1.50	217.30	218.80	HS 0-5
6R	Aug. 25	0140	225.5	235.0	9.5	0.88	9.3					
								1	0.88	225.50	226.38	
7R	Aug. 25	0305	235.0	244.6	9.6	3.65	38.0					
								1	1.50	235.00	236.50	
								2	1.17	236.50	237.67	HS 0-5
								3	0.98	237.67	238.65	
8R	Aug. 25	0405	244.6	254.1	9.5	4.87	51.2					
								1	1.50	244.60	246.10	
								2	1.50	246.10	247.60	
								3	1.50	247.60	249.10	IW 1-10/HS 10-15
								4	0.30	249.10	249.40	
								CC	0.07	249.40	249.47	
9R	Aug. 25	0505	254.1	263.7	9.6	4.94	51.4					
								1	1.50	254.10	255.60	
								2	1.50	255.60	257.10	HS 0-5
								3	1.50	257.10	258.60	
								4	0.29	258.60	258.89	
								CC	0.15	258.89	259.04	
10R	Aug. 25	0605	263.7	273.4	9.7	4.21	43.4					
								1	1.50	263.70	265.20	
								2	1.50	265.20	266.70	
								3	1.00	266.70	267.70	
								CC	0.21	267.70	267.91	
11R	Aug. 25	0710	273.4	283.0	9.6	6.51	67.8					
								1	1.50	273.40	274.90	IW 140-150
								2	1.50	274.90	276.40	HS 0-5
								3	1.50	276.40	277.90	
								4	1.50	277.90	279.40	
								5	0.48	279.40	279.88	
								CC	0.03	279.88	279.91	
12R	Aug. 25	0810	283.0	292.7	9.7	3.63	37.4					
								1	1.50	283.00	284.50	
								2	1.50	284.50	286.00	
								3	0.43	286.00	286.43	HS 0-5
								CC	0.20	286.43	286.63	
13R	Aug. 25	0900	292.7	302.4	9.7	8.29	85.4					
								1	1.50	292.70	294.20	
								2	1.50	294.20	295.70	
								3	1.50	295.70	297.20	
								4	1.50	297.20	298.70	
								5	1.50	298.70	300.20	HS 0-5
								6	0.62	300.20	300.82	
								CC	0.17	300.82	300.99	
14R	Aug. 25	0955	302.4	312.1	9.7	2.90	29.9					
								1	1.50	302.40	303.90	IW 135-150
								2	1.27	303.90	305.17	HS 0-5
								CC	0.13	305.17	305.30	
15R	Aug. 25	1055	312.1	321.6	9.5	3.60	37.9					
								1	1.50	312.10	313.60	
								2	1.50	313.60	315.10	HS 0-5
								3	0.41	315.10	315.51	
								CC	0.19	315.51	315.70	
16R	Aug. 25	1150	321.6	331.1	9.5	4.66	49.0					

Table 1 (continued).

Core	Date (1994)	Time (UTC)	Sub-bottom (m)		Cored (m)	Recovered (m)	Recovery (%)	Section	Length (m)	Depth (mbsf)		Samples
			Top	Bottom						Top	Bottom	
17R	Aug. 25	1250	331.1	340.6	9.5	7.69	80.9	1	1.50	321.60	323.10	HS 0-5
								2	1.50	323.10	324.60	
								3	1.47	324.60	326.07	
								CC	0.19	326.07	326.26	
								1	1.50	331.10	332.60	
								2	1.50	332.60	334.10	
18R	Aug. 25	1355	340.6	350.2	9.6	6.37	66.3	3	1.50	334.10	335.60	IW 135-150 HS 0-5
								4	1.50	335.60	337.10	
								5	1.50	337.10	338.60	
								6	0.16	338.60	338.76	
								CC	0.03	338.76	338.79	
								1	1.50	340.60	342.10	
19R	Aug. 25	1525	350.2	359.8	9.6	2.70	28.1	2	1.50	342.10	343.60	HS 0-5
								3	1.50	343.60	345.10	
								4	1.50	345.10	346.60	
								CC	0.37	346.60	346.97	
								1	1.50	350.20	351.70	
								2	0.98	351.70	352.68	
20R	Aug. 25	1635	359.8	369.5	9.7	7.55	77.8	CC	0.22	352.68	352.90	HS 0-5
								1	1.50	359.80	361.30	
21R	Aug. 25	1735	369.5	379.1	9.6	7.70	80.2	2	1.50	361.30	362.80	IW 133-150 HS 0-5
								3	1.50	362.80	364.30	
								4	1.50	364.30	365.80	
								5	1.50	365.80	367.30	
								CC	0.05	367.30	367.35	
								1	1.50	369.50	371.00	
22R	Aug. 25	1845	379.1	388.6	9.5	8.34	87.8	2	1.50	371.00	372.50	HS 0-5
								3	1.50	372.50	374.00	
								4	1.50	374.00	375.50	
								5	1.50	375.50	377.00	
								6	0.20	377.00	377.20	
								1	1.50	379.10	380.60	
23R	Aug. 25	1955	388.6	398.1	9.5	7.75	81.6	2	1.50	380.60	382.10	HS 0-5
								3	1.50	382.10	383.60	
								4	1.50	383.60	385.10	
								5	1.50	385.10	386.60	
								6	0.58	386.60	387.18	
								CC	0.26	387.18	387.44	
24R	Aug. 25	2100	398.1	407.7	9.6	6.42	66.9	1	1.50	388.60	390.10	IW 136-150 HS 0-5
								2	1.50	390.10	391.60	
								3	1.50	391.60	393.10	
								4	1.50	393.10	394.60	
								5	1.50	394.60	396.10	
								6	0.25	396.10	396.35	
25R	Aug. 25	2200	407.7	417.3	9.6	6.08	63.3	1	1.50	398.10	399.60	HS 0-5
								2	1.50	399.60	401.10	
								3	1.50	401.10	402.60	
								4	1.50	402.60	404.10	
								5	0.17	404.10	404.27	
								CC	0.25	404.27	404.52	
26R	Aug. 25	2300	417.3	427.0	9.7	5.74	59.2	1	1.50	407.70	409.20	HS 0-5
								2	1.50	409.20	410.70	
								3	1.50	410.70	412.20	
								4	1.34	412.20	413.54	
								CC	0.24	413.54	413.78	
								1	1.50	417.30	418.80	
27R	Aug. 26	0000	427.0	436.6	9.6	6.45	67.2	2	1.50	418.80	420.30	IW 135-150 HS 0-5
								3	1.50	420.30	421.80	
								4	1.24	421.80	423.04	
								1	1.50	427.00	428.50	
28R	Aug. 26	0100	436.6	446.2	9.6	6.45	67.2	2	1.50	428.50	430.00	HS 0-5
								3	1.50	430.00	431.50	
								4	0.85	431.50	432.35	
								5	0.86	432.35	433.21	
								CC	0.24	433.21	433.45	
								1	1.50	436.60	438.10	
29R	Aug. 26	0150	446.2	455.9	9.7	5.74	59.2	2	1.50	438.10	439.60	HS 0-5
								3	1.50	439.60	441.10	
								4	1.50	441.10	442.60	
								5	0.45	442.60	443.05	
								1	1.50	446.20	447.70	
29R	Aug. 26	0150	446.2	455.9	9.7	5.74	59.2	2	1.50	447.70	449.20	IW 130-150
								3	1.50	449.20	450.70	
								4	1.20	450.70	451.90	
								CC	0.04	451.90	451.94	
								1	1.50	446.20	447.70	

Table 1 (continued).

Core	Date (1994)	Time (UTC)	Sub-bottom (m)		Cored (m)	Recovered (m)	Recovery (%)	Section	Length (m)	Depth (mbsf)		Samples
			Top	Bottom						Top	Bottom	
30R	Aug. 26	0250	455.9	465.5	9.6	5.87	61.1	1	1.50	455.90	457.40	
								2	1.50	457.40	458.90	
								3	1.50	458.90	460.40	
								4	1.37	460.40	461.77	
31R	Aug. 26	0350	465.5	475.2	9.7	6.03	62.1	1	1.50	465.50	467.00	HS 0-5
								2	1.50	467.00	468.50	
								3	1.50	468.50	470.00	
								4	1.50	470.00	471.50	
								CC	0.03	471.50	471.53	
32R	Aug. 26	0450	475.2	484.9	9.7	5.96	61.4	1	1.50	475.20	476.70	IW 130-150/HS 145-150
								2	1.50	476.70	478.20	
								3	1.50	478.20	479.70	
								4	1.20	479.70	480.90	
								CC	0.26	480.90	481.16	
33R	Aug. 26	0550	484.9	494.5	9.6	6.16	64.1	1	1.50	484.90	486.40	HS 0-5
								2	1.50	486.40	487.90	
								3	1.50	487.90	489.40	
								4	1.45	489.40	490.85	
								CC	0.21	490.85	491.06	
34R	Aug. 26	0650	494.5	504.1	9.6	7.59	79.0	1	1.50	494.50	496.00	HS 0-5
								2	1.50	496.00	497.50	
								3	1.50	497.50	499.00	
								4	1.12	499.00	500.12	
								5	1.50	500.12	501.62	
								6	0.44	501.62	502.06	
35R	Aug. 26	0750	504.1	513.8	9.7	5.53	57.0	CC	0.03	502.06	502.09	IW 113-131 HS 0-5
								1	1.36	504.10	505.46	
								2	1.42	505.46	506.88	
								3	1.31	506.88	508.19	
								4	1.41	508.19	509.60	
36R	Aug. 26	0850	513.8	523.5	9.7	7.04	72.6	CC	0.03	509.60	509.63	HS 0-5
								1	1.50	513.80	515.30	
								2	1.50	515.30	516.80	
								3	1.29	516.80	518.09	
								4	1.43	518.09	519.52	
37R	Aug. 26	0100	523.5	533.2	9.7	6.15	63.4	5	1.19	519.52	520.71	HS 0-5
								CC	0.13	520.71	520.84	
								1	1.42	523.50	524.92	
								2	1.45	524.92	526.37	
								3	1.17	526.37	527.54	
38R	Aug. 26	1105	533.2	542.8	9.6	6.77	70.5	4	1.37	527.54	528.91	IW 118-138 HS 0-5
								5	0.74	528.91	529.65	
								1	1.47	533.20	534.67	
								2	1.38	534.67	536.05	
								3	1.20	536.05	537.25	
39R	Aug. 26	1220	542.8	552.4	9.6	8.25	85.9	4	1.38	537.25	538.63	HS 0-5
								5	1.34	538.63	539.97	
								1	1.38	542.80	544.18	
								2	1.29	544.18	545.47	
								3	1.35	545.47	546.82	
								4	1.47	546.82	548.29	
40R	Aug. 26	1340	552.4	561.9	9.5	5.02	52.8	5	1.26	548.29	549.55	HS 0-5
								6	1.53	549.55	551.08	
								1	1.39	552.40	553.79	
								2	1.29	553.79	555.08	
41R	Aug. 26	1550	561.9	571.4	9.5	2.77	29.1	3	1.25	555.08	556.33	HS 0-5
								4	1.09	556.33	557.42	
								1	1.42	561.90	563.32	
								2	1.35	563.32	564.67	
42R	Aug. 26	1740	571.4	581.0	9.6	1.64	17.1	1	1.33	571.40	572.73	HS 0-5
								2	0.31	572.73	573.04	
43R	Aug. 26	1915	581.0	590.7	9.7	1.15	11.8	1	0.90	581.00	581.90	HS 0-5
								CC	0.25	581.90	582.15	
44R	Aug. 26	2105	590.7	600.4	9.7	8.01	82.6	1	1.50	590.70	592.20	IW 110-130 HS 0-5
								2	1.24	592.20	593.44	
								3	1.50	593.44	594.94	
								4	1.30	594.94	596.24	
								5	1.26	596.24	597.50	
								6	0.67	597.50	598.17	
								7	0.54	598.17	598.71	
45R	Aug. 26	2250	600.4	610.0	9.6	4.12	42.9	1	1.50	600.40	601.90	HS 0-5
								2	1.50	601.90	603.40	

Table 1 (continued).

Core	Date (1994)	Time (UTC)	Sub-bottom (m)		Cored (m)	Recovered (m)	Recovery (%)	Section	Length (m)	Depth (mbsf)		Samples
			Top	Bottom						Top	Bottom	
46R	Aug. 27	0030	610.0	619.6	9.6	3.28	34.1	3	0.80	603.40	604.20	
								CC	0.32	604.20	604.52	
								1	0.89	610.00	610.89	
								2	0.97	610.89	611.86	
47R	Aug. 27	0145	619.6	629.3	9.7	4.05	41.7	3	1.20	611.86	613.06	
								4	0.22	613.06	613.28	
								1	0.50	619.60	620.10	
								2	1.47	620.10	621.57	
48R	Aug. 27	0320	629.3	638.9	9.6	6.94	72.3	3	1.46	621.57	623.03	IW 32-50 HS 0-5
								4	0.62	623.03	623.65	
								1	0.50	619.60	620.10	
								2	1.47	620.10	621.57	
49R	Aug. 27	0445	638.9	648.5	9.6	8.75	91.1	3	1.46	621.57	623.03	
								4	0.62	623.03	623.65	
								1	0.93	629.30	630.23	
								2	1.31	630.23	631.54	
								3	1.40	631.54	632.94	
								4	1.05	632.94	633.99	
50R	Aug. 27	0630	648.5	658.1	9.6	5.78	60.2	5	1.11	633.99	635.10	
								6	1.14	635.10	636.24	
								1	1.36	638.90	640.26	
								2	1.50	640.26	641.76	
								3	1.50	641.76	643.26	
								4	1.20	643.26	644.46	
								5	1.12	644.46	645.58	
51R	Aug. 27	0755	658.1	667.7	9.6	7.01	73.0	6	1.47	645.58	647.05	
								7	0.60	647.05	647.65	
								1	1.44	648.50	649.94	
								2	1.45	649.94	651.39	
52R	Aug. 27	0920	667.7	677.4	9.7	5.00	51.5	3	1.41	651.39	652.80	IW 124-144/HS 139-144
								4	1.48	652.80	654.28	
								1	1.20	658.10	659.30	
								2	1.32	659.30	660.62	
53R	Aug. 27	1045	677.4	687.0	9.6	8.83	92.0	3	1.40	661.82	663.28	
								4	1.46	661.82	663.28	
								5	1.47	663.28	664.75	
								6	0.36	664.75	665.11	
								1	1.29	667.70	668.99	
								2	1.40	668.99	670.39	
54R	Aug. 27	1225	687.0	696.5	9.5	7.33	77.1	3	1.22	670.39	671.61	
								4	1.09	671.61	672.70	
								1	1.45	677.40	678.85	
								2	1.38	678.85	680.23	
								3	1.33	680.23	681.56	
								4	1.40	681.56	682.96	
								5	1.43	682.96	684.39	
55R	Aug. 27	1415	696.5	706.0	9.5	7.73	81.3	6	1.13	684.39	685.52	IW 120-140/HS 135-140
								7	0.71	685.52	686.23	
								1	1.40	687.00	688.40	
								2	1.26	688.40	689.66	
								3	1.50	689.66	691.16	
								4	1.50	691.16	692.66	
56R	Aug. 27	1550	706.0	715.5	9.5	5.87	61.8	5	1.36	692.66	694.02	
								6	0.31	694.02	694.33	
								1	1.26	696.50	697.76	
								2	1.33	697.76	699.09	
								3	1.50	699.09	700.59	
								4	1.47	700.59	702.06	
57R	Aug. 27	1745	715.5	725.2	9.7	6.87	70.8	5	1.44	702.06	703.50	IW 85-95 IW 36-46/120-130 IW 68-78 IW 68-78
								6	0.73	703.50	704.23	
								1	1.40	706.00	707.40	
								2	1.46	707.40	708.86	
								3	1.45	708.86	710.31	
								4	1.10	710.31	711.41	
58R	Aug. 27	1930	725.2	734.9	9.7	7.73	79.7	5	1.10	721.27	722.37	
								1	1.42	715.50	716.92	
								2	1.39	716.92	718.31	
								3	1.48	718.31	719.79	
								4	1.48	719.79	721.27	
59R	Aug. 27	2125	734.9	744.5	9.6	9.93	103.0	5	1.10	721.27	722.37	IW 125-145/HS 140-145
								1	1.47	725.20	726.67	
								2	1.44	726.67	728.11	
								3	1.50	728.11	729.61	
								4	1.40	729.61	731.01	
								5	1.50	731.01	732.51	
	Aug. 27	2125	734.9	744.5	9.6	9.93	103.0	6	0.42	732.51	732.93	
								1	1.50	734.90	736.40	
								2	1.33	736.40	737.73	

Table 1 (continued).

Core	Date (1994)	Time (UTC)	Sub-bottom (m)		Cored (m)	Recovered (m)	Recovery (%)	Section	Length (m)	Depth (mbsf)		Samples	
			Top	Bottom						Top	Bottom		
60R	Aug. 27	2305	744.5	754.1	9.6	5.40	56.2	CC	3	1.30	737.73	739.03	IW 130-150/HS 145-150
									4	1.50	739.03	740.53	
									5	1.39	740.53	741.92	
									6	1.45	741.92	743.37	
									7	1.18	743.37	744.55	
									0.28	744.55	744.83		
									1	1.42	744.50	745.92	
61R	Aug. 28	0045	754.1	763.6	9.5	5.09	53.6		2	1.50	745.92	747.42	
									3	1.50	747.42	748.92	
									4	0.98	748.92	749.90	
									1	1.41	754.10	755.51	
62R	Aug. 28	0215	763.6	773.1	9.5	4.77	50.2		2	1.46	755.51	756.97	
									3	1.36	756.97	758.33	
									4	0.86	758.33	759.19	
									1	1.45	763.60	765.05	
63R	Aug. 28	0340	773.1	782.8	9.7	0.54	5.6		2	1.50	765.05	766.55	IW 130-150/HS 145-150
									3	1.50	766.55	768.05	
									4	0.32	768.05	768.37	
									1	0.54	773.10	773.64	
64R	Aug. 28	0525	782.8	792.4	9.6	4.24	44.1		1	1.46	782.80	784.26	
									2	1.16	784.26	785.42	
									3	1.17	785.42	786.59	
									4	0.45	786.59	787.04	
65R	Aug. 28	0720	792.4	802.1	9.7	7.66	78.9		1	1.15	792.40	793.55	IW 95-115/HS 110-115
									2	1.24	793.55	794.79	
									3	1.40	794.79	796.19	
									4	1.44	796.19	797.63	
									5	1.36	797.63	798.99	
									6	1.07	798.99	800.06	
66R	Aug. 28	0900	802.1	811.7	9.6	5.72	59.6		1	1.31	802.10	803.41	
									2	1.46	803.41	804.87	
									3	1.36	804.87	806.23	
									4	1.00	806.23	807.23	
									5	0.59	807.23	807.82	
67R	Aug. 28	1040	811.7	821.4	9.7	7.19	74.1		1	1.51	811.70	813.21	
									2	1.38	813.21	814.59	
									3	1.37	814.59	815.96	
									4	1.43	815.96	817.39	
									5	1.50	817.39	818.89	
68R	Aug. 28	1210	821.4	831.1	9.7	5.73	59.1		1	1.40	821.40	822.80	IW 125-145/HS 140-145
									2	1.26	822.80	824.06	
									3	1.45	824.06	825.51	
									4	1.20	825.51	826.71	
									5	0.42	826.71	827.13	
69R	Aug. 28	1420	831.1	840.8	9.7	6.13	63.2		1	1.43	831.10	832.53	
									2	1.37	832.53	833.90	
									3	1.46	833.90	835.36	
									4	1.24	835.36	836.60	
									5	0.53	836.60	837.13	
70R	Aug. 28	1645	840.8	850.4	9.6	7.92	82.5		1	1.21	840.80	842.01	
									2	1.45	842.01	843.46	
									3	1.50	843.46	844.96	
									4	1.44	844.96	846.40	
									5	1.48	846.40	847.88	
									6	0.84	847.88	848.72	
71R	Aug. 28	1850	850.4	860.1	9.7	6.47	66.7		1	1.50	850.40	851.90	
									2	1.47	851.90	853.37	
									3	1.50	853.37	854.87	
									4	1.33	854.87	856.20	
									5	0.67	856.20	856.87	
72R	Aug. 28	2125	860.1	869.7	9.6	8.64	90.0		1	1.50	860.10	861.60	IW 113-133/HS128-133
									2	1.24	861.60	862.84	
									3	1.31	862.84	864.15	
									4	1.50	864.15	865.65	
									5	1.47	865.65	867.12	
									6	1.26	867.12	868.38	
									7	0.36	868.38	868.74	
73R	Aug. 28	2345	869.7	879.4	9.7	9.91	102.0		1	1.50	869.70	871.20	
									2	1.50	871.20	872.70	
									3	1.28	872.70	873.98	
									4	1.50	873.98	875.48	
									5	1.47	875.48	876.95	
									6	1.24	876.95	878.19	
									7	1.18	878.19	879.37	

Table 1 (continued).

Core	Date (1994)	Time (UTC)	Sub-bottom (m)		Cored (m)	Recovered (m)	Recovery (%)	Section	Length (m)	Depth (mbsf)		Samples
			Top	Bottom						Top	Bottom	
74R	Aug. 28	0320	879.4	889.1	9.7	3.13	32.2	8	0.24	879.37	879.61	
								1	1.50	879.40	880.90	
								2	1.40	880.90	882.30	
75R	Aug. 28	0505	889.1	898.7	9.6	0.34	3.5	CC	0.23	882.30	882.53	
								1	0.34	889.10	889.44	
								1	0.96	898.70	899.66	
76R	Aug. 28	0655	898.7	908.3	9.6	0.83	8.6	1	0.96	898.70	899.66	
77R	Aug. 29	0915	908.3	918.0	9.7	3.81	39.3	1	1.21	908.30	909.51	
								2	1.50	909.51	911.01	
								3	1.24	911.01	912.25	
78R	Aug. 29	1330	918.0	927.6	9.6	2.76	28.7	1	1.50	918.00	919.50	
								2	1.50	919.50	921.00	
79R	Aug. 29	1555	927.6	937.2	9.6	3.38	35.2	1	0.64	927.60	928.24	Transition back to sediments
								2	1.45	928.24	929.69	
								3	1.50	929.69	931.19	
80R	Aug. 29	1815	937.2	946.8	9.6	0.81	8.4	1	0.81	937.20	938.01	
81R	29	2110	946.8	956.4	9.6	1.98	20.6	1	1.50	946.80	948.30	
								2	0.50	948.30	948.80	
82R	Aug. 29	0040	956.4	966.0	9.6	1.19	12.4	1	1.03	956.40	957.43	
83R	Aug. 29	0300	966.0	975.6	9.6	7.96	82.9	CC	0.16	957.43	957.59	
								1	1.33	966.00	967.33	
								2	0.98	967.33	968.31	
								3	1.43	968.31	969.74	
								4	1.14	969.74	970.88	
								5	1.26	970.88	972.14	
								6	1.50	972.14	973.64	
								7	1.06	973.64	974.70	
84R	Aug. 29	0525	975.6	985.3	9.7	8.56	88.2	1	1.47	975.60	977.07	
								2	0.75	977.07	977.82	
								3	1.15	977.82	978.97	
								4	0.96	978.97	979.93	
								5	1.50	979.93	981.43	
								6	1.05	981.43	982.48	
								7	1.36	982.48	983.84	
								8	0.60	983.84	984.44	
85R	Aug. 29	0725	985.3	995.0	9.7	3.08	31.7	1	1.42	985.30	986.72	
								2	1.43	986.72	988.15	
								3	0.47	988.15	988.62	
86R	Aug. 29	0940	995.0	1004.6	9.6	7.33	76.3	1	1.25	995.00	996.25	IW 1-25/HS 20-25
								2	1.45	996.25	997.70	
								3	1.32	997.70	999.02	
								4	1.34	999.02	1000.36	
								5	1.27	1000.36	1001.63	
								6	0.85	1001.63	1002.48	
								7	0.00	1002.48	1002.48	
87R	Aug. 29	1215	1004.6	1014.2	9.6	3.68	38.3	1	1.50	1004.60	1006.10	
								2	1.44	1006.10	1007.54	
								3	1.05	1007.54	1008.59	
88R	Aug. 29	1455	1014.2	1017.2	3.0	0.01	0.3	1	0.01	1014.20	1014.21	
89R	Aug. 30	2145	1017.2	1023.7	6.5	5.74	88.3	1	1.42	1017.20	1018.62	
								2	1.40	1018.62	1020.02	
								3	1.45	1020.02	1021.47	
								4	1.50	1021.47	1022.97	
								5	0.19	1022.97	1023.16	
90R	Aug. 31	0250	1023.7	1033.2	9.5	5.66	59.6	1	1.39	1023.70	1025.09	HS 140-142
								2	1.45	1025.09	1026.54	
								3	1.41	1026.54	1027.95	
								4	1.50	1027.95	1029.45	
								5	0.72	1029.45	1030.17	
91R	Aug. 31	0830	1033.2	1042.9	9.7	4.61	47.5	1	1.50	1033.20	1034.70	HS 0-5
								2	1.50	1034.70	1036.20	
								3	1.44	1036.20	1037.64	
								4	0.25	1037.64	1037.89	
92R	Aug. 31	1415	1042.9	1052.6	9.7	1.50	15.4	1	1.50	1042.90	1044.40	HS 145-150
								2	0.42	1044.40	1044.82	
93R	Aug. 31	2015	1052.6	1062.2	9.6	7.13	74.3	1	1.46	1052.60	1054.06	
								2	1.41	1054.06	1055.47	
								3	1.42	1055.47	1056.89	
								4	1.27	1056.89	1058.16	

Table 1 (continued).

Core	Date (1994)	Time (UTC)	Sub-bottom (m)		Cored (m)	Recovered (m)	Recovery (%)	Section	Length (m)	Depth (mbsf)		Samples
			Top	Bottom						Top	Bottom	
94R	Sept. 1	0040	1062.2	1071.9	9.7	4.68	48.2	5	1.47	1058.16	1059.63	HS 145-150
								6	0.72	1059.63	1060.35	
95R	Sept. 1	0420	1071.9	1081.5	9.6	7.46	77.7	1	1.50	1062.20	1063.70	HS 0-1
								2	1.23	1063.70	1064.93	
								3	1.47	1064.93	1066.40	
								4	0.70	1066.40	1067.10	
96R	Sept. 1	0740	1081.5	1091.2	9.7	7.78	80.2	1	0.94	1071.90	1072.84	HS 0-1
								2	1.45	1072.84	1074.29	
								3	1.50	1074.29	1075.79	
								4	1.30	1075.79	1077.09	
								5	1.33	1077.09	1078.42	
								6	1.27	1078.42	1079.69	
97R	Sept. 1	1015	1091.2	1100.9	9.7	6.43	66.3	1	1.42	1081.50	1082.92	
								2	1.45	1082.92	1084.37	
								3	1.48	1084.37	1085.85	
								4	1.41	1085.85	1087.26	
								5	1.28	1087.26	1088.54	
								6	0.87	1088.54	1089.41	
98R	Sept. 1	1430	1100.9	1110.5	9.6	10.03	104.5	1	1.27	1091.20	1092.47	
								2	1.50	1092.47	1093.97	
								3	1.33	1093.97	1095.30	
								4	1.50	1095.30	1096.80	
								5	1.07	1096.80	1097.87	
								6	0.00	1097.87	1097.87	
99R	Sept. 1	1725	1110.5	1120.2	9.7	10.05	103.6	1	1.34	1100.90	1102.24	
								2	1.45	1102.24	1103.69	
								3	1.27	1103.69	1104.96	
								4	1.31	1104.96	1106.27	
								5	1.46	1106.27	1107.73	
								6	1.50	1107.73	1109.23	
								7	1.50	1109.23	1110.73	
								8	0.31	1110.73	1111.04	
100R	Sept. 1	2050	1120.2	1129.8	9.6	7.02	73.1	1	1.50	1110.50	1112.00	
								2	1.50	1112.00	1113.50	
								3	1.50	1113.50	1115.00	
								4	1.47	1115.00	1116.47	
								5	1.50	1116.47	1117.97	
								6	1.50	1117.97	1119.47	
								7	0.71	1119.47	1120.18	
								8	0.37	1120.18	1120.55	
101R	Sept. 2	0205	1129.8	1139.4	9.6	6.55	68.2	1	1.32	1120.20	1121.52	HS 0-1
								2	1.50	1121.52	1123.02	
								3	1.37	1123.02	1124.39	
								4	1.50	1124.39	1125.89	
								5	1.37	1125.89	1127.26	
102R	Sept. 2	0610	1139.4	1149.1	9.7	2.22	22.9	1	1.34	1129.80	1131.14	
								2	1.41	1131.14	1132.55	
								3	1.47	1132.55	1134.02	
								4	1.50	1134.02	1135.52	
								5	1.30	1135.52	1136.82	
103R	Sept. 2	0915	1149.1	1158.7	9.6	8.28	86.2	1	1.15	1139.40	1140.55	HS 110-115
								2	1.25	1140.55	1141.80	
Coring totals								1	1.25	1149.10	1150.35	
								2	1.44	1150.35	1151.79	
								3	1.43	1151.79	1153.22	
								4	1.50	1153.22	1154.72	
								5	1.46	1154.72	1156.18	
								6	1.27	1156.18	1157.45	
Washing totals												
Combined totals					971.7	556.24	57.20					
					187.0	0.3						
					1158.7	556.54						

Notes: Hole 953A located at 28°39.023'N, 15° 8.681'W, water depth from sea surface = 3577.8 m. Hole 953B located at 28°39.015'N, 15°8.680'W, water depth from sea surface = 3577.8 m. Hole 953C located at 28°39.014'N, 15°8.671'W, water depth from sea surface = 3577.8 m.

clastic sediments have been used in conjunction with other lithologic and sedimentological criteria to subdivide the sequence into seven major units and three subunits, although the input of coarse material to the site has varied considerably during the past ~16 m.y. (Fig. 2).

### Unit I

Interval: Sections 157-953A-1H-1 to 157-953A-2R-2

Depth: 0-197 mbsf  
Age: late Pliocene to Holocene

Unit I is 197 m thick and consists of gray to pale white clayey nanofossil ooze with foraminifers interbedded with graded nanofossil clay-silt (thin to medium bedded), massive foraminifer sands (medium to thick bedded), stratified foraminifer lithic sands (medium bedded), foraminifer lithic silts and sands (thin bedded), pumice sands

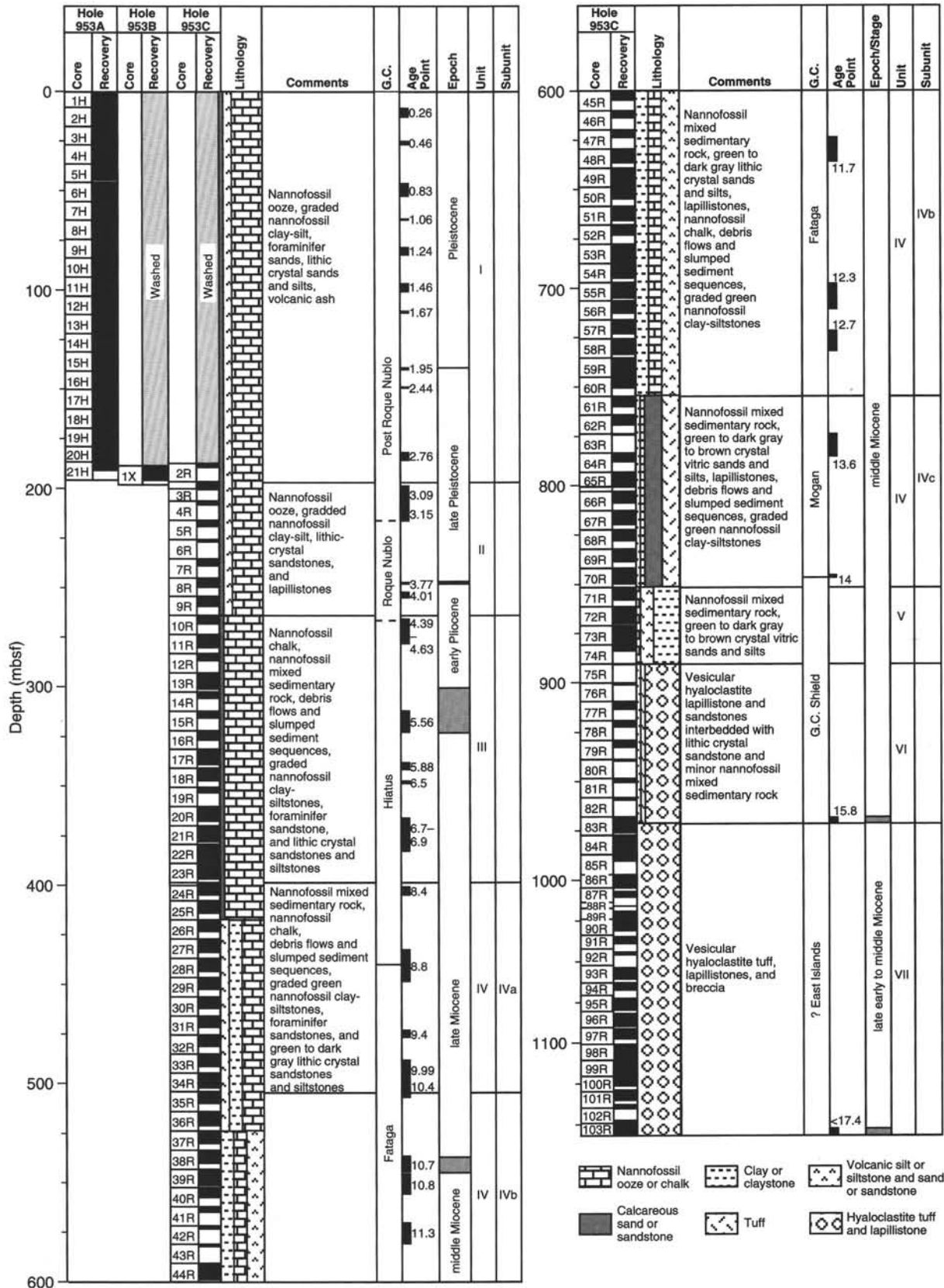


Figure 1. Lithologic summary for Holes 953A, 953B, and 953C, showing the main lithologic units identified with age and a generalized graphic lithology. G.C. = the phases of volcanic activity on Gran Canaria.

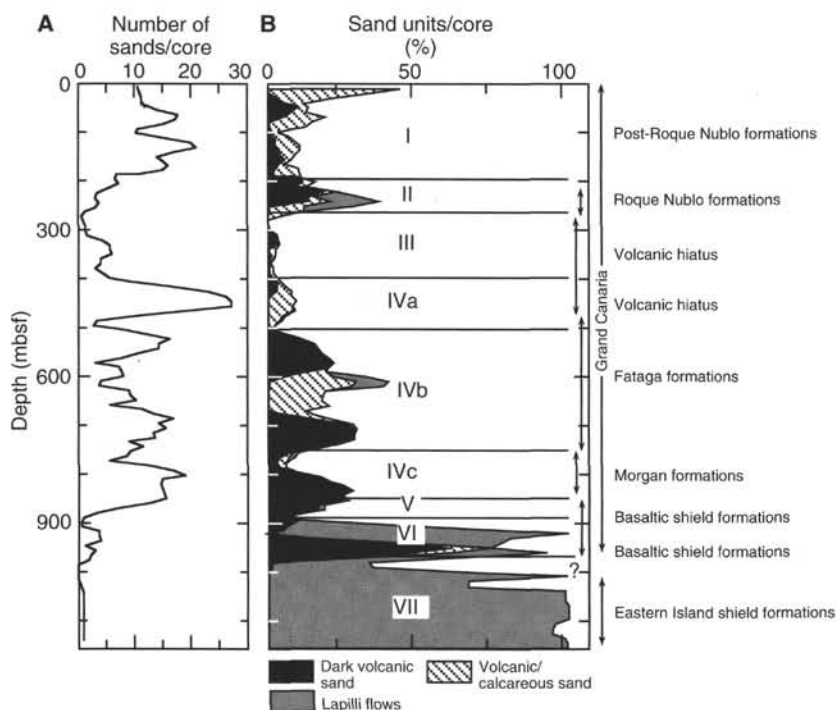


Figure 2. Variation in (A) the number of coarse volcaniclastic layers per core as a function of sub-bottom depth and (B) the percentage of coarse (greater than sand size) volcaniclastic layers per core.

(medium to thick bedded), and volcanic ash (thin bedded). The dominant lithology is gray to pale white clayey nannofossil ooze that formed by pelagic and hemipelagic sedimentation. The remaining interbeds represent mixed volcaniclastic and carbonate sediment emplacement by gravity flow processes and fallout from explosive volcanic eruptions.

#### Clayey Nannofossil Ooze

The dominant lithology of Unit I is brownish-gray, clayey nannofossil ooze with foraminifers. In the uppermost cores of Unit I, the ooze is light brown and becomes gray to light gray with increasing depth. In general, the sediment appears homogeneous with scattered mottling and is slightly to moderately bioturbated. It consists primarily of a mixture of clay minerals, coccolith plates, foraminifer tests and fragments, and minor silty volcaniclastic debris, comprising lithic, vitric, and crystal fragments. Calcium carbonate data show that the pelagic sediment has remained relatively uniform, except for a few samples, during the interval of deposition for Unit I (Fig. 3).

#### Graded Nannofossil Clay and Clay with Nannofossils

A distinctive sedimentary deposit in Unit I consists of nannofossil clay, clay with nannofossils, or clay that grades downward into silt or silty sand. A typical unit has an upper part that is clay or silty clay-size material and is slightly to moderately bioturbated. The boundary with the overlying sediment is usually gradational (Fig. 4). With increasing depth the upper unit grades into a silty or sandy silt base that is darker in color, often parallel laminated, and typically constitutes less than 20% of the entire deposit thickness. The contact with the underlying sediments is almost always sharp (Fig. 4) and sometimes inclined. Thicknesses of these units vary between about 5 and 20 cm, with many roughly 10 cm. The transition between the basal silt/sand and the upper clayey part may be gradational or sharp.

Many of these graded units vary from gray in the upper part to very dark gray or black at the base. There is, however, a certain amount of variation in the overall color gradation from one unit to the next. Smear slide examination shows that the basal silt/sand units

consist of mixtures of calcareous debris (foraminifer tests, nannofossils, and other bioclasts), small mafic rock fragments, feldspar, clinopyroxene, hornblende, and sideromelane. Some of the volcanic particles are rounded, although many units contain unaltered, angular shards of sideromelane. The overall color of the units is strongly dependent upon the relative proportions of calcareous and volcanic debris. The darkest layers have the highest amount of volcaniclastic material and the lowest carbonate contents. Lighter gray units contain more carbonate, up to 50%.

In Cores 157-953C-1H to 157-953C-16H these graded layers contain abundant fresh volcaniclastic material. However, below this level many layers contain a high proportion of zeolites, most notably phillipsite, which is interpreted as the alteration product of sideromelane.

#### Volcaniclastic Sands

Two principal types of thick bedded volcaniclastic sands occur within Unit I as interbeds in the gray nannofossil ooze. The first are beds of volcaniclastic sand mixed to varying degrees with calcareous components and are parallel laminated throughout. They are usually gray to very dark gray, have sharp upper and lower contacts, and are homogeneous in grain size or are slightly normally graded. Volcanic components include sideromelane, clinopyroxene, hornblende, Fe-Ti oxides, and mafic volcanic lithic fragments. The carbonate components consist dominantly of shallow water foraminifers, bryozoan fragments, pteropods, and other types of bioclasts.

Characteristically, the laminations alternate in color from light to dark, reflecting variations in the abundance of calcareous (light) and volcaniclastic debris (dark). Thicknesses of these units are usually about 50 cm, although considerable variation exists.

A less common type of volcaniclastic sand consists of medium to thick bedded units of pumice sand, which are typically ungraded to normally graded, gray to light greenish gray, and poorly sorted. Pumice from these units is gray, of low density, and slightly rounded. Variable amounts of calcareous debris, lithics, and crystals are mixed with the pumice.

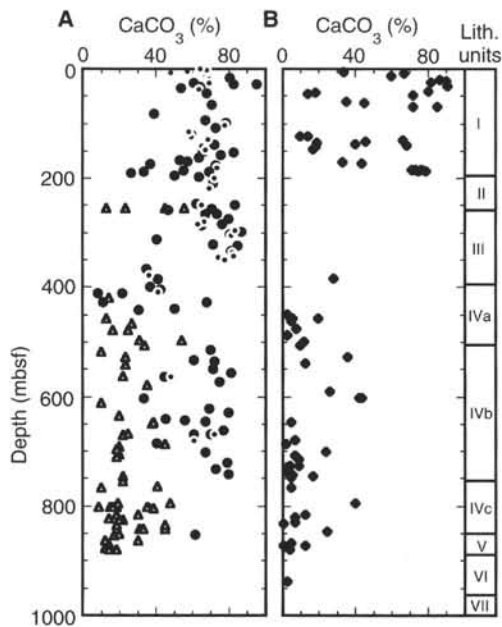


Figure 3. Variation in the calcium carbonate content of (A) pelagic sediment (filled circles) and turbidite muds (open triangles) and (B) silt or sand bases of turbidites (filled diamonds) as a function of sub-bottom depth.

#### Calcareous Sands and Silts

There is a large variety of calcareous-rich sand and silt units within Unit I. At one extreme are thick bedded, coarse-grained calcareous sands that contain abundant shallow-water foraminifers, bryozoans, pteropods, and other types of bioclasts. They are structureless or slightly normally graded and are up to 1 m thick. Volcaniclastic debris is usually present in minor amounts. More commonly, foraminifer sands occur as thin bedded units with sharp lower and upper contacts. A relatively wide range of lithologies can be represented by such layers primarily as a result of mixing of calcareous debris with volcaniclastic material. The layers are usually structureless, moderately sorted, gray to light gray, and contain a significant amount of silt, and they differ from the graded beds described above by the lack of a dark-gray clayey top.

Unit I also contains numerous very thin bedded units of mixed calcareous and volcaniclastic material. These layers typically have sharp bases and slightly bioturbated tops, are structureless, and usually are silt or fine sand size. Many of these layers form discontinuous bands in the nannofossil ooze as a result of bioturbation.

#### Volcanic Ash-fall Layers

A minor but important lithology of Unit I are very thin bedded layers of volcanic ash derived from eolian transport of pyroclastic material from explosive eruptions. They can be recognized by their greenish color and distinctive lithology. This material occurs as (1) discrete layers, (2) bioturbated but visible patches, and (3) dispersed ash in the clayey nannofossil ooze. Discrete layers have a sharp base, bioturbated top, and are well sorted. An excellent example is found in Section 157-953C-16H-03 (Fig. 5). This layer consists of >95% clear glass shards with tubular vesicles, bubble wall, and pumice fragment morphologies (Fig. 6), crystals of feldspar, amphibole and biotite, and minor biogenic fragments. The mean size of the shards in this layer is 40  $\mu\text{m}$ .

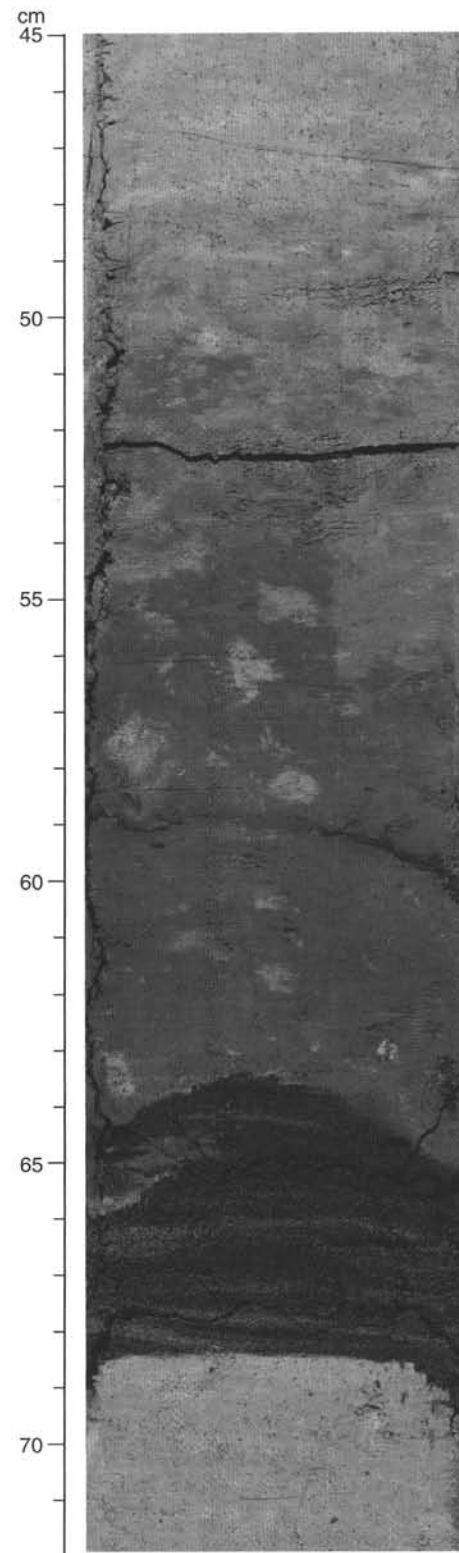


Figure 4. Turbidite unit that grades from clayey nannofossil mixed sediment to black foraminifer lithic sand at base. Note the bioturbated top, laminated sandy base, and sharp bottom contact. Interval 157-953A-13H-5, 45–72 cm.

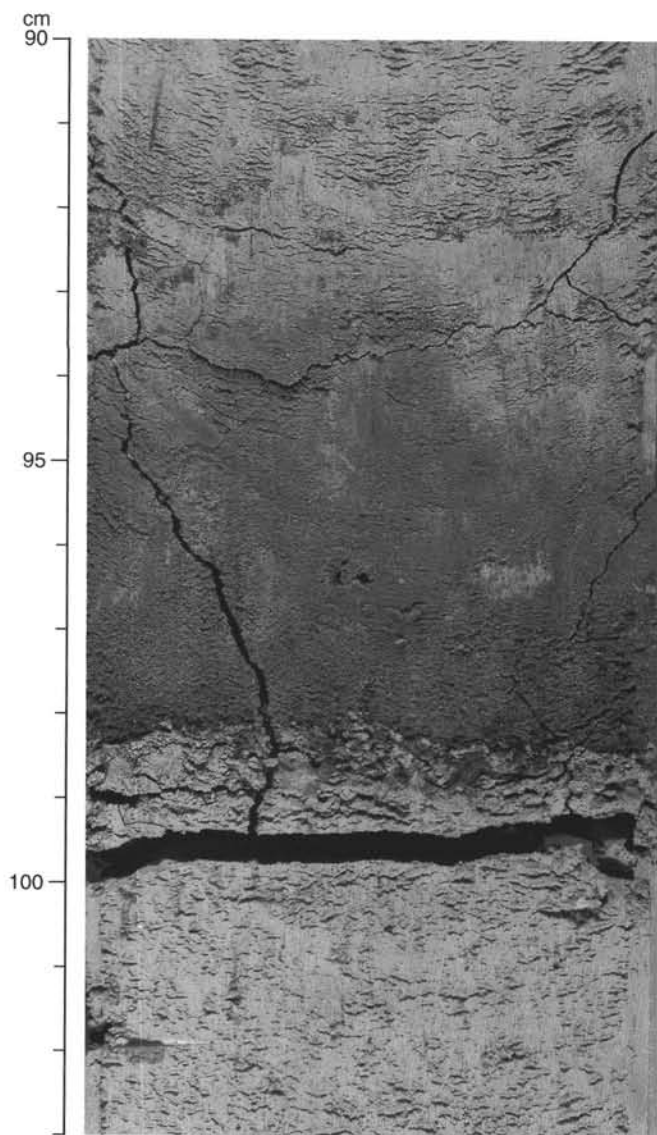


Figure 5. Volcanic ash-fall layer within a section of nanofossil ooze. Note the sharp basal contact and bioturbated top. Interval 157-953A-16H-3, 90–103 cm.

## Unit II

Interval: Sections 157-953C-3R-1 to 157-953C-9R-4  
Depth: 197–264 mbsf  
Age: late Pliocene

Unit II is 67 m thick and consists of gray to pale white clayey nanofossil ooze with foraminifers that is interbedded with graded nanofossil clay-silt, foraminifer lithic silt and sands (thin beds), and basaltic lapillistones. It is distinguished from Unit I mainly by an increase in the amount of coarse, basaltic volcaniclastic sediment (Fig. 2) and the presence of thick to very thick bedded basaltic lapillistones and coarse sandstones.

Most basaltic lapillistones and sandstones consist of a thick normally graded base overlain by a thinner deposit of nanofossil claystone or nanofossil mixed sediment. These thinner units are often parallel laminated and bioturbated near their tops. The sandstones are composed mostly of rounded basaltic lithics, and clinopyroxene, commonly with zeolitic cement.

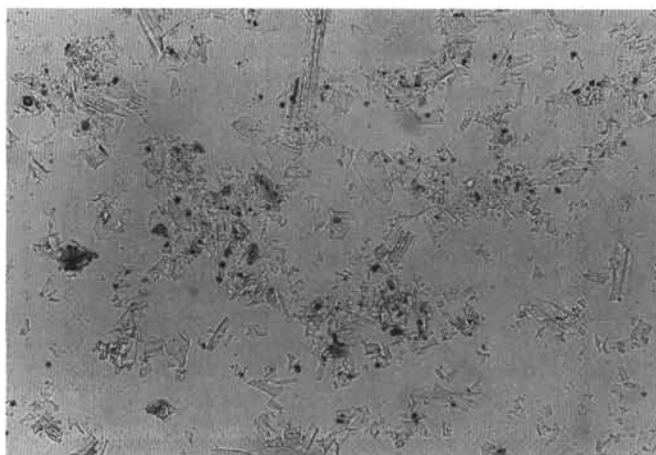


Figure 6. Photomicrograph of a smear slide from a volcanic ash-fall layer in Unit I. The layer consists dominantly of bubble wall, tubular, and pumice shards with rare crystals of feldspar. Field of view is 4.0 mm wide. Sample 157-953A-5H-3, 54–55 cm.

## Unit III

Interval: Sections 157-953C-10R-1 to 157-953C-23R-6  
Depth: 264–398 mbsf  
Age: early Pliocene to late Miocene

Unit III is 134 m thick. The dominant lithology is gray to brownish-gray, clayey nanofossil ooze that is interbedded with minor graded nanofossil clay-silt, foraminifer lithic silts and sands, and foraminifer sands. It differs from Unit II by having a much lower proportion of coarse-grained basaltic volcaniclastics (Fig. 2).

In Cores 157-953C-16R, 157-953C-19R, 157-953C-20R, 157-953C-21R, and 157-953C-22R there are chaotic mixtures of clayey nanofossil ooze, clayey nanofossil mixed sediment, and foraminifer lithic sands and silts. They range in thickness from 0.5 to about 1.5 m. In many instances the sequences show soft sediment deformation structures indicating slumping of unconsolidated sediments. In some, however, sediments occur as discrete clasts with sharp boundaries supported in a matrix of finer grained sediment. Such sequences may have been emplaced by debris flows.

## Unit IV

Interval: Sections 157-953C-24R-1 to 157-953C-70R-6  
Depth: 398–850 mbsf  
Age: late to middle Miocene

Unit IV is 452 m thick and contains a great variety of sedimentary lithologies that reflect the mixing of distinct volcanic, pelagic, and neritic components. The major lithologies include nanofossil chalk, nanofossil mixed sedimentary rock, foraminifer sands, lithic-crystal sands and silts, lithic and vitric lapillistones, vitric tuffs, nanofossil claystone, and claystone. Unit IV has been subdivided into three subunits based on the frequency and lithology of volcaniclastic sediments emplaced by sediment gravity flows.

### Subunit IVa

Interval: Sections 157-953C-26R-1 to 157-953C-34R-6  
Depth: 398–504 mbsf

Subunit IVa consists of nanofossil mixed sedimentary rock and nanofossil chalk interbedded with nanofossil claystones and claystones that typically grade downward into dark lithic-crystal siltstone

or sandstone. The subunit is distinguished from Unit III by (1) the increasing abundance of volcanoclastic siltstones and sandstones (Fig. 2), (2) the change in color of the mixed sedimentary rocks, nannofossil claystone, and lithic crystal siltstones and sandstones from gray/dark gray to green/dark green, and (3) a decrease in the amount of nannofossil chalk.

Abundant green to dark gray nannofossil claystone and claystone occur as medium bedded units that grade downward into thin siltstone or sandstone bases. The upper contacts are generally moderately to extensively bioturbated whereas lower contacts are almost always sharp. Many of the siltstone and sandstone bases are parallel laminated, or more rarely, cross-laminated (Fig. 7). Such units are interpreted as the deposits of turbidity currents that interrupted the background pelagic sedimentation of nannofossil chalk. The claystone parts of these units consist of ~75% clay minerals, 10% nannofossils, 10% foraminifers, and 5% volcanic minerals such as clinopyroxene, alkali feldspar, and biotite. Siltstone and sandstone bases can vary widely in their lithology as a result of the mixing of volcanoclastic and carbonate components. In Core 157-953C-30R the base of one of these units is composed of 35% felsic rock fragments, mostly phonolite, 20% mafic rock fragments, 2% pumice, 1% sideromelane fragments, 10% plagioclase, 4% clinopyroxene, and trace amounts of clay minerals. One of the characteristic features of the crystal lithic siltstones and sandstones of Subunit IVa is the common occurrence of felsic rock fragments and their isolated phenocrysts such as alkali feldspar, green clinopyroxene, amphibole, and biotite.

Nannofossil mixed sedimentary rock is also a common lithology in Subunit IVa and is usually gray to green. It may form the top of graded units or occur as interbeds with gradational contacts to the surrounding sediments. Often it is coarser grained than nannofossil ooze as a result of the presence of volcanic minerals and rock fragments of silt and sand size. In Core 157-953C-34R there is a coarse grained variety that consists of 20% basaltic rock fragments, 20% nannofossils, 25% clay minerals, 20% zeolite, 5% foraminifers, 5% bioclasts, and 5% plagioclase.

Foraminifer sands constitute a relatively minor proportion of Subunit IVa, occurring as thin to medium bedded units with sharp bases and moderately bioturbated tops. Some units are massive whereas others show normal grading and parallel lamination. In Core 157-953C-28R a foraminifer sand unit contains 65% foraminifers, 16% nannofossils, 10% clay minerals, 5% bioclasts, 1% plagioclase, and 3% alkali feldspar. These layers vary from light to medium gray depending upon the amount of volcanoclastic material.

Subunit IVa also has several intervals of slump deposits in Cores 157-953C-33R and 157-953C-35R. In Core 157-953C-35R, a 3 m sequence of highly deformed sediment contains two thick-bedded intervals of very poorly sorted lapillistone (Fig. 8). The majority of clasts are matrix supported, up to 3 cm long, and consist of angular mafic and felsic lava fragments.

#### Subunit IVb

Interval: Sections 157-953C-34R-6 through 157-953C-60R-6  
Depth: 504–754 mbsf

Subunit IVb is 250 m thick and consists of gray to green nannofossil mixed sedimentary rock interbedded with nannofossil claystone and claystone that typically grades downward into dark lithic, crystal or vitric siltstone, and sandstone bases. The subunit is distinguished from Subunit IVa by the increasing thickness and grain size of volcanoclastic sandstones (Fig. 2) and the more common occurrence of debris flow and slump deposits.

A characteristic feature of Subunit IVb is the occurrence of thick to very thick bedded volcanoclastic sandstones with varying proportions of lithic, crystal, vitric, and biogenic components. Many of these units are structureless with sharp basal contacts and slightly bioturbated tops. Some beds exhibit normal grading and a transition

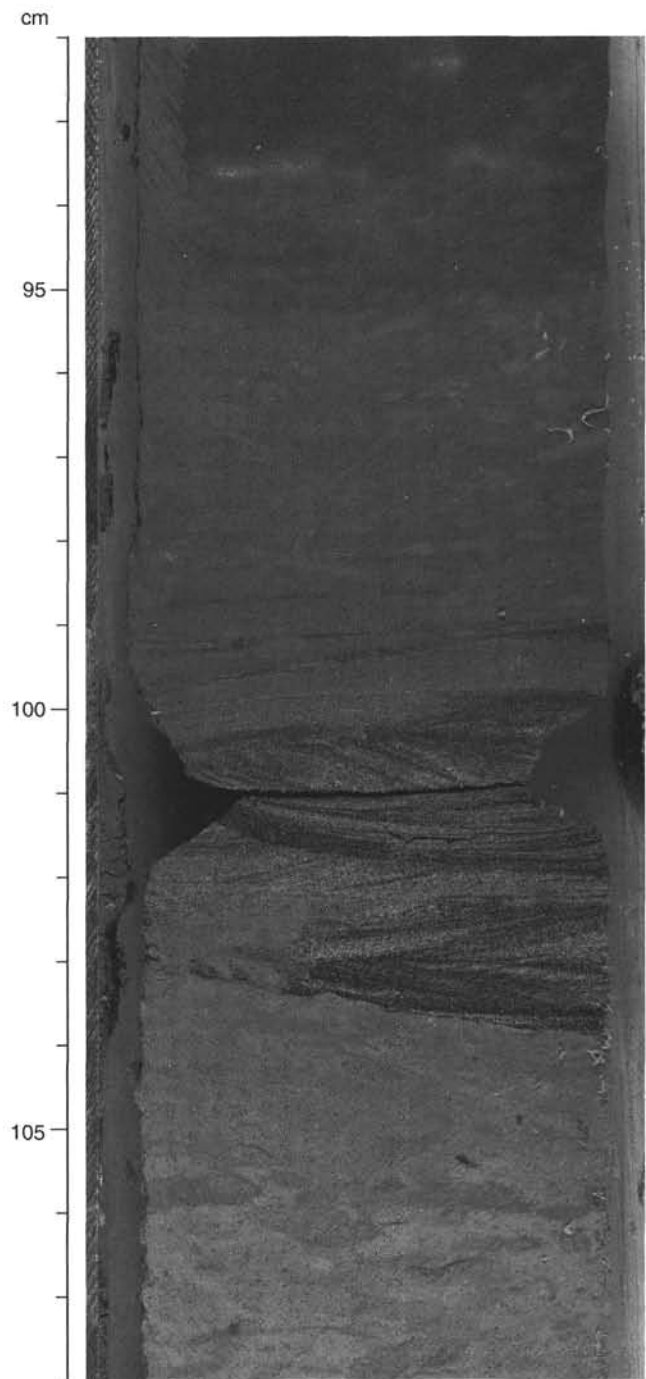


Figure 7. Cross-laminated base of a turbidite deposit from Subunit IVa. Interval 157-953C-34R-5, 92–108 cm.

to parallel laminated structures in their tops. Sandstones composed of particles with greatly contrasting density, such as low density vesicular pumice and dense mafic rock fragments, may show reversed grading (Fig. 9). Light gray sandstones often contain greater abundances of calcareous material. For example, a massive sandstone in Section 157-953C-51R-1 is composed of 25% foraminifers, 20% nannofossils, 20% pumice fragments, 5% basalt lithic fragments, and 1% clinopyroxene.

Some sandstones are composed almost entirely of vitric components such as pumice and glass shards with lesser amounts of crystals

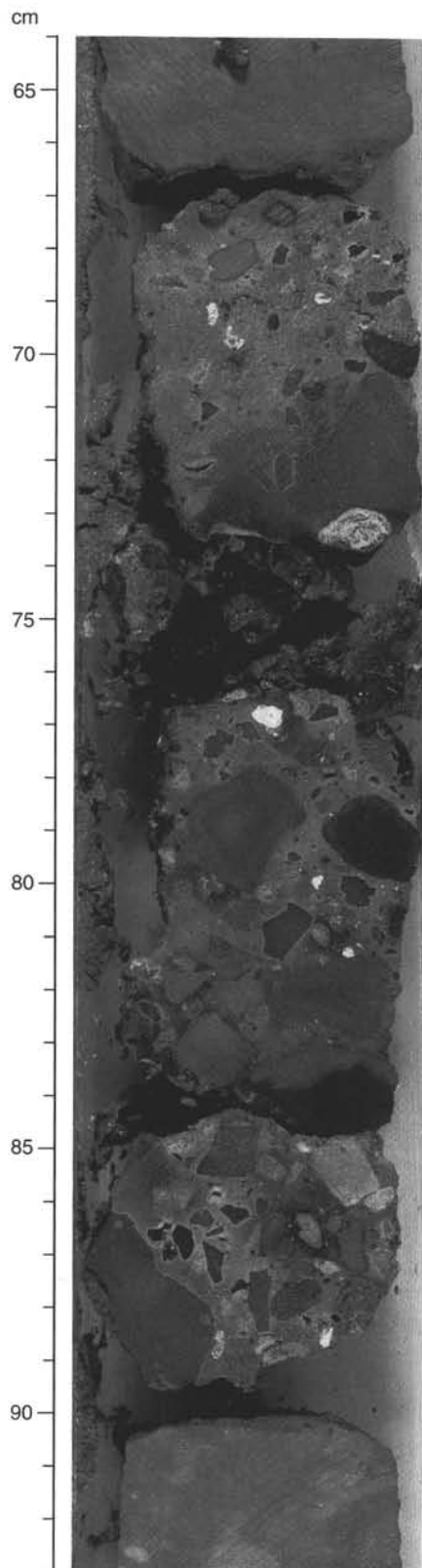


Figure 8. Poorly sorted lapillistone interval within slumped sediments of Subunit VIa. Note the large angular clasts of mafic and felsic volcanic rocks supported in a silty sand matrix. Interval 157-953C-35R-2, 64–93 cm.

and lithic fragments. Pumice and scoria fragments range up to 5 mm, vary from white to black, and are highly vesicular (Fig. 10). The dominant crystals in order of decreasing abundance are alkali feldspar, plagioclase, green clinopyroxene, aegirine, hornblende, biotite, and Fe-Ti oxides. Most crystals are anhedral to subhedral and can range up to 2 mm in diameter.

As in Subunit IVa, graded claystone to sandstone units also form important depositional units in Subunit IVb. However, these deposits are more usually thick bedded and display a greater variety of sedimentary structures than in Subunit IVa. A typical unit consists of either gray to dark green clayey nannofossil mixed sedimentary rock, nannofossil claystone, or claystone that grades downward to siltstone, and finally sandstone at the base. The upper contact of the deposit is usually moderately to extensively bioturbated and structureless. Downcore, the clay to silt-size material is usually parallel laminated and at the base the sandstone divisions are either parallel or cross laminated. Many of the laminated bases show a distinctive alternation in color that reflects the different lithology of the components (Fig. 11).

Very coarse-grained lithologies constitute a minor fraction of Subunit IVa. In Core 157-953C-45R a thick bedded lapillistone (1.3 m) contains angular to subangular clasts of phonolite and basalt up to 2 cm in diameter, matrix-supported, and normally graded. Finer grained material consists of sideromelane, clinopyroxene, alkali feldspar, tachylite, and foraminifer fragments. A similar but coarser variety of this deposit occurs in Section 157-953C-50R-3 as a massive lithic breccia with angular to subangular clasts of phonolite and basalt up to 4 cm in diameter (Fig. 12). Some phonolite fragments contain large alkali feldspar phenocrysts, whereas basaltic fragments are microlitic and contain clinopyroxene glomerocrysts and plagioclase microlites in a brownish or oxidized glassy matrix.

Slump deposits occur intermittently throughout Subunit IVb and are present in Cores 157-953C-37R, -46R, -47R, and -50R.

#### *Subunit IVc*

Interval: Sections 157-953C-61R-1 to 157-953C-70R-6  
Depth: 754–850 mbsf

Subunit IVc is 96 m thick and consists of interbedded nannofossil mixed sedimentary rock, green to brown crystal vitric sandstones and siltstones, lapillistones, vitric tuff, and graded green nannofossil clay-sandstones. Nannofossil chalk is present as a minor lithology. The subunit is distinguished from Subunit IVb primarily by a large increase in the abundance of coarse and fine vitric material in the siltstone and sandstone units.

Vitric-rich sandstones, tuffs, and lapillistones commonly occur throughout Subunit IVc as discrete units interbedded with subordinate amounts of nannofossil mixed sedimentary rock or nannofossil chalk. Sandstones commonly form the base of graded sequences that have an upper part consisting of nannofossil mixed sedimentary rock, nannofossil claystone or claystone, with abundant fine grained vitric components. In some cases the upper parts may be dominated by glass shards and crystals. The deposits are typically medium to thick bedded with sharp bases and bioturbated tops. They are interpreted as turbidite deposits. In Section 157-953C-62R-4 a basal sandstone consists dominantly of clear glass shards with minor amounts of alkali feldspar, biotite, green pyroxene, and foraminifer fragments.

Massive vitric sandstones without graded tops are another variety of coarse-grained deposit in Subunit IVc. They are typically medium to thin bedded, slightly normally graded, and they also have sharp basal contacts. Some units consist of a mixture of felsic and mafic pumice, with crystals and dense mafic lithics. In such units, low density felsic pumice is concentrated in the middle of the deposit while higher density components are more abundant at the base.

A characteristic feature of Subunit IVc is the occurrence of vitric tuffs that are virtually devoid of other sedimentary components.

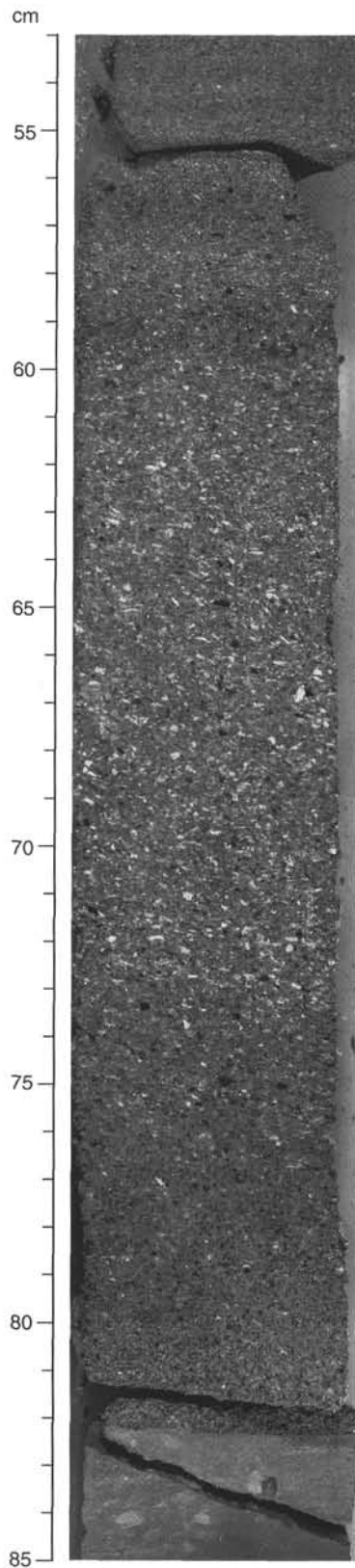


Figure 9. Coarse-grained turbidite showing the concentration of white pumice grains in the middle of the deposit. These clasts are large but have a lower density than the darker grains at the base. Interval 157-953C-54R-1, 53–85 cm.

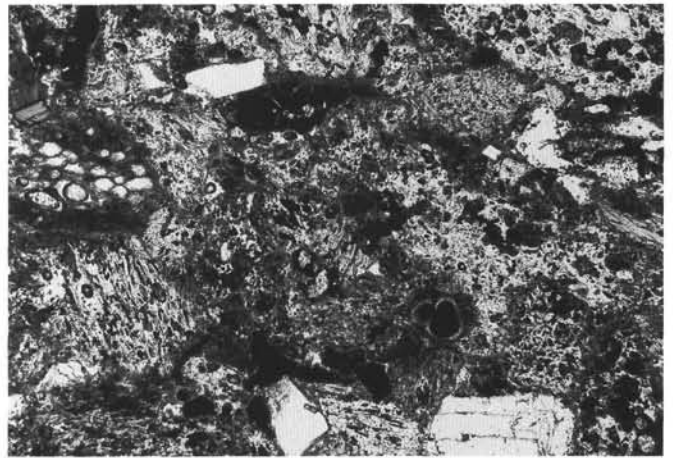


Figure 10. Photomicrograph showing vesicular felsic pumice clasts from a vitric crystal sandstone deposit in Subunit IVb. Phenocrysts and microphenocrysts of alkali feldspar, amphibole, and biotite occur as individual crystals in the sandstone matrix. Field of view is 4.0 mm wide. Interval 157-953C-59R-5, 113–118 cm.

These deposits may be the result of direct influx of pyroclastic material into the sea during explosive eruptions on nearby Gran Canaria. An excellent example is a thick bedded unit in Section 157-953C-65R-6, which grades downward from a fine-grained, structureless vitric tuff at the top through a zone of parallel and convolute laminations into a structureless coarse vitric tuff at the base. It consists of about 90% clear glass shards with thin bubble wall and tubular vesicular morphologies (Fig. 13). Small pumice fragments ranging in size from 200  $\mu\text{m}$  to 1 cm in diameter are also present and are typically very highly vesiculated. Angular to subangular crystals occur throughout with the dominant types as alkali feldspar, amphibole, and Fe-Ti oxides.

Coarse-grained vitric lithic lapillistones are much less abundant and are typically structureless, very thick bedded, with matrix-supported clasts. In Section 157-953C-64R-1 a vitric-lithic lapillistone consists of felsic pumice, subangular basalt fragments, and large crystals of plagioclase, alkali feldspar, amphibole, and biotite. Minor constituents include obsidian, sideromelane fragments, and small pieces of gabbro. The larger components are contained within a fine-grained matrix with nanofossils, foraminifer fragments, and clay minerals.

A minor but distinctive depositional sequence in Subunit IVc consists of thin bedded nanofossil mixed sedimentary rocks that show a sharp color change within the depositional unit from pale bluish green above to olive green below. The upper contacts of these units are usually moderately to extensively bioturbated and the bases are sharp. In many cases the bases have a thin layer of gray to dark gray siltstone. Examination of smear slides of this material shows abundant rounded quartz grains. These units bear many similarities to the thick bedded organic-rich turbidite sequences that were recovered at Sites 950, 951, and 952 on the Madeira Abyssal Plain and are likely to be derived from the same source considering that quartz does not occur in the volcanic rocks of the Canary Islands except as minor groundmass components in the rhyolitic ignimbrites of Gran Canaria (Schmincke, 1982).

### Unit V

Interval: Sections 157-953C-71R-1 to 157-953C-74R-6  
Depth: 850–889 mbsf  
Age: middle Miocene

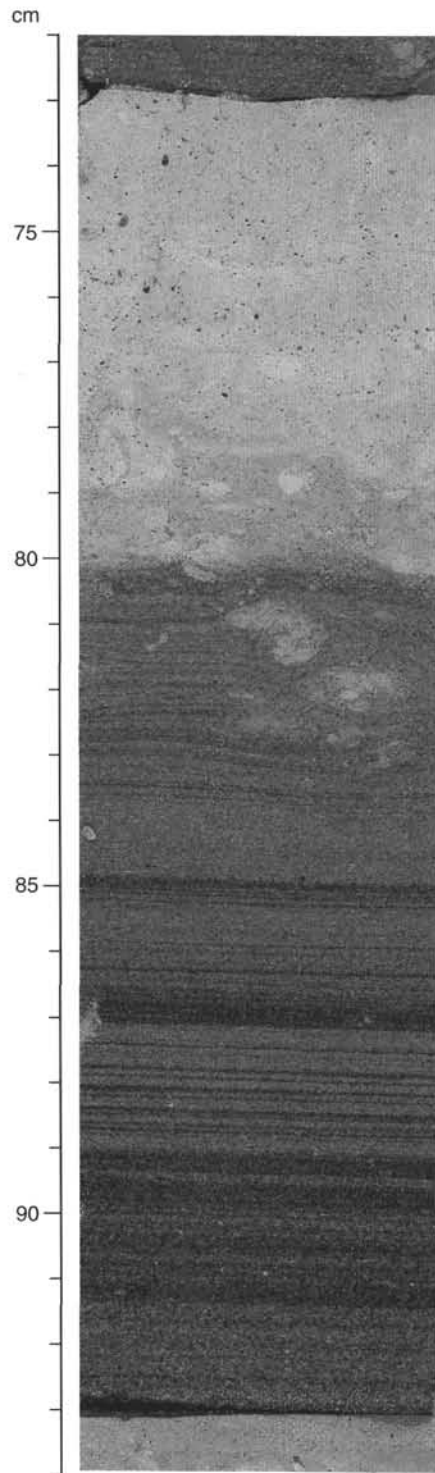


Figure 11. Parallel laminated base of a turbidite deposit from Subunit IVb. Note the alternation in color of the parallel lamination resulting from the fractionation of calcareous (light) and volcanoclastic (dark) components. Interval 157-953C-48R-5, 72–94 cm.

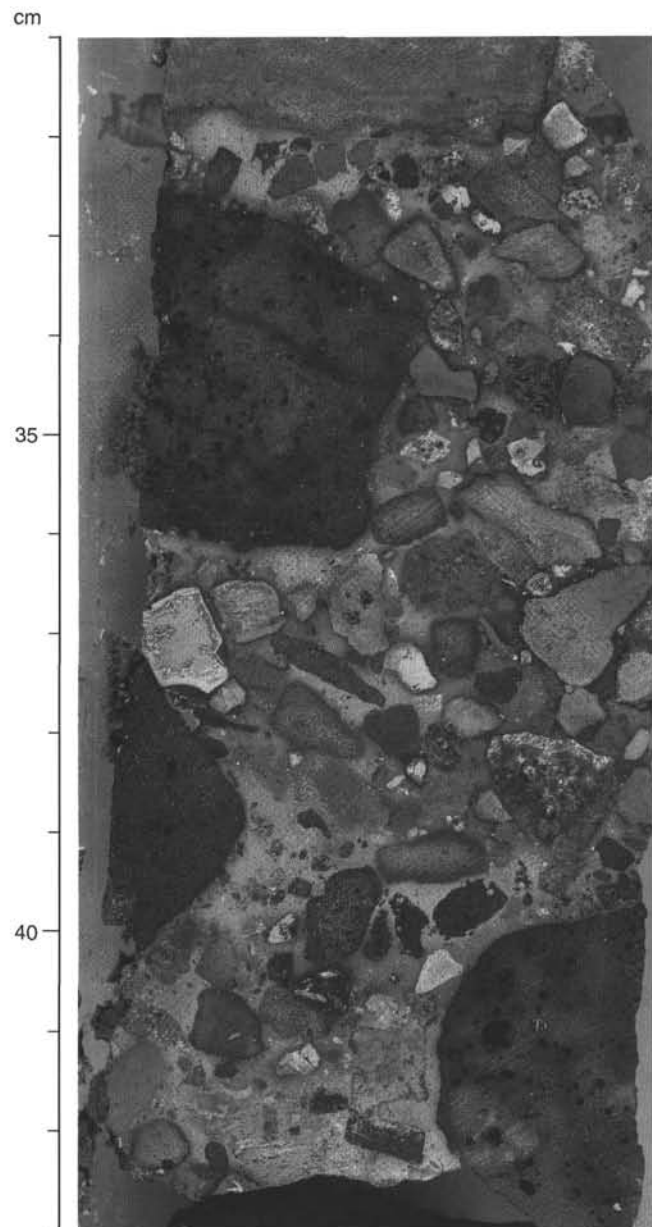


Figure 12. Poorly sorted lapillistone with pebble and cobble sized clasts of basalt and phonolite in a silty fine crystal-lithic sand matrix. Note the great diversity of lithologies and shapes of the large clasts. Interval 157-953C-50R-4, 31–43 cm.

Unit V is 49 m thick and is comprised of nannofossil mixed sedimentary rock, nannofossil claystone, claystone, lithic crystal siltstones and sandstones, and lapillistone. The unit is distinguished from Subunit IVc by the absence of felsic volcanoclastic material, a decrease in the thickness of sandstone deposits, and a sharp change in color from predominantly gray, dark gray, and green in Unit IVc to a dark purplish gray in Unit V.

Graded sequences of dark gray to purple gray nannofossil claystone or claystone that grade downward into basal lithic-crystal siltstone and sandstone dominant in Unit V. The sequences occur mostly as numerous thin to medium bedded units with bioturbated tops and sharp bases. Many show change from structureless tops through par-

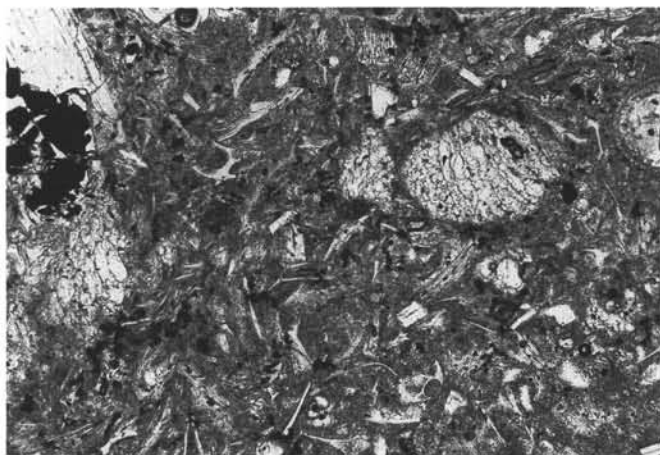


Figure 13. Photomicrograph showing vesicular felsic glass shards from a vitric tuff in Subunit IVc. Rare phenocrysts and microphenocrysts of alkali feldspar, amphibole, and biotite occur as individual crystals. Field of view is 4.0 mm wide. Sample 157-953C-65R-6, 100–101 cm.

allel laminated in middle portions to cross laminated at the base. Sandstone and siltstone bases of turbidite sequences typically consist of crystal and mafic rock fragments. For example, in Section 157-953C-71R-5 a thick bedded sandstone is composed of 60% tachylite and crystalline basalt grains, 30% zeolites, 10% clinopyroxene, and minor altered olivine and sideromelane fragments. Other sandstones consist of a higher proportion of mafic vitric material. In the interval 157-953C-73R-4, 25–28 cm, the base of a dark gray, medium-bedded turbidite is composed of abundant hyaloclastite shards that are highly altered, tachylite basalt clasts, and lesser amounts of clinopyroxene and biogenic debris (Fig. 14).

Very coarse-grained deposits are rare in Unit V. Only one lapillistone occurs in the interval 157-953C-71R-4, 0–40 cm. It is thick bedded and normally graded with sharp upper and lower contacts. The dominant components are altered sideromelane fragments and basaltic clasts of both tachylitic and crystalline variety.

Gray to dark gray, clayey nannofossil mixed sedimentary rock is also a relatively minor lithology of Unit V and occurs as thin to very thin bedded intervals between graded turbidite sequences. It is commonly moderately to extensively bioturbated and in many cases is only present within burrows at the top of individual turbidites. In some cores it also occurs as the mud portion of turbidite beds that have a distinctive color change from pale bluish green to dark olive green at the base. These are similar to the units described in Subunit IVc. They are typically thin to medium bedded, have bioturbated tops and are in sharp contact with the underlying sediment.

### Unit VI

Interval: Sections 157-953C-75R-1 to 157-953C-83R-3

Depth: 889–969 mbsf

Age: middle Miocene (but the time represented by the unit is difficult to constrain because microfossil-bearing sediments are rare)

Unit VI is 80 m thick and consists largely of thick to very thick bedded basaltic sandstone, lapillistone, and breccia with minor interbedded thinner units of calcareous claystone and nannofossil mixed sedimentary rock. The unit is distinguished from Subunit V by the great abundance of thick bedded, coarse-grained units of predominantly mafic volcanoclastic sediment (Fig. 2).

Sandstone and lapillistone occur as thin to very thick bedded layers that are commonly normally graded. In many instances lapilli-

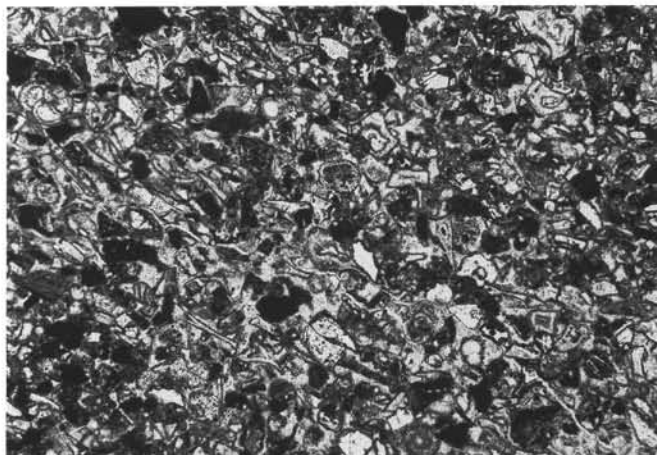


Figure 14. Photomicrograph of a vitric lithic sandstone from Unit V showing hyaloclastite grains, tachylite basalt fragments, clinopyroxene and calcareous biogenic debris. Field of view is 4.0 mm wide. Sample 157-953C-73R-4, 25–28 cm.

stones grade into breccia. The composition of the sandstone and lapillistone varies considerably from one unit to the next but the major components are altered vesicular glass, crystallized and tachylitic basaltic rock fragments, altered sideromelane, clinopyroxene, plagioclase, and minor biogenic debris. Many of the lapillistone units, and especially the breccias, contain large fragments of basalt with varying degrees of alteration. These clasts range up to 20 cm in diameter based on lengths in the core and may have been considerably larger. Commonly they are moderately vesicular with many of the vesicles being filled by zeolites. Some are rounded but most are angular to subangular. In Core 157-953C-78R a basaltic lapillistone contains a pillow basalt fragment with a well-developed quenched rim ~0.5 cm thick (Fig. 15). Hyaloclastite fragments in these deposits are generally ash to lapilli size, are moderately vesicular, and have been completely altered.

Nannofossil mixed sedimentary rock, nannofossil claystone, and claystones occur as thin to medium bedded deposits between the thicker and coarser grained lapillistone and breccia. Their occurrence is limited to Cores 157-953C-79R and 157-953C-83R where they typically form turbidite sequences grading from nannofossil claystone to lithic-crystal siltstones and sandstones.

### Unit VII

Interval: Sections 157-953C-83R-4 to 157-953C-103R-7

Depth: 969–1158.7 mbsf

Age: late-early Miocene, but as with Unit VI its duration is poorly constrained

Unit VII consists entirely of dark green hyaloclastite tuffs, lapillistones, and breccias. It is distinguished from Unit VI by an increased abundance of altered hyaloclastite fragments and a lack of interbedded fine-grained sediment. Lithologically it is the most homogeneous unit of Site 953 and extends for a minimum of 190 m.

Altered hyaloclastite fragments, tachylite, crystalline basalt, and crystals of plagioclase, clinopyroxene, altered olivine, Fe-Ti oxides, and rare plagioclase are the major components of the deposits of Unit VII. Hyaloclastite fragments are usually ash to lapilli size and comprise both vesiculated and blocky types (Fig. 16). The most common deposit type is very thick bedded (up to 20 m), and consists of hyaloclastite tuffs and lapillistones that grade downward into hyaloclastite breccias. The disparity in size between the matrix and lithic clasts increases with depth in an individual sequence; the breccia bases are

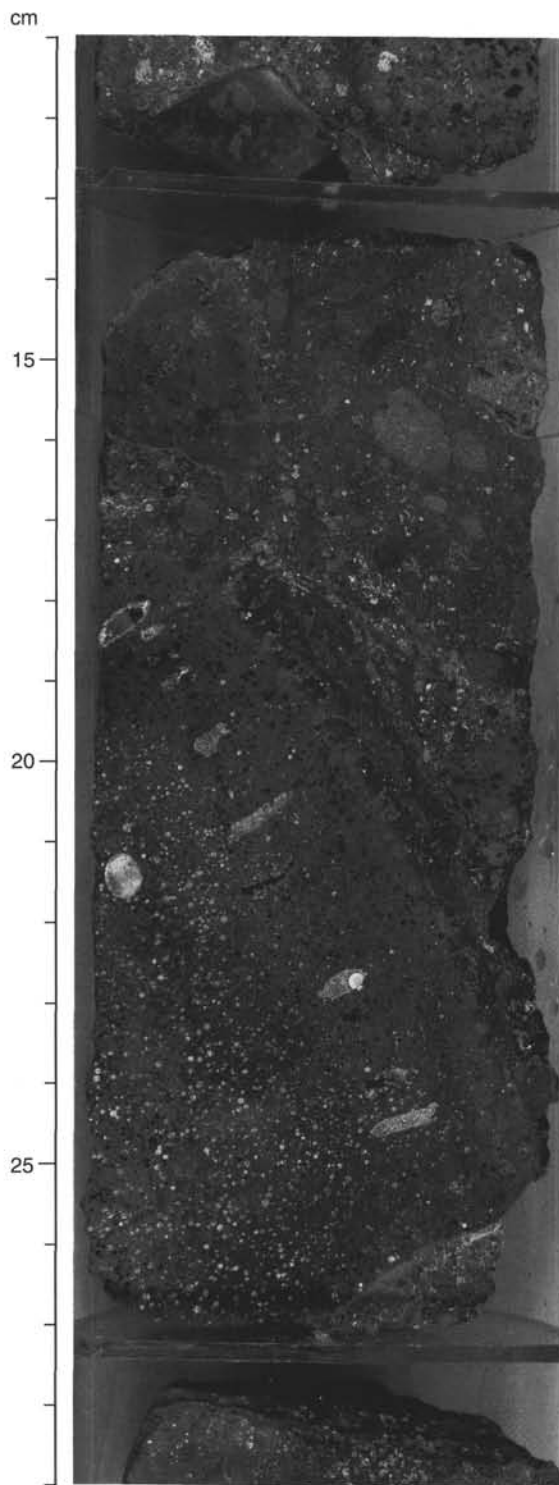


Figure 15. Pillow basalt clast in a basaltic lapillistone from Unit VI. Note the remnant quenched rim of the pillow clast and the slightly vesicular interior. Interval 157-953C-78R-1, 11–29 cm.



Figure 16. Photomicrograph of hyaloclastite fragments from a hyaloclastite tuff in Unit VII. Note the moderate vesicularity of the hyaloclastite grains. Clinopyroxene, altered olivine, and clasts of basalt are also present. Field of view is 8.0 mm wide. Sample 157-953C-87R-2, 79–82 cm.

very poorly sorted. In a single unit basalt clasts can vary from less than a centimeter in the upper tuffaceous part to more than 20 cm in the basal breccia. The accessory basalt clasts are moderately vesicular to dense nonvesicular. They vary from dark gray to reddish orange. Most are clinopyroxene-olivine-phyric. Abundant pseudomorphs of olivine in some basalt clasts indicate that picritic types are also present.

A second variety of hyaloclastite-bearing deposits is medium bedded hyaloclastite tuffs with relatively minor grading and a lower content of large basalt clasts. Many of these units are parallel laminated and some are cross-bedded at the base. In Core 157-953-98R a thick-bedded, hyaloclastite lapillistone overlays a laminated hyaloclastite tuff. Just below this contact the laminations in the upper part of the tuff are deformed and convoluted, suggesting slumping when the overlying lapillistone was deposited (Fig. 17).

### Depositional History

The oldest sediments recovered at Site 953 are middle to late early Miocene (~15–16 Ma, Unit VII), during which time the site was being inundated with basaltic hyaloclastites mixed with a variety of basalt clasts (Fig. 18). The poor sorting, slight reverse grading at the base, and the matrix-supported nature of many of the very thick bedded hyaloclastite deposits suggest debris flow deposition. Finer grained, parallel, laminated hyaloclastite tuffs were more likely deposited from high-concentration turbidity currents. The vesicular nature of hyaloclastite fragments suggests that they were formed by shallow submarine eruption of basaltic magma. The lack of interbedded pelagic sediments between the hyaloclastite tuffs, lapillistones, and breccia suggests that either the sedimentation rate of this material was high enough to prevent significant accumulation of pelagic sediment or that the debris flows and turbidity currents were consistently eroding any pelagic material that had accumulated between events. In Unit VI intervals of pelagic and fine-grained turbidites are found between coarse deposits that were probably emplaced by a similar mechanism as in Unit VII and thus a high sedimentation rate may be the preferred explanation for the lack of pelagic sediments in Subunit VII.

Unit VI represents a more compositionally diverse source of material to Site 953 during the middle Miocene. Lapillistone and breccias contain a higher proportion of basaltic lithic clasts, many of which are vesicular. The diversity of basalt lithologies, the presence

of vesicles in both lithic clasts and hyaloclastites, and the reddish oxidized color of many fragments suggest that they formed by both sub-aerial and shallow submarine volcanism. The material was emplaced by debris flows and turbidity currents. However, in Unit VI the occurrence of interbeds of nannofossil mixed sedimentary rock and claystone indicates that the influx of material may have been slightly less frequent than in Unit VII.

Coarse hyaloclastite debris drastically decreases in passing from Unit VI to Unit V (Fig. 2). Sedimentation during Unit V was dominated by numerous turbidites that deposited thin to medium bedded claystone-sandstone sequences of predominantly mafic composition. The regular repetition of these units is a characteristic feature of Unit V. Throughout Unit V there appears to have been an increase in the number of turbidites although this is not reflected by a major increase in the total amount of sand per core (Fig. 2), and thus the events must have been of relatively small volume.

At about 14 Ma (Subunit IVc) two fundamental changes occurred: an increase in the thickness and number of sand units being deposited, and the first appearance of felsic vitric components in the sequence. In Core 157-953C-70R the occurrence of zircon in a deposit with basalt fragments and pumice is correlated to the P1 ignimbrite on Gran Canaria (Schmincke, 1994). High precision single crystal dating of the P1 deposit yields an age of 14 Ma (Bogaard et al., 1988) and thus forms an important chronostratigraphic horizon at Site 953. This ignimbrite signals the beginning of the highly explosive Mogan phase of volcanism on Gran Canaria (13.4–14 Ma) and is a likely source of the volcanoclastics in Subunit IVc (Fig. 1). Material from this phase of volcanism was transported to the basin by turbidity currents and debris flows to form vitric tuffs and lapillistones. Some units may be the distal equivalents of pyroclastic flows that entered the sea around Gran Canaria. In Core 157-953C-64R-1 a crystal tuff contains felsic pumice, alkali feldspar, amphibole, and biotite, which is correlated to the Fataga stage of volcanism on Gran Canaria inferred to have occurred at 9.5–13.4 Ma, according to single crystal dating (Schmincke, 1994).

The distinctive turbidites that are pale to bluish green near their tops but show an abrupt color change to olive green toward the base may have been derived from a more distal source such as the continental margin of Africa based on the occurrence of quartz in their basal siltstones. Similar organic-rich turbidites are a prominent sediment type of the Madeira Abyssal Plain west of Site 953 and were recovered at Sites 950, 951, and 952. Deposition of such units is unusual as there is presently a topographic barrier limiting access of this material to Site 953. The occurrence of these layers in the middle Miocene may result from (1) lower inter-island submarine ridges, (2) a different source area of organic-rich turbidites that could reach the site by obscure routes involving reflection or refraction around local topography, or (3) particularly large turbidity currents that were able to surmount topographic barriers and locally deposit thin bedded equivalents of flows that may have continued to the Madeira Abyssal Plain.

The transition from Unit IVc to IVb at about 13.4 Ma is marked by a decrease in the abundance of felsic vitric material being supplied by turbidity currents and other types of sediment gravity flows. For the next 3 m.y. the flux of volcanoclastic sediment to the site was high as shown by a broad region of high sand content and the large number of events per core (Fig. 2). Deposition of material occurred primarily by turbidity currents that supplied large volumes of felsic volcanoclastic material. The lithology and color of this material suggest that the Fataga stage of volcanism and the erosion of its subaerial products were a major source of this sediment. Pelagic sedimentation during this interval was dominated by nannofossil ooze (Fig. 3).

At about 10.5 Ma the flux of volcanoclastic material decreased but the number of turbidite events increased (Fig. 2). Formation of Subunit IVa was dominated by a combination of pelagic sedimentation that produced intervals of nannofossil mixed sedimentary rock and nannofossil chalk (Fig. 3) and an intermittent influx of turbidity cur-

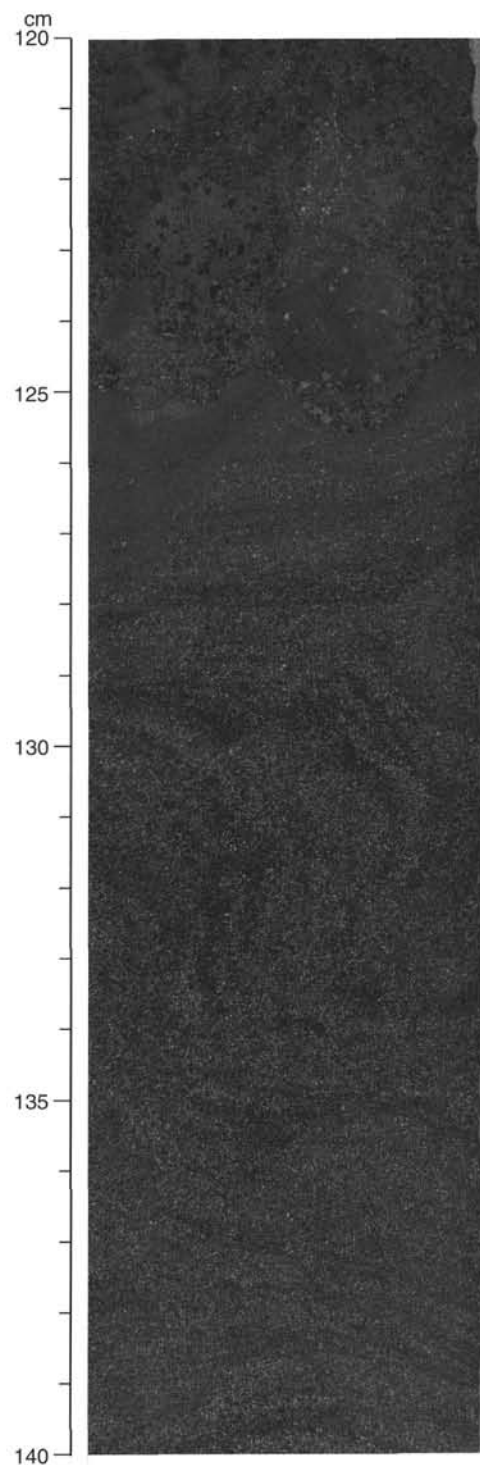


Figure 17. Base of a thick hyaloclastite lapillistone (upper) in contact with a hyaloclastite tuff (lower) from Unit VII. Note the convoluted and disrupted nature of the laminations in the lower unit. Interval 157-953C-98R-7, 120–140 cm.

rents that produced graded intervals of nannofossil mixed sedimentary rock or claystone to lithic crystal siltstones and sandstones.

The transition to Unit III in the late Miocene at about 8 Ma is marked by a further reduction in the influx of volcanoclastic material to some of the lowest levels recorded at the site (Fig. 2). During the

next 4 m.y. sedimentation was dominantly pelagic with only occasional influxes of coarse volcanoclastic or shallow water carbonate. There is some indication that the carbonate content of the pelagic component increased over this period (Fig. 3). The general lull in volcanoclastic input represented by Unit III corresponds to a volcanic hiatus on Gran Canaria that is estimated to have lasted from ~4.5 to 9.0 Ma (Schmincke, 1994).

In the late Pliocene a pulse of mafic volcanoclastic material to the site is represented by a sequence of dark, medium to thick-bedded turbidites. This marks the transition into Unit II at about 4 Ma and falls near the start of the Roque Nublo phase of volcanism on Gran Canaria that is inferred to have started at ~4.3 Ma and peaked at 4 Ma (Schmincke, 1994). Pelagic sedimentation at this time was dominated by nannofossil ooze (Fig. 3). A sharp drop in the abundance of sand layers at ~3 Ma marks the transition to Unit I (Fig. 2).

For the remaining 3 m.y. to the present, sedimentation at Site 953 was dominantly pelagic (nannofossil ooze) with an increase in the amount of shallow water carbonate delivered by turbidity currents and an intermittent supply of dominantly mafic volcanoclastic material most likely derived by the reworking of subaerial volcanic deposits. The increase in the flux of shallow water carbonate to the site is reflected in the markedly higher carbonate contents of turbidite bases within Unit I as compared to earlier units (Fig. 3). This increase may be related to the onset of glacial-interglacial cycles in the Pleistocene and the generation of turbidites during sea-level fluctuations. Fallout of felsic volcanic ash also occurred during this period, although its source is probably from highly explosive eruptions on the island of Tenerife. Tephra fall layers of similar age and mineralogy have also been found at Site 397, south of Gran Canaria (Schmincke and von Rad, 1979).

In summary, the supply of volcanoclastic material by sediment gravity flows and fallout has played a fundamental role in determining the lithostratigraphy of Site 953. This supply has changed dramatically both in its rate and lithology from the late Miocene to the present and reflects the proximity of the site to the volcanically active Canary Islands. To a first order, the variations in the marine record show an excellent correlation to the volcanic history of Gran Canaria. Although other sources may have supplied volcanoclastic material to the site, it is apparent that the lithostratigraphy has been controlled to a large degree by the mid-Miocene to recent subaerial and submarine volcanism of this island.

## BIOSTRATIGRAPHY

### Introduction

The age of sediments from Holes 953A, 953B, and 953C ranges from Pleistocene to early Miocene (Fig. 18). The recovery of calcareous nannofossils and planktonic foraminifers was good for zonal assignment and age determination.

Samples were taken from core catchers and split cores for foraminifer analysis, and preferentially from split cores for calcareous nannofossils. In the lower part of the sequence several samples were taken from turbiditic mud, dark volcanic sand, and calcareous sand, although we tried to sample pelagic ooze and avoid turbidites and slumped intervals wherever possible. Preservation was good and abundance was moderate to high for calcareous nannofossils and planktonic foraminifers to about 300 mbsf. Below this depth abundance and preservation gradually decreased.

Biostratigraphic resolution based on planktonic foraminifers deteriorated in the middle to early Miocene section, but nannofossil zones and subzones were well determined to 968.22 mbsf. The nannofossil and foraminifer zones are in close agreement within sampling resolution. Based on both foraminifer and nannofossil evidence, the Pleistocene/Pliocene boundary is placed between the lowest occurrence of *Globorotalia truncatulinoides* at 140.56 mbsf (Sample 157-953A-15H-CC, 0–2 cm) and the next sample downcore containing

*Discoaster brouweri* at 141.17 mbsf (Sample 157-953A-16H-1, 57 cm). There was some difficulty determining the Pliocene/Miocene boundary at Site 953 as a result of the rare occurrence of key marker species. However, foraminifer and nannofossil data place the boundary between the highest sample without definite *Globorotalia juanai* at 300.82 mbsf (Sample 157-953C-13R-CC, 0–2 cm) and the highest sample with *Discoaster quinqueramus* at 324.42 mbsf (Sample 157-953C-16R-2, 38 cm).

### Calcareous Nannofossils

Site 953 recovered an essentially complete early Miocene to Pleistocene sequence. Remarkably, every nannofossil zone and most subzones were found from CN3 in the early Miocene to CN15 in the Pleistocene. The only subzones not distinguished were those in CN10 (early Pliocene), where the subzonal marker species were very rare and sporadic in their occurrence. No major hiatuses were recognized, despite the presence of many turbidites with demonstrably erosive bases, suggesting that the depth of erosion caused by these turbidites was not large relative to the thickness of the sediments.

In the lower part of the section where turbidites were frequent, we sampled from burrows, many of which were infilled with lighter colored calcareous sediment. This burrow infill is interpreted to be representative of the original overlying hemipelagic sediment, which has since been eroded off by a succeeding turbidite. Many of the turbidites were volcanoclastic and thus they did not contribute significant reworked nannofossils to the burrow infill, so this approach seemed to give excellent results.

Preservation was good, and abundance was generally very high in the Pleistocene, with preservation gradually declining from the late Pliocene down. Abundances were generally moderate to high from the late Pliocene to the middle Miocene, below which abundances were low and preservation was poor (Table 2). *Discoaster* species were relatively rare, particularly in the middle Miocene.

Identifiable reworking was very rare, with the exception of some *Discoaster* species, *Helicosphaera sellii* and *Calcidiscus macintyreii* in the latest Pliocene to Pleistocene, and *Reticulofenestra pseudoumbilicus* in the late Pliocene. Sporadic occurrences of Cretaceous species were noted, along with a single specimen of an Eocene species in Sample 157-953A-4H-CC.

### Pleistocene

Pleistocene nannofossils were recovered from Samples 157-953A-1H-1, 125 cm (1.26 mbsf), to 157-953A-15H-CC (140.56 mbsf). The highest sample, 157-953A-1H-1, 125.5 cm (1.26 mbsf), was below the acme of *Emiliania huxleyi* in Zone CN15, indicating an age older than 82 Ka (Thierstein et al., 1977). The lowest occurrence of *E. huxleyi* could not be positively determined with the light microscope. Instead, the downcore change in dominance from *Gephyrocapsa* spp. smaller than about 3  $\mu\text{m}$  to *G. "caribbeanica"* larger than about 3  $\mu\text{m}$ , which occurs at the base of oxygen isotope Stage 7 (Weaver, 1983), was used to approximate the boundary between Zones CN15 and CN14. This change occurs between Samples 157-953A-2H-1, 74 cm (8.34 mbsf), and 157-953A-2H-4, 132 cm (13.42 mbsf).

The highest occurrence of *Pseudoemiliania lacunosa* in Sample 157-953A-3H-CC marks the base of Subzone CN14b. The highest occurrence of *Reticulofenestra asanoi* was in Sample 157-953A-6H-6, 65.5 cm (53.76 mbsf), and the lowest occurrence of *R. asanoi* was in Sample 157-953A-7H-CC (64.73 mbsf), which also contains the lowest occurrence of forms similar to *Gephyrocapsa oceanica* (i.e., forms with a large, open center and a bridge subparallel to the short axis), marking the base of Subzone CN14a.

Several events occur within Subzone CN13b: the highest occurrence of large (>5.5  $\mu\text{m}$  maximum diameter) *Gephyrocapsa* spp. in Sample 157-953A-9H-7, 25 cm (83.35 mbsf), and the lowest occurrence in Sample 157-953A-11H-3, 103 cm (97.13 mbsf). The highest

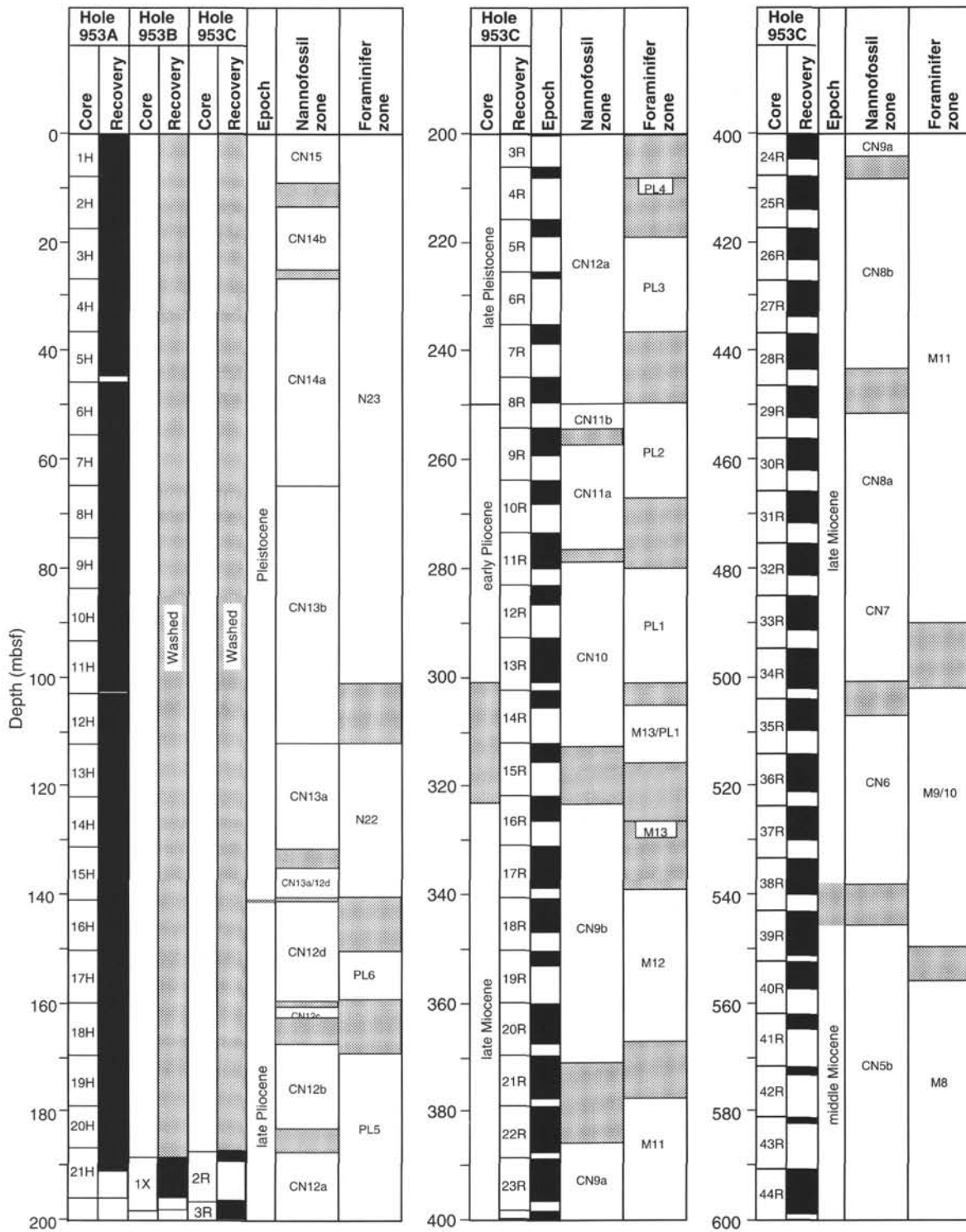


Figure 18. Nannofossil and foraminifer zonation at Site 953.

consistent occurrence of *Calcidiscus macintyreii* (>11 μm) was in Sample 157-953A-11H-6, 73 cm (101.33 mbsf). *C. macintyreii* was observed sporadically above this level but was considered reworked. The lowest occurrence of medium *Gephyrocapsa* spp. (>3 μm and <5.5 μm maximum diameter) in Sample 157-953A-12H-7, 61 cm (112.21 mbsf), was used to approximate the base of Zone CN13b.

*Helicosphaera sellii* was relatively common at this site; however, its highest occurrence in Sample 157-953A-9H-CC appears high rel-

ative to the highest consistent occurrence of *C. macintyreii* and the lowest occurrence of the large *Gephyrocapsa*.

#### Pliocene

*Discoaster brouweri* and *D. triradiatus* occurred rarely from Samples 157-953A-15H-3, 100 cm (135.10 mbsf), to 157-953A-15H-CC (140.56 mbsf), which is above the lowest occurrence of the

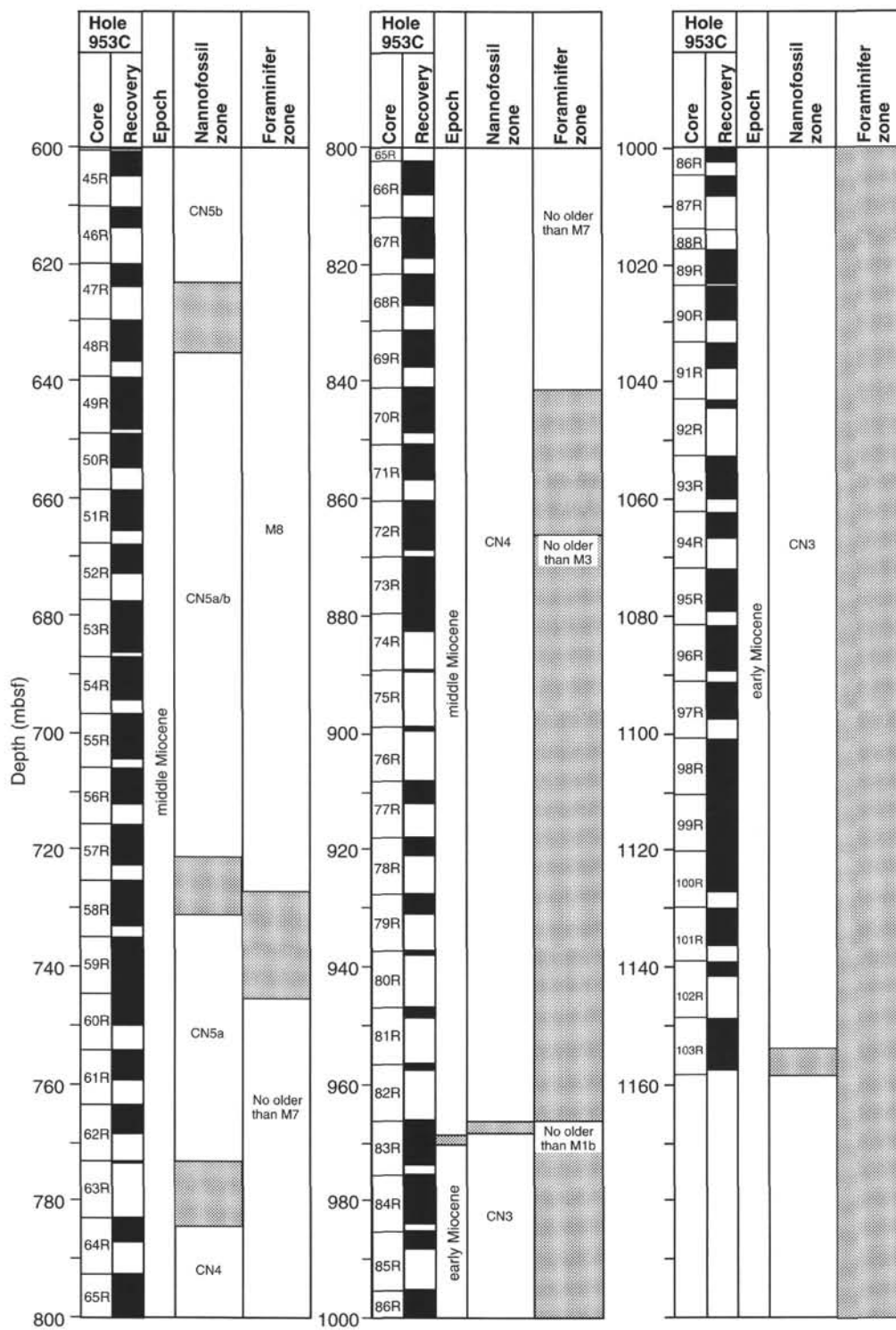


Figure 18 (continued).

planktonic foraminifer *Globorotalia truncatulinoides* in Sample 157-953A-15H-CC, 0–2 cm (140.56 mbsf). The FO datum of *G. truncatulinoides* defines the base of Zone N22 and is known to occur slightly above the LO datum of *D. brouweri* (see Tables 2 and 3 of the “Explanatory Notes,” this volume), so it is likely that these discoasters above the lowest occurrence of *G. truncatulinoides* in Hole 953A are reworked. Sample 157-953A-16H-1, 57 cm (141.17 mbsf), below the

lowest occurrence of *G. truncatulinoides*, was interpreted as the top of Subzone CN12d.

The highest occurrence of *Discoaster pentaradiatus* in Sample 157-953A-18H-1, 123 cm (160.83 mbsf), marked the top of Subzone CN12c, with the highest occurrence of *D. surculus* in Sample 157-953A-18H-6, 79 cm (167.89 mbsf), marking the top of Subzone CN12b. Subzone CN12a was indicated by the highest occurrence of

Table 2. Abundance, preservation, and lithology of samples used in nannofossil zonation, Site 953.

Core, section, interval (cm)	Depth (mbsf)	Abundance	Preservation	Zone	Lithology
157-953A-					
1H-1, 125.5–125.5	1.26	VH	G	CN15	Hemipelagic ooze
1H-3, 62–62	3.62	VH	G	CN15	Hemipelagic ooze
1H-5, 63–63	6.63	VH	G	CN15	Hemipelagic ooze
1H-CC, 0–0	7.45	M	M	CN15	Calcareous turbidite sand
2H-1, 74–74	8.34	VH	G	CN15	Hemipelagic ooze
2H-4, 132–132	13.42	VH	G	CN14b	Hemipelagic ooze
2H-6, 53–53	15.63	VH	G	CN14b	Hemipelagic ooze
2H-CC, 0–0	16.98	VH	G	CN14b	Hemipelagic ooze
3H-2, 33–33	18.93	VH	G	CN14b	Hemipelagic ooze
3H-6, 41.5–41.5	25.02	VH	G	CN14b	Hemipelagic ooze
3H-CC, 0–0	26.84	H	G	CN14a	Calcareous/volcanic turbidite sand
4H-1, 107–107	27.67	VH	G	CN14a	Hemipelagic ooze
4H-6, 93–93	35.03	VH	G	CN14a	Hemipelagic ooze
4H-CC, 0–0	36.29	H	M	CN14a	Turbidite sand
5H-1, 118–118	37.28	VH	G	CN14a	Hemipelagic ooze
5H-CC, 0–0	44.35	H	M	CN14a	Turbidite sand
6H-1, 72–72	46.32	VH	G	CN14a	Hemipelagic ooze
6H-6, 65.5–65.5	53.76	VH	G	CN14a	Hemipelagic ooze
6H-CC, 0–0	55.12	VH	G	CN14a	Hemipelagic ooze
7H-3, 103–103	59.13	VH	G	CN14a	Hemipelagic ooze
7H-6, 95–95	63.55	VH	G	CN14a	Hemipelagic ooze
7H-CC, 0–0	64.73	VH	G	CN14a	Hemipelagic ooze
8H-1, 42–42	65.02	VH	G	CN13b	Hemipelagic ooze
8H-6, 80–80	72.90	VH	G	CN13b	Hemipelagic ooze
9H-4, 36–36	78.96	VH	G	CN13b	Hemipelagic ooze
9H-7, 25–25	83.35	VH	G	CN13b	Hemipelagic ooze
9H-CC, 0–0	83.73	VH	G	CN13b	Hemipelagic ooze
10H-1, 86–86	84.46	VH	G	CN13b	Hemipelagic ooze
10H-6, 97–97	92.07	VH	G	CN13b	Hemipelagic ooze
10H-CC, 0–0	93.44	VH	G	CN13b	Hemipelagic ooze
11H-1, 113–113	94.23	VH	G	CN13b	Hemipelagic ooze
11H-3, 103–103	97.13	VH	G	CN13b	Hemipelagic ooze
11H-6, 73–73	101.33	VH	G	CN13b	Hemipelagic ooze
12H-1, 54–54	103.14	H	M	CN13b	Hemipelagic ooze
12H-7, 61–61	112.21	H	G	CN13b	Hemipelagic ooze
12H-CC, 0–0	112.28	VH	G	CN13a	Hemipelagic ooze
13H-1, 57–57	112.67	VH	G	CN13a	Hemipelagic ooze
13H-7, 15–15	121.25	H	G	CN13a	Hemipelagic ooze
13H-CC, 0–0	121.62	VH	G	CN13a	Hemipelagic ooze
14H-1, 54–54	122.14	VH	G	CN13a	Hemipelagic ooze
14H-7, 44–44	131.04	VH	G	CN13a	Hemipelagic ooze
14H-CC, 0–0	131.41	VH	G	CN13a	Hemipelagic ooze
15H-1, 51–51	131.61	H	G	CN13a	Hemipelagic ooze
15H-3, 100–100	135.10	VH	G	CN13a/12d	Hemipelagic ooze
15H-6, 69–69	139.29	VH	G	CN13a/12d	Hemipelagic ooze
15H-CC, 0–0	140.56	VH	M	CN13a/12d	Hemipelagic ooze
16H-1, 57–57	141.17	VH	G	CN12d	Hemipelagic ooze
16H-3, 113–113	144.73	H	G	CN12d	Hemipelagic ooze
16H-7, 50–50	150.10	VH	M	CN12d	Hemipelagic ooze
16H-CC, 0–0	150.44	H	M	CN12d	Turbidite
17H-6, 43–43	158.03	VH	M	CN12d	Hemipelagic ooze
17H-CC, 0–0	159.61	H	M	CN12d	Hemipelagic ooze
18H-1, 123–123	160.83	VH	G	CN12c	Hemipelagic ooze
18H-3, 10–10	162.70	VH	G	CN12c	Hemipelagic ooze
18H-6, 79–79	167.89	VH	G	CN12b	Hemipelagic ooze
18H-CC, 0–0	169.41	H	M	CN12b	Hemipelagic ooze
19H-6, 24–24	176.84	H	M	CN12b	Hemipelagic ooze
19H-CC, 0–0	178.70	H	M	CN12b	Hemipelagic ooze
20H-2, 6–6	180.16	H	G	CN12b	Hemipelagic ooze
20H-4, 13–13	183.23	H	M	CN12b	Hemipelagic ooze
20H-7, 4–4	187.64	H	M	CN12a	Hemipelagic ooze
20H-CC, 0–0	188.45	H	M	CN12a	Hemipelagic ooze?
21H-3, 132–132	192.42	H	M	CN12a	Hemipelagic ooze
21H-CC, 0–0	192.60	H	M	CN12a	Hemipelagic ooze?
157-953B-					
1X-2, 65–65	189.96	H	M	CN12a	Hemipelagic ooze
1X-6, 123–123	194.99	H	P	CN12a	Hemipelagic ooze
157-953C-					
3R-3, 46–46	199.96	VH	M	CN12a	Hemipelagic ooze
4R-1, 94–94	207.04	H	M	CN12a	Hemipelagic chalk
5R-2, 67–67	217.97	H	M	CN12a	Hemipelagic chalk
6R-1, 81–81	226.31	H	G	CN12a	Hemipelagic chalk
7R-1, 123–123	236.23	H	G	CN12a	Hemipelagic chalk
8R-4, 17–17	249.27	H	G	CN12a	Hemipelagic chalk
8R-CC, 0–0	249.40	H	M	CN11b	Turbidite
9R-1, 8–8	254.18	H	G	CN11b	Hemipelagic chalk
9R-3, 81–81	257.91	H	M	CN11a	Hemipelagic claystone
10R-1, 130–130	265.00	H	G	CN11a	Hemipelagic claystone
10R-CC, 0–0	267.70	H	M	CN11a	Hemipelagic chalk
11R-1, 15–15	273.55	H	M	CN11a	Hemipelagic chalk
11R-3, 57–57	276.97	H	M	CN11a	Hemipelagic chalk
11R-CC, 0–0	279.88	H	G	CN10	Hemipelagic chalk
13R-1, 93–93	293.63	VH	P	CN10	Calcareous turbidite
14R-2, 48–48	304.38	VH	P	CN10	Hemipelagic chalk
15R-2, 38–38	313.98	VH	P	CN10	Hemipelagic chalk
16R-2, 132–132	324.42	VH	P	CN9b	Slumped hemipelagic chalk?
17R-1, 140–140	332.50	VH	P	CN9b	Hemipelagic chalk

Table 2 (continued).

Core, section, interval (cm)	Depth (mbsf)	Abundance	Preservation	Zone	Lithology
17R-5, 144-144	338.54	VH	P	CN9b	Hemipelagic chalk
18R-1, 36-36	340.96	VH	P	CN9b	Hemipelagic chalk
18R-3, 101-101	344.61	VH	P	CN9b	Hemipelagic chalk
19R-1, 6-6	350.26	H	P	CN9b	Hemipelagic chalk
19R-1, 48-48	350.68	VH	P	CN9b	Hemipelagic chalk
19R-1, 143-143	351.63	H	P	CN9b	Slumped hemipelagic ooze?
20R-2, 79-79	362.09	H	P	CN9b	Hemipelagic chalk
21R-2, 102-102	372.02	H	P	CN9b	Hemipelagic chalk
22R-5, 18-18	385.28	H	P	CN9a	Hemipelagic chalk
23R-2, 63-63	390.73	H	M	CN9a	Hemipelagic chalk
23R-4, 87-87	393.97	M	M	CN9a	Hemipelagic chalk
24R-1, 30-30	398.40	H	M	CN9a	Hemipelagic chalk
24R-5, 4.5-4.5	404.15	H	M	CN9a	Hemipelagic chalk
25R-1, 32-32	408.02	M	M	CN8b	Hemipelagic claystone
25R-4, 10-10	412.30	M	M	CN8b	Hemipelagic chalk
26R-1, 58-58	417.88	H	M	CN8b	Hemipelagic chalk
26R-4, 107-107	422.87	M	M	CN8b	Hemipelagic chalk
27R-1, 34-34	427.34	M	G	CN8b	Hemipelagic claystone
27R-5, 18-18	432.53	M	M	CN8b	Hemipelagic claystone
28R-1, 41-41	437.01	H	P	CN8b	Hemipelagic chalk
28R-7, 25-25	442.85	H	M	CN8b	Hemipelagic chalk
28R-7, 40-40	443.00	L	M	CN8b	Hemipelagic chalk
29R-4, 54-54	451.24	H	G	CN8a	Hemipelagic chalk
30R-4, 22-22	460.62	M	G	CN8a	Hemipelagic claystone
31R-2, 25.5-25.5	467.26	H	P	CN8a	Hemipelagic chalk
32R-2, 86-86	477.56	H	P	CN8a	Hemipelagic chalk
32R-CC, 7-7	480.97	M	P	CN7	Hemipelagic claystone
33R-1, 78.5-78.5	485.69	H	P	CN7	Hemipelagic claystone
33R-3, 32-32	488.22	H	P	CN7	Hemipelagic chalk
34R-5, 50-50	500.62	H	P	CN7	Hemipelagic chalk
35R-3, 5-5	506.93	H	P	CN6	Hemipelagic chalk
36R-5, 53-53	520.05	M	P	CN6	Hemipelagic chalk
37R-5, 16-16	529.07	H	P	CN6	Hemipelagic chalk
38R-4, 56-56	537.81	H	P	CN6	Hemipelagic chalk
39R-2, 94-94	545.12	H	P	CN5b	Hemipelagic chalk
39R-6, 95-95	550.50	H	P	CN5b	Hemipelagic chalk
40R-3, 87-87	555.95	M	P	CN5b	Hemipelagic chalk
41R-2, 77-77	564.09	M	M	CN5b	Hemipelagic chalk
42R-1, 44-44	571.84	M	G	CN5b	Hemipelagic chalk
43R-1, 48-48	581.48	M	G	CN5b	Hemipelagic chalk
44R-7, 14-14	598.31	H	G	CN5b	Hemipelagic chalk
45R-3, 17-17	603.57	H	G	CN5b	Hemipelagic chalk
46R-4, 14-14	613.20	H	G	CN5b	Hemipelagic chalk
47R-4, 32-32	623.35	H	G	CN5b	Hemipelagic chalk
48R-6, 22-22	635.32	H	G	CN5a/b	Hemipelagic chalk
49R-5, 19-19	644.65	H	G	CN5a/b	Hemipelagic chalk
50R-3, 128-128	652.67	M	M	CN5a/b	Hemipelagic claystone
51R-6, 10-10	664.85	M	M	CN5a/b	Hemipelagic chalk
52R-3, 72-72	671.11	M	P	CN5a/b	Hemipelagic chalk
53R-7, 68-68	686.20	M	P	CN5a/b	Hemipelagic chalk
54R-5, 93-93	693.59	M	P	CN5a/b	Hemipelagic chalk
55R-3, 14-14	699.23	M	P	CN5a/b	Hemipelagic chalk
56R-3, 4-4	708.90	M	P	CN5a/b	Hemipelagic claystone
57R-5, 9-9	721.36	M	P	CN5a/b	Hemipelagic chalk
58R-5, 60-60	731.61	M	P	CN5a	Hemipelagic chalk
59R-6, 23-23	742.15	M	M	CN5a	Hemipelagic chalk
60R-3, 42-42	747.84	L	P	CN5a	Hemipelagic claystone
61R-2, 28-28	755.79	M	M	CN5a	Hemipelagic chalk
62R-2, 9-9	765.14	M	M	CN5a	Hemipelagic claystone
63R-1, 1-1	773.11	M	P	CN5a	Turbidite claystone
64R-2, 8-8	784.34	L	P	CN4	Hemipelagic chalk
65R-6, 5-5	799.04	M	P	CN4	Hemipelagic claystone
66R-1, 2-2	802.12	L	P	CN4	Hemipelagic claystone
67R-2, 113-113	814.34	L	P	CN4	Hemipelagic chalk
68R-5, 21-21	826.92	L	P	CN4	Hemipelagic claystone
69R-4, 37-37	835.73	L	P	CN4	Hemipelagic chalk
70R-2, 70-70	842.71	L	P	CN4	Hemipelagic chalk
70R-6, 42-42	848.30	L	P	CN4	Hemipelagic claystone
71R-1, 84-84	851.24	VL	P	CN4	Hemipelagic claystone
72R-5, 23-23	865.88	VL	P	CN4	Hemipelagic claystone
73R-3, 16-16	872.86	VH	M	CN4	Hemipelagic claystone
74R-2, 96-96	881.86	VL	M	CN4	Hemipelagic claystone?
75R-1, 3-3	889.13	M	M	CN4	Hemipelagic claystone
78R-1, 139-139	919.39	VL	P	CN4	Lapillistone (matrix)
79R-2, 45-45	928.69	L	P	CN4	Hemipelagic claystone
80R-1, 1-1	937.21	L	P	CN4	Turbidite?
83R-1, 64-64	966.64	L	M	CN4	Hemipelagic claystone
83R-2, 89-89	968.22	L	M	CN3	Hemipelagic claystone
85R-2, 119-119	987.91	B			Basaltic debris
86R-6, 47-47	1002.10	B			Basaltic debris
103-4, 23-23	1153.23	L	P	CN3	Carbonate layer in basaltic debris

Note: Key to abbreviations for abundance and preservation in "Explanatory Notes" (this volume).

*D. tamalis* in Sample 157-953A-20H-7, 4 cm (187.64 mbsf). The only two samples from Hole 953B, Samples 157-953B-1X-2, 65 cm (189.96 mbsf), and 157-953B-1X-6, 123 cm (194.99 mbsf), were also placed in Subzone CN12a.

*Reticulofenestra pseudumbilicus* (>7 µm maximum diameter) occurred in several samples above the highest occurrence of *Sphenolithus* spp. The last occurrence datum of *Reticulofenestra pseudumbilicus* (>7 µm) is stratigraphically slightly below that of *Sphenolithus* spp. (Table 2 of the "Explanatory Notes," this volume), so we consider the *R. pseudumbilicus* specimens occurring above *Sphenolithus* spp. to be reworked. The top of Subzone CN11b was placed in Sample 157-953C-8R-CC (249.40 mbsf) because of the co-occurrence of *Sphenolithus* spp. and *R. pseudumbilicus*. This assignment is also supported by foraminiferal evidence. The LO datum of the planktonic foraminifer, *Globorotalia margaritae*, which is slightly older than *R. pseudumbilicus*, occurred at the same level where *R. pseudumbilicus* and *Sphenolithus* spp. co-occur (Sample 157-953C-8R-CC, 0–2 cm, 249.40 mbsf). Subzone CN11b seems anomalously thin here, as the lowest occurrence of *Discoaster tamalis* occurs just below this level in Sample 157-953C-9R-1, 8 cm (254.18 mbsf). The reworking of *R. pseudumbilicus* and the relative thinness of Subzone CN11b suggest a condensed section or a short hiatus at this level.

The top of Zone CN10 was marked in Sample 157-953C-11R-CC (279.88 mbsf) by the highest occurrence of *Amaurolithus tricorniculatus*. The subzones of Zone CN10, which are based on the FA of *Ceratolithus acutus*, *C. rugosus*, and *Discoaster asymmetricus*, could not be distinguished as these species were rare and very sporadic in their occurrence.

### Miocene

The highest occurrence of *Discoaster quinquerramus* in Sample 157-953C-16R-2, 132 cm (324.42 mbsf) indicates the top of Subzone CN9b in the late Miocene. This is in relatively good agreement with the planktonic foraminifer zonation, which indicates definite Zone M13 (late Miocene) in Sample 157-953C-16R-CC (326.07 mbsf) with undifferentiated late Miocene to early Pliocene in the two samples above that (Samples 157-953C-14R-CC, 305.17 mbsf, and 157-953C-15R-CC, 315.51 mbsf). It should be noted that the marker for Zone CN9, *D. quinquerramus*, was quite rare in Samples 157-953C-16R-2, 132 cm (324.42 mbsf), and 157-953C-17R-1, 140 cm (332.50 mbsf). Additional shore-based examination of Cores 157-953C-14R and 157-953C-15R may improve the placement of this zonal boundary.

The highest and lowest occurrences of *Amaurolithus amplificus*, a very useful non-zonal marker, were observed in Samples 157-953C-18R-3, 101 cm, and 157-953C-19R-1, 48 cm. The lowest occurrence of *A. delicatus*, which marks the base of Subzone CN9b, and the lowest common occurrence of large (>7 µm maximum diameter) *Reticulofenestra pseudumbilicus* specimens, occur in Sample 157-953C-21R-2, 102 cm (372.02 mbsf). Below this level, small *Reticulofenestra* specimens are abundant, with the larger morphotypes rare and sporadic in their occurrence. This interval correlates to the *R. pseudumbilicus* paracme of Rio et al. (1990) and the small *Reticulofenestra* interval of Young (1990) and Young et al. (1994). The lowest occurrence of *Discoaster quinquerramus* was difficult to determine because of poor preservation, but it seems to occur in Sample 157-953C-24R-5, 4.5 cm (404.15 mbsf), and marks the base of Subzone CN9a.

The base of the *Reticulofenestra pseudumbilicus* paracme was indicated by the highest occurrence of common large specimens of *Reticulofenestra pseudumbilicus* (>7 µm maximum diameter) in Sample 157-953C-28R-5, 25 cm (442.85 mbsf). The lowest occurrence of *Discoaster loeblichii* in Sample 157-953C-28R-5, 40 cm (443.00 mbsf), indicated the base of Subzone CN8b.

Sample 157-953C-32R-CC, 7 cm (480.97 mbsf), contained the highest occurrence of *D. hamatus*, indicating the top of Zone CN7, with the lowest occurrence of this species in Sample 157-953C-34R-

5, 50 cm (500.62 mbsf), indicating the base of this zone. Supporting the placement of the lower boundary of Zone CN7 was the lowest occurrence of *D. bellus* in Sample 157-953C-35R-3, 5 cm (506.93 mbsf), directly below the lowest occurrence of *D. hamatus*. Sample 157-953C-38R-4, 56 cm (537.81 mbsf) contains the lowest occurrence of *Catinaster coalitus*, which indicates the base of Zone CN6.

The highest consistent occurrence of *Coccolithus miopelagicus* (>13 µm maximum diameter) was in Sample 157-953C-39R-6, 95 cm (550.50 mbsf). Rare specimens were seen higher in the cores but were considered reworked. The highest occurrence of *Discoaster kugleri* was in Sample 157-953C-43R-1, 48 cm (581.48 mbsf). The FO of *D. kugleri* is a difficult datum to use as its presence is often rare and sporadic (see Young et al., 1994). Since *D. kugleri* was rare in all of the samples in which it was found, we correlated its lowest occurrence in Sample 157-953C-47R-4, 32 cm (623.35 mbsf), with the first common occurrence datum of Raffi and Flores (in press), rather than the actual FO datum, which defines the base of Subzone CN5b (Table 2 of the "Explanatory Notes," this volume). This prevented an accurate determination of the boundary between Subzones CN5a and 5b; however, we were able to approximate the position of this boundary using the highest occurrence of *Calcidiscus premacintyreii* in Sample 157-953C-58R-5, 60 cm (731.61 mbsf). The interval between the lowest occurrence of *Discoaster kugleri* and the highest occurrence of *C. premacintyreii* is zoned as CN5a/b undifferentiated.

The top of Zone CN4, marked by the highest occurrence of *Sphenolithus heteromorphus*, was in Sample 157-953C-64R-2, 8 cm (784.34 mbsf). Below this level, biostratigraphic resolution decreased markedly because of a combination of low zonal resolution in the early and middle Miocene, and declining preservation and abundance in the unsuitable lithologies. The top of Zone CN3 was marked by the top of *Helicosphaera ampliaperata* in Sample 157-953C-83R-2, 89 cm (968.22 mbsf). No further productive hemipelagic material occurred below this down to Core 157-953C-103R, where Sample 157-953C-103R-4, 1 cm (1153.23 mbsf), was assigned to Zone CN3 because it contained *Sphenolithus heteromorphus* and *Helicosphaera ampliaperata*. The sample also contained *Calcidiscus premacintyreii*, suggesting the upper part of CN3, younger than 17.4 Ma. Discoasters were present in very low numbers and were very poorly preserved, preventing the determination of two events that occur in this interval, the *Discoaster deflandrei* acme and the FO of the *D. exilis* group.

### Planktonic Foraminifers

The analysis of core-catcher samples for foraminifers proved effective at Site 953. The core-catchers sampled mainly pelagic oozes and a few calcareous sands from the surface to Sample 157-953C-27R-CC, 0–2 cm (433.22 mbsf). Below this depth the core catcher samples are mainly dark laminated volcanic sands mixed with oozes, therefore we sampled identified pelagic oozes or calcareous sands from split cores.

The abundance and preservation of planktonic foraminifers in calcareous sand and pelagic ooze and chalk was good from the surface to Sample 157-953C-13R-CC, 0–2 cm (300.81 mbsf). Below this point the recovery was relatively good to Sample 157-953C-39R-6, 3–5 cm (549.58 mbsf), but preservation deteriorated markedly below this depth (Table 3).

Zones were defined with good resolution from the surface (Sample 157-953A-1H-CC, 0–2 cm) to Sample 157-953C-39R-6, 3–5 cm (549.58 mbsf). Resolution decreased downhole as a result of the absence of lithologies suitable for foraminifer analysis and marker globorotaliid species.

### Pleistocene

Well-preserved and abundant (Table 3) Pleistocene planktonic foraminifers are recorded from Cores 157-953A-1H to 157-953A-15H in pelagic ooze. The Pleistocene marker species, *Globorotalia truncatulinoides*, is present from Samples 157-953-1H-CC, 0–2 cm,

to 157-953A-15H-CC, 0–2 cm (140.56 mbsf), and defines the range of the Pleistocene.

The sequence is divided into Zone N23 (Fig. 18) from the surface to Sample 157-953A-11H-CC, 0–2 cm (101.41 mbsf), and Zone N22 from Sample 157-953A-12H-CC, 0–2 cm (112.28 mbsf), to Sample 157-953A-15H-CC, 0–2 cm, based on the FO of *Globigerina calida calida*. The base of Zone N22 is placed at 140.56 mbsf using of the FA datum of *Globorotalia truncatulinoides*.

The Pleistocene community contains common to abundant cool subtropical species including *Globorotalia inflata* and dominantly dextral *Neogloboquadrina pachyderma*. Tropical species like *Pulleniatina obliquiloculata obliquiloculata* and *Pulleniatina finalis* are few to common, and menardine globorotaliids taxa are almost absent. *Globorotalia menardii cultrata* is rare in Sample 157-953A-1H-CC, 0–2 cm.

### Pliocene

The Pliocene ranges from Sample 157-953A-16H-CC, 0–2 cm (150.44 mbsf), to Sample 157-953C-13R-CC, 0–2 cm (300.82 mbsf). An abundant, diverse, and well-preserved planktonic foraminifer assemblage is recorded in this interval.

Zone PL6 is recognized in Samples 157-953A-16H-CC, 0–2 cm, and 157-953A-17H-CC, 0–2 cm, and the base of the zone is defined by the extinction of *Globorotalia miocenica* above Sample 157-953A-18H-CC, 0–2 cm (169.41 mbsf). Samples from 157-953A-18H-CC, 0–2 cm, to 157-953C-3R-CC, 0–2 cm (200.25 mbsf), belong in Zone PL5 and show the concurrent range of *Globorotalia miocenica* and *Globorotalia exilis*. The base of the zone lies above the last appearance of *Dentoglobigerina altispira* recorded in Sample 157-953C-4R-CC, 0–2 cm (207.97 mbsf). This sample also contains common *Globorotalia multicamerata* without *Sphaeroidinellopsis seminulina* and can be assigned to Zone PL4.

Zone PL3 occurs from Sample 157-953C-5R-CC, 0–2 cm (218.81 mbsf), to Sample 157-953C-7R-1, 125–127 cm (236.25 mbsf). The top of the zone is characterized by the extinction of *Sphaeroidinellopsis seminulina*. *Dentoglobigerina altispira*, which is usually present within the zone, is very rare and recorded only in Sample 157-953C-5R-CC, 0–2 cm. The base of Zone PL3 lies above the highest occurrence of *Globorotalia margaritae* recorded in Sample 157-953C-8R-CC, 0–2 cm.

Samples from 157-953C-8R-CC, 0–2 cm (249.40 mbsf), to 157-953C-10R-CC, 0–2 cm (267.70 mbsf), contain common to abundant *Globorotalia margaritae* and *Sphaeroidinellopsis seminulina*, which define Zone PL2, and also *Globorotalia puncticulata* and dextral menardine globorotaliids including *Globorotalia menardii menardii*, *Globorotalia menardii cultrata*, and *Globorotalia multicamerata*. The base of Zone PL2 lies above the highest occurrence of *Globigerina nepenthes*, which is present in Sample 157-953C-11R-CC, 0–2 cm, at 279.88 mbsf. Samples from 157-953C-11R-CC, 0–2 cm, to 157-953C-13R-CC, 0–2 cm, are assigned to Zone PL1 based on the concomitant presence of *Globigerina nepenthes* and *Globorotalia margaritae*. They also contain few to common dextral *Neogloboquadrina acostaensis* and *Sphaeroidinellopsis seminulina*.

The base of Zone PL1 cannot be firmly placed based on our preliminary data. Unfortunately, the highest stratigraphic occurrence of *Globoquadrina dehiscens*, which defines the top of Zone M13 (Berggren, 1977), is within Zone M11 at the Leg 157 sites. We tentatively assign Samples 157-953C-14R-CC, 0–2 cm, and 157-953C-15R-CC, 0–2 cm, to the undifferentiated Zone M13/PL1 because Sample 157-953C-14R-CC, 0–2 cm, (305.17 mbsf) contains one specimen close to *Globoquadrina dehiscens*, and one specimen close to *Globorotalia juanai*, which last occurs in the base of Zone PL1.

### Miocene

Sample 157-953-16R-CC, 0–2 cm, bears *Globorotalia margaritae* and *Globorotalia juanai* and belongs in Zone M13. Samples from

157-953C-17R-CC, 0–2 cm (388.76 mbsf), to 157-953C-20R-CC, 0–2 cm (367.30 mbsf), contain *Globorotalia conomiozea*, *Neogloboquadrina acostaensis*, *Globigerina nepenthes*, *Sphaeroidinellopsis seminulina*, and menardine globorotaliids and can be assigned to Zone M12. The FA of *Globorotalia conomiozea* defines the base of the zone.

Samples between 377.21 and 489.98 mbsf contain a poorly to moderately preserved late Miocene assemblage with *Dentoglobigerina altispira*, *Globigerina nepenthes*, *Globorotalia linguaensis*, and *Sphaeroidinellopsis seminulina*. Several samples (157-953C-28R-2, 130–132 cm, 157-953C-29R-4, 52–53 cm, and 157-953C-29R-CC, 0–2 cm) contain an impoverished assemblage with no age diagnostic taxa. The FA of *Neogloboquadrina acostaensis* is recorded in Sample 157-953C-33R-4, 59–62 cm (489.98 mbsf), and defines the base of Zone M11.

Preservation is poor in samples taken from pelagic oozes between 501.80 and 549.58 mbsf (Samples from 157-953C-34R-6, 18–20 cm, to 157-953C-39R-6, 3–5 cm). Since the planktonic community is composed of few taxa like *Globigerina druryi*, *Globoquadrina dehiscens*, *Globoquadrina venezuelana*, and *Neogloboquadrina continua*, excluding *Globorotalia paralangaensis*, the boundary between Zones M9 and M10 cannot be located. *Globigerina nepenthes* occurs in almost all samples and is a good marker for the definition of Zone M9. The bottom of the zone is recorded in Sample 157-953C-39R-6, 3–5 cm, based on the lowest occurrence of the nominate taxon.

Below this sample preservation and abundance deteriorated markedly in all facies including turbidite mud, calcareous sand, slumped beds, tuffaceous nannofossil mud, and pelagic ooze. Poorly preserved foraminifers occur sporadically in samples from Sample 157-953C-40R-3, 79–81 cm (555.87 mbsf) to 157-953C-83R-1, 49–51 cm (966.49 mbsf). Several samples are barren of foraminifers or contain no age diagnostic taxa. *Dentoglobigerina altispira*, *Globigerinoides trilobus*, *Orbulina universa*, *Globoquadrina dehiscens*, *Globoquadrina venezuelana*, *Neogloboquadrina cf. continua*, *Globorotalia siakensis*, and *Globorotalia mayeri* occur sporadically within this interval.

*Globorotalia linguaensis* is rare in Sample 157-953C-55R-1, 33–35 cm (696.83 mbsf), and *Sphaeroidinellopsis seminulina* occurs commonly. Samples from 157-953C-40R-3, 79–81 cm, to 157-953C-58R-2, 127–129 cm, are tentatively assigned to Zone M8. Reworking is suspected based on the presence of specimens close to *Globorotalia peripheroronda* in Sample 157-953C-46R-4, 4–6 cm, and *Globorotalia fohsi* in Sample 157-953C-52R-3, 83–85 cm.

Samples from 157-953C-60R-1, 47–49 cm (744.97 mbsf), to 157-953C-70R-1, 117–119 cm (841.97 mbsf), can be no older than Zone M7 based on the presence of few to common specimens of *Orbulina universa*.

Sample 157-953C-72R-5, 98–100 cm, contains few specimens of *Globoquadrina dehiscens*, *Globorotalia mayeri*, *Globorotalia siakensis*, and *Sphaeroidinellopsis* spp. and can be no older than Zone M3 based on the range of *Sphaeroidinellopsis* spp. No more samples were collected in the interval between 866.64 and 966.49 mbsf because of the absence of foraminifers from the thin, altered pelagic units among the pre-Mogan volcanoclastic deposits. The last sample, 157-953C-83R-1, 49–51 cm (966.49 mbsf), from a thin pelagic unit contains poorly preserved *Dentoglobigerina altispira* and *Globoquadrina dehiscens* and can be no older than Subzone M1b.

## PALEOMAGNETISM

### Introduction

Paleomagnetic measurements of the NRM after demagnetization to 25 mT were made on the APC cores recovered from Hole 953A, the one XCB core from Hole 953B, and the rotary cores from Hole 953C. The APC cores from Hole 953A presented no major difficulty and a magnetostratigraphy was established for the nearly 200 m

**Table 3. Abundance, preservation, and lithology of samples used in foraminifer zonation, Site 953.**

Core, section, interval (cm)	Top depth (mbsf)	Bottom depth (mbsf)	Abundance	Preservation	Zone	Lithology
157-953A-						
1H-CC, 0-2	7.44	7.46	A	G	N23	Calcareous sand
2H-CC, 0-2	16.97	16.99	A	G	N23	Pelagic ooze
3H-CC, 0-2	26.83	26.85	A	G	N23	Calcareous sand
4H-CC, 0-2	36.28	36.30	C	M	N23	Calcareous sand
5H-CC, 0-2	44.34	44.36	C	M	N23	Basaltic sand
6H-CC, 0-2	55.11	55.13	A	M	N23	Pelagic ooze
7H-CC, 0-2	64.72	64.74	A	M	N23	Pelagic ooze
8H-CC, 0-2	74.11	74.13	A	G	N23	Calcareous turbidite
9H-CC, 0-2	83.72	83.74	A	G	N23	Pelagic ooze
10H-CC, 0-2	93.43	93.45	A	M	N23	Pelagic ooze
11H-CC, 0-2	101.40	101.42	A	M	N23	Pelagic ooze
12H-CC, 0-2	112.27	112.29	A	M	N22	Pelagic ooze
13H-CC, 0-2	121.61	121.63	B		?	Dark calcareous sand
14H-CC, 0-2	131.40	131.42	A	G	N22	Pelagic ooze
15H-CC, 0-2	140.55	140.57	A	G	N22	Pelagic ooze
16H-CC, 0-2	150.43	150.45	A	G	PL6	Pelagic ooze
17H-CC, 0-2	159.60	159.62	A	G	PL6	Pelagic ooze
18H-CC, 0-2	169.40	169.42	A	G	PL5	Pelagic ooze
19H-CC, 0-2	178.69	178.71	C	M	PL5	Pelagic ooze
20H-CC, 0-2	188.44	188.46	A	M	PL5	Disturbed ooze with sand patches
21H-CC, 0-2	192.59	192.61	A	M	PL5	Pelagic ooze
157-953B-						
1X-CC, 25-29	195.49	195.53	A	G	PL5	Pelagic ooze
157-953C-						
2R-CC, 0-2	188.96	188.98	A	G	PL5	Pelagic ooze
3R-CC, 0-2	200.24	200.26	A	G	PL5	Pelagic ooze
4R-CC, 0-2	207.96	207.98	A	M	PL4	Disturbed pelagic ooze
5R-CC, 0-2	218.80	218.82	A	M	PL3	Disturbed pelagic ooze
6R-CC, 0-2	226.38	226.40	A	G	PL3	Disturbed pelagic ooze
7R-1, 125-127	236.24	236.26	C	M	PL3	Disturbed pelagic ooze
8R-CC, 0-2	249.39	249.41	A	G	PL2	Disturbed pelagic ooze
9R-CC, 0-2	258.88	258.90	C	P	PL2	Disturbed pelagic ooze
10R-CC, 0-2	267.69	267.71	C	P	PL2	Disturbed pelagic ooze
11R-CC, 0-2	279.87	279.89	A	M	PL1	Pelagic ooze/chalk
12R-CC, 0-2	286.42	286.44	C	P	PL1	Pelagic ooze
13R-CC, 0-2	300.81	300.83	C	M	PL1	Pelagic ooze
14R-CC, 0-2	305.16	305.18	C	P	M13/PL1	Pelagic ooze
15R-CC, 0-2	315.50	315.52	C	M	M13/PL1	Disturbed pelagic ooze
16R-CC, 0-2	326.06	326.08	C	M	M13	Pelagic ooze
17R-CC, 0-2	338.75	338.77	C	M	M12	Pelagic ooze
18R-CC, 0-2	345.59	345.61	F	P	M12	Pelagic ooze
19R-CC, 0-2	352.67	352.69	C	P	M12	Slumped beds
20R-CC, 0-2	367.29	367.31	F	P	M12	Pelagic ooze
21R-CC, 0-2	377.20	377.22	F	P	M11	Pelagic ooze
22R-CC, 0-2	387.18	387.19	A	P	M11	Disturbed pelagic ooze
23R-CC, 0-2	396.35	396.37	F	P	M11	Pelagic ooze
24R-CC, 0-2	404.27	404.28	C	M	M11	Pelagic ooze
25R-CC, 0-2	413.54	413.55	C	M	M11	Disturbed pelagic ooze
26R-CC, 0-2	423.04	423.06	C	M	M11	Disturbed ooze turbidite
27R-CC, 0-2	433.21	433.22	C	P	M11	Dark sand mixed with ooze
28R-2, 130-132	439.39	439.41	C	M	M11/M10?	Top of graded ooze
29R-4, 52-53	451.21	451.22	C	M	M8?	Pelagic ooze
29R-CC, 0-2	451.89	451.91	C	M	M9/M10	Dark laminated volcanic sand
30R-1, 7-9	455.99	456.01	F	P	M11	Pelagic ooze
31R-2, 125-128	467.98	468.01	F	P	M11	Pelagic ooze
32R-2, 86-88	477.55	477.57	C	P	M11	Pelagic ooze
33R-4, 59-62	489.97	490.00	C	P	M11	White unit
34R-6, 18-20	501.79	501.81	F	P	M9/M10	Pelagic ooze
35R-4, 81-83	508.99	509.01	F	P	M9/M10	Pelagic ooze
36R-5, 50-53	520.00	520.03	A	P	M9/M10	Pelagic ooze
37R-5, 15-17	529.06	529.08	A	P	M9/M10	Ooze mixed with dark volcanic sand
38R-5, 84-86	539.46	539.48	C	P	M9/M10	Pelagic ooze
39R-6, 3-5	549.57	549.59	A	P	M9/M10	Pelagic ooze
40R-3, 79-81	555.86	555.88	F	P	M8	Pelagic ooze
41R-2, 115-117	564.46	564.48	F	P	M8/M7	Turbiditic mud mixed with ooze
42R-1, 53-55	571.92	571.94	R	P	?	Pelagic ooze
43R-1, 44-46	581.43	581.45	F	P	M8?	Pelagic ooze
44R-7, 12-14	598.28	598.30	F	P	?	?
45R-1, 7-9	600.46	600.48	R	P	?	Pelagic ooze
46R-4, 4-6	613.09	613.11	F	M	M7?	Pelagic ooze
47R-1, 23-25	619.82	619.84	R	P	?	Slumped beds
48R-6, 101-103	636.10	636.12	R	P	?	Calcareous sand
48R-2, 42-44	630.64	630.66	B		?	Turbidite mud
49R-3, 67-70	642.41	642.44	F	M	M8?	Turbidite mud
49R-1, 68-69	639.57	639.58	F	P	M8?	Calcareous sand
50R-3, 103-105	652.41	652.43	C	P	?	Slumped beds
51R-1, 89-91	658.98	659.00	C	P	M8	Pelagic ooze
52R-3, 83-85	671.21	671.23	C	P	M8	Turbidite mud
53R-2, 53-55	679.37	679.39	C	P	M8	Pelagic ooze
54R-5, 90-93	693.54	693.57	F	P	M8?	Pelagic ooze
55R-1, 33-35	696.82	696.84	F	P	M8	Pelagic ooze
56R-3, 3-4	708.88	708.89	F	P	M8	Pelagic ooze
57R-5, 9-11	721.35	721.37	F	P	M8	Pelagic ooze
58R-2, 127-129	727.93	727.95	F	P	M8	Pelagic ooze
59R-6, 26-28	742.17	742.19	R	P	?	Pelagic ooze

Table 3 (continued).

Core, section, interval (cm)	Top depth (mbsf)	Bottom depth (mbsf)	Abundance	Preservation	Zone	Lithology
60R-1, 47-49	744.96	744.98	F	P	No older than M7	Pelagic ooze
61R-2, 36-38	755.86	755.88	F	P	No older than M7	Tuffaceous nannofossil mud
62R-2, 9-11	765.13	765.15	R	P	?	Glass-rich silt or sandstone
64R-2, 8-10	784.33	784.35	R	P	?	Dark volcanic siltstone
65R-4, 108-111	797.26	797.29	F	P	M7 M9/10	Dark volcanic siltstone
66R-1, 27-29	832.36	832.38	F	P	M7/M8	Dark calcareous sand
70R-1, 117-119	841.96	841.98	A	P	No older than M7	Pelagic
71R-1, 80-82	851.19	851.21	F	P	?	Pelagic
72R-5, 98-100	866.63	866.65	C	P	No older than M3	Pelagic
73R-3, 76-80	873.46	873.48	C	P	?	Pelagic
83R-1, 49-51	966.48	966.5	F	P	No older than M1b	Pelagic

Note: Key to abbreviations for abundance and preservation in "Explanatory Notes" (this volume). Asterisks (\*) mark the Pleistocene/Pliocene and Pliocene/Miocene boundaries.

drilled at this hole. The rotary cores from Hole 953C spanned a much longer interval of time than previous Leg 157 holes. We therefore approached the magnetostratigraphy differently because we were no longer able to track each successive reversal in our record. However, the paleontological age-depth determinations were sufficiently precise that we could match the longer and more distinctive chrons magnetically and then work back to the shorter chrons.

Discrete samples were analyzed by AF demagnetization. Rock magnetic studies continued to investigate the variation of recording ability found in the discrete samples and to document the magnetic properties of the various lithologies.

### Hole 953A

Plots of inclination from pelagic interbeds, with interpreted chron boundaries, are shown in Figure 19 and the depths of the various chron boundaries are given in Table 4. The intensity and the susceptibility results from MST measurements are shown in Figure 20.

The inclination change recording the onset of the Brunhes was observed between 41.3 and 42.7 mbsf. A change in inclination, accompanied by a change in declination in the tensor tool corrected data, is seen in a sequence of marly pelagic interbeds. An earlier change in inclination unaccompanied by a declination change was seen at 42.5 mbsf in the same sequence. This record is sufficiently detailed to warrant shore-based study. Moreover, the synchronous change in declination and inclination at the time of the reversal suggests that the drill contamination is not important in this interval of core.

The top of C1r.1n (Jaramillo) is well defined between 51.4 and 51.5 mbsf. The onset is less clear because it falls near a region of possibly disturbed core. We therefore give an extended range of between 65.4 and 68.1 mbsf for the onset. Within the Jaramillo a brief reversed interval between 58 and 60 mbsf appears.

The Cobb Mountain is seen between 75 and 78 mbsf. The persistent observation of the Cobb Mountain on Leg 157 confirms a growing impression that this feature may reflect worldwide field behavior and may provide a useful magnetostratigraphic marker.

The top of C2n (Olduvai) is marked by an inclination change that takes place over a nearly 3 m interval from 95.1 to 97.8 mbsf and is in continuous pelagic interbeds. However, no change in declination in the long-core measurement is observed. The onset of the Olduvai is at 136 mbsf, and again there is no accompanying change in declination, suggesting that declination is not reliable in this interval.

There appears to be a record of the Réunion Event between 145.9 and 146.9 mbsf. This falls in fine pale pelagic ooze with only minor interruptions from sands.

The occurrence of the top of the Gauss is obscured by convoluted bedding and we are only able to give an extended range of between 155.9 and 160.7. At the end of the APC cores, the Gauss normal continues.

The intensity of NRM and the susceptibility shown in Figure 20 exhibit long period fluctuations with periods of some tens of meters. These are seen more clearly in the susceptibility in this interval. Fine-scale correlation can be traced between the various lithologies as observed at the earlier sites.

### Hole 953C

Continuing plots of inclination from pelagic interbeds, with interpreted chron boundaries, are shown in Figure 19 and the locations of the various chron boundaries are continued in Table 4. The intensity and the susceptibility results from MST measurements are shown in Figure 20.

The rotary drill cores from Hole 953C provide so long a magnetic record that it is not practical to describe each boundary individually; refer to Table 4 for details. Here we simply give examples of the way in which certain key points in the record were fixed in relation to paleontological markers. Only then could we locate and fix the remaining chrons. We again compared the magnetic record against the core photographs to exclude intervals of disturbed core or of unsuitable lithology.

In the shallowest depths, we were not able to identify satisfactorily the Kaena and Mammoth subchrons, but the short positive subchrons within the Gilbert were evident although not recorded in their entirety.

The determined top of nannofossil Subzone CN9b helped to clarify the location of the onset of the reversed Gilbert chron at 336 mbsf. Similarly the biozone CN6 helped to identify the long normal Chron C5n. This chron could then be traced in detail to its onset with the diagnostic short positive C5r.1n.

The nannofossil Subzones CN5a to CN5b provided a link to the short reversed interval within Chron C5An. The boundary of nannofossil Zones CN4 and CN5a falls in the reversed Chron C5A Br, which is poorly recorded, but ~10 m below this we see the top of the long distinctive C5ACn. Below 800 m, we were not able to establish a reliable magnetostratigraphy.

The NRM intensity and susceptibility plots for Hole 953C (Fig. 20) show similar long wavelength structures as did the Hole 953A data. There is a peak at 240 mbsf preceded by a shallow low and a gradual increase to a high at 570 mbsf. In the lowermost 600 m of core, sharper lows occur at 650, 800, and 1000 mbsf, with corresponding, but somewhat broader, peaks centered at 730, 900, and 1100 mbsf. The peak at 200 mbsf correlates with the lithologic Unit II and possibly reflects the presence of lithic crystal sandstones and lapillistones. The shallow low at 400 mbsf correlates with the period of reduced sedimentation rate, and the boundary between lithologic Units III and IVa. This lies in the volcanic hiatus, which appears to be marked by a gradual reduction in flux of magnetic material throughout much of its duration. The low at 650 mbsf falls within the lithologic Subunit

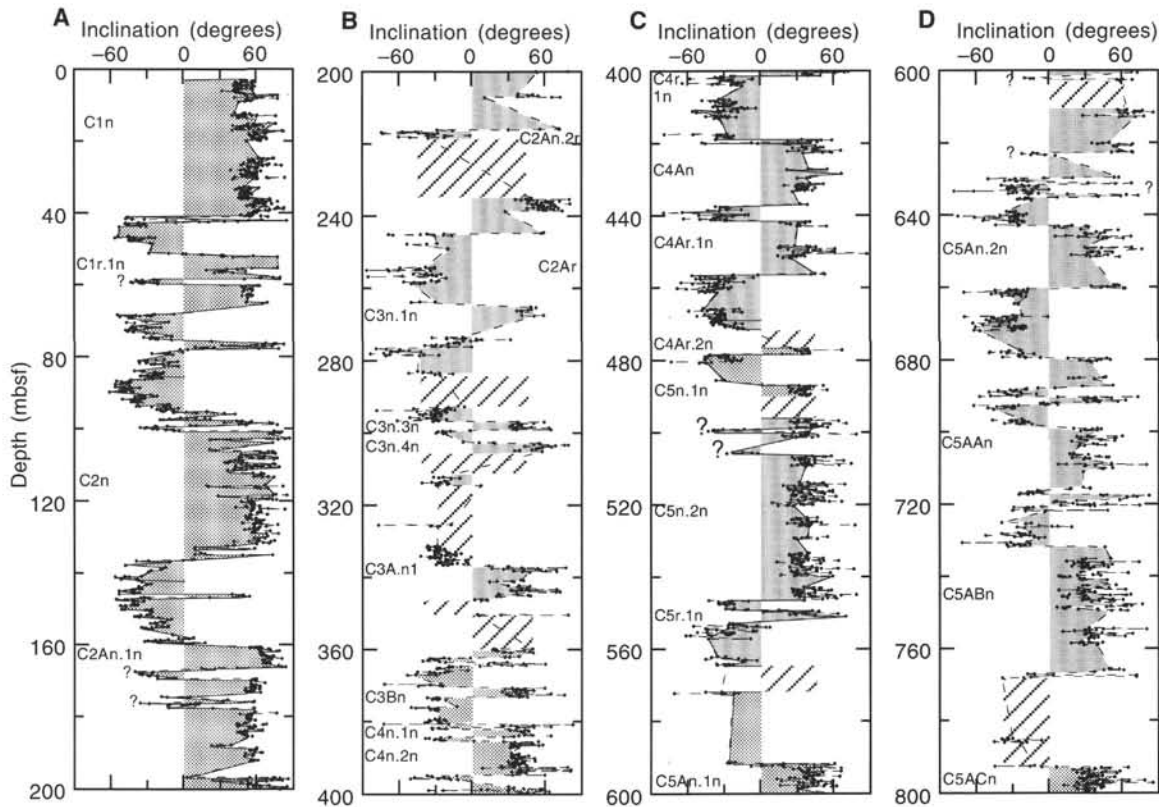


Figure 19. Magnetic data, NRM (25 mT), and interpreted polarity chrons from APC cores from Hole 953A, and RCB cores from Hole 953C. Inclination data from undisturbed pelagic interbeds, with interpreted polarity chrons. A. Holes 953A and 953C. B, C, and D. Hole 953C. Shaded area = interpreted polarity, hatched area = intervals of poor recovery.

IVb at an age of 12 Ma, while the earlier lows are at 800 and 1000 mbsf in the lithologic Units IVc and VII, at ages of ~13.5 and 16 Ma. The former appears to coincide with the upper termination of the Mogan Group. The possible relation between the magnetic remanence intensity and the susceptibility, and the influx of volcanic material may be worth investigating as a proxy for volcanic input.

### Rock Magnetism

The demagnetization characteristics of NRM, ARM, and IRM, and measurements of weak field susceptibility were conducted as part of the preliminary rock magnetism analyses, the magnitudes of which have also revealed systematic differences between the various lithologies. For example, in Figure 21 the intensity of ARM is plotted against weak field susceptibility (King diagram) for a group of samples from Holes 953A and 953C. The set from Hole 953A were undifferentiated pelagic interbeds and gave a linear trend indicative of a common composition and grain size of the material, with the only variation being in the amount of magnetic material present. The set of samples from Hole 953C varied in color and grain size. However, with the exception of a single coarse dark sand, which clearly had more coarse magnetic material, the remainder again gave a linear trend with the fine dark pelagic beds being the most strongly magnetic. The most magnetic samples in Hole 953C were more magnetic than any in Hole 953A.

Discrete samples were analyzed to establish the NRM, ARM, and IRM demagnetization characteristics. The behavior ranged from excellent directional behavior on Zijdeveld criteria and AF demagnetization characteristics consistent with a primary NRM of depositional origin, to samples whose magnetization was evidently controlled

by the drill effects. Figure 22 gives Schmidt nets, Zijdeveld, and relative intensity plots for four samples. Two of these have normal and two reversed polarity. All have similar inclinations, which suggests that there is no significant normal overprint, although the inclinations give slightly low paleolatitudes for this site. The declinations are randomly distributed, consistent with the rotary nature of the coring. These results demonstrate that the drilling contamination has not had a serious effect on the magnetization of these samples.

In addition to the standard samples, we investigated the behavior of basalt clasts because its primary magnetization should be a TRM, and therefore its demagnetization characteristics are predictable and quite different from those of remanence from drilling contamination. The NRM was single component and its magnitude was approximately equal to the ARM given in a 0.1 mT, with an alternating field of 100 mT. It was also a factor of 100 smaller than the saturation IRM. These parameters are entirely consistent with a TRM acquired in the geomagnetic field. We can thus be confident that these fine-grained basalts exhibited no significant effect of drilling. Additional samples will be analyzed on shore, but it is clear from this analysis that the drill effects are dependent upon the mechanical, as well as magnetic properties of the rock. Apparently, the more lithified rocks are less susceptible to drill contamination than the plastic clays and muds from higher level cores.

To elucidate this question of drilling contamination, the stable NRM directions from the whole core measurements were compared with the discrete directions and found to be consistent. In these more lithified cores there are lengths of section approaching a meter, which have remained intact, and provide a test of the declination record where they include a reversal. For example, in Section 157-953C-30R-1, a reversal is recorded in a 40 cm intact interval. Both declina-

Table 4. Polarity chrons: ages and correlated core intervals.

Boundary	Name	Age (Ma)	Top		Bottom		Comments
			Core, section (cm)	Depth (mbsf)	Core, section (cm)	Depth (mbsf)	
C1n (o)	Brunhes/Matuyama	0.78	5H-5, 55	41.2	5H-5, 65	42.6	Rebound
C1r.1n (t)	Jaramillo (t)	0.99	6H-4, 125	51.3	6H-4, 135	51.5	Possible event in Jaramillo
C1r.1n (o)	Jaramillo (o)	1.07	8H-1, 75	65.3	8H-3, 55	68.0	Drilling disturbance
	Cobb Mtn (t)		9H-1, 150	75.3	9H-2, 5	75.7	
	CobbMtn (o)		9H-3, 85	77.9	9H-3, 95	78.0	
C2n (t)	Olduvai (t)	1.77	11H-2, 45	95.0	11H-4, 15	97.8	
C2n (o)	Olduvai (o)	1.95	15H-4, 65	136.2	15H-4, 75	136.3	
	Reunion (t)		16H-4, 75	145.8	16H-4, 85	145.9	
	Reunion (o)		16H-5, 15	146.7	16H-5, 25	146.8	
C2An (t)	Gauss (t)	2.60	17H-4, 125	155.8	18H-1, 105	160.7	Convoluted beds
C2An.2r (t)	Mammoth (t)	3.22	5R-1, 35	216.2	5R-1, 45	216.3	
C2An.2r (o)	Mammoth (o)						Low recovery and drilling disturbance
C2Ar (t)	Matuyama/Gilbert	3.58	8R-1, 50	244.8	8R-1, 25	244.9	"
C3n1n (t)	Cochiti (t)	4.18	10R-1, 145	265.1			Low recovery and drilling disturbance
C3n1n (o)	Cochiti (o)	4.29			10R-3, 95	267.7	"
C3n3n (t)	Sidjufall (t)	4.80	13R-3, 150	296.9			"
C3n3n (o)	Sidjufall (o)	4.89			13R-5, 65	299.4	"
C3n3n (t)	Thvera (t)	4.98	14R-1, 115	302.6			"
C3n3n (o)	Thvera (o)	5.23	14R-2, 125	305.2	15R-1, 15	312.3	
C3A.n1 (t)		5.87	17R-4, 115	336.7	17R-4, 125	336.9	
C3A.n1 (o)		6.12	20R-2, 95	362.3	20R-2, 105	362.4	
C3Bn (t)		6.92	21R-1, 75	370.2	21R-1, 115	370.6	
C3Bn (o)		7.07	21R-3, 75	373.3	21R-3, 85	373.4	
C4n.1n (t)		7.41	22R-2, 15	380.8	22R-2, 25	380.9	
C4n.1n (o)		7.53	22R-2, 105	381.7	22R-2, 115	381.7	
C4n.2n (t)		7.62	22R-2, 145	382.1	22R-3, 15	382.3	Section end
C4n.2n (o)		8.03	23R-5, 15	394.8	23R-5, 25	394.9	
C4r.1n (t)		8.17	23R-6, 145	396.1	24R-1, 25	398.4	End of core
C4r.1n (o)		8.21	24R-3, 15	401.2	24R-3, 25	401.4	
C4An (t)		8.63	26R-2, 15	418.9	26R-2, 25	419.0	
C4An (o)		8.95	28R-1, 35	437.0	28R-1, 95	437.6	
C4Ar.1n (t)		9.14	28R-4, 25	441.4	28R-4, 65	441.7	
C4Ar.1n (o)		9.22	30R-1, 45	456.4	30R-1, 55	456.4	
C4Ar.2n (t)		9.48	31R-4, 145	471.4	32R-2, 15	476.9	Convoluted beds
C4Ar.2n (o)		9.54	32R-3, 15	478.3	32R-3, 25	478.4	
C5n.1n (t)		9.64	33R-1, 75	485.6	33R-2, 45	486.8	
C5n.2n (o)		10.84	39R-3, 105	546.5	39R-3, 115	546.6	
C5r.1n (t)		10.94	39R-5, 95	549.2	39R-5, 105	549.3	
C5r.1n (o)		10.99	39R-6, 135	550.9	40R-1, 55	553.0	End of core and drilling disturbance
C5An.1n (t)		11.84	44R-1, 95	591.6	44R-2, 25	592.4	
C5An.1n (o)		11.99	47R-4, 45	623.5	48R-1, 45	629.8	
C5An.2n (t)		12.10	49R-3, 115	642.9	49R-3, 125	643.0	
C5An.2n (o)		12.32	51R-2, 115	660.4	51R-2, 125	660.5	
C5AAn (t)		12.93	55R-2, 15	697.9	55R-3, 5	699.1	
C5AAn (o)		13.08	57R-2, 55	717.5	57R-2, 65	717.6	
C5ABn (t)		13.25	58R-5, 75	731.8	58R-5, 105	732.1	
C5ABn (o)		13.45	62R-3, 15	766.7	62R-4, 5	768.1	
C5ACn (t)		13.67	65R-1, 35	792.7	65R-1, 45	792.8	

Note: (o) = onset, (t) = top.

tion and inclination change strongly, suggesting that we no longer have a dominant declination error. Similar phenomena are seen in a number of cores, such as Sections 157-953C-32R-3, 157-953C-39R-3, and 157-953C-58R-5, where there are reversals in continuous lengths of core.

### Conclusion

A preliminary magnetostratigraphy for Holes 953A, 953B, and 953C has been generated to a depth of 800 mbsf, which is consistent with the biostratigraphy, and indeed is not an entirely independent data set, being constrained broadly by those results. It appears that the drilling contamination is less important in these more lithified cores than in the MAP site cores, suggesting that the drilling overprint is caused by the deformation of the soft unconsolidated muds in the field of the drill string.

### PETROGRAPHY, MINERALOGY, AND GEOCHEMISTRY OF VOLCANICLASTIC SEDIMENTS

A wide variety of volcaniclastic sediments were recovered at Site 953, including fine-grained ash-fall layers, crystal-lithic silts and

sands with biogenic clasts, pumiceous sands, vitric tuffs with variable crystal and lithic contents, and hyaloclastite tuffs, lapillistones and lapilli breccias. The stratigraphic succession of lithic, crystal, and vitric components and the trace element geochemistry of whole-rock and sediment samples closely parallel the subaerial volcanic stratigraphy of Gran Canaria. In addition, the first appearance of certain diagnostic minerals and rock fragments is very useful for subdividing the lithostratigraphic section (Table 5).

### Petrography and Mineralogy

Unit I (0–197 mbsf) contains numerous beds of crystal-lithic silt and sand, with variable proportions of biogenic clasts, minor pumiceous sands, and many fine-grained ash layers. Tachylitic basalt clasts are the dominant lithic component of the silts and sands, together with less abundant clasts of crystalline basalt. Trachyphonolite lava (groundmass aegirine) and fine-grained tuff fragments are also present. Crystals are mostly plagioclase and clinopyroxene (including Ti-augite) with less abundant brown amphibole (Fig. 23) and biotite. Pumice fragments and sideromelane are present in variable amounts and are abundant in some beds (up to 60 modal% sideromelane in interval 157-953A-8H-1, 123–124 cm). The ash fall layers are composed chiefly of fresh, colorless glass shards presumably of phonolitic composition (Fig. 6). With the exception of these ash

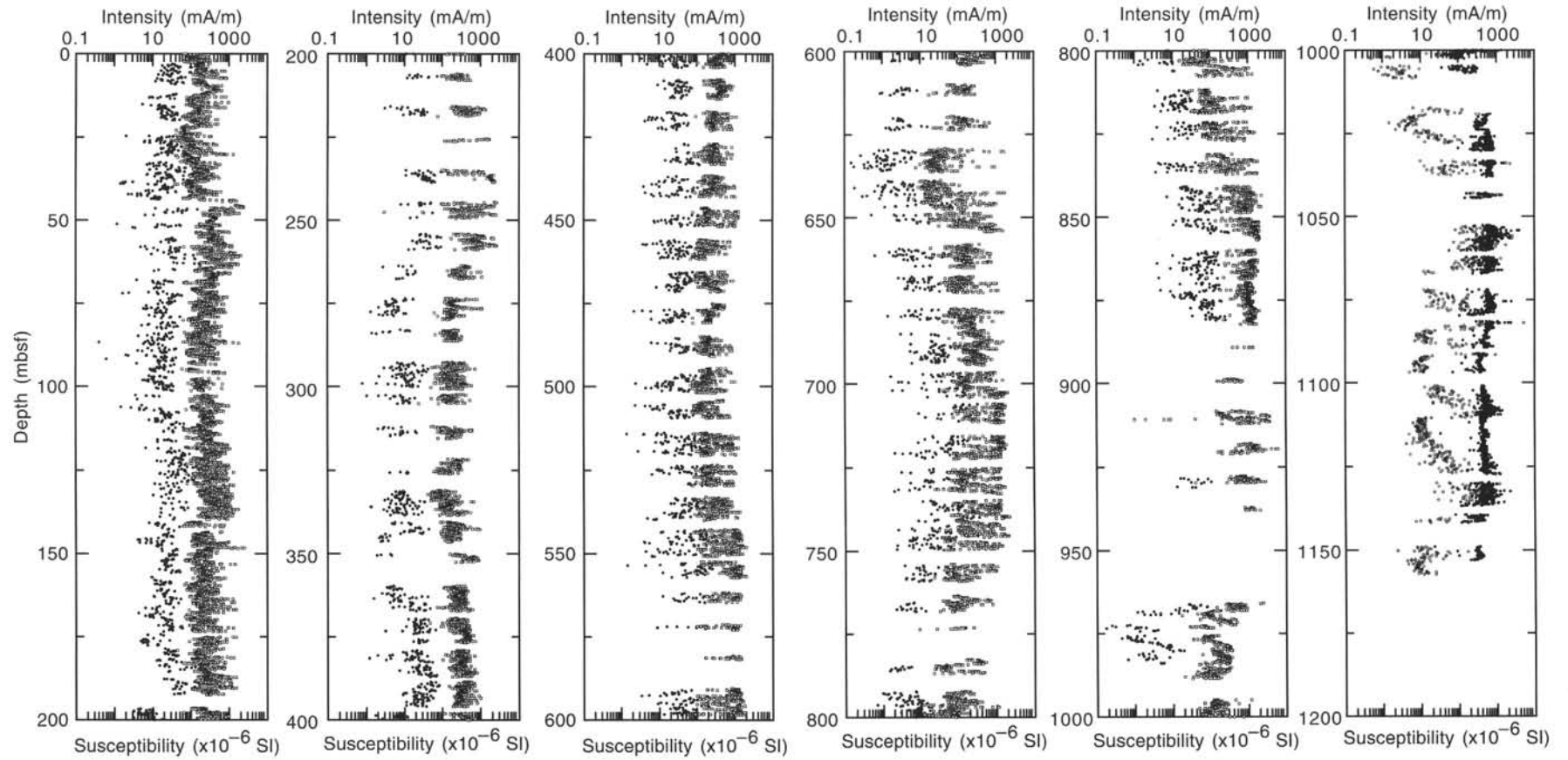


Figure 20. 25 mT NRM intensity (filled circles) and susceptibility (open squares) for Holes 953A and 953C.

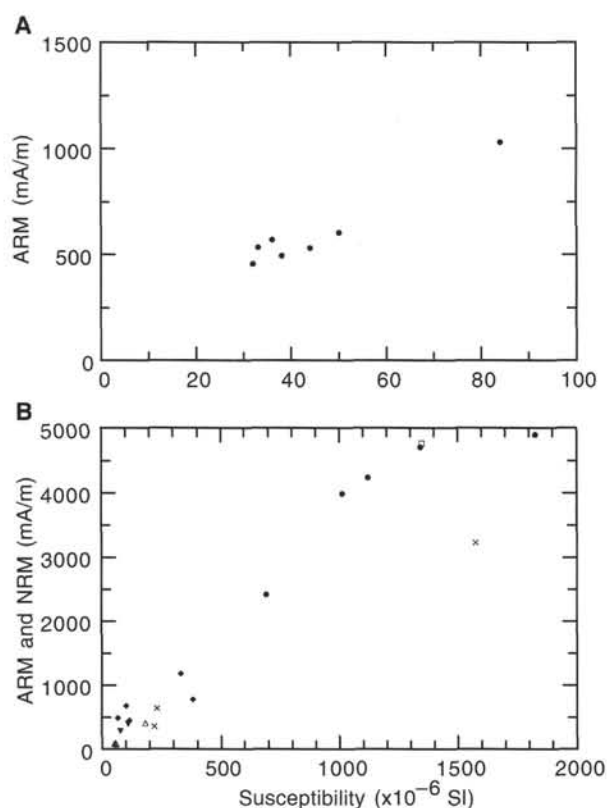


Figure 21. King diagram. ARM (0.1;100 mT) vs. weak field susceptibility for (A) Hole 953A and (B) Hole 953C. Filled circle = dark to light dark claystones, open square = dark claystones with nanofossils, filled diamond = nanofossil chalks with clay, open triangle = light dark clayey sandstones and green tuffs, filled triangle = coarse light gray nanofossil clay and vitric tuff, and x = dark sands and siltstones.

layers, which probably are the result of explosive eruptions of Teide Volcano (Tenerife), the volcanoclastic components found in Unit I appear to be largely the result of erosion of the Miocene Fataga Group (trachyphonolite) and Pliocene Roque Nublo Group (Ti-augite, brown amphibole) of Gran Canaria, together with input from the late Pliocene to Holocene Post-Roque Nublo basalts and basanites (sideromelane, crystals, basaltic lithics).

Unit II (197–263 mbsf) contains thin beds of foraminifer-lithic silt and sand, along with basaltic sandstones and lapillistones. Volcanic lithic components are generally similar to those found in Unit I; tachylite to crystalline basalt clasts and less abundant trachyphonolite lava and tuff fragments dominate. Crystals are chiefly plagioclase and Ti-augite, with lesser amounts of alkali feldspar and brown amphibole, and minor biotite and aegirine. Minor sideromelane is present in many of the sands and, less frequently, pumice, but felsic glass shards are rare. Volcanic components from Unit II probably are dominantly from the Roque Nublo Group on Gran Canaria (plagioclase, Ti-augite, brown amphibole) whose age corresponds to the time interval represented by this unit, with lesser input from erosion of the Fataga Group.

Unit III (263–398 mbsf) contains thin beds of foraminifer-lithic silt and sand but has much less basaltic sandstone and lapillistone than is found in Unit II. Lithic clasts are dominantly trachyphonolite lava (diagnostic aegirine) and fine-grained tuff. Tachylitic basalt clasts are less abundant, and minor medium-grained phonolite and trachyte clasts are present. Alkali feldspar is most abundant among crystal components, together with lesser amounts of clinopyroxene (Ti-augite), biotite, alkali amphibole, brown amphibole, and plagioclase.

class. Glass shards and pumice are rare, except in Core 157-953A-10R. Unit III corresponds with a late Miocene to Pliocene volcanic hiatus on Gran Canaria, and is characterized by a paucity of both mafic and felsic vitric components.

Unit IV (398–850 mbsf) has been subdivided into three subunits based on the frequency and lithology of volcanoclastic sediments (see “Lithostratigraphy,” this chapter).

Subunit IVa (398–504 mbsf) contains numerous beds of claystone and nanofossil claystone that grade downward into dark, lithic-crystal-vitric siltstones and sandstones. Lithic clasts are mainly trachyphonolite pumice, tuff, and lava together with minor tachylitic basalt. Crystals are dominantly alkali feldspar, with lesser amounts of green clinopyroxene (aegirine-augite), biotite, and alkali amphibole. Glass shards and small pumice fragments are abundant. Minor sideromelane is also present. Volcanic components from Unit IVa, especially the abundant felsic vitric clasts, are most likely derived from the upper Fataga Group.

Subunit IVb (504–754 mbsf) also contains numerous beds of graded lithic-crystal-vitric siltstone and sandstone, as found in Subunit IVa. Abundant lithic clasts include both basaltic and trachyphonolite rock fragments. Basalts are mostly tachylite, with some plagioclase-phyric and crystalline varieties. Trachyphonolite fragments include both fine-grained tuff (Fig. 24) and lava, with groundmass crystals of aegirine and alkali amphibole. Very rare clasts of medium-grained gabbro are present. Crystals are dominantly alkali feldspar, with lesser amounts of clinopyroxene (mostly aegirine-augite), biotite, and alkali amphibole. Many sediments contain abundant felsic glass shards (bubble-wall and tricusate) and small pumice (tubular vesicles), together with minor amounts of nonvesicular felsic glass (perlitic obsidian) and altered sideromelane. The mineralogy and abundant trachyphonolite tuff and lava clasts appear to be largely derived from Fataga Group lava flows, ignimbrites, and tephra fall deposits.

Subunit IVc (754–850 mbsf) contains numerous beds of vitric-crystal siltstone, sandstone, and lapillistone, and vitric tuffs. Felsic glass shards and small pumice are abundant in many sediments and are the dominant component of the vitric tuffs (Fig. 25; also Fig. 13). Minor amounts of obsidian and sideromelane are also present. Alkali feldspar is the dominant crystal component, together with lesser amount of green clinopyroxene (aegirine-augite), alkali amphibole, and biotite. Basaltic clasts are a minor component and are present only in some breccias and lapillistones. They are mostly tachylitic, with some plagioclase- and clinopyroxene-phyric varieties. Some contain large clinopyroxene glomerocrysts. Very rare clasts of gabbro are present. The first appearance of biotite in interval 57-953B-64R-1, 142–146 cm (Fig. 26), and its presence in all stratigraphically higher cores, marks the beginning of Fataga Group volcanism. Coarse basaltic ash in Sample 157-953B-70R-3, 4–7 cm (Fig. 27), is equivalent to the basaltic component of ignimbrite P1, a compositionally zoned cooling unit that is an important stratigraphic marker at the base of the Mogan Group (Schmincke, 1994). The occurrence of zircon in felsic pumice in the same bed further substantiates this interpretation.

Unit V (889–889 mbsf) contains lithic-crystal siltstones, sandstones, lapillistones, and minor hyaloclastite tuffs. Lithic clasts are dominantly basalt, with all textural transitions from tachylite to crystalline. Some clasts of intermediate lavas such as hawaiiite and mugearite are present. Reddish-brown oxidized clasts also occur. Crystals are chiefly clinopyroxene (Ti-augite), together with minor olivine pseudomorphs, very rare basaltic hornblende, and plagioclase. Some lithologies contain abundant altered sideromelane shards, including both vesicular and nonvesicular types (Fig. 14). The abundance of basaltic clasts suggests that the volcanoclastic components are derived from the subaerial shield lavas and pyroclastics on Gran Canaria.

Unit VI (889–969 mbsf) consists largely of basaltic sandstone, lapillistone, and breccia. Basaltic clasts ranging texturally from tach-

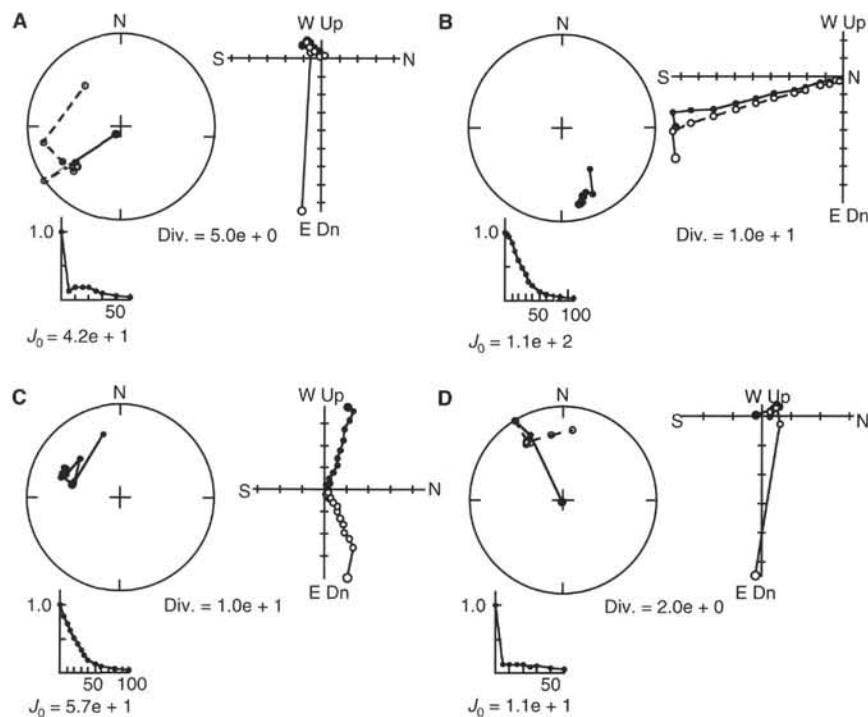


Figure 22. AF demagnetization behavior of discrete samples, Schmidt net, Zijderveld diagram, and intensity plots. **A.** Sample 157-953C-49R-3, 116 cm. **B.** Sample 157-953C-62R-1, 5 cm. **C.** Sample 157-953C-67R-4, 23 cm. **D.** Sample 157-953C-87R-1, 111 cm.

ylite to crystalline are abundant, and many contain large, subhedral phenocrysts of both augite and pigeonite(?). Large olivine phenocrysts pseudomorphed by fine-grained, fibrous alteration products (chlorite?) are common in the lower part of the unit. Some basalt clasts are highly vesicular. Crystalline clasts have groundmass plagioclase and Ti-augite. Some clasts of intermediate lavas such as mugearite and benmoreite are present. Large subhedral crystals of clinopyroxene also occur as isolated crystals. Olivine pseudomorphs are restricted to the lower part of the unit. Most sediments contain variable amounts of altered sideromelane shards. They are moderately to highly vesicular in the upper part of the unit, grading downward to nonvesicular to slightly vesicular. This decrease in vesicularity is in part coincident with an increase in the abundance of picritic basalt lithic clasts. Clinopyroxene phenocrysts, glomerocrysts, and minor olivine pseudomorphs occur in the sideromelane shards. Because this unit contains both subaerially erupted basalt clasts and abundant hyaloclastite, it probably corresponds to the transition from shallow submarine to emergent shield stage of Gran Canaria.

Unit VII (969–1159 mbsf) consists entirely of hyaloclastite tuff, lapillistone, and breccia. Dominant lithic clasts are picritic basalt, ranging from tachylite to crystalline, with abundant large olivine pseudomorphs (Fig. 28), rare fresh olivine, and clinopyroxene (augite and pigeonite?). Large clinopyroxene glomerocrysts are common. Basalt clasts range from highly vesicular to dense, nonvesicular tachylite. Large grains of tabular prehnite fill some vesicles (92R-2, 35–42 cm). Crystalline clasts have groundmass plagioclase and Ti-augite. Some oxidized, reddish-brown clasts are also present. All sediments contain abundant altered sideromelane (see Fig. 16). All transitions from nonvesicular to highly vesicular are observed, frequently within the same thin section. Some intervals are dominated by nonvesicular to slightly vesicular shards. Olivine pseudomorphs and clinopyroxene phenocrysts are common in sideromelane shards and as isolated crystals. As with Unit VI, this unit also contains both subaerially-erupted basalt clasts and abundant hyaloclastite, and probably corresponds to the transition from shallow submarine to emergent shield stage of Gran Canaria. In particular, the abundance of nonve-

sicular shards indicates that some material was derived from basaltic eruptions in relatively deep water.

## Geochemistry

44 samples from Site 953 were analyzed by XRF for major and trace element abundances. The results are given in Table 6. Analytical conditions and uncertainties are discussed in the "Petrography, Mineralogy, and Geochemistry of Volcaniclastic Sediments" section of the "Explanatory Notes" (this volume). Samples were taken largely from the lower half of the sequence at Hole 953C (Cores 157-953C-45R through 157-953C-103R), as it contains the most abundant volcaniclastic sediments. Both coarse (sand-sized) and fine-grained (silty) sediments were analyzed. The samples include relatively pure vitric tuffs, sandstones composed of biogenic debris, volcanic rock clasts and single crystals, and basaltic hyaloclastites completely altered to clay and zeolites from the lowermost part of the hole (below 850 mbsf). Thin sections were prepared from most of the chemically analyzed samples (see previous section for discussion).

Of the nine analyzed trace elements, four (Cr, Ni, V, and Cu) were classified as compatible, as they are enriched in the mafic rocks. The incompatible elements enriched in the felsic rocks include Zr, Nb, Ce, Y, Rb, and Zn. Ba and Sr show intermediate behavior as they are both strongly fractionated in alkali feldspar and plagioclase, two common phenocryst phases, and they are also highly mobile. In addition, Sr occurs in calcareous biogenic material.

Major and trace element variation diagrams are shown in Figures 29 and 30. Although most of the analyzed samples are impure, inasmuch as they represent mixtures of different volcanic and nonvolcanic components, the major and trace element concentrations clearly mirror the different chemical characteristics of the magmatic groups on the island from which they were derived during the last ~16 m.y. Even data for elements such as  $K_2O$  and  $Na_2O$ , which are highly mobile in the marine environment, form surprisingly coherent patterns. In order to distinguish better the volcanic component in these sediments, the major element data shown in Figure 29 were recalculated

to account for the abundance of  $\text{CaCO}_3$  contributed from biogenic material. This was done by assuming that all weight LOI in excess of 10 wt% was  $\text{CO}_2$ , so that an equivalent amount of  $\text{CaO}$  was subtracted from the analysis. The value of 10 wt% was chosen because it is typical of the biogenic-poor sediments at this site and therefore was assumed to be from  $\text{H}_2\text{O}$  loss. For two highly calcareous samples, the entire LOI was assumed to result from loss of  $\text{CO}_2$ .

Volcaniclastic sediments in Unit IV have  $\text{SiO}_2$  contents from 49 to 68 wt% (all values on  $\text{CaCO}_3$ -free basis), with most values greater than 55 wt% (Fig. 29). Concentrations of  $\text{MgO}$ ,  $\text{Fe}_2\text{O}_3$ , and  $\text{TiO}_2$  are relatively low, whereas alkalis and  $\text{Al}_2\text{O}_3$  are relatively high. These data indicate evolved source compositions similar to the alkaline magmas that erupted on Gran Canaria during the Miocene. Volcaniclastic sediments with evolved compositions in Subunits IVa and IVb have lower  $\text{SiO}_2$  and  $\text{MgO}$  and generally higher  $\text{Al}_2\text{O}_3$ ,  $\text{K}_2\text{O}$ , and  $\text{Na}_2\text{O}$  than do those in Subunit IVc. These systematic differences in major element compositions clearly reflect the chemical differences between volcanic rocks from the Mogan and Fataga Groups. Rocks of the Mogan Group are mainly anorthoclase-bearing, peralkaline rhyolites and trachytes similar in composition to the sediments of Subunit IVc, in contrast to the Fataga Group volcanics (Subunits IVa and IVb), which are moderately silica-undersaturated trachyphonolites.

Trace element data for sediments in Unit IV (Fig. 30) show relatively high concentrations of Nb (40–250 ppm), Zr (330–1310 ppm), Ce (100–430 ppm), and Rb (30–110 ppm), moderate concentrations of Ba (25–760 ppm) and Sr (70–1090 ppm), and relatively low Ni (mostly <30 ppm) and Cr (mostly  $\leq 75$  ppm). The high concentrations of many incompatible elements (Zr, Nb, Ce) are a further characteristic of evolved alkaline magmas from the Mogan and Fataga Groups, which can be distinguished using Zr/Nb ratios (Schmincke, 1982). Sediments in the lower part of Subunit IVb and in IVc have much higher Zr/Nb (5.9–7.3) than those in the middle and upper parts of Subunit IVb and in IVa (Zr/Nb largely 3.0–4.3). These differences correspond to peralkaline rhyolites of the Mogan Group (high Zr/Nb) and trachyphonolites of the Fataga Group (low Zr/Nb), in agreement with the provenance of the volcaniclastic sediments indicated by both major element and petrographic data.

Basaltic tuffs, lapillistones, and breccias in Units V, VI, and VII have low  $\text{SiO}_2$  contents and very high  $\text{MgO}$  ( $\leq 17$  wt%; Fig. 29). They also have high total Fe and  $\text{TiO}_2$ , which is a characteristic of mafic magmas from the Canary Islands (Schmincke, 1982). Relative to the evolved felsic rocks of Unit IV, they have generally lower abundances of incompatible trace elements and much higher concentrations of Ni (mostly 400–860 ppm), Cr (161–1100 ppm), and V (150–780 ppm; Fig. 30). In particular, the very high Ni contents and the abundance of large olivine pseudomorphs found in Unit VII indicate that olivine-rich to picritic magmas were dominant during the submarine and shallow emergent shield phases that are represented by this unit.

## INORGANIC GEOCHEMISTRY

### Introduction and Operation

A total of 42 interstitial-water samples were taken between 5.95 and 997.70 mbsf at Site 953 (Table 7). The sampling strategy and analytical methods generally followed those employed at Sites 950–952. Pore waters were successfully extracted at regular intervals down to 856 mbsf, but only a single sample was obtained below this. Additionally, a suite of five closely spaced pore-water samples were collected between 698.61 and 710.11 mbsf to study variation in the vicinity of a thick lithic crystal sandstone at 702.74 mbsf. Samples were analyzed for pH, salinity, chlorinity, alkalinity, sulfate, ammonia, sodium, potassium, lithium, silica, calcium, magnesium, and strontium (see “Explanatory Notes,” this volume). The bulk mineral-

ogies of selected samples were assessed qualitatively by XRD analysis.

In the uppermost beds (Unit I; see “Lithostratigraphy,” this chapter), modest changes in pore-water composition are driven by the bacterially mediated oxidation of organic matter and the dissolution of biogenic silica. Much more extreme pore-water variation is seen below 200 mbsf. Here, diagenetic alteration of the volcanogenic fraction (which constitutes a very high proportion of the sediment), particularly the dissolution of volcanic glasses and the precipitation of smectites and zeolites, produces complex depth profiles. Lithological variation exerts a major control on pore-water geochemistry at Site 953.

### Sulfate, Ammonia, and Alkalinity

Sulfate (Fig. 31) decreases from 25.9 mmol/L at 6 mbsf (slightly less than the 28.9 mmol/L typical seawater value), to moderate values of ~16–17 mmol/L at 170 mbsf. The low gradient of the profile indicates low rates of sulfate reduction at Site 953, a consequence of the low organic matter content (typically <0.2%; see “Organic Geochemistry,” this chapter). Decreasing sulfate in the uppermost 100 m is matched by increasing ammonia production. Below 190 mbsf, pore-water  $\text{SO}_4^{2-}$  increases strongly to high values of around 35 mmol/L at 500 mbsf, before decreasing back to seawater-like values of 27–28 mmol/L between 680–860 mbsf. This marked peak in sulfate occurs in the upper part of Unit IV (Fig. 31), a sequence of glass-rich sediments underlying the nanofossil ooze and chalk-dominated sediments of Units I–III (see “Lithostratigraphy,” this chapter). The abnormally high  $\text{SO}_4^{2-}$  levels recorded at Site 953 may be attributed to the dissolution of sulfur-rich glasses in the sediments. The deepest sample at 997 mbsf is relatively depleted in  $\text{SO}_4^{2-}$ , containing only 17.4 mmol/L.

Alkalinity increases from 3.79 mmol/L at 6 mbsf (significantly higher than the 2.3  $\mu\text{mol/L}$  seawater value), to a maximum of 5.45 mmol/L around 14 mbsf (Fig. 31), before declining to a minimum of 0.3 mmol/L at 275 mbsf. Alkalinity concentrations increase slightly to 1.9 mmol/L at 596 mbsf. Increased alkalinity in the upper beds may be attributed to  $\text{H}_2\text{S}$  and  $\text{HCO}_3^-$  production accompanying sulfate reduction. As at Sites 950–952, the upper alkalinity maximum occurs above the sulfate and calcium minima and the ammonia maximum, indicating that carbonate precipitation at and below 50 mbsf is consuming alkalinity.

Ammonia concentrations are low and variable in the interstitial waters at Site 953. Ammonia increases progressively from 100 to 420  $\mu\text{mol/L}$  at around 90 mbsf (Fig. 31), and then broadly decreases to a minimum of about 140  $\mu\text{mol/L}$  around 510 mbsf. An inverse relationship between sulfate and ammonia is apparent in the upper beds, confirming that sulfate reduction of organic matter is generating  $\text{NH}_4^+$ , but variation is less than at Sites 950–952. Changes of ammonia concentration in the deeper parts of the sequence may be attributed largely to  $\text{NH}_4^+$  reactions with clay minerals.

### Salinity and Chloride

Salinity (Fig. 32) increases steadily from seawater values (35 g/kg) in the upper 110 mbsf, reaching a maximum of 47 g/kg at 856 mbsf. The deepest sample yielded only 39 g/kg. The slope of the salinity profile increases significantly below 600 mbsf.

Chloride (Fig. 32) shows a similar trend to salinity, increasing from around 570 mmol/L (already above the typical seawater value of 559 mmol/L) in the upper 50 m of sediment to 729 mmol/L at 856 mbsf, before falling to 594 mmol/L in our deepest sample. This Cl<sup>-</sup> minimum may result from the release of chemically bound water at depth from clay minerals; XRD data indicate well-crystallized smectites in the matrix of the basaltic lapillistones and breccias at this level (Unit VII). High salinities and chlorinities are attributed to the gen-

**Table 5. Summary of volcanoclastic components, Site 953.**

Unit	Subunit	Core (top)	Depth (mbsf)	Age (Ma)	Period	Lithologies with volcanic components
I		1H	0.0	0.0	Post-Roque Nublo	Foraminifer-lithic-crystal silt and sand, pumice sand Volcanic ash
II		3R	197	2.8	Roque Nublo	Foraminifer-lithic sand, basaltic lapillistone
III		10R	263	4.5	Volcanic hiatus	Foraminifer-lithic silt and sand
IV	a	26R	398	8.3	Late Fataga	Lithic-crystal siltstone and sandstone
	b	34R	504	10.0	Early and middle Fataga	Lithic-crystal siltstone, sandstone, lapillistone, and debris flow
	c	61R	754	13.4	Early Fataga and Mogan	Lithic-crystal siltstone, sandstone, and lapillistone, vitric tuff
V		71R	850	14.0	Subaerial shield	Lithic-crystal siltstones and sandstones, minor hyaloclastite tuff
VI		75R	889	14.7	Submarine and emergent shield	Hyaloclastite lapillistone and tuff, basaltic breccia and coarse sandstone
VII		83R-2	969	15.8	Submarine and emergent shield	Hyaloclastite tuff, lapillistone, and lapilli breccia



Figure 23. Photomicrograph of a calcareous lithic sandstone from Unit I containing abundant brown amphibole characteristic of the Roque Nublo volcanics. Field of view is 4.0 mm wide. Sample 157-953A-20H-6, 125–129 cm.



Figure 24. Photomicrograph of a lithic crystal sandstone from Subunit IVb that contains clasts of fine-grained, banded trachyphonolite tuff from the Miocene Fataga Group, together with phenocrysts of alkali feldspar and pale-green clinopyroxene (aegirine-augite). Field of view is 4.0 mm wide. Sample 157-953C-49R-7, 57–58 cm.

eration of alkali- and alkali earth-rich brines from the alteration of volcanoclastic debris (see below).

### Sodium, Potassium, and Lithium

Pore-water potassium concentrations (Fig. 33) decline from slightly higher (11.9 mmol/L) than seawater values, to about 4 mmol/L between 250 and 450 mbsf, before rising again in the lower beds. Phillipsite first appears in the sequence around 190 mbsf, so the potassium minimum is probably caused by the precipitation of that mineral. Between 450 and 770 mbsf, potassium increases to more than 8 mmol/L within the upper beds of Subunit IVc, before decreasing suddenly to 3.68 mmol/L at the top of Unit V. Rising potassium levels in the lower parts of Unit IV must be caused by the liberation of alkalis from volcanic glasses in this interval. The rapid fall in pore-water po-

tassium at the top of Unit V may be attributed to the precipitation of heulandite/clinoptilolite in the matrix of these crystal vitric sands. In the deepest sample, potassium rises again to 9.03 mmol/L in the pore water of Unit VII.

The upper part of the sodium profile (Fig. 33) is variable, but sodium increases markedly from seawater-like values of 470–490 mmol/L in the upper 185 mbsf, to a maximum of 793 mmol/L at 699 mbsf, before declining again to 503 mmol/L in our deepest sample. Natrolite was identified in Subunits IVa and IVb by XRD analysis. The high sodium concentrations of the interstitial waters in these beds combined with the appearance of a Na-zeolite indicate Na-rich brines are being derived from the breakdown of sodic glasses. Declining sodium concentrations in Units IVc–VII correspond to in-

Table 5 (continued).

Unit	Rock fragments	Volcanic components	
		Crystals	Vitric clasts
I	Basalt (tachylite > crystalline), trachyphonolite lava and tuff	Plagioclase, clinopyroxene > brown amphibole > biotite Minor clinopyroxene > biotite, plagioclase	Pumice, sideromelane Glass shards
II	Basalt (tachylite, crystalline), trachyphonolite lava and tuff	Plagioclase, Ti-augite > alkaline feldspar, brown amphibole > biotite, aegirine	Minor sideromelane, pumice
III	Trachyphonolite lava and tuff basalt (tachylite)	Alkaline feldspar > clinopyroxene, biotite, alkaline amphibole, brown amphibole, plagioclase	Very minor glass shards and pumice
IV	Trachyphonolite lava, tuff, and pumice basalt (tachylite)	Alkaline feldspar > clinopyroxene, biotite, alkaline amphibole, plagioclase	Glass shards, pumice, minor sideromelane
	Basalt (tachylite > crystalline) and trachyphonolite (Fataga) lava and tuff	Alkaline feldspar > green clinopyroxene > biotite, alkaline amphibole > plagioclase, olivine	Glass shards, pumice, minor obsidian, sideromelane
	Basalt (tachylite > crystalline)	Alkaline feldspar > green clinopyroxene > alkaline amphibole > biotite	Glass shards, pumice, minor obsidian, sideromelane
V	Basalt (tachylite, crystalline), minor differentiated lava (mugearite)	Clinopyroxene, Ti-augite >> olivine pseudomorphs, brown amphibole, plagioclase, alkaline feldspar	Sideromelane
VI	Basalt (tachylite, crystalline, picrite), minor differentiated lavas (benmoreite)	Coarse subhedral clinopyroxene, minor coarse olivine pseudomorphs	Abundant sideromelane (largely vesicular)
VII	Picritic basalt (tachylite, crystalline)	Abundant coarse olivine pseudomorphs and clinopyroxene	Abundant sideromelane (nonvesicular to highly vesicular)

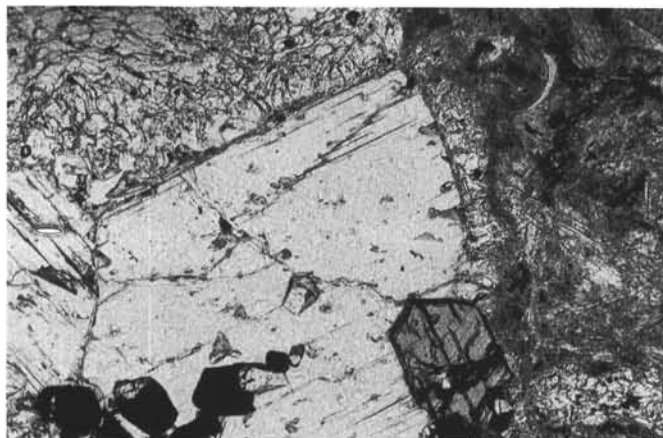


Figure 25. Photomicrograph of a coarse-grained vitric tuff from Subunit IVc that contains a crystal of alkali amphibole included in a large alkali feldspar phenocryst within a pumice clast. These features are characteristic of Mogan Group peralkaline rhyolites on Gran Canaria. Note fine-grained matrix of glass shards at left. Field of view is 3.2 mm wide. Sample 157-953C-65R-6, 100–101 cm.

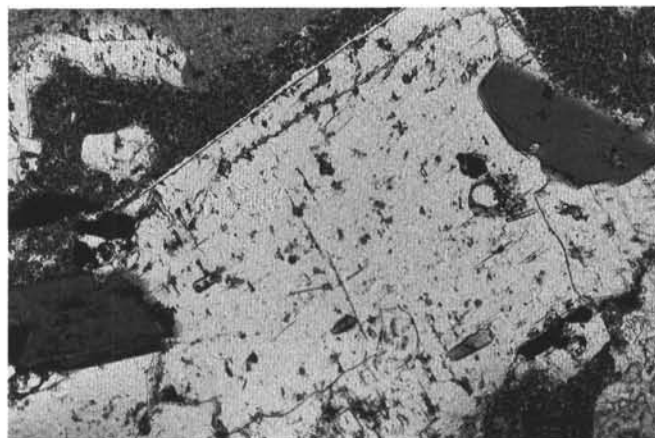


Figure 26. Photomicrograph of a lapillistone from Subunit IVc showing biotite and a small crystal of aegirine-augite included in a plagioclase phenocryst. This occurrence of biotite probably marks the onset of Fataga Group volcanism. Field of view is 3.2 mm wide. Sample 157-953C-64R-1, 142–146 cm.

creasing amounts of other Na-zeolites in vesicles, vugs, and veins in these beds.

Lithium (Fig. 33) decreases from 22 (less than the typical seawater value of 27  $\mu\text{mol/L}$ ) to 19  $\mu\text{mol/L}$  in the uppermost 40 m, and then generally increases, but displays significant variation down to the bottom of the hole. Lithium increases from 19 to 32  $\mu\text{mol/L}$  between 40 and 128 mbsf; silica (see below) displays a similar trend at this depth. Lithium release to interstitial waters here could be associated with reactions involving dissolution of volcanic glass and/or biogenic silica.

Below 128 mbsf, lithium decreases to a second minimum of 19  $\mu\text{mol/L}$  at 248 mbsf. These low concentrations could be attributed to

the uptake of lithium by zeolites (phillipsite first appears around 190 mbsf). A second broad peak in lithium concentrations occurs at 400 mbsf close to the Unit III/IV boundary. Decreasing lithium below 400 mbsf results in a further minimum of 23  $\mu\text{mol/L}$  around 500 mbsf (base of Subunit IVa), before rising to a final maximum of 47  $\mu\text{mol/L}$  at 827 mbsf, within the lower part of Subunit IVc. Significant mineralogical changes occur in these intervals with the appearance of smectites below 400 mbsf and analcime below 500 mbsf.

High concentrations of lithium in the lower part of Subunit IVb and particularly in Subunit IVc might be attributable to the breakdown of Li silicate-rich glasses or the dissolution of biogenic silica, since this interval is also characterized by high concentrations of dissolved silica (see below). The large decrease in pore-water lithium in



Figure 27. Photomicrograph of a coarse basaltic tuff from Subunit IVc that contains abundant tachylitic ash, colorless felsic pumice, and phenocrysts of alkali amphibole and feldspar. This tuff is probably correlative with the P1 ignimbrite at the base of the Mogan Group on Gran Canaria. Field of view is 4.0 mm wide. Sample 157-953C-70R-1, 117–119 cm.

Units V–VII may reflect uptake of alkali metals by zeolites and/or diagenetic clay minerals.

### Silica

Silica rises from a surficial value of around 313  $\mu\text{mol/L}$ , to a maximum of 517  $\mu\text{mol/L}$  at around 100 mbsf (Fig. 34), before declining to low values of around 120  $\mu\text{mol/L}$  between 200 and 700 mbsf. This increase in pore-water silica may be due to the dissolution of volcanic ash and/or biogenic silica in Unit I. A small peak of 165  $\mu\text{mol/L}$  silica occurs around 620 mbsf.

Below 740 mbsf, silica concentrations rise sharply to high and variable concentrations in Unit IVc, reaching 693  $\mu\text{mol/L}$  at 827 mbsf. These high concentrations are associated with beds containing relatively well-preserved volcanic glasses of peralkaline trachytic to rhyolitic composition (see “Sediment Geochemistry,” this chapter) and also with the presence of thin organic-rich green turbidites in the sequence. By analogy to similarly aged sediments at Site 952, these turbidites may contain biogenic silica. Below this, albeit on the basis of very limited data (two values), silica concentrations are low, indicating silica removal from pore waters.

The overriding control that lithology exerts on silica pore-water profiles is particularly well expressed in Site 953. Low silica concentrations in the middle and at the bottom of the sequence are correlated with the precipitation of diagenetic smectites and zeolites; high concentrations are associated with the dissolution of silica-rich volcanic glasses and/or biogenic silica in Units I and IVc.

### Magnesium, Calcium, and Strontium

Magnesium contents (Fig. 35) decline consistently in the pore waters at Site 953, from near-seawater values of 48 mmol/L (already less than a typical seawater value of 54 mmol/L) at 6 mbsf, to a minimum of 2 mmol/L at 998 mbsf. However, the profile displays two separate gradients, an upper steep linear decline between the sediment/water interface and 200 mbsf, which is consistent with the diffusional supply of  $\text{Mg}^{2+}$  from seawater to that depth, and below that, a more gentle general decline toward the bottom of the section. Minor divergences from this trend occur between 300 and 400 and 540 and 710 mbsf where concentrations temporarily increase to around 14 mmol/L. Low concentrations in the basal beds may be attributed to the precipitation of chlorite.

Calcium decreases from 7.2 mmol/L (Fig. 35) at 6 mbsf to a minimum of 4.8 mmol/L at 40 mbsf, indicating  $\text{Ca}^{2+}$  uptake into the solid



Figure 28. Photomicrograph of a hyaloclastite tuff from Unit VII showing tachylitic glass that contains large olivine phenocrysts that have been replaced by fine-grained fibrous chlorite. Note bladed zeolites in pore spaces. Field of view is 8.0 mm wide. Sample 157-953C-92R-2, 35–42 cm,  $\times 2.5$ .

phase at that level. Below this, concentrations rise again to 40.3 mmol/L at 248 mbsf, before decreasing sharply below, producing a minimum of 6.1 mmol/L at 620 mbsf. The upper  $\text{Ca}^{2+}$  minimum coincides with the base of the upper alkalinity peak, which is consistent with calcite precipitation around 40 mbsf consuming bicarbonate.

Decreasing pore-water  $\text{Mg}^{2+}$  below 150 mbsf and increasing  $\text{Ca}^{2+}$  concentrations probably result largely from diagenetic reactions within the silicate fraction, principally the dissolution of volcanic glasses and the precipitation of smectites and zeolites. Maximum  $\text{Ca}^{2+}$  removal is occurring around 620 mbsf in association with high Mg/Ca and Sr/Ca ratios (Fig. 35), while the strong positive Ca-gradient below this (reaching a maximum of 111 mmol/L at 856 mbsf), provides evidence for Ca being derived principally from alteration of the underlying basaltic volcanoclastic rocks in Units V–VII. Abundant calcite cements in the lower half of Unit IV suggest that high pore-water  $\text{Ca}^{2+}$  is attaining carbonate saturation in these beds.

Contents of dissolved strontium in the upper 130 m increase from 137 to 1130  $\mu\text{mol/L}$  before decreasing to a minimum of 464  $\mu\text{mol/L}$  at 540 mbsf. Pore-water strontium then increases progressively to a maximum value of 1120  $\mu\text{mol/L}$  in our lowest sample. Mg/Ca and Sr/Ca ratios show well-correlated trends (Fig. 35), which are the mirror images of the  $\text{Ca}^{2+}$  profile, emphasizing the very different behavior of calcium compared with the other two alkali earths.

## ORGANIC GEOCHEMISTRY

The shipboard organic geochemistry program at Site 953 followed the procedures used for Sites 950–952.

### Volatile Hydrocarbons

Concentrations of methane ( $\text{C}_1$ ) and ethane ( $\text{C}_2$ ) gases were monitored in every core by the standard ODP headspace-sampling technique as part of the SSP program. The methane content remained constantly low throughout the entire lithologic sequence of Site 953, fluctuating between 2 and 14 ppmv with a maximum 34 ppmv at 1080 mbsf (Fig. 36). No ethane was detected.

### Carbon, Nitrogen, and Sulfur Concentrations

Results for determinations of organic carbon, total carbon, total nitrogen, and total sulfur are presented in Figure 37 and Table 8. A total of 319 samples were analyzed for carbonate. Results were related to lithology as for the Sites 950–952. However, the carbonate anal-

yses could not be used as effectively in selecting samples containing possible organic carbon as in the previous sites because of the generally much lower amounts of organic carbon in the Site 953 lithologic units. Significant amounts of organic carbon occur only in a short interval around 804 mbsf within green turbidites.

In order to test the possibility of the occurrence of organic carbon in other lithologic units, representative samples were run on the CNS instrument. A total of 51 samples were analyzed for organic carbon, nitrogen, and sulfur (Table 8). There is no apparent correlation with lithology or depth (Fig. 37). In most cases concentrations of organic carbon were below detection or found only in very small amounts (0.02%–0.17%). In the olive-green turbidites around 804 mbsf (~13.6 Ma), organic carbon was consistently enriched, ranging between 0.29% and 0.45% TOC. A higher value of 2%–60% TOC was obtained at 5.78 mbsf, and elevated amounts occurred in two other analyses: at 26 mbsf (0.45%) and 148 mbsf (0.47%). Values of sulfur and nitrogen follow organic carbon, but as those values are very small, any interpretation of C/N ratios would be meaningless. The green organic-rich turbidites with oxidized pale green, organic-lean tops, found in Cores 157-953C-65R, 66R, and 67R, resembles the organic-rich facies from MAP Sites 950–952.

## PHYSICAL PROPERTIES

### Introduction

Measured physical properties included nondestructive GRAPE bulk density, magnetic susceptibility, natural gamma-ray, and *P*-wave velocity from whole-round core sections by using MST, as well as thermal conductivity following the full-needle probe method. Shear strength, longitudinal *P*-wave velocity, and index properties were measured from split sections on discrete samples (see “Explanatory Notes,” this volume). Although core recovery at Hole 953C was moderate, missing intervals affected the continuity of the physical properties. In general, physical properties variations on Site 953 define intervals that agree closely with the lithostratigraphic units (see “Lithostratigraphy,” this chapter) or they indicate compositional changes within the sediment.

### Whole-core Measurements

#### MST

Whole-round measurements of GRAPE density and magnetic susceptibility were made on all cores throughout Holes 953A, 953B, and 953C. However, because of the void spaces between sediment core and the plastic liner, *P*-wave velocity was measured only in Hole 953A. The natural gamma activity was recorded on some cores in Hole 953A; however, measurements were not performed in Holes 953B and 953C because of time constraints. Cores from Hole 953A were allowed to thermally equilibrate to room temperature for approximately 4 hr before MST logging; cores from Holes 953B and 953C were measured immediately. Sampling rate was typically one measurement every 1.5 to 2 cm for the *P*-wave logger, 2.5 cm for the GRAPE, 3 cm for magnetic susceptibility, and 30 cm for the natural gamma activity. For details on the MST sensors see the “Explanatory Notes” of the Leg 156 *Initial Reports* volume. Data obtained from all four sensors are shown on Figures 38 through 49.

#### Magnetic Susceptibility

Volumetric magnetic susceptibility was measured in all recovered cores from Holes 953A, 953B, and 953C. The volume magnetic susceptibility data for Holes 953A (0–192 mbsf) and 953C (187–1157 mbsf) are plotted on Figures 38 and 42, respectively. In general, magnetic susceptibility trends downcore are generally useful for lithological interpretation and stratigraphic correlations between holes, and at

Site 953 the trends have been provocative because of their correlation with volcanic intervals.

The magnetic susceptibility data for Hole 953A (Fig. 38) shows numerous high-amplitude spikes of up to  $1500 \times 10^{-6}$  SI units that are related mainly to volcanoclastic sands. This behavior continues in Hole 953C (Fig. 42) up to 260 mbsf, which coincides with the boundary between lithostratigraphic Units II and III (see “Lithostratigraphy,” this chapter). The interval between 260 and 500 mbsf (Units III and IVa) is characterized by a more quiet signal in the susceptibility, and the amplitude of the peaks are lower. Between 520 and 760 mbsf numerous high-amplitude magnetic susceptibilities were measured. This interval corresponds to lithostratigraphic Subunit IVb with its marked increase of volcanoclastic turbidites. The susceptibility increases from very low values at the top of Subunit IVc to more than  $1500 \times 10^{-6}$  SI units at the bottom, while values in Unit V are constantly high (around  $1500 \times 10^{-6}$  SI units). The susceptibility again has low values at the top of Unit VII, an increase in values up to 1060 mbsf ( $1500 \times 10^{-6}$  SI units), and then shows a decrease in values farther downcore.

#### GRAPE Bulk Density

The GRAPE density data collected at Holes 953A and 953C are displayed in Figures 39 and 43, respectively. GRAPE density data from the RCB cores were not corrected for drilling disturbances (reduced diameter), as the diameter of the recovered material was highly variable. Therefore, although the GRAPE data give an excellent indication of downcore trends, the use of GRAPE density values should be treated with caution. Filtered data points correspond to the average data value within a 0.125 m filter window for Hole 953A and a 1 m filter window for Hole 953C because of the low recovery in this hole. Along the profile for Hole 953A (Fig. 39), the larger peaks correspond to sand layers having densities between 1.75 and 2.0 g/cm<sup>3</sup>. The general trend of the average GRAPE density data shows an increase downcore from values close to 1.55 g/cm<sup>3</sup> near the mud line to 1.78 g/cm<sup>3</sup> at ~190 mbsf. Drilling disturbance may explain why some Hole 953C GRAPE density values are lower than those determined from discrete samples (up to a 0.3 g/cm<sup>3</sup> difference, sometimes even more). In spite of the discrepancies in some intervals, GRAPE density shows a general downcore trend similar to that of the densities determined from discrete samples.

#### *P*-wave Velocity

*P*-wave velocity was measured at Hole 953A to 192 mbsf. Filtered data are plotted against depth in Figure 40. The velocity increases from ~1480 m/s at the seafloor to 1575 m/s at 192 mbsf, with variations between 1450 and 1700 m/s. These velocities are close to the water velocity, which means that the sediments of Hole 953A have a high water content. In Holes 953B and 953C the velocity was not measured because of drilling disturbances that led to void spaces between the core liner and the sediment.

#### Natural Gamma Ray

The natural gamma-ray emission was measured in Hole 953A up to 167 mbsf with a gap between Cores 157-953A-11H and 157-953A-18H. The total gamma counts and their percentage in the different energy windows are displayed in Figure 41. Channels 2 and 3 represent low energies, whereas Channels 4 and 5 represent high energies. Channel 1 is the sum of the other four channels.

There are several high total gamma counts in the upper 15 m of the hole (up to 720 counts). The interval between 15 and 35 mbsf has less counts than the rest of the profile. Further downcore the counts are on a higher level again but shows a large scatter. The maximal counts were measured at 92 mbsf (735 counts).

Table 6. XRF major and trace element analyses of whole-rock samples, Site 953.

Hole, core/section:	953C-7R-2	953C-29R-3	953C-30R-1	953C-45R-1	953C-45R-2	953C-45R-2	953C-48R-6	953C-49R-7	953C-50R-4	953C-50R-4
Interval (cm):	1-4	107-108	118-120	55-58	63-67	114-117	108-111	58-60	81-83	98-100
Depth (mbsf):	236.51	450.27	457.08	600.95	602.53	603.04	636.18	647.63	653.61	653.78
Lithologic unit:	II	IVa	IVa	IVb						
Major elements										
(wt%)										
SiO <sub>2</sub>	44.25	60.04	59.99	59.16	42.98	40.26	57.77	60.96	62.90	43.90
TiO <sub>2</sub>	3.43	1.04	1.05	1.17	1.00	1.24	0.94	1.13	1.16	5.57
Al <sub>2</sub> O <sub>3</sub>	12.97	16.08	16.58	15.82	11.40	10.42	16.46	17.18	15.16	14.27
Fe <sub>2</sub> O <sub>3</sub>	13.09	6.89	5.57	5.71	4.11	7.42	4.35	5.08	7.86	15.45
MnO	0.16	0.08	0.08	0.23	0.22	0.39	0.16	0.17	0.12	0.15
MgO	9.61	2.79	2.03	2.33	1.08	3.92	1.88	1.93	1.04	3.73
CaO	11.53	2.60	3.39	5.48	33.38	31.33	9.67	2.41	0.33	11.01
Na <sub>2</sub> O	2.96	6.35	6.57	5.97	3.03	2.53	5.14	6.23	6.47	3.08
K <sub>2</sub> O	1.30	4.02	4.26	4.67	2.44	2.26	3.46	4.95	5.34	0.83
P <sub>2</sub> O <sub>5</sub>	0.70	0.08	0.09	0.15	0.23	0.33	0.09	0.13	0.05	1.83
Total	100.00	99.97	99.61	100.69	99.87	100.10	99.92	100.17	100.43	99.82
LOI	6.64	9.48	10.30	8.94	24.53	23.70	1.23	9.67	1.90	1.74
Trace elements										
(ppm)										
Cr	316	6	7	23	38	73	8	21	0	30
Ni	124	9	6	14	16	29	8	15	7	29
Cu	80	5	6	9	13	13	2	4	0	71
V	282	27	32	71	60	72	39	36	72	413
Zn	106	227	208	188	77	190	186	155	120	154
Sr	870	252	260	353	761	585	324	254	72	1086
Ba	345	139	160	310	196	279	164	763	25	159
Rb	17	75	82	75	46	32	56	76	110	15
Y	26	66	56	54	31	36	53	54	67	39
Zr	286	973	974	717	519	417	855	573	652	328
Nb	71	251	253	224	123	110	223	180	215	41
Ce	101	428	420	341	194	179	317	328	337	102
Zr/Nb	4.1	3.9	3.9	3.2	4.2	3.8	3.8	3.2	3.0	8.0

Table 6 (part 3).

Hole, core/section:	953C-73R-1	953C-73R-4	953C-76R-1	953C-77R-2	953C-82R-1	953C-83R-4	953C-83R-5	953C-83R-6	953C-84R-3	953C-84R-7	953C-85R-1
Interval (cm):	129-131	25-28	23-26	52-54	42-44	41-45	119-121	64-68	57-60	47-50	8-12
Depth (mbsf):	870.99	874.23	898.93	910.03	956.82	970.15	972.07	972.78	978.39	982.95	985.38
Lithologic unit:	V	V	VI	VI	VI	VII	VII	VII	VII	VII	VII
Major elements											
(wt%)											
SiO <sub>2</sub>	38.12	47.19	45.22	41.11	43.46	46.30	46.28	46.60	46.83	46.38	45.54
TiO <sub>2</sub>	1.91	3.00	3.39	4.82	4.08	3.35	3.13	3.91	3.62	3.67	3.57
Al <sub>2</sub> O <sub>3</sub>	10.46	12.13	9.27	9.30	9.47	10.04	9.22	12.25	10.81	10.27	7.88
Fe <sub>2</sub> O <sub>3</sub>	8.38	13.01	13.68	15.13	14.80	13.74	13.34	13.28	13.19	13.92	14.61
MnO	0.13	0.19	0.18	0.11	0.19	0.18	0.18	0.18	0.17	0.19	0.22
MgO	4.51	10.21	15.55	6.68	14.28	16.46	16.28	10.36	11.09	11.89	13.14
CaO	31.44	7.39	8.10	18.66	9.53	5.80	7.29	7.43	8.13	8.43	8.02
Na <sub>2</sub> O	1.68	4.14	2.15	1.85	2.95	3.05	2.45	3.48	3.49	3.23	2.49
K <sub>2</sub> O	2.77	1.22	1.17	0.93	0.46	0.62	0.43	1.85	1.20	0.95	0.30
P <sub>2</sub> O <sub>5</sub>	0.35	0.42	0.81	0.69	0.54	0.43	0.41	0.53	0.47	0.47	0.48
Total	99.75	98.90	99.52	99.28	99.76	99.97	99.01	99.87	99.00	99.40	96.25
LOI	19.60	5.34	6.48	14.00	4.25	7.24	5.71	8.92	6.83	6.50	4.51
Trace elements											
(ppm)											
Nb	26	37	42	78	56	37	37	41	41	42	40
Zr	162	202	283	376	331	254	243	304	258	268	278
Y	18	22	23	27	25	23	23	27	25	24	24
Sr	562	291	300	300	345	394	447	480	609	528	372
Rb	44	18	15	28	5	16	8	49	28	18	4
Zn	73	110	114	130	117	113	110	111	111	114	125
Cu	61	129	102	103	96	113	105	126	120	121	129
Ni	101	402	547	422	481	575	639	174	350	453	691
Cr	161	892	657	1012	718	620	751	421	544	854	695
V	152	266	251	784	281	254	222	264	301	268	174
Ce	50	50	78	145	108	53	57	66	66	77	80
Ba	217	541	191	45	92	166	37	354	163	79	0
Zr/Nb	6.3	5.4	6.7	4.8	5.9	6.9	6.6	7.4	6.3	6.4	6.9

Table 6 (part 2).

953C-51-R-1 109-113 659.19 IVb	953C-51R-5 32-37 663.6 IVb	953C-52R-1 13-18 667.83 IVb	953C-52R-2 88-91 669.87 IVb	953C-52R-3 38-41 670.77 IVb	953C-59R-5 113-118 741.66 IVb	953C-59R-6 12-16 742.04 IVb	953C-60R-1 32-34 744.82 IVb	953C-61R-4 16-18 758.49 IVc	953C-63R-1 49-53 773.59 IVc	953C-65R-6 98-100 799.97 IVc	953C-67R-2 61-63 813.82 IVc
50.84	50.16	48.41	43.57	49.56	62.56	50.92	62.74	43.10	65.70	64.85	65.51
0.97	1.20	2.46	2.34	0.88	1.35	2.09	0.97	0.60	0.91	0.75	0.98
14.13	13.53	13.60	11.16	12.67	13.94	12.47	15.47	9.36	14.13	14.06	11.49
4.57	4.53	10.28	10.31	6.06	7.65	6.85	4.85	2.16	4.50	3.74	5.29
0.09	0.15	0.12	0.16	0.11	0.13	0.23	0.12	0.42	0.22	0.16	0.26
1.42	1.12	4.41	6.44	2.88	3.16	3.14	1.69	0.16	1.31	0.84	0.92
19.45	20.51	12.31	19.58	22.06	3.22	16.09	3.91	36.77	3.16	6.52	7.14
4.77	4.91	5.31	2.64	1.91	5.04	4.36	5.86	2.47	5.59	5.45	4.84
3.23	3.74	2.38	1.80	3.48	2.92	2.79	3.80	2.34	3.82	3.44	2.96
0.15	0.21	0.52	0.42	0.15	0.14	0.39	0.17	0.17	0.13	0.13	0.12
99.62	100.06	99.80	98.42	99.76	100.11	99.33	99.58	97.55	99.47	99.94	99.51
19.55	18.40	13.08	13.19	18.81	8.69	12.86	11.06	23.44	9.38	11.88	11.56
191	159	86	75	81	199		176	64	185	155	210
813	556	638	510	583	1172		1106	592	1183	1054	1314
26	40	44	35	32	55		56	27	77	65	95
536	453	569	786	784	303		326	838	155	289	646
62	61	43	34	90	55		81	34	91	84	73
69	94	179	128	98	208		158	130	182	121	230
11	7	73	131	20	10		4	10	7	6	7
21	16	79	194	33	26		8	11	9	8	8
28	45	219	226	55	33		8	42	14	10	20
81	84	178	191	96	63		35	37	30	37	58
357	268	156	130	131	352		308	192	368	288	432
224	464	393	216	426	253		383	188	323	459	475
4.3	3.5	7.4	6.8	7.2	5.9		6.3	9.3	6.4	6.8	6.3

Table 6 (part 4).

953C-89R-1 61-64 1017.81 VII	953C-89R-1 61-64 1017.81 VII	953C-89R-5 5-7 1023.02 VII	953C-90R-1 4-7 1023.74 VII	953C-90R-4 130-132 1029.26 VII	953C-93R-4 20-24 1057.09 VII	953C-97R-4 50-53 1095.8 VII	953C-98R-2 62-64 1102.86 VII	953C-98R-6 140-147 1109.13 VII	953C-100R-4 145-148 1125.84 VII	953C-101R-5 78-80 1136.3 VII	953C-103R-6 67-70 1156.85 VII
45.89	45.89	45.95	45.74	46.03	46.29	45.62	45.88	45.41	44.84	45.61	45.87
3.04	3.04	3.16	3.10	2.87	3.39	3.51	3.42	3.20	4.35	4.11	3.73
9.02	9.02	8.82	9.08	8.07	9.58	9.42	9.29	9.58	12.50	9.29	9.89
13.52	13.52	14.08	13.58	13.96	13.57	13.61	13.68	14.11	12.47	14.64	13.46
0.18	0.18	0.19	0.18	0.19	0.19	0.19	0.18	0.20	0.20	0.19	0.18
16.40	16.40	16.78	16.26	16.62	14.45	14.42	14.97	14.56	10.05	12.06	13.16
8.48	8.48	8.13	8.20	8.24	9.18	8.80	8.69	9.69	9.64	9.96	9.09
2.14	2.14	2.63	2.69	2.10	2.00	2.53	2.20	1.75	3.99	2.25	2.60
0.64	0.64	0.36	0.37	0.60	0.69	0.89	0.90	0.67	1.01	1.05	0.95
0.41	0.41	0.41	0.40	0.38	0.44	0.50	0.48	0.44	0.77	0.51	0.57
99.72	99.72	100.51	99.60	99.06	99.78	99.49	99.69	99.61	99.82	99.67	99.50
5.15	5.15	5.93	5.49	3.65	0.96	5.98	6.04	2.62	5.33	2.88	6.08
36	36	35	36	34	33	40	39	36	57	42	46
232	232	246	235	216	268	290	282	255	415	284	343
22	22	21	21	21	25	23	23	23	31	23	24
456	456	482	465	354	510	512	507	924	463	624	560
10	10	4	3	7	5	13	13	6	16	13	14
108	108	117	110	110	119	114	111	113	113	119	118
92	92	86	100	81	112	102	98	105	110	54	102
707	707	770	730	863	648	583	592	697	171	506	491
873	873	889	838	1103	1119	712	780	1201	262	1186	548
225	225	222	224	199	256	223	230	285	293	306	245
51	51	61	61	55	69	72	67	61	112	73	91
167	167	53	37	52	175	160	145	104	221	143	68
6.4	6.4	7.0	6.6	6.4	8.1	7.3	7.2	7.1	7.4	6.8	7.5

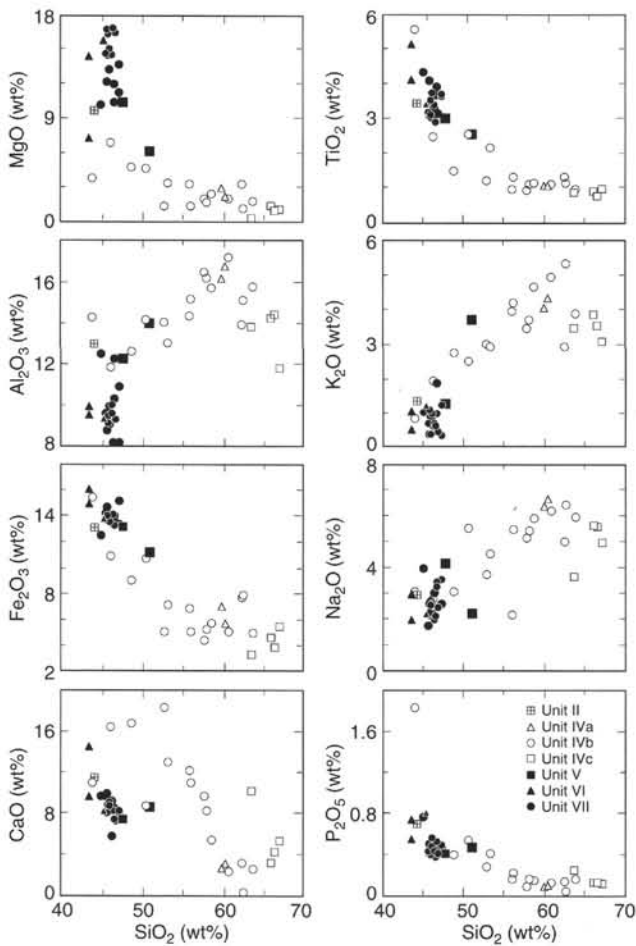


Figure 29. Major element variation diagrams plotted vs.  $\text{SiO}_2$  for volcanoclastic sediments and single rock clasts from Site 953. All analyses from Table 6, for which LOI is greater than 10 wt% have been renormalized to account for biogenic  $\text{CaCO}_3$  as described in the text.

### Correlation of MST Results

Data collected from GRAPE density, magnetic susceptibility, and *P*-wave velocity sensors on Site 953 are shown together in Figures 44 through 49. These data confirm the presence of significant variations in physical properties at a relatively fine scale. There is a marked correlation between these data. The densities show a positive correlation with the velocities. The correlation between the magnetic susceptibility and the density is more complicated. While peaks of high susceptibility in the upper 500 m correspond both to high and low densities, there is a trend to a positive correlation below 500 mbsf. In general, volcanic intervals are characterized by very high magnetic susceptibility.

### Thermal Conductivity

Thermal conductivity measurements were routinely performed on two or three sections of each core. Needles were inserted 50 cm from the top of each measured section on all cores from Hole 953A, from the mud line to a depth of 192 mbsf. The values for the thermal conductivity varies from 0.93 to 1.43 W/(m·K). The data are compiled in Table 9 and shown in Figure 50 together with the porosity, water content, and carbonate content (see "Lithostratigraphy," this chapter). A

negative correlation is clearly discernible between the thermal conductivity and the porosity and also with the water content. For example, while thermal conductivity increases, porosity decreases. Even though the sampling locations for the carbonate content and the thermal conductivity measurements are different from each other, these parameters correlate positively.

### Discrete Measurements on Split Cores

#### Index Properties

Index properties, including wet- and dry-bulk density, water content, porosity, void ratio, and grain density were measured or calculated from weights and volumes of discrete samples, both in saturated and dry states. Sampling rate for index properties was approximately one per section. Bulk density was calculated following Method B; dry-bulk density, grain density, porosity, and void ratio were calculated using Method C (see "Explanatory Notes" and "Site 950," this volume). Values of the index properties for Site 953 are presented in Table 10 and Figure 51.

Lithologic Unit I is characterized by a downcore increase of bulk density as well as by a decrease in water content and porosity. Large bulk densities are caused by volcanoclastic sands and lapillistones. The bulk density in lithologic Units II and III is continuous, increasing to 350 mbsf, but the scatter is reduced because of the great decrease in the occurrence of volcanoclastic sands. Unit III is distinguished by its very constant grain density (approximately 2.77 g/cm<sup>3</sup>) down to 400 mbsf.

Lithologic Subunit IVa is characterized by a constant mean of the index properties. Claystones have low values in the bulk and grain density while having a high porosity and water content. Bulk density increases slightly in Subunit IVb, and grain density clearly increases from 2.5 g/cm<sup>3</sup> at the top to 2.9 g/cm<sup>3</sup> at the bottom of Subunit IVc.

In lithologic Unit V the values for the index properties are fairly constant; approximately 2.3 g/cm<sup>3</sup> for bulk density, 2.9 g/cm<sup>3</sup> for grain density, a porosity of 35%, and a 15% water content.

In lithologic Unit VI, bulk density increases downcore. After a large drop at the boundary between Units VI and VII, density again increases downcore to ~1050 mbsf where the density then begins to decrease again.

### P-wave Velocity

The *P*-wave velocity was measured in Hole 953A with the DSV transducers inserted along the core axis. After Core 157-953A-9H, the sediments became too lithified to use the DSV. In Hole 953C the Hamilton Frame was used to obtain compressional velocities. The measurements were made with the core in the liner and typically 1 to 5 values per section were determined. The results are listed in Table 11 for Hole 953A and in Table 12 for Hole 953C. A plot of all velocity data is shown in Figure 52.

Although there is a gap in the data from 76 to 187 mbsf, a linear increase from 1.5 km/s at the seafloor to 2.9 km/s at the bottom of lithostratigraphic Unit V (see "Lithostratigraphy," this chapter) can be recognized. Some high velocity values are apparent in this interval that are related to lapillistones (245 and 601 mbsf) and volcanic breccia (653 mbsf). In lithostratigraphic Unit VII the velocity increases rapidly to values around 4.5 km/s at 1060 mbsf and then decreases to about 3.5 km/s at the bottom of Hole 953C. Large basaltic clasts show velocities up to 6 km/s.

### Undrained Shear Strength

Undrained shear strength of the cored sediments was measured using the motorized vane shear or estimated using the handheld penetrometer. The vane shear device was used to a depth of 130 mbsf on Core 157-953A-14H, beyond which the sediments began cracking upon insertion of the vane. Below 19 mbsf sediment strength was also

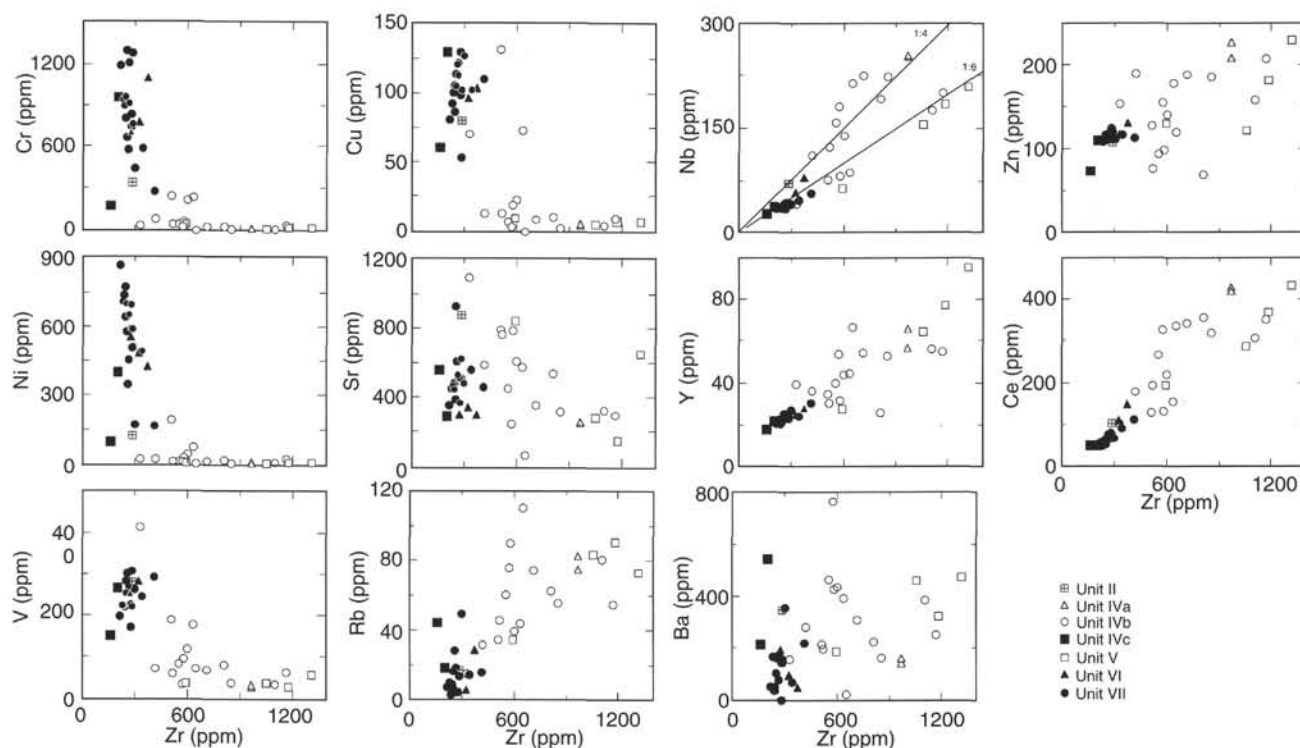


Figure 30. Trace element variation diagrams plotted vs. Zr for volcaniclastic sediments and single rock clasts from Site 953.

estimated with the handheld penetrometer. The penetrometer was used until the bottom of Hole 953A where the sediment strength approached the measurable limits of the tool (~250 kPa). A comparison of the results obtained by the two systems gives a fairly good correlation, although penetrometer readings tend to give higher values than those obtained with the vane shear. Data are presented in Table 13 and Figure 53.

Strength values increase downhole from very low values (near zero) on the seafloor to 150 kPa at about 125 mbsf. Penetrometer measurements show a slight increase in strength below this depth with a large scatter. This scatter can be correlated with water content (Fig. 53): higher water content corresponds to lower shear strength.

### Discussion

The physical properties from Site 953 show a close relationship to the lithologic units. The bulk and grain density correspond especially well to these divisions. The grain density in Unit III is almost constant without a large scatter indicating a very homogenous composition. Some of the measured physical properties (e.g., magnetic susceptibility) are especially useful for characterization of volcaniclastic intervals in the sediments. The velocity and bulk density generally increase downhole with high values in lithologic Unit VII. The velocity measurements allowed a comparison with the seismic reflection data during drilling. Thermal conductivity and shear strength increase with depth, and changes in the water content are clearly visible in these two data sets.

## DOWNHOLE MEASUREMENTS

### Logging Operations

The quad combination tool string was run successfully at Hole 953C. The deployment of the other tool strings was precluded by a stuck drill string that forced the hole to be abandoned. The WHC was

used during logging to counter ship heave resulting from the mild sea-state conditions (0.2–1.0 m heave). The base of the drill pipe was set at 372 mbsf, below the level of unconsolidated sands in the upper portion of the hole. A summary of the logging tool strings used on Leg 157, the basis of their measurement principles, and logging operations are discussed in the “Explanatory Notes” chapter (this volume). A summary of the logging operations at Hole 953C is given in Table 14.

Total penetration in Hole 953C was 1157.8 mbsf. A downgoing log was recorded at 1500 ft/hr from the end of the pipe to 985 mbsf, where further downward progress was prevented by an obstruction encountered by the base of the tool at 1017 mbsf. A main upgoing log was then recorded at a logging speed of 900 ft/hr from 975 mbsf to the mud line. During the upgoing log considerable overpull (4–500 lb) was encountered, which was thought to result from a combination of a narrow borehole and debris falling down from the unstable hole above, from 975 to 911 mbsf and again from 934 to 908 mbsf. At the end of the upgoing log the tool was run back into open hole to see if it was possible to pass the upper bridge, but downward progress was stopped by an obstruction at 477 mbsf. Having pulled out of the hole with the quad tool string an attempt to run the drill string past this upper bridge resulted in the drill string becoming stuck. Subsequently the drill string was severed with an explosive charge and the hole abandoned.

### Log Quality

The main logs recorded at Hole 953C are shown in Figures 54, 55, and 56. The logs are generally of high quality, although some depth errors are present caused by cable stretching when the tool was sticking in the borehole (see tension log, Fig. 56). The affected intervals are marked on Figures 55 and 56 and it may be noted that the depths affected are different for the various tool sensors. Log data are recorded as a function of time but are buffered by the uphole Schlumberger MAXIS unit and written to disk as a function of depth. Any

Table 7. Pore-water chemistry, Site 953.

Core, section, interval (cm)	Depth (mbsf)	pH	Salinity (g/kg)	Cl (mmol/L)	Alkalinity (mmol/L)	SO <sub>4</sub> (mmol/L)	NH <sub>4</sub> (μmol/L)	Na (mmol/L)	K (mmol/L)	Li (μmol/L)	SiO <sub>2</sub> (μmol/L)	Ca (mmol/L)	Mg (mmol/L)	Sr (μmol/L)	Mg/Ca (molar ratio)	Sr/Ca (molar ratio)
157-953A-																
1H-4, 145-150	5.95	7.71	35.0	567	3.79	25.9	100	480	11.9	22	313	7.22	48.7	137	6.75	0.019
2H-4, 145-150	13.55	7.68	35.0	572	5.45	24.2	205	476	11.5	20	435	5.78	46.7	191	8.08	0.033
3H-3, 145-150	21.55	7.62	35.0	563	4.51	20.8	259	486	10.5	20	393	4.93	46.5	232	9.43	0.047
4H-4, 145-150	32.55	7.66	35.0	573	4.78	20.4	305	466	9.73	19	384	4.94	43.3	316	8.77	0.064
5H-3, 145-150	40.55	7.68	34.5	572	3.62	19.8	342	484	9.90	19	369	4.84	43.2	414	8.93	0.086
6H-4, 145-150	51.55	7.82	34.5	574	3.07	20.2	393	465	9.56	20	391	5.21	39.6	503	7.60	0.097
7H-3, 145-150	59.55	7.87	35.0	573	2.72	18.6	397	474	9.19	22	380	5.39	38.0	615	7.05	0.114
8H-5, 145-150	72.05	7.83	34.0	577	2.47	18.3	411	471	8.62	22	406	7.01	38.4	763	5.48	0.109
9H-5, 143-150	81.53	7.71	35.0	583	2.45	18.5	424	493	8.91	23	404	7.75	36.3	875	4.68	0.113
10H-5, 142-150	91.02	7.52	35.0	581	1.89	18.7	420	492	8.65	25	517	10.5	35.0	936	3.33	0.089
12H-5, 145-150	110.05	7.36	35.0	581	1.32	18.1	335	474	7.29	26	517	16.6	29.0	1080	1.75	0.065
14H-4, 140-145	127.50	7.35	35.5	579	0.56	18.9	318	480	6.28	32	294	21.4	24.0	1130	1.12	0.053
16H-5, 145-150	148.05	7.70	36.0	587	0.59	16.9	324	483	5.37	27	306	24.5	21.2	1110	0.87	0.045
18H-5, 140-150	167.00	7.05	36.0	594	0.35	16.5	297	486	4.52	27	205	28.0	20.0	1040	0.71	0.037
20H-4, 140-150	184.50	8.08	36.0	593	0.35	17.3	308	490	4.77	26	132	32.0	19.0	1000	0.59	0.031
157-953C-																
3R-2, 140-150	199.40	7.85	37.0	602	0.62	19.5	324	532	5.38	24	127	34.1	24.0	909	0.70	0.027
8R-3, 0-10	247.60	8.02	36.0	610	0.52	20.6	333	549	4.13	19	105	40.3	12.5	844	0.31	0.021
11R-1, 140-150	274.80	7.82	36.0	612	0.28	20.1	338	553	3.91	24	114	37.1	12.1	832	0.33	0.022
14R-1, 135-150	303.75	7.68	37.0	610	0.61	22.1	313	557	3.86	27	128	31.7	12.7	765	0.40	0.024
17R-4, 135-150	336.95	8.06	37.0	612	0.40	24.6	250	589	3.82	30	112	27.2	14.7	664	0.54	0.024
20R-4, 133-150	365.63	8.18	37.0	612	0.47	26.1	275	604	3.90	33	82	25.2	13.4	637	0.53	0.025
23R-4, 136-150	394.46	7.48	37.0	605	1.20	28.6	234	618	4.05	34	108	22.5	13.4	601	0.60	0.027
26R-4, 135-150	423.15	8.01	38.0	615	0.56	28.7	162	650	4.10	30	107	18.8	12.5	614	0.66	0.033
29R-2, 130-150	449.00	8.78	38.0	613	1.01	33.1	168	645	4.04	26	131	16.8	9.6	577	0.57	0.034
32R-3, 130-150	479.50	8.58	39.0	605	1.05	34.6	162	696	4.21	23	126	14.4	9.9	585	0.68	0.041
35R-3, 113-131	508.01	8.12	38.0	609	0.73	35.5	142	713	4.30	23	119	11.1	10.7	523	0.96	0.047
38R-4, 118-138	538.43	8.53	39.0	642	1.35	35.0	150	710	4.43	24	98	7.87	10.5	464	1.33	0.059
44R-4, 110-130	596.04	8.64	39.0	640	1.90	33.8	160	750	4.90	24	149	6.72	14.6	551	2.17	0.082
47R-1, 32-50	619.92	8.23	40.0	657	1.60	31.3	167	755	5.35	26	165	6.10	14.3	609	2.34	0.100
50R-1, 124-144	649.74	8.27	40.5	667	1.74	29.6	196	762	5.36	29	144	8.81	14.5	605	1.65	0.069
53R-4, 120-140	682.76	ND	42.0	676	ND	26.6	137	776	6.05	33	112	17.9	13.2	775	0.74	0.043
55R-2, 85-95	698.61	ND	44.0	725	ND	26.1	ND	793	6.73	35	144	24.8	14.5	770	0.58	0.031
55R-3, 120-130	700.29	ND	43.0	713	ND	27.2	149	776	5.90	35	150	26.2	13.2	744	0.50	0.028
55R-4, 68-78	701.27	ND	45.0	723	ND	27.7	189	770	5.86	38	135	28.8	15.1	805	0.52	0.028
55R-5, 68-78	702.74	ND	42.0	684	ND	28.3	202	740	6.29	33	163	29.5	14.9	784	0.51	0.027
56R-3, 125-145	710.11	7.61	43.0	693	0.61	28.3	180	753	5.77	26	126	30.3	14.8	779	0.49	0.026
59R-4, 130-150	740.33	7.72	44.0	720	0.59	27.0	200	769	7.23	34	253	42.7	11.9	812	0.28	0.019
62R-3, 130-150	767.85	8.96	44.0	728	1.35	27.1	214	768	8.02	38	596	52.2	7.3	764	0.14	0.015
65R-1, 95-115	793.35	ND	ND	719	ND	26.0	ND	727	7.36	35	324	67.9	6.3	ND	0.09	ND
68R-4, 125-145	826.76	8.73	46.0	720	1.03	27.4	187	716	5.48	47	693	82.6	5.7	796	0.07	0.010
71R-4, 113-133	856.00	9.29	47.0	729	1.37	26.8	235	652	3.68	35	71	111	5.4	921	0.05	0.008
86R-3, 0-25	997.70	ND	39.0	594	ND	17.4	ND	503	9.03	21	110	104	1.9	1120	0.02	0.011

Note: ND = not determined due to insufficient pore water.

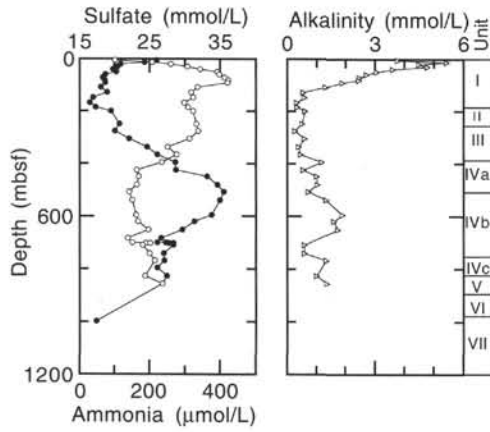


Figure 31. Interstitial-water sulfate (filled circles), ammonia (open circles), and alkalinity at Site 953.

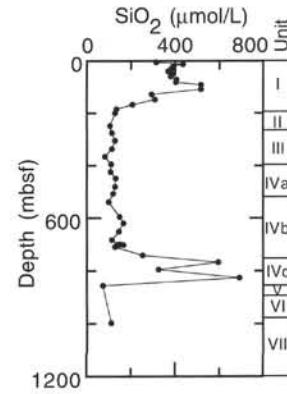


Figure 34. Interstitial-water silica at Site 953.

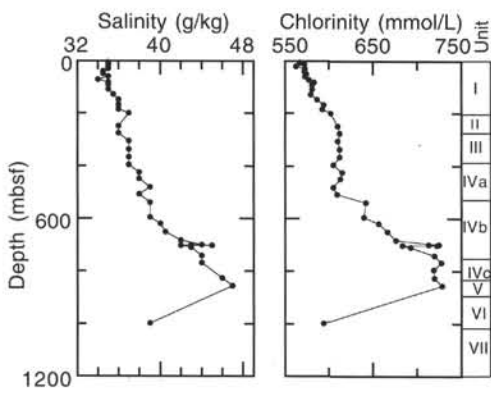


Figure 32. Interstitial-water salinity and chlorinity at Site 953.

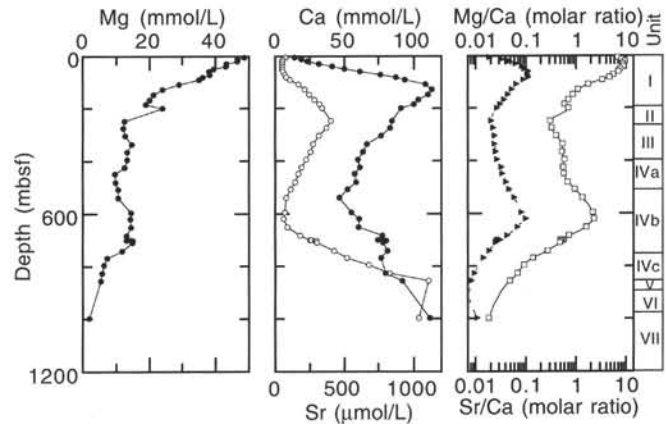


Figure 35. Interstitial-water magnesium, strontium (filled circles), calcium (open circles), and Sr/Ca (filled triangles) and Mg/Ca (open squares) molar ratios at Site 953.

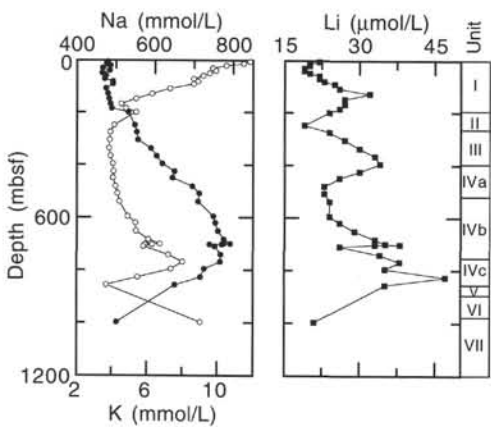


Figure 33. Interstitial-water sodium (filled circles), potassium (open circles), and lithium at Site 953.

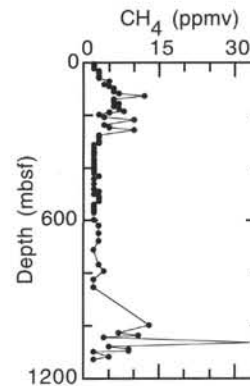


Figure 36. Methane concentrations in headspace samples from Site 953.

data degrading events (such as tool sticking), which occur at a discrete time, will affect the different tool sensors on the tool string at a different depth, since the tool strings have an intrinsic length (31 m in the case of the quad). These depth-shift errors will be corrected in post-cruise processing of the data. The natural gamma-ray logs in Figure 54 are taken from the downgoing log and are unaffected by

these tool sticking problems. The main physical logs in Figures 55 and 56 are, with the exception of induction, taken from the upgoing log, which has depth uncertainties from ~975–880 mbsf and again from ~575–470 mbsf. Because of the dangerous levels of overpull the HLDT caliper was closed to reduce drag over the intervals 955–941, 934–908, and 524–486 mbsf. The density, caliper, and photoelectric logs are therefore invalid over these three short intervals. Excepting these three intervals, the caliper log (Fig. 55) shows that the borehole was in good condition with little rugosity and therefore the density

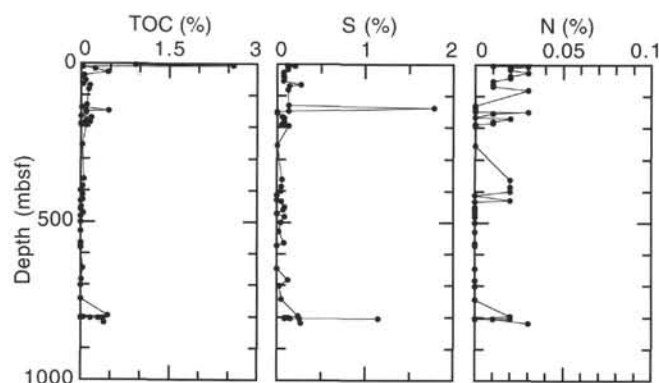


Figure 37. Concentration profiles of TOC, total sulfur, and total nitrogen at Site 953.

data are of higher quality than that collected at Holes 950A and 952A, where density dropouts were apparent.

Despite a fair amount of cycle skipping and other noise present in the raw sonic data, shipboard processing of the traveltimes has eliminated most of these excursions. The sonic velocity presented in Figure 55 is the processed data. Post-cruise wave-form analysis could further improve the quality of these data.

Hole width (Fig. 55) also affects the natural gamma-ray activity log by raising the count rate where the hole is narrow and lowering it where it is wide. Post-cruise processing will correct for these environmental factors. Natural gamma-ray data were also recorded through the drill pipe up to the mud line. These data require further processing to remove the (variable) attenuation caused by the presence of the drill pipe on the gamma-ray flux from the formation.

## Results

### Variation of Logs with Depth

The open-hole interval logged in Hole 953C (~372–987 mbsf) covers lithologic Units III to VII (late Miocene to middle Miocene), which are based on the recovered cores (see "Lithostratigraphy," this chapter). The sequence is dominated by pelagic fine grained sediments and coarser volcanoclastic material.

The variations in the downhole log data reflect very well the different lithologies distinguished in the core and for this reason the core-based lithologic units are retained for description of the logs. The gamma-ray logs are particularly diagnostic in defining the amount and affinity of volcanoclastic material, delineating the Fataga, Mogan, and basaltic shield phases of Gran Canaria.

The short section covered by the logs of Unit III, consisting of nannofossil oozes and foraminifer-lithic sands, is not distinctive in the logs, though it exhibits an increase in total gamma-ray with depth toward the boundary with Unit IV below.

Unit IV contains a wide variety of sedimentary lithologies reflecting the mixing of distinct volcanoclastic, pelagic, and minor neritic components. This mixing is apparent from an overview of both the physical and chemical logs (Figs. 54, 55, and 56), which often exhibit a rapid variation between end-member base lines. The mixing is particularly apparent in the total gamma-ray log in Subunit IVb (Fig. 55) and in the bulk-density log in the lower parts of Subunits IVb and IVc. The total gamma-ray log represents a mixing (from high to low gamma-ray) of felsic volcanic material, turbidite clay, mafic volcanic, and carbonate components. The base-line gamma-ray is highest in Subunit IVa, which is probably a reflection of less carbonate-rich pelagic material, rather than an increase in volcanics relative to Subunits IVb and IVc. The K component of the gamma-ray is noticeably higher in Subunit IVa, although it is uncertain whether this reflects

Table 8. Elemental and organic carbon compositions of core samples, Site 953.

Core, section, interval (cm)	Depth (mbsf)	Inorganic carbon (%)	CaCO <sub>3</sub> (%)	Total carbon (%)	TOC (%)	Total nitrogen (%)	Total sulfur (%)
157-953A-							
1H-4, 3-4	4.53	6.84	57.0	7.77	0.93	0.01	0.11
1H-4, 128-129	5.78	7.68	64.0	10.28	2.60	0.03	0.20
2H-2, 43-44	9.53	8.00	66.6	8.03	0.03	0.02	0.12
2H-6, 127-129	16.37	8.19	68.2	8.43	0.24	0.02	0.12
3H-7, 22-23	26.32	7.25	60.4	7.70	0.45	0.03	0.07
4H-6, 116-117	35.26	6.45	53.7	6.50	0.05	0.02	0.07
5H-4, 89-90	41.49	7.14	59.5	7.18	0.04	0.02	0.08
6H-6, 45-46	53.55	6.09	50.7	6.16	0.07	0.01	0.07
7H-7, 5-6	64.15	5.39	44.9	5.42	0.03	0.01	0.27
8H-4, 56-57	69.66	8.61	71.7	8.76	0.15	0.01	0.14
9H-6, 16-17	81.76	4.64	38.7	4.77	0.13	0.03	0.12
14H-7, 19-20	130.79	7.60	63.3	7.70	0.10	BD	0.13
15H-5, 52-53	137.62	0.55	4.6	0.56	0.01	BD	1.78
16H-6, 35-36	148.45	2.03	16.9	2.50	0.47	BD	0.13
17H-1, 69-70	151.00	7.88	65.6	7.97	0.09	0.03	BD
17H-4, 61-62	155.00	7.97	66.4	8.05	0.08	0.01	BD
18H-5, 93-94	166.53	6.24	52.0	6.16	BD	BD	0.06
19H-1, 46-47	169.56	6.84	57.0	7.01	0.17	0.02	0.08
20H-3, 58-59	182.18	7.95	66.2	8.04	0.09	0.01	0.08
20H-5, 42-43	185.02	9.13	76.1	9.28	0.15	0.01	0.07
21H-1, 16-17	188.26	4.01	33.4	3.69	BD	BD	0.07
21H-2, 59-60	190.19	3.13	26.1	3.09	0.03	BD	0.05
157-953B-							
1X-5, 4-5	193.18	6.55	54.6	6.55	BD	BD	0.05
1X-6, 48-49	194.24	4.22	35.2	4.30	0.08	BD	0.13
157-953C-							
9R-2, 32-33	255.92	8.46	70.5	8.48	0.02	BD	BD
20R-3, 85-86	363.65	5.18	43.1	5.23	0.05	0.02	0.06
22R-5, 112-113	386.22	4.94	41.2	4.97	0.03	0.02	0.05
24R-2, 52-53	400.12	4.41	36.7	4.34	BD	0.02	0.04
25R-3, 128-129	411.98	0.88	7.3	0.91	0.03	BD	BD
27R-1, 124-126	428.24	8.04	67.0	8.07	0.03	0.02	BD
27R-5, 56-58	432.91	2.30	19.2	2.30	BD	BD	0.05
29R-4, 71-73	451.41	4.18	34.8	4.19	0.01	BD	0.09
30R-3, 42-43	459.32	1.54	12.8	1.53	BD	BD	0.07
31R-4, 39-41	470.39	5.99	49.9	6.03	0.04	BD	BD
32R-CC, 15-16	481.05	0.48	4.0	0.43	BD	BD	0.09
34R-5, 18-20	500.30	1.39	11.6	1.38	BD	BD	0.04
37R-4, 107-108	528.61	0.73	6.1	0.72	BD	BD	0.02
41R-2, 96-98	564.28	5.28	44.0	5.28	BD	BD	0.08
42R-1, 120-121	572.60	1.13	9.4	1.05	BD	BD	BD
49R-6, 56-59	646.14	8.05	67.1	8.08	0.03	BD	BD
53R-4, 77-78	682.33	0.83	6.9	0.84	0.01	BD	0.12
55R-4, 130-131	701.89	2.84	23.7	2.61	BD	BD	0.03
60R-1, 8-9	744.58	0.72	6.0	0.71	BD	BD	0.05
65R-4, 33-34	796.52	2.24	18.7	2.69	0.45	0.02	0.24
66R-2, 12-14	803.53	1.88	15.7	1.92	0.04	BD	0.09
66R-2, 20-22	803.61	0.97	8.1	0.91	BD	BD	0.12
66R-2, 65-67	804.06	2.06	17.2	2.06	BD	BD	0.09
66R-2, 73-75	804.14	1.76	14.7	2.14	0.38	0.02	1.15
66R-2, 79-80	804.20	2.14	17.8	2.30	0.16	BD	0.15
66R-2, 84-86	804.25	1.83	15.2	2.12	0.29	0.01	0.25
67R-5, 79-80	818.18	3.66	30.5	4.05	0.39	0.03	0.27

Note: BD = below detection.

higher turbidite clay deposition or perhaps more potassic felsic volcanoclastic material.

The transition down to Subunit IVb is apparent as a decrease in the total gamma-ray (Fig. 54) at ~500 mbsf, a few meters higher than where it is defined in the lithostratigraphic units. This decrease probably reflects the increase in carbonate content of the background pelagic sedimentation as seen in carbonate analyses on core (see "Organic Geochemistry," this chapter). The physical logs of bulk density, resistivity, and sonic velocity show generally increasing values with depth through Unit IV. Two coarser lapillistone intervals noted in Cores 157-953C-45R and 50R are clearly seen in the resistivity and sonic velocity logs (Fig. 55). Toward the base of Subunit IVb there is an increasing trend in bulk density that may represent the gradual increase in basaltic fragments in the volcanoclastics although this is not apparent in the cores.

The transition to Subunit IVc below is marked by a sharp decrease in the average bulk density and a slight decrease in resistivity. This represents the change to the vitric volcanoclastics of the Mogan stage

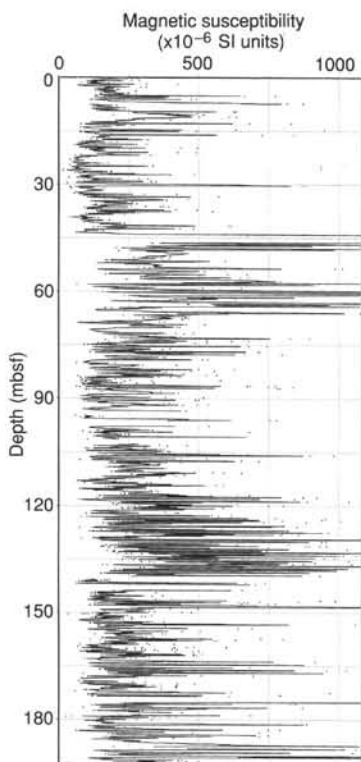


Figure 38. MST magnetic susceptibility, Hole 953A. Filtered data indicated by lines, raw data by discrete points.

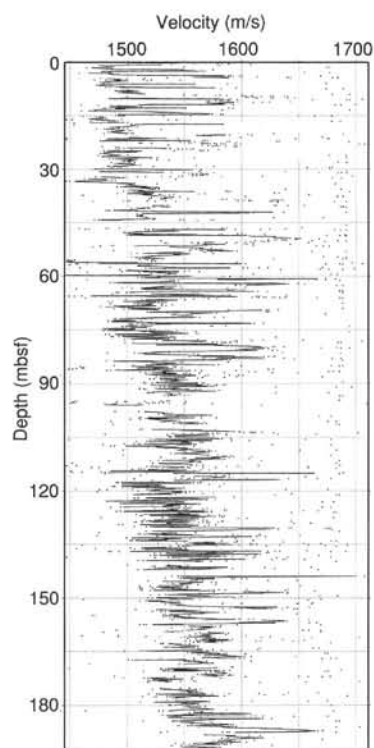


Figure 40. MST *P*-wave velocity, Hole 953A. Filtered data indicated by lines, raw data by discrete points.

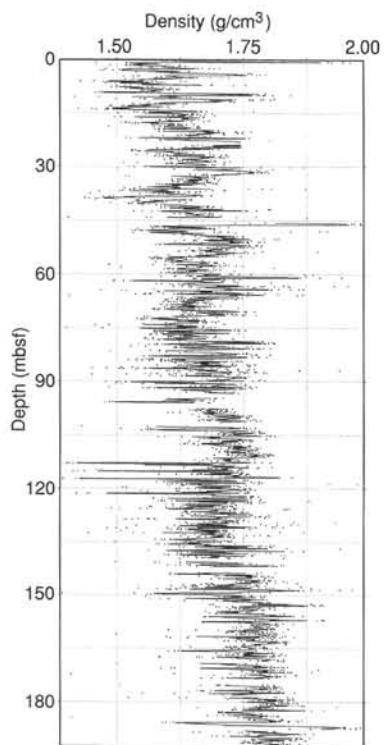


Figure 39. MST GRAPE density, Hole 953A. Filtered data indicated by lines, raw data by discrete points.

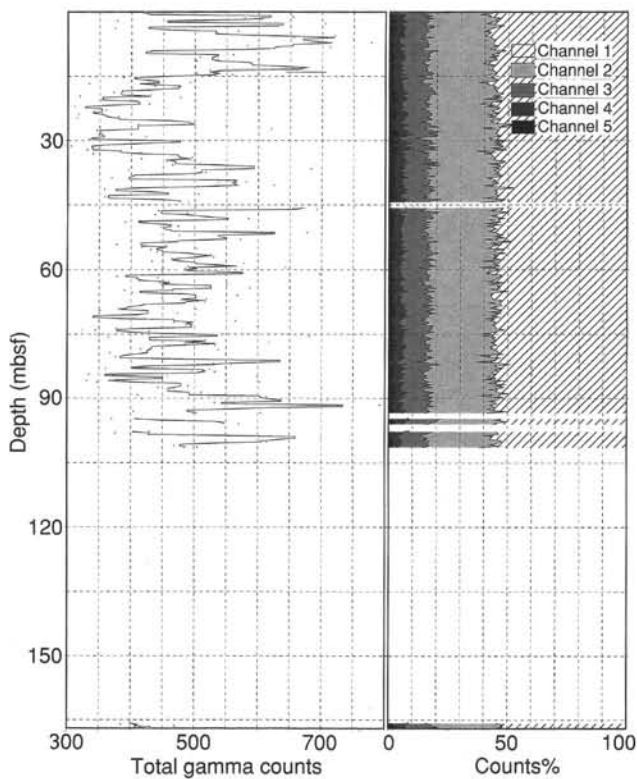


Figure 41. MST total natural gamma ray and percentage counts by channel, Hole 953A. Filtered data indicated by lines, raw data by discrete points.

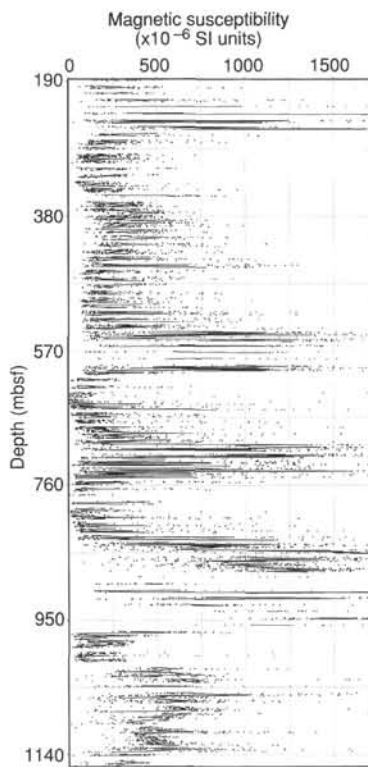


Figure 42. MST magnetic susceptibility, Hole 953C. Filtered data indicated by lines, raw data by discrete points.

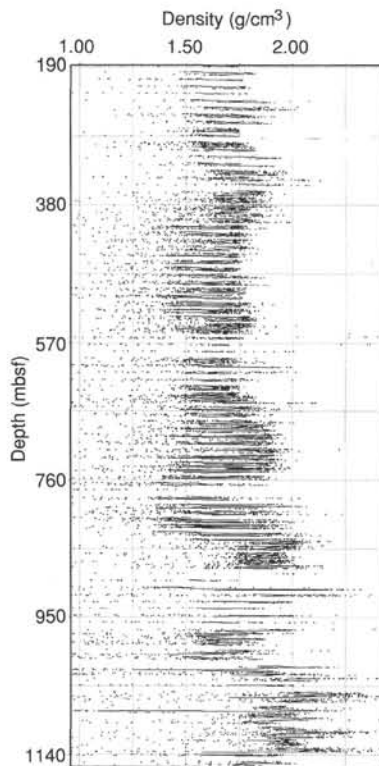


Figure 43. MST GRAPE density, Hole 953C. Filtered data indicated by lines, raw data by discrete points.

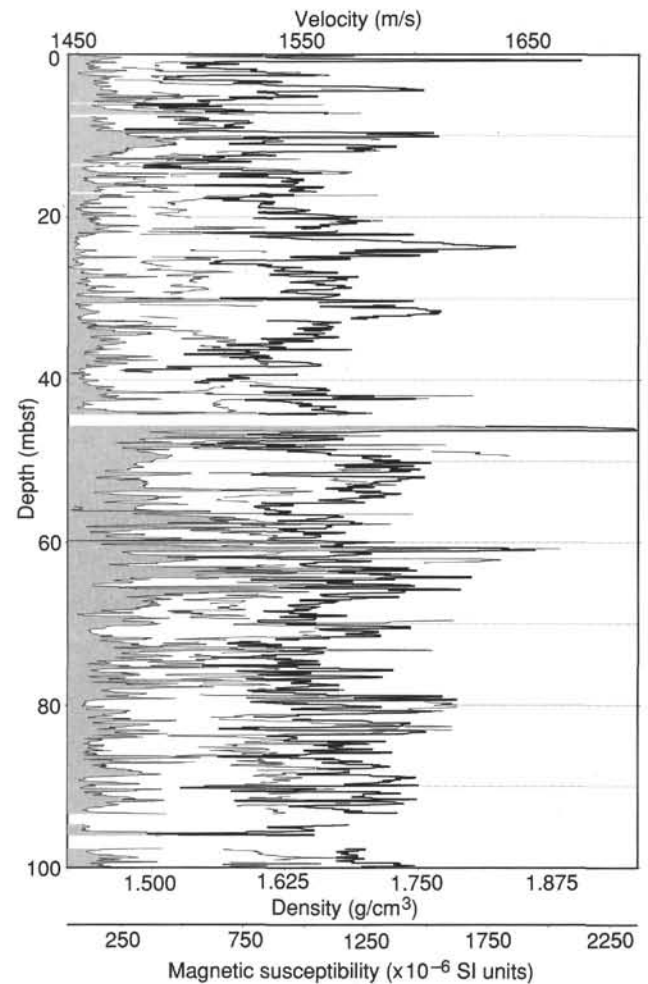


Figure 44. Filtered MST magnetic susceptibility (shading), velocity (light trace), and gamma-ray density (bold trace) for 0–100 mbsf, Hole 953A.

volcanism, containing much more (less dense) pumiceous material. The chemical change is also distinct on the gamma-ray logs with high Th and U values relative to K, which is diagnostic of the highly evolved Mogan volcanics (Schmincke, 1982).

Unit V represents the abrupt change from felsic to basaltic material of the shield phase of Gran Canaria. This transition is very well picked out by a sharp decrease in Th and U (Fig. 54). Bulk density, resistivity, and sonic velocity also increase considerably at ~845 mbsf, a few meters above the lithologic unit boundary recognized in the cores. The increases in the physical logs represent the compositional change to the more dense mafic material, rather than a textural change, as these units are less coarse than the overlying Unit IV. At the base of Unit V at 887 mbsf a high spike in the Th and U logs may indicate a thin and more evolved volcaniclastic deposit within this mafic stage.

From the gamma-ray logs, Units VI and VII show a chemical composition similar to that of Unit V. The excursions from this are a slight K peak from 930 to 950 mbsf and a very high K peak at 970 mbsf that may be caused by enrichment from seawater. The physical logs of resistivity and sonic velocity show a pronounced increase with depth over Unit VI, with the resistivity logs perhaps delineating individual debris flows. A good example of this is found from 929 to 912 mbsf (Fig. 55), which appears to show a graded debris flow with a higher resistivity coarse base, grading upward to a finer grained less resistive top.

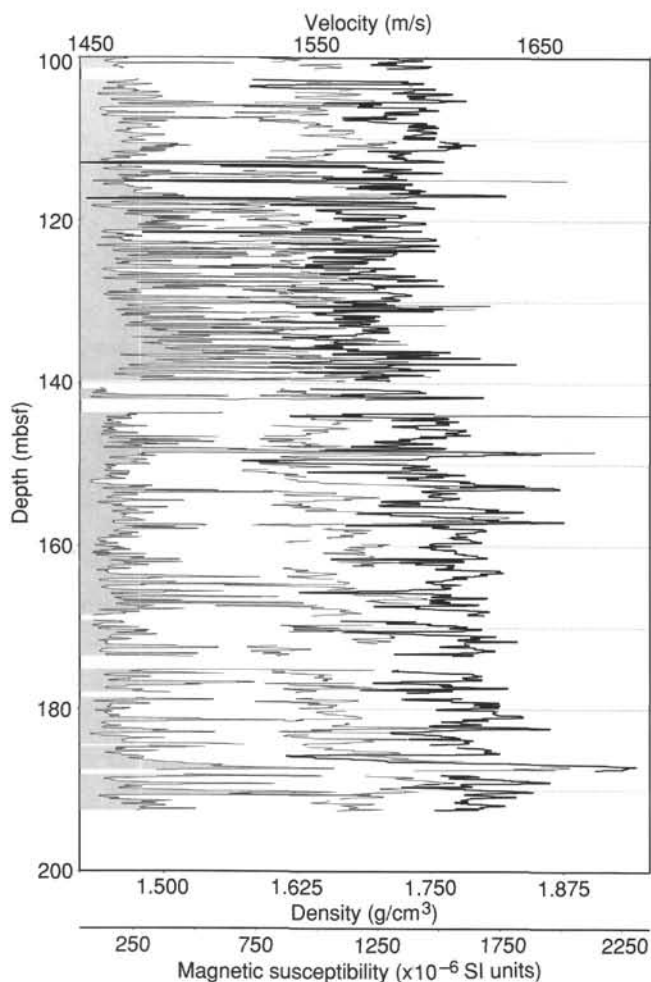


Figure 45. Filtered MST magnetic susceptibility (shading), velocity (light trace), and gamma-ray density (bold trace) for 100–193 mbsf, Hole 953A.

### Temperature

The Lamont-Doherty temperature tool was deployed on the one run of the quad combination tool string in Hole 953A (Fig. 57). An accurate thermal gradient cannot be obtained from these measurements; cold seawater is circulated in the hole during drilling, which cools the adjacent formation. A minimum of three bottom-hole temperature measurements over a period of time are required to extrapolate the virgin bottom-hole temperature and hence calculate the true thermal gradient. Nevertheless, a temperature of 16°C was obtained at 985 mbsf, and with a mud line temperature of 2.6°C, the thermal gradient must be greater than 13.6°C/km.

### Porosity Estimates

Estimates of formation porosity can be derived from log data via several different methods. Porosity has been calculated from resistivity, sonic velocity and bulk-density logs, and obtained from the neutron porosity log, which gives a direct estimate of porosity. The resulting porosities are compared with the discrete index properties measurements on core in Figure 58 (see “Physical Properties”) and the differences are briefly discussed in relation to the core lithological variations.

Porosity was calculated from the resistivity log by assuming that Archie’s law (Archie, 1942) is valid for these sediments. The Archie equation for saturated sediments is expressed as follows:

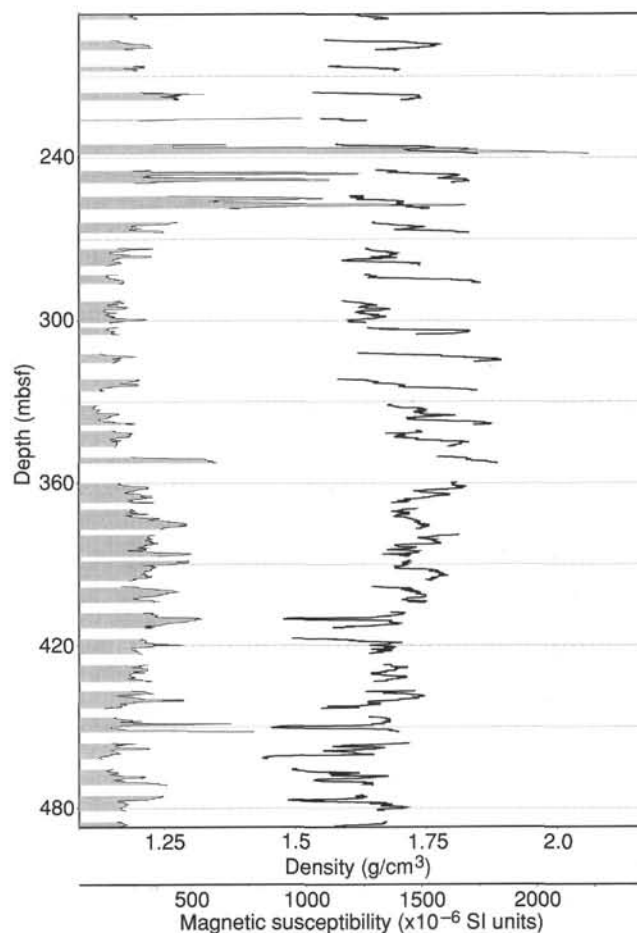


Figure 46. Filtered MST magnetic susceptibility (shading) and gamma-ray density (lines) for 187–493 mbsf, Hole 953C.

$$R_t = a \phi^{-m} R_w,$$

where  $R_t$  and  $R_w$  are the resistivity in the formation, as measured by the SFLU tool in this case, and the resistivity of the pore water,  $\phi$  is the porosity, and  $a$  and  $m$  are parameters dependent on the lithology and texture of the sediment.  $R_w$  was calculated from shipboard pore-water salinities (see “Inorganic Geochemistry”). The calculated values were corrected for temperature, as measured in the hole by the Lamont-Doherty temperature logging tool. The parameters  $a$  and  $m$  were estimated from a cross plot of  $\ln R_t/R_w$  and  $\ln \phi$ , where the porosity is taken from the independently determined index properties. By assuming the equation (Wyllie et al., 1958):

$$\ln R_t/R_w = -m \ln \phi + \ln a,$$

derived from Archie’s relation,  $a$  and  $m$  were derived from a linear least squares best fit of the data. The values found were  $a = 1.05$  and  $m = 2.5$ . The porosities obtained with these values are shown in Figure 58.

The derivation of porosities from the sonic interval transit times is based on the time-average equation:

$$\phi_w = (t_{log} - t_{ma}) / (t_f - t_{ma}),$$

where  $t$  is interval transit times for matrix ( $t_{ma}$ ) and pore fluid ( $t_f$ ),  $t_{log}$  is the interval transit time measured by the sonic tool. The  $t_{ma}$

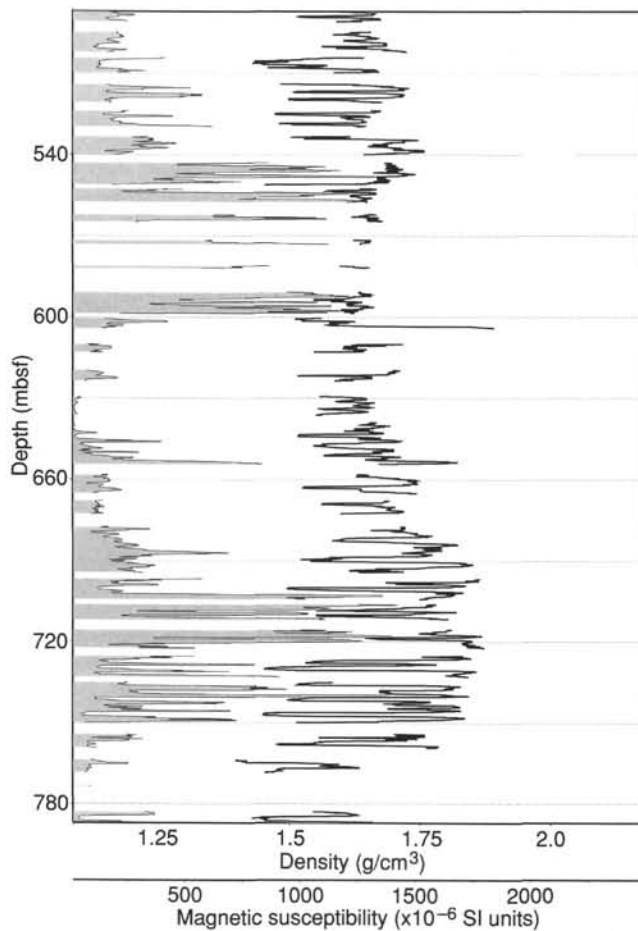


Figure 47. Filtered MST magnetic susceptibility (shading) and gamma-ray density (lines) for 493–793 mbsf, Hole 953C.

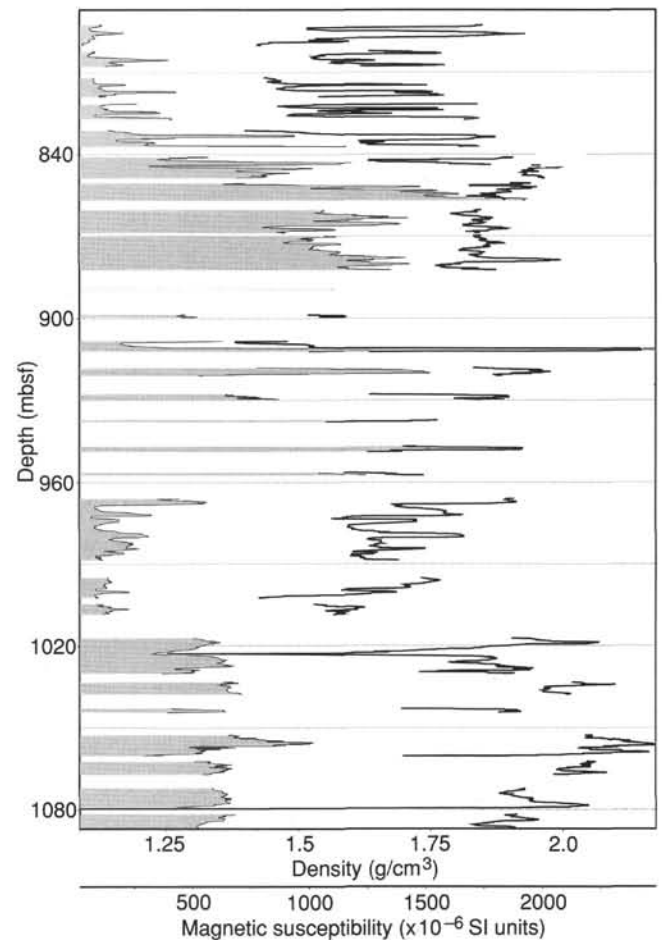


Figure 48. Filtered MST magnetic susceptibility (shading) and gamma-ray density (lines) for 793–1093 mbsf, Hole 953C.

was estimated under the assumption that the matrix was a mixture of calcite and quartz. The proportions estimated from CaCO<sub>3</sub> wt% measurements (see “Organic Geochemistry”). The following equation was applied:

$$t_{ma} = C t_{calcite} + (1 - C) t_{quartz}$$

where  $C = \text{CaCO}_3 \text{ wt\%/100}$ , and  $t_{calcite}$  and  $t_{quartz}$  are interval transit times for calcite (46.5  $\mu\text{s/f}$ ) and quartz (55.1  $\mu\text{s/f}$ ). The transit time for the pore fluid was estimated from the known salinities, temperatures, and depths by applying the relation:

$$V_p = 1449.2 + 4.6T - 0.055T^2 + 0.00029T^3 + (1.34 - 0.01T) \times (S - 35) + 0.016z$$

(Clay and Medwin, 1977), where  $T$  is temperature in °C,  $S$  is salinity in ppt,  $z$  is the depth in meters, and  $V_p$  is the  $P$ -wave velocity in m/s.

The calculated porosities appear systematically too high as compared to the index porosity measurements. This is to be expected as the measured interval transit times may depend on textural properties that are not taken into account. The discrepancy cannot be eliminated by a simple correction factor as suggested elsewhere (e.g., Serra, 1984). The best fit to the core porosities was found by using a correction linearly dependent on depth  $(0.00037z + 0.552)\phi_w$ . The curve obtained with this correction is shown in Figure 58.

Porosity was calculated from the density log using the relationship:

$$\phi_d = \rho_{ma} - \rho_f / \rho_{ma} - \rho_f$$

The matrix density ( $\rho_{ma}$ ) is estimated from the CaCO<sub>3</sub> data in a way analogous to the one described for the interval transit times and assuming a density of 2.65 g/cm<sup>3</sup> for quartz and 2.71 g/cm<sup>3</sup> for calcite. The fluid density ( $\rho_f$ ) was assumed to be constant 1.04 g/cm<sup>3</sup>. The resultant porosity curve is shown in Figure 58. The porosity directly measured from the neutron porosity tool is shown in Figure 58.

Over the interval 450–800 mbsf the four wireline tool porosities show, with a few exceptions, a very good fit to the reference porosities. The fit is generally between the limits  $\pm 5\%$  porosity.

Over the interval 800–840 mbsf all four porosity curves deviate strongly from the index property values, which are 10%–15% lower than the wireline values. This discrepancy seems to indicate that the laboratory values are not representative in this interval, which is in the lower part of the lithologic Unit IVc. The apparent deviations seen in the porosity curves in the interval below 900 mbsf result in part from the depth mismatch caused by the problems of tool sticking.

Over the interval 370–450 mbsf the porosity values calculated from resistivity are systematically about 10% porosity too high in comparison to the reference porosities (the core porosity values). The neutron porosity shows poor correlation, especially in the high poros-

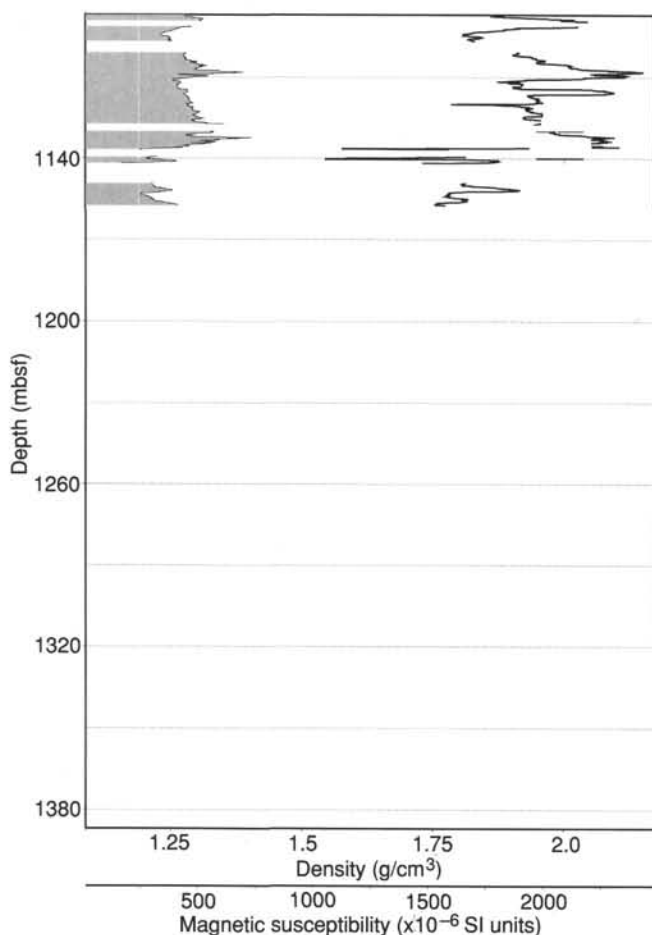


Figure 49. Filtered MST magnetic susceptibility (shading) and gamma-ray density (lines) for 1093–1159 mbsf, Hole 953C.

ity zones. The density-porosity is in good agreement with the reference except over the interval 480–530 mbsf and below 890 mbsf. Below 910 mbsf the caliper arm of the HLDT had to be closed, causing anomalously low bulk-density measurements.

Overall, the best correlation with core measurements is from the resistivity log and the poorest from the neutron porosity. The poorer quality of the neutron porosity is attributable to the fact that the eccentricizing bow spring designed for this tool cannot be run in ODP operations because of internal diameter limitations of the drill pipe.

### Matrix Densities

A matrix density log has been calculated by combining porosity values with bulk-density measurements using the expression:

$$\rho_{ma} = (\rho_b - \rho_f \times \phi) / (1 - \phi),$$

where  $\phi$  is the porosity,  $\rho_b$  the density tool reading, and  $\rho_f = 1.024 \text{ g/cm}^3$  the density of the pore water. The porosity input log used is the mean of the calculated resistivity-porosity and sonic-porosity logs.

The results are plotted in Figure 59 together with grain densities determined from measurements on discrete core samples (see “Physical Properties”). Data from 540–480 mbsf were not calculated because of the effect of the closure of the HLDT caliper arm. The ob-

Table 9. Thermal conductivity measurements, Hole 953A.

Core, section, interval (cm)	Depth (mbsf)	Method	TCcorr (W/[m-K])	Standard error (W/[m-K])	Drift (°/min)
157-953A-					
1H-3, 50	3.50	F	1.317	0.00985	0.065
2H-1, 50	8.10	F	1.138	0.01630	-0.003
2H-3, 50	11.10	F	0.931	0.00911	-0.010
3H-1, 50	17.60	F	1.137	0.00898	0.010
3H-3, 50	20.60	F	1.039	0.01064	0.031
4H-1, 50	27.10	F	1.168	0.01378	0.013
4H-3, 40	30.00	F	1.364	0.01278	0.111
4H-5, 50	33.10	F	1.280	0.02109	0.028
5H-1, 50	36.60	F	1.201	0.01322	0.090
5H-3, 50	39.60	F	1.141	0.00885	0.060
6H-1, 50	46.10	F	1.308	0.01242	0.033
6H-3, 50	49.10	F	0.929	0.00969	-0.057
7H-1, 50	55.60	F	1.055	0.00948	-0.018
7H-3, 50	58.60	F	1.992	0.00987	0.150
8H-1, 50	65.10	F	1.055	0.01090	-0.019
8H-3, 50	68.10	F	1.062	0.01020	0.004
8H-5, 50	71.10	F	1.066	0.01263	0.021
9H-1, 50	74.60	F	1.093	0.01510	0.022
9H-3, 50	77.60	F	1.032	0.01417	0.004
10H-1, 50	84.10	F	1.227	0.01404	0.001
10H-3, 50	87.10	F	1.048	0.01459	-0.011
11H-1, 60	93.70	F	1.154	0.01204	-0.015
11H-3, 50	96.60	F	1.048	0.01316	-0.002
12H-1, 50	103.10	F	1.238	0.00975	0.012
12H-3, 50	106.10	F	1.141	0.01110	0.020
12H-5, 50	109.10	F	1.081	0.01611	-0.014
13H-1, 50	112.60	F	1.075	0.01065	0.012
13H-3, 50	115.60	F	1.097	0.01066	0.003
14H-1, 50	122.10	F	1.236	0.01116	0.016
14H-3, 50	125.10	F	1.156	0.01488	0.033
15H-1, 50	131.60	F	1.280	0.01204	0.024
15H-3, 50	134.60	F	1.142	0.01325	0.036
16H-1, 50	141.10	F	1.314	0.00665	0.027
16H-3, 50	144.10	F	0.987	0.01430	0.030
16H-5, 50	147.10	F	1.178	0.01392	0.024
17H-1, 50	150.60	F	1.132	0.01601	0.001
17H-3, 50	153.60	F	1.206	0.01606	-0.002
18H-1, 50	160.10	F	1.431	0.01414	0.036
18H-3, 50	163.10	F	1.086	0.01334	-0.035
18H-5, 50	166.10	F	1.165	0.01305	0.014
19H-1, 50	169.60	F	1.364	0.00837	0.019
19H-5, 50	175.60	F	1.091	0.01572	-0.024
20H-1, 40	179.00	F	1.216	0.00882	0.012
20H-1, 40	179.00	F	1.174	0.00973	0.050
20H-3, 50	182.10	F	1.086	0.00931	-0.016
20H-5, 50	185.10	F	1.199	0.01192	-0.011
21H-1, 50	188.60	F	1.399	0.01588	0.032
21H-3, 50	191.60	F	0.980	0.01034	-0.029

Notes: Method used either F = full-space or H = half-space; TCcorr = thermal conductivity corrected for drift.

served deviation between the two data series is small, generally less than 5%.

The average value is fairly constant, close to  $2.7 \text{ g/cm}^3$  (about the density of calcite) down to about 750 mbsf. From 800 to 850 mbsf the average values increase to about  $2.9 \text{ g/cm}^3$  reflecting an increase in the content of basaltic volcanic material toward the base of the drilled sequence.

### Synthetic Seismogram

Over the interval 371–960 mbsf the sonic log was of good quality in Hole 953C. A synthetic seismogram was calculated by convolution of the log with a seismic wavelet (Fig. 60) derived from the pre-site survey seismic data. Before the convolution, spikes with extreme values were muted from the sonic log. The depth scale was transformed to a two-way traveltimes scale by stepwise integration of the interval transit times. After interpolation and resampling of the interval transit times the convolution was performed. The resulting synthetic seismic trace was sixfold duplicated and pasted into the seismic profile shown in Figure 61. A good correlation is found with most of

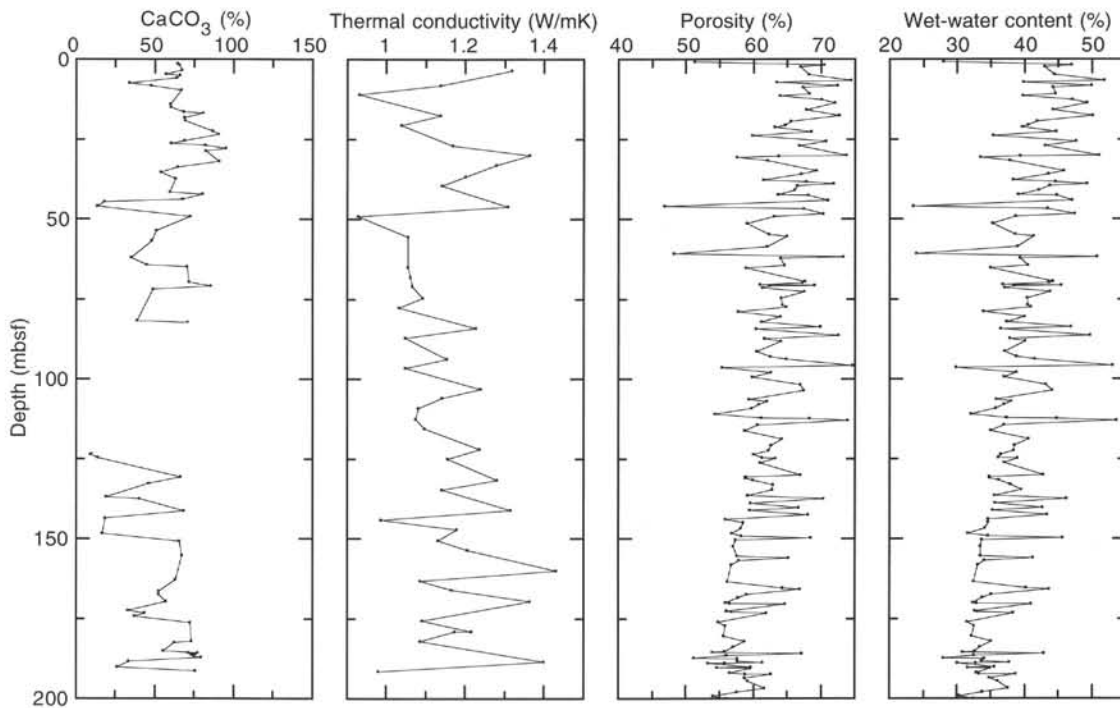


Figure 50. Hole 953A carbonate content, thermal conductivity, porosity, and wet-water content.

the reflectors, and it seems that a precise correlation from core observations to the seismic profile will be possible.

Based on a combination of MST-velocities and velocities obtained from the sonic log a depth-two-way traveltime relationship was established for Site 953 as shown in Figure 62.

### SEDIMENT ACCUMULATION RATES

A sediment accumulation curve has been constructed for Site 953 (Fig. 63) based on 33 nannofossil, 11 planktonic foraminiferal, and 43 paleomagnetic age determinations. One age point was determined by lithologic and stratigraphic correlation to the base of the Mogan Formation on Gran Canaria, giving a total of 88 points (Table 15). Estimation of accumulation rates in the deeper part of the hole may be improved by later study of single crystal dates, nannofossil FO, and paleomagnetic data. All microfossil datum levels were identified in pelagic layers or in burrow infills of hemipelagic sediment.

Ages are well constrained by microfossils and paleomagnetism down to about 800 mbsf. Below this depth, only the base of the Mogan Formation and two nannofossil datums could be determined, as the lithologies for Units IVc to VII were mainly volcanoclastic and had very few hemipelagic layers.

#### Sediment Accumulation Rates

From zero to 250 mbsf (0–3.7 Ma) in lithologic Unit I and the upper part of Unit II, the datum levels indicate a constant accumulation rate of 66 m/m.y. This high sedimentation rate reflects a combination of the background pelagic accumulation rate and the input of numerous calcareous and volcanic turbidites from Gran Canaria. The Roque Nublo phase of volcanism on Gran Canaria between ~4.5 and 3.3 Ma was associated with the input of volcanoclastic turbidites. Following this, through the latest Pliocene and Pleistocene, the contribution of volcanoclastic flows decreased and was replaced by calcareous turbidites from shallow water areas.

From 250 to 360 mbsf (3.7–6.2 Ma) in the lower part of lithologic Unit II and the upper part of Unit III, the accumulation rate is 46 m/

m.y., probably reflecting the hiatus in volcanic activity on Gran Canaria that began at ~9 Ma. From 360 to 390 mbsf (6.2–8.2 Ma) in the middle part of Unit III, a much lower accumulation rate of 18 m/m.y. prevailed. This low rate may reflect very little input from Gran Canaria combined with a low pelagic sediment accumulation rate. From 390 to 590 mbsf (8.2–11.8 Ma) in the lower part of Unit III, Subunit IVa, and the upper part of Subunit IVb, the rate increased to 55 m/m.y., probably reflecting input from the later part of the Fataga phase of volcanism on Gran Canaria from 13.3 to 9 Ma. The continuation of this increased rate after cessation of the Fataga phase of volcanism at 9 Ma probably results from continuing erosion of highland areas built up during volcanism.

Below 590 mbsf and down to 843.5 mbsf (11.8–14 Ma) in lithologic Subunits IVb and IVc, the accumulation rate was more than double: 112 m/m.y. This rate is mainly constrained by paleomagnetic datums, which seem to indicate a slightly lower rate than the widely spaced microfossil datum levels. This high rate seems to reflect the voluminous Mogan and early Fataga phases of volcanism on Gran Canaria, which were dominated by pyroclastic deposits.

Below this depth, only two datum points exist, both based on nannofossils from very thin pelagic layers. Despite their wide spacing, these nannofossil datum levels provide well constrained maximum and minimum ages for the interval from 843.5 mbsf to the base of the hole at 1157.45 mbsf. From 843.5 to 968.22 mbsf (14–15.8 Ma) in lithologic Units V and VI, the average accumulation rate is 70 m/m.y. This rate is probably a minimum, and seems to reflect the submarine and subaerial growth of the basaltic shield of Gran Canaria. From 968.22 to 1153.23 mbsf (15.8–17.4 Ma) in lithologic Unit VII, the average accumulation rate is much higher at 118.2 m/m.y., and may reflect shield volcanism that was occurring during this time on the island of Fuerteventura, or a major seamount west of Fuerteventura that is close to Site 953.

### SEISMIC STRATIGRAPHY

In view of the relatively simple nature of the sedimentary sequence encountered in the pre-site survey data at Site 953, it was

Table 10. Index properties, Holes 953A, 953B, and 953C.

Core, section, interval (cm)	Depth (mbsf)	WCw (%)	WCd (%)	BD <sub>b</sub> (g/cm <sup>3</sup> )	BD <sub>c</sub> (g/cm <sup>3</sup> )	GD <sub>b</sub> (g/cm <sup>3</sup> )	GD <sub>c</sub> (g/cm <sup>3</sup> )	DD <sub>b</sub> (g/cm <sup>3</sup> )	DD <sub>c</sub> (g/cm <sup>3</sup> )	Por <sub>b</sub> (%)	Por <sub>c</sub> (%)	VR <sub>b</sub>	VR <sub>c</sub>
157-953A-													
1H-2, 83-85	2.33	43.02	75.51	1.62	1.59	2.88	2.75	0.92	0.91	67.99	66.95	2.12	2.03
1H-4, 31-33	4.81	44.39	79.82	1.61	1.57	2.98	2.75	0.90	0.88	69.92	68.20	2.32	2.14
1H-5, 52-54	6.52	51.81	107.51	1.49	1.47	2.93	2.77	0.72	0.71	75.43	74.43	3.07	2.91
1H-5, 117-119	7.17	39.86	66.28	1.65	1.63	2.79	2.68	1.00	0.98	64.37	63.45	1.81	1.74
2H-1, 49-51	8.09	49.86	99.44	1.48	1.49	2.68	2.71	0.74	0.75	72.26	72.42	2.61	2.63
2H-1, 117-119	8.77	44.25	79.36	1.58	1.56	2.80	2.66	0.88	0.87	68.42	67.36	2.17	2.06
2H-3, 23-25	10.83	44.60	80.49	1.60	1.57	2.90	2.74	0.88	0.87	69.50	68.29	2.28	2.15
2H-3, 85-87	11.45	39.78	66.07	1.67	1.64	2.87	2.74	1.01	0.99	64.94	63.86	1.85	1.77
2H-4, 50-52	12.60	47.07	88.92	1.46	1.53	2.33	2.70	0.77	0.81	66.94	70.08	2.03	2.34
2H-5, 10-12	13.70	49.24	96.99	1.53	1.50	2.90	2.72	0.77	0.76	73.33	72.07	2.75	2.58
2H-6, 81-83	15.91	44.22	79.28	1.58	1.57	2.79	2.73	0.88	0.88	68.35	67.85	2.16	2.11
3H-1, 63-65	17.73	50.12	100.50	1.55	1.49	3.16	2.71	0.77	0.74	75.62	72.70	3.10	2.66
3H-2, 83-85	19.43	41.86	72.01	1.47	1.60	2.14	2.71	0.85	0.93	60.05	65.56	1.50	1.90
3H-3, 50-52	20.60	40.46	67.95	1.66	1.64	2.87	2.75	0.99	0.97	65.57	64.63	1.90	1.83
3H-3, 121-123	21.31	39.60	65.57	1.63	1.63	2.67	2.68	0.99	0.99	63.08	63.17	1.71	1.72
3H-4, 95-97	22.55	44.67	80.73	1.59	1.57	2.87	2.77	0.88	0.87	69.32	68.54	2.26	2.18
3H-5, 80-82	23.90	35.37	54.73	1.76	1.73	2.91	2.79	1.14	1.12	60.82	59.84	1.55	1.49
3H-6, 95-97	25.55	47.61	90.88	1.48	1.52	2.50	2.73	0.78	0.80	68.92	70.77	2.22	2.42

Notes: WCw = water content (% wet sample weight), WCd = water content (% dry sample weight), BD = bulk density, GD = grain density, DD = dry density, Por = porosity, and VR = void ratio. Suffixes "b" and "c" on column heads indicate value calculated using Method B and Method C, respectively (see "Explanatory Notes," this volume).

Only a part of this table is reproduced here. The entire table appears on the CD-ROM (back pocket).

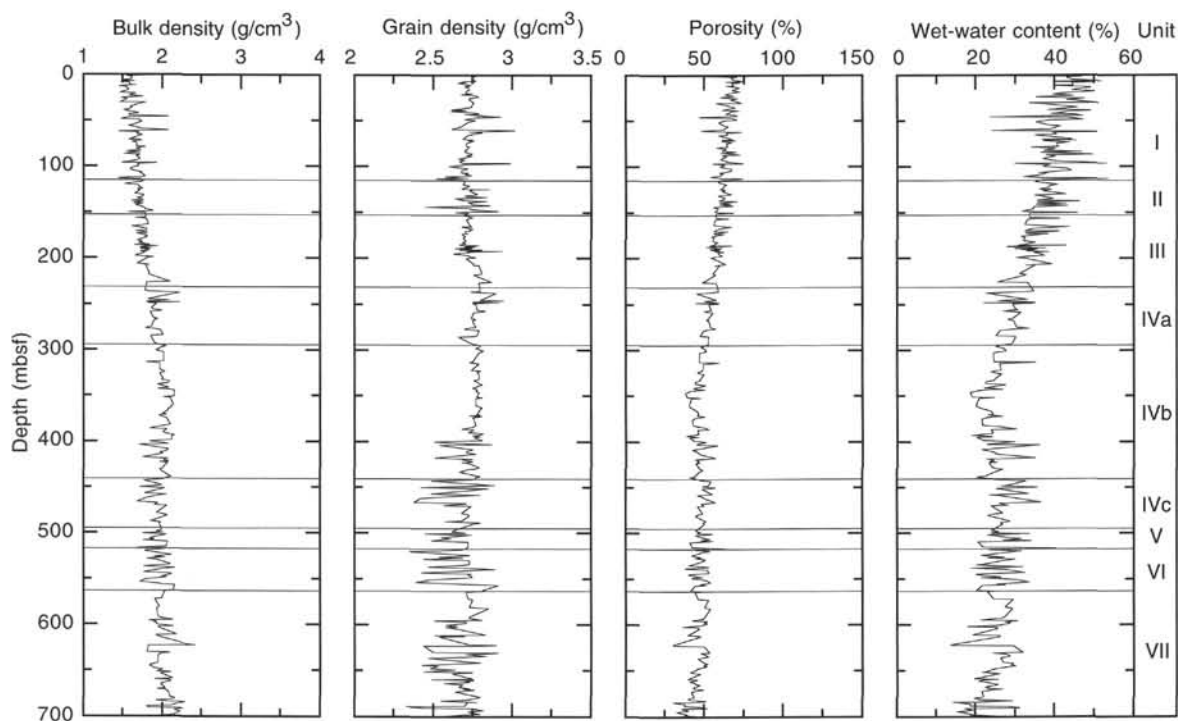


Figure 51. Site 953 bulk density (Method B), grain density (Method C), porosity (Method C), and wet-water content. Roman numerals refer to lithostratigraphic units.

found unnecessary to acquire supplementary reflection seismic data at this site. The following description is based on selected reflection seismic lines from the pre-site survey data.

Site 953 is located on seismic Line P134, which has a south-south-east-north-northwest radial direction relative to Gran Canaria. The line is crossed by Line P135 12 km north of Site 953. This south-southeast-north-northwest line is radial relative to Fuerteventura (Fig. 64). Line drawings displaying a simplistic view of the reflectors in the two lines have been spliced at the crossing point in a composite profile shown in Figure 65.

On a large scale the seismic profiles show the characteristics of an infill sequence with onlap onto the flanks of Gran Canaria and Fuerteventura. At the flanks of the islands the internal reflectors image compound systems of mounded units with more or less chaotic internal structures. This flank facies is most extensive at Gran Canaria where chaotic patterns in the deeper parts are succeeded by relatively regular stacks of mounded structures in the upper two-thirds of the sequence.

Outside the flank facies, which extend 10–20 km from Gran Canaria and 5–10 km from Fuerteventura, the seismic facies changes

**Table 11. P-wave velocity measured by the DSV, Hole 953A.**

Core, section, interval (cm)	Depth (mbsf)	Velocity (km/s)	Temperature (°C)
157-953A-			
1H-2, 21-28	1.71	1.51	20.2
1H-5, 49-56	6.49	1.45	20.3
3H-1, 61-68	17.71	1.51	18.3
3H-2, 81-88	19.41	1.53	20.4
3H-3, 119-126	21.29	1.55	20.2
3H-6, 92-99	25.52	1.52	20.2
4H-1, 36-43	26.96	1.53	21.7
4H-6, 78-85	34.88	1.55	20.6
5H-2, 65-72	38.25	1.55	20.7
5H-2, 14-21	37.74	1.56	21.2
5H-4, 23-30	40.83	1.54	20.3
6H-2, 124-131	48.34	1.51	20.5
6H-7, 26-33	54.86	1.58	20.8
7H-1, 37-44	55.47	1.56	21.7
8H-6, 48-55	72.58	1.56	20.7
9H-2, 84-91	76.44	1.51	20.6

**Table 12. P-wave velocity measured by the Hamilton Frame, Hole 953C.**

Core, section, interval (cm)	Depth (mbsf)	Velocity (km/s)
157-953C-		
2R-1, 58-60	187.58	1.66
3R-1, 75-77	197.25	1.72
3R-1, 76-78	197.26	1.77
4R-1, 34-36	206.44	1.99
5R-1, 14-16	215.94	1.74
5R-1, 135-137	217.15	1.67
6R-1, 8-10	225.58	2.44
7R-1, 13-15	235.13	1.78
7R-1, 38-40	235.38	1.74
7R-1, 145-147	236.45	2.67
7R-2, 23-25	236.73	2.94
7R-2, 49-51	236.99	3.05
7R-2, 80-82	237.30	3.06
7R-2, 105-107	237.55	3.12
7R-3, 2-4	237.69	2.98
7R-3, 61-63	238.28	3.41
7R-3, 92-94	238.59	3.68
8R-1, 6-8	244.66	3.58
8R-1, 19-21	244.79	2.28
8R-1, 62-64	245.22	1.97
8R-1, 93-95	245.53	1.66
8R-1, 121-123	245.81	2.99

**Only a part of this table is reproduced here. The entire table appears on the CD-ROM (back pocket).**

into a more regular basin-fill facies with parallel or basinward diverging reflector patterns. The relationships between the flank facies and the basin-fill facies are highly different between the two islands. At Gran Canaria the seismic units in the basin fill commonly continue into the mounds of the flank facies, whereas the basin-fill units onlap the flank facies at Fuerteventura.

In a zone extending 20-30 km into the basin from the front of the flank facies, a marginal basin-fill facies can be distinguished at both islands. This facies is characterized by a series of wedges and mound sheets with maximum thickness at or close to the flank. Units with concordant reflectors are found as intercalations. The wedges and mound sheets thin out basinward and grade into the subparallel basin-fill units.

The elements of this tripartite facies architecture, flank facies, marginal basin facies, and distal basin facies, are most completely developed around Gran Canaria.

Site 953 is located in the marginal basin facies area of Gran Canaria (Fig. 65). In seismic Profile P134 the basin-fill sequences are penetrated to a maximum depth of 1.2 s twt. According to the two-way traveltme/depth relationship (Fig. 66) derived from seismic velocities measured in the physical properties lab and velocities from the sonic log, this corresponds to a depth of about 1300 mbsf. The total depth cored, 1159 mbsf, corresponds to 1.05 s twt.

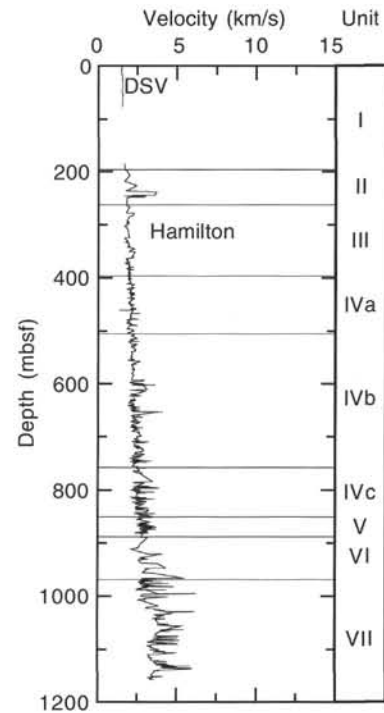


Figure 52. P-wave velocity measured by DSV and Hamilton Frame, Site 953. Roman numerals refer to lithostratigraphic units.

**Table 13. Strength measurements, Holes 953A and 953B.**

Core, section, interval (cm)	Depth (mbsf)	Pk str (kPa)	Res (kPa)	Pen (kPa)
157-953A-				
1H-2, 25-26	1.75	8	3	
1H-5, 53-54	6.53	12	5	
3H-1, 64-65	17.74	19	8	
3H-2, 84-85	19.44	27	17	
3H-2, 91-92	19.51			49
3H-3, 122-123	21.32	16	6	
3H-3, 128-129	21.38			69
3H-6, 95-96	25.55	20	11	
3H-6, 100-101	25.60			49
4H-1, 34-35	26.94			49
4H-1, 39-40	26.99	18	8	
4H-3, 45-46	30.05	14	11	
4H-3, 47-48	30.07			34
4H-6, 81-82	34.91	39	17	
4H-6, 83-84	34.93			54
4H-7, 33-34	35.93	35	16	
4H-7, 34-35	35.94			59
5H-2, 16-17	37.76			78
5H-2, 17-18	37.77	38	23	
5H-2, 68-69	38.28	3	1	

Note: Pk str = peak strength, undrained shear strength as measured by the vane shear, Res = residual shear strength, and Pen = unconfined shear strength as measured by the penetrometer, converted to kPa.

**Only a part of this table is reproduced here. The entire table appears on the CD-ROM (back pocket).**

The section, shown in detail in Figure 67, is composed of three main units. The upper unit, A, 0-900 ms (0-900 mbsf) corresponds to lithostratigraphic Units I-V. It contains numerous internal reflectors and bands of reflectors with high amplitude, relatively short periods, and high continuity. Reflectors are almost parallel, with a very gentle 0-0.5° northern dip. Three reflector bands are emphasized and marked as 1-3 in Figure 67. The two-way traveltimes for the reflector bands are 275-300, 525-575, and 775-850 ms corresponding to

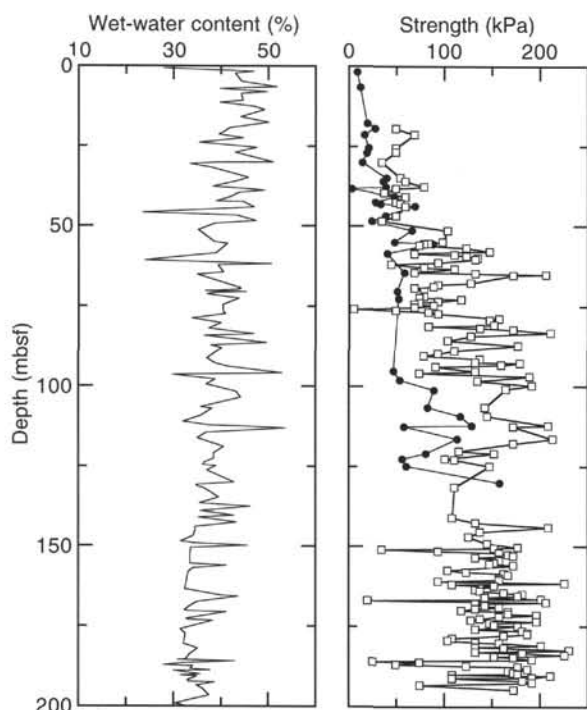


Figure 53. Wet-water content and strength data determined by vane shear (filled circles) and handheld penetrometer methods (open squares), Hole 953A.

depth intervals 220–250, 490–525, and 760–850 mbsf, respectively. Reflector bands 1 and 3 correlate with deposits referred to the volcanic phases Roque Nublo and Mogan, respectively. Reflector band 2 corresponds to the later part of the Fataga phase. The reflector bands may be significant markers for regional mapping.

The reflectors in the deepest part of Unit A overlap the surface of Unit B, defined by a high-amplitude and long-period reflector with a discontinuous, mounded structure. Correlation from mound to mound is often hampered by complex interfingering reflector patterns. At Site 953 the surface of Unit B has an average northward slope of about  $1^\circ$ . Internal reflectors form a shingled, northward dipping pattern. At Site 953 Unit B is found in the interval 895–940 ms twt corresponding to 900–965 mbsf. The base of Unit B is defined in the vicinity of the site by a nearly horizontal, high-amplitude reflector that fades out southward as the thickness of Unit B increases. Unit B thins out north of Site 953 and is correlated with lithostratigraphic Unit VI, hyaloclastite and lapillistone from the shield phase of Gran Canaria.

The upper surface of the deepest unit, C, is defined by the base of Unit B. The few internal reflectors in Unit C are approximately hori-

zontal and the continuity is low, probably because of the reduced signal/noise ratio below the strongly reflecting Unit B. To the north where Unit B is thin the signal/noise ratio improves and a number of continuous, long-period reflectors appear. Unit C correlates with lithostratigraphic Unit VII.

## REFERENCES

- Archie, G.E., 1942. The electrical resistivity log as an aid in determining some reservoir characteristics. *Trans. Am. Inst. Min. Metall. Pet. Eng.*, 146:54–62.
- Clay, C.S., and Medwin, H., 1977. *Acoustical Oceanography: Principles and Applications*: New York (Wiley).
- Bogaard, P., Schmincke, H.-U., Freundt, A., Hall, C., and York, D., 1988. Eruption ages and magma supply rates during the Miocene evolution of Gran Canaria: single crystal  $^{40}\text{Ar}/^{39}\text{Ar}$  laser ages. *Naturwissenschaften*, 75:616–617.
- Berggren, W.A., 1977. Late Neogene planktonic foraminiferal biostratigraphy of the Rio Grande Rise (South Atlantic). *Mar. Micropaleontol.*, 2:265–313.
- Raffi, I., and Flores, J.A., in press. Pleistocene through Miocene calcareous nannofossils from eastern equatorial Pacific Ocean (ODP Leg 138). In Pisias, N.G., Mayer, L.A., Janecek, T.R., Palmer-Julson, A., and van Andel, T.H. (Eds.), *Proc. ODP, Sci. Results*, 138: College Station, TX (Ocean Drilling Program).
- Rio, D., Fornaciari, E., and Raffi, I., 1990. Late Oligocene through early Pleistocene calcareous nannofossils from western equatorial Indian Ocean (Leg 115). In Duncan, R.A., Backman, J., Peterson, L.C., et al., *Proc. ODP, Sci. Results*, 115: College Station, TX (Ocean Drilling Program), 175–235.
- Schmincke, H.-U., 1982. Volcanic and chemical evolution of the Canary Islands. In von Rad, U., Hinz, K., Sarnthein, M., and Seibold, E. (Eds.), *Geology of the Northwest African Continental Margin*: Berlin (Springer), 273–306.
- Schmincke, H.-U., 1994. *Geological Field Guide: Gran Canaria* (7th ed.): Kiel, Germany (Pluto Press).
- Schmincke, H.-U., and von Rad, U., 1979. Neogene evolution of Canary Island volcanism inferred from ash layers and volcanoclastic sandstones of DSDP Site 397 (Leg 47A). In von Rad, U., Ryan, W.B.F., et al., *Init. Repts. DSDP*, 47 (Pt. 1): Washington (U.S. Govt. Printing Office), 703–725.
- Serra, O., 1984. *Fundamentals of Well-Log Interpretation* (Vol. 1): *The Acquisition of Logging Data*. Dev. Pet. Sci., 15A. Amsterdam (Elsevier).
- Thierstein, H.R., Geitzenauer, K., Molfino, B., and Shackleton, N.J., 1977. Global synchronicity of late Quaternary coccolith datum levels: validation by oxygen isotopes. *Geology*, 5:400–404.
- Weaver, P.P.E., 1983. An integrated stratigraphy of the upper Quaternary of the King's Trough Flank area, N.E. Atlantic. *Oceanol. Acta*, 6:451–456.
- Wyllie, M.R.J., Gregory, A.R., and Gardner, H.F., 1958. An experimental investigation of the factors affecting elastic wave velocities in porous media. *Geophysics*, 23:400.
- Young, J.R., 1990. Size variation of Neogene *Reticulofenestra* coccoliths from Indian Ocean DSDP cores. *J. Micropaleontol.*, 9:71–85.
- Young, J.R., Flores, J.-A., and Wei, W., 1994. A summary chart of Neogene nannofossil magnetobiostratigraphy. *J. Nannoplankton Res.*, 16:21–27.

Ms 157IR-107

**NOTE:** For all sites drilled, core-description forms (“barrel sheets”) and core photographs can be found in Section 6, beginning on page 561. Smear-slide and thin-section data are given in Section 7, beginning on page 835. The CD-ROM (back pocket, this volume) contains physical properties and geochemical data, MST data, logging data, and color core photographs (Sites 950 and 953 only).

**Table 14. Summary of logging operations, Hole 953A.**

Date (September 1994)	Time (UTC)	Activity
2	09:20	Last core on deck. Prepare hole for logging.
3	05:20	Hole preparation complete, rig up wireline.
	06:45	RIH with NGT-LSS-CNT-HLDT-DIT (+TLT).
	08:13	Start downgoing log from EOP to 985 mbsf, downward progress halted by an obstruction at 1017 mbsf. Tried to work tool down, lost hole rapidly.
	09:52	Upgoing log at 900 ft/hr from 975 mbsf to mudline. Considerable overpull encountered (4 5000 lb) from 975 911 mbsf and again from 575 499 mbsf. HLDT caliper closed to reduce drag over the intervals 955 941 mbsf, 934 908 mbsf and 524 486 mbsf to avoid dangerous level of overpull.
	13:48	Upgoing log completed at mudline. Tool string RIH, sat down on obstruction at 477 mbsf.
	14:05	POOH.
	15:10	Tool out of hole, pull wireline rig aside.
	16:15	RIH with drill string to ream and wash through bridges.
	19:30	Drill string stuck at 526 mbsf.
	21:00	Decision to sever drill pipe, further logging attempts abandoned.

Note: Drillers TD = 1157.8 mbsf, WD = 3588.9 mbrf, EOP = 372 mbsf.

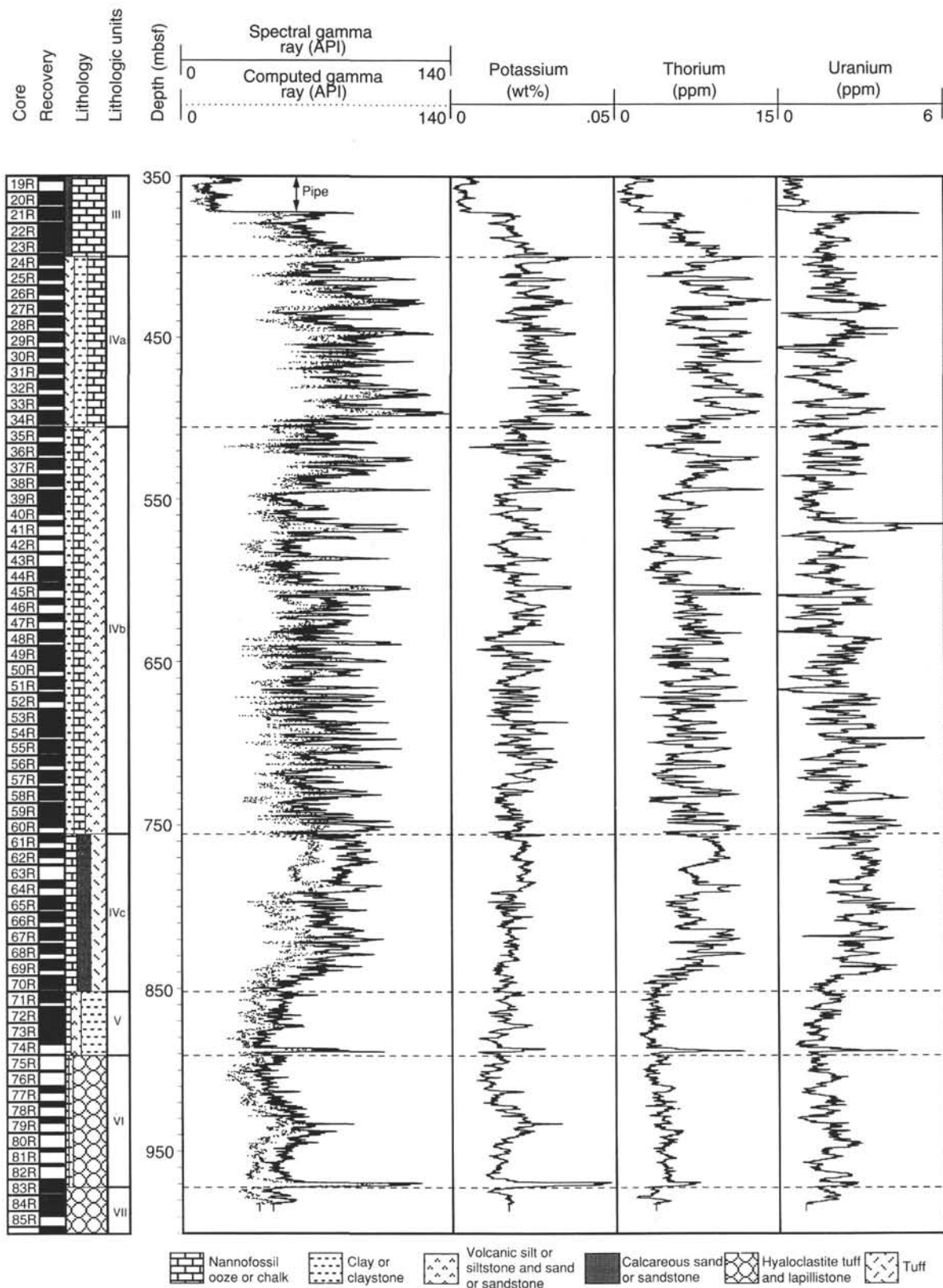


Figure 54. Hole 953C data from the NGT recorded on the quad combination tool string. The left track shows the total and the computed gamma-ray counts; tracks for K, U, and Th components of the total gamma-ray signal follow.

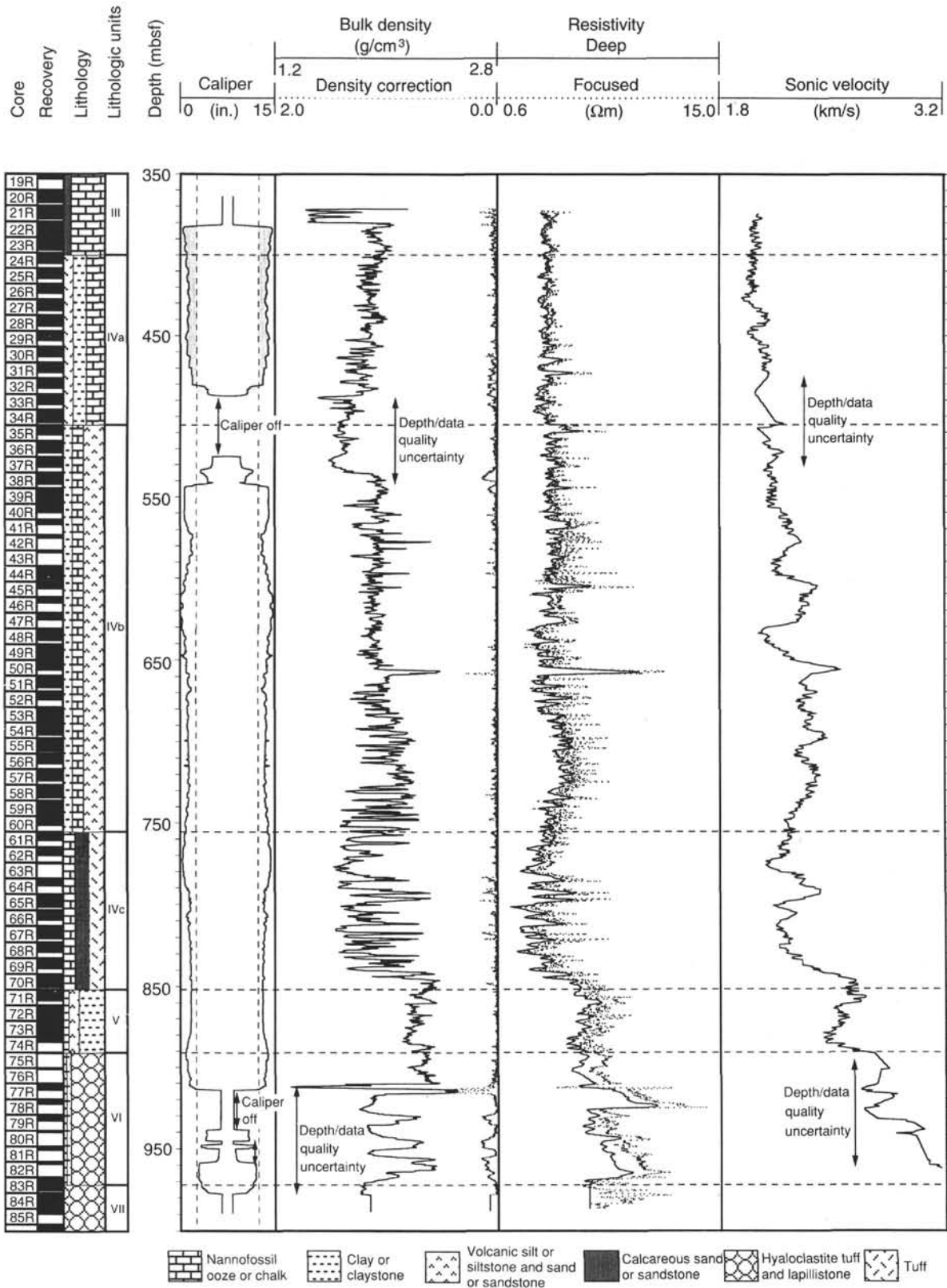


Figure 55. Hole 953C physical logs summary. Caliper data from the HLDT shown with bulk-density data from the HLDT, deep phasor induction and spherically focused resistivity from the phasor DIT, and sonic velocity data from the LSS. The central white area in the caliper log represents the RCB bit size (9-7/8 in.); shading represents the “washed out” portion of the hole from the bit size to actual measured diameter. The sonic velocity data have been processed to remove cycle skips.

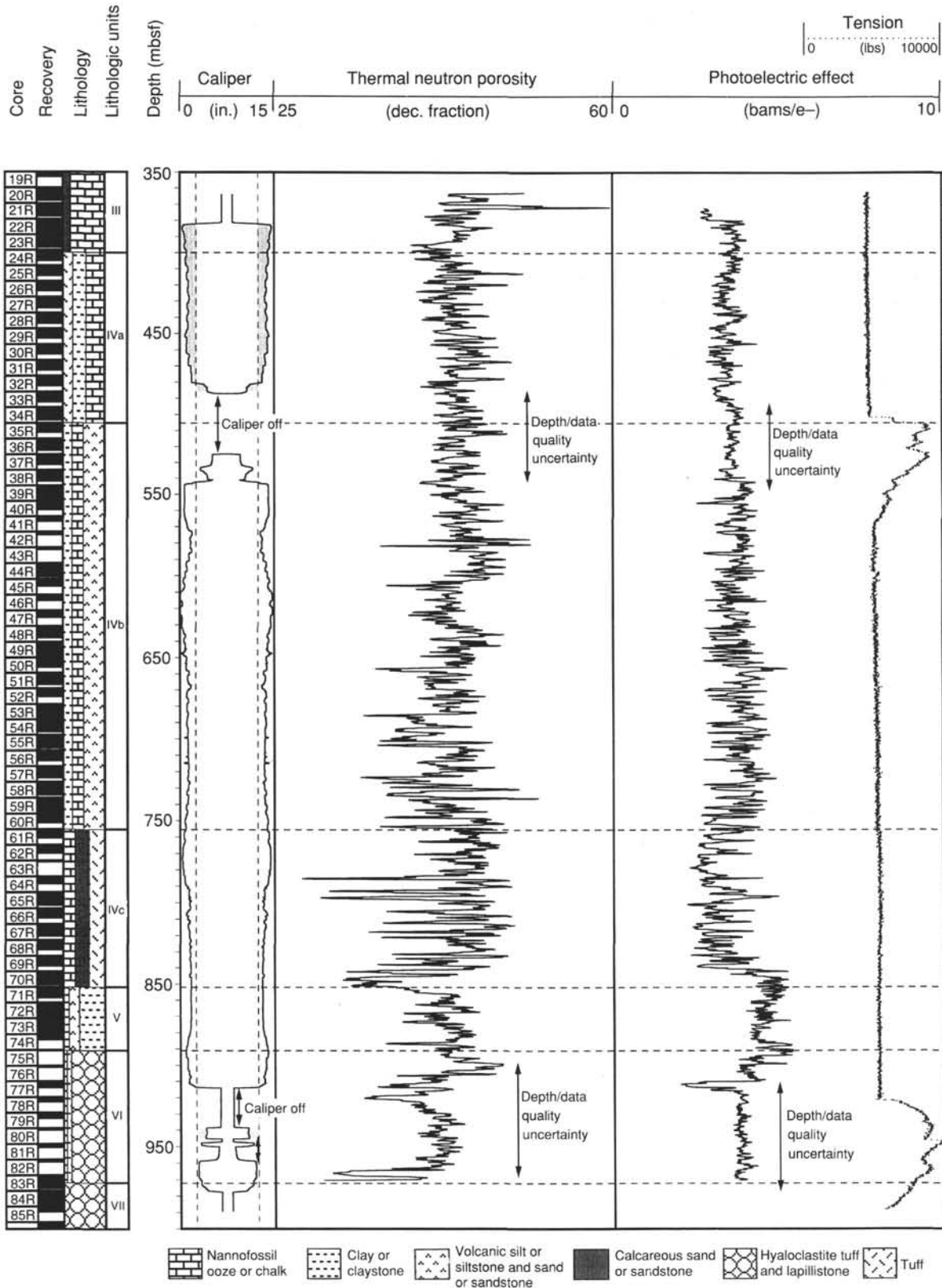


Figure 56. Hole 953C caliper data from the HLDT shown with thermal neutron porosity from the CNT, photoelectric factor from the HLDT, together with the tension record from the main upgoing log of the quad combination tool string. The neutron porosity log has been smoothed by a 5 point (2.5 ft) running average box filter.

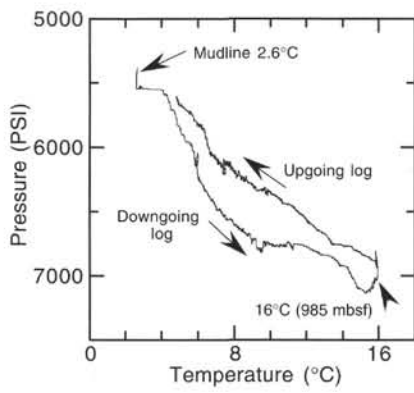


Figure 57. Pressure vs. temperature plot taken from the Lamont-Doherty temperature logging tool run on the quad tool string.

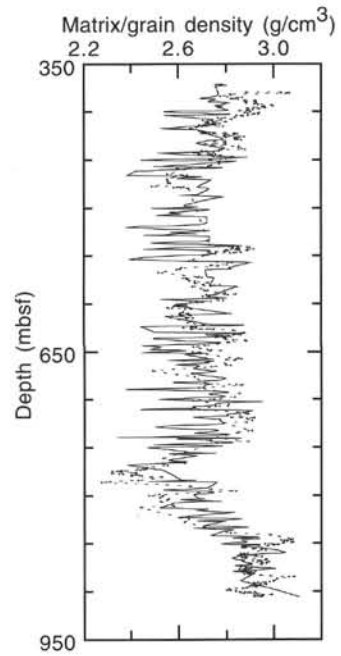


Figure 59. Log calculated grain-density measurements compared to index property measurements on discrete core samples. The calculated grain densities are derived by combining the log porosity, taken as an average of the calculated induction-porosity and sonic-porosity, with the log bulk-density measurements. Solid line = grain density (IP), broken line = matrix density (calc.).

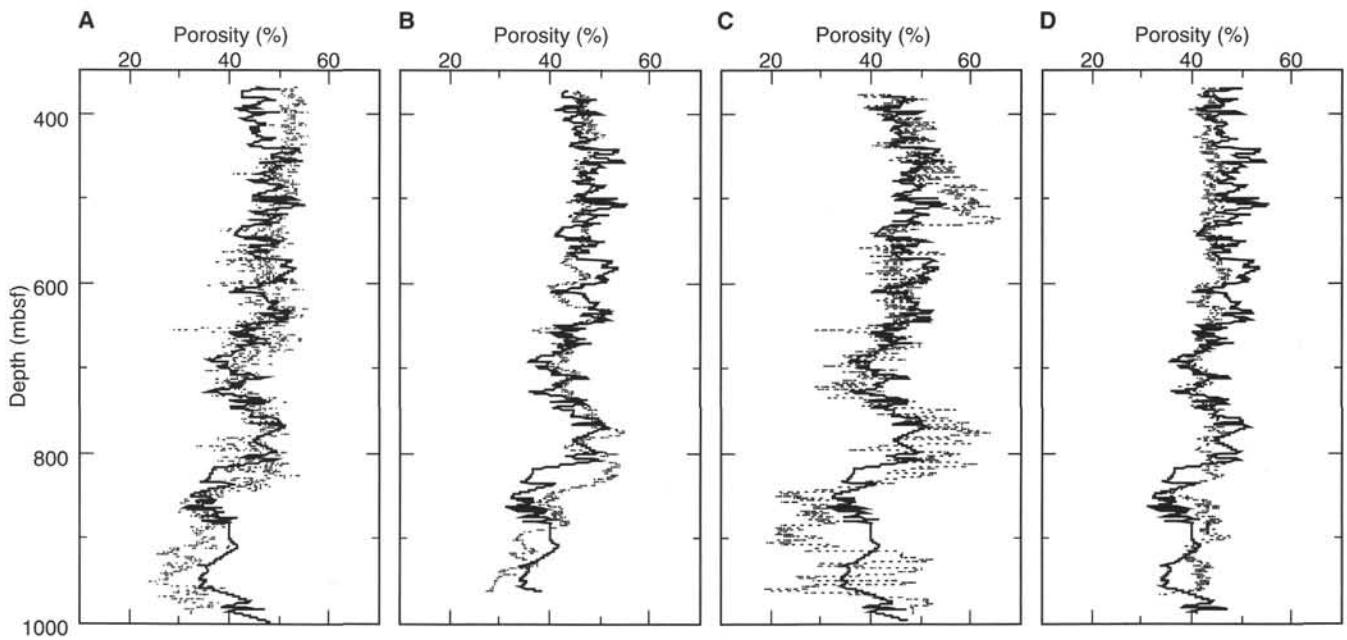


Figure 58. Calculated porosity logs compared to porosity measurements on discrete core samples from (A) resistivity (SFLU), (B) sonic velocity, (C) bulk (gamma) density, and (D) thermal neutron porosity.

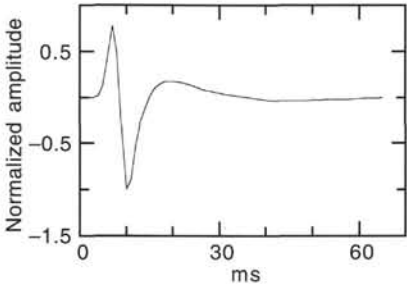


Figure 60. Wavelet used in the calculation of the synthetic seismogram derived from the pre-site seismic survey data. Amplitudes normalized by max. amplitude.

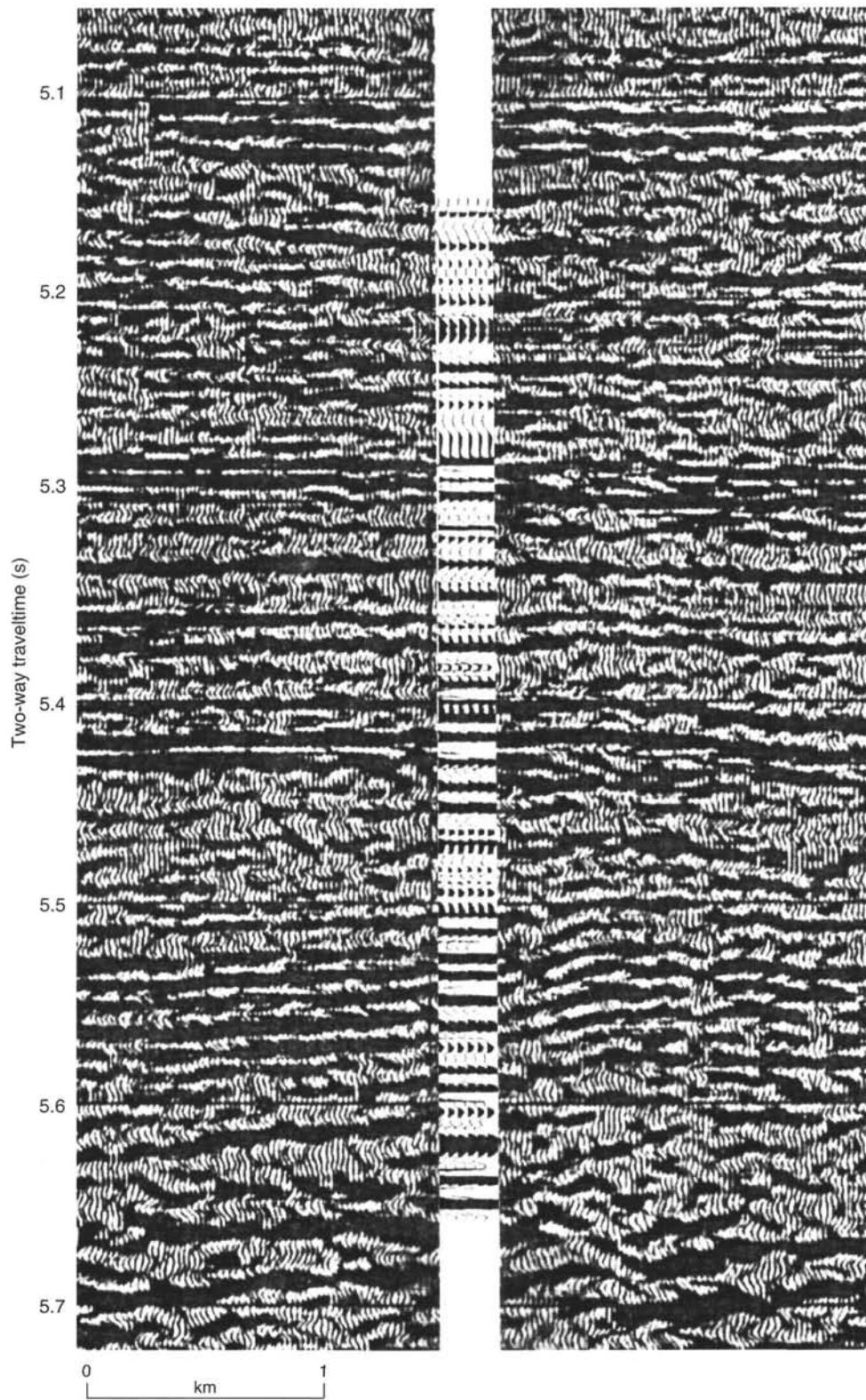


Figure 61. Synthetic seismogram calculated from the downhole density and sonic velocity data pasted into the seismic reflection profile.

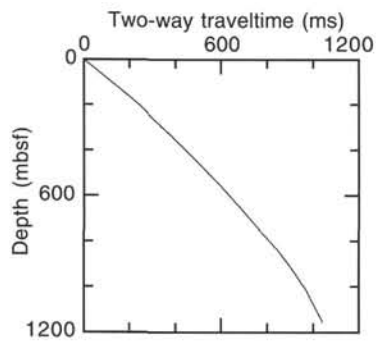


Figure 62. Relationship derived from sonic log and MST data between depth and two-way traveltime, measured from the seafloor reflector.

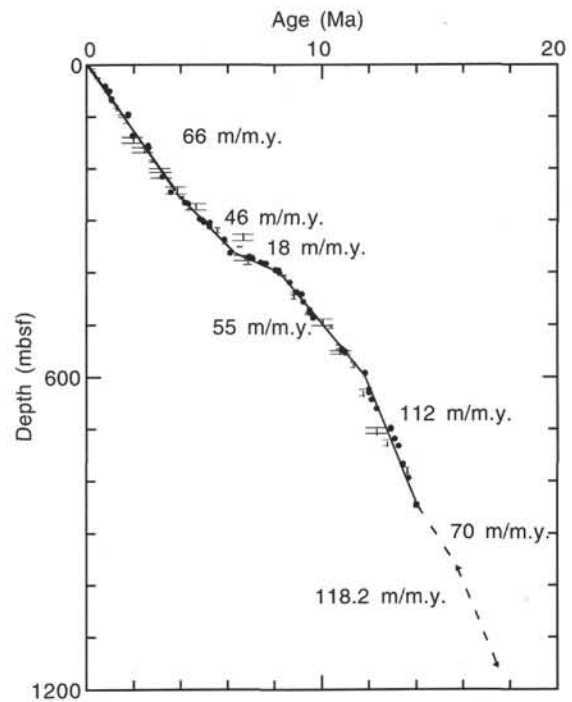


Figure 63. Sediment accumulation rates for Hole 952A. Vertical bars represent distances between sample points. Numbers refer to datum levels given in Table 15. Solid line = foraminifer age, broken line = nannofossil age, filled circle = paleomagnetic age, right-pointing triangle = nannofossil minimum age, left-pointing triangle = maximum age, and filled square = base Mogan age.

Table 15. Datum levels used in calculation of sediment accumulation rate curves.

	Event	Sample		Depth (mbsf)		Age (Ma)
		Top	Bottom	Top	Bottom	
1	FO abundant small <i>Gephyrocapsa</i>	157-953A-2H-1, 74	157-953A-2H-4, 132	8.34	13.42	0.26
2	LO <i>P. lacunosa</i>	3H-6, 41.5	3H-CC, 0	25.0	226.84	0.46
3	C1n (o)/Brunhes-Matuyama	5H-5, 55	5H-5, 65	41.20	42.60	0.78
4	LO <i>R. asanoi</i>	6H-1, 72	6H-6, 65.5	46.32	53.76	0.83
5	C1r.1n (t)/Jaramillo (t)	6H-4, 125	6H-4, 135	51.30	51.50	0.99
6	FO <i>R. asanoi</i>	7H-CC, 0	8H-1, 42	64.73	65.02	1.06
7	C1r.1n (o)/Jaramillo (o)	8H-1, 75	8H-3, 55	65.30	68.00	1.07
8	LO large <i>Gephyrocapsa</i> (>5.5 μm)	9H-4, 36	9H-7, 25	78.96	83.35	1.24
9	FO large <i>Gephyrocapsa</i> (>5.5 μm)	11H-3, 103	11H-6, 73	97.13	101.33	1.46
10	LO <i>C. macintyreii</i>	11H-3, 103	11H-6, 73	97.13	101.33	1.60
11	FO medium <i>Gephyrocapsa</i> (>3μm)	12H-7, 61	12H-CC, 0	112.21	112.28	1.67
12	C2n (t)/Olduvai (t)	11H-2, 45	11H-4, 15	95.00	97.80	1.77
13	FO <i>Gr. truncatulinoides</i>	15H-CC, 0-2	16H-CC, 0-2	140.55	150.45	1.92
14	LO <i>D. brouweri</i>	15H-CC, 0	16H-1, 57	140.56	141.17	1.95
15	C2n (o)/Olduvai (o)	15H-4, 65	15H-4, 75	136.20	136.30	1.95
16	LO <i>Gr. miocenica</i>	17H-CC, 0-2	18H-CC, 0-2	159.60	169.42	2.37
17	LO <i>D. pentaradiatus</i>	17H-CC, 0	18H-1, 123	159.61	160.83	2.44
18	C2An (t)/Gauss (t)	17H-4, 125	18H-1, 105	155.80	160.70	2.60
19	LO <i>D. surculus</i>	18H-3, 10	18H-6, 79	162.70	167.89	2.61
20	LO <i>D. tamalis</i>	20H-4, 13	20H-7, 4	183.23	187.64	2.76
21	LO <i>G. altispira</i>	157-953C-3R-CC, 0-2	157-953C-4R-CC, 0-2	200.24	207.98	3.09
22	LO <i>S. seminulina</i>	4R-CC, 0-2	5R-CC, 0-2	207.98	218.82	3.15
23	C2An.2r (t)/Mammoth (t)	5R-1, 35	5R-1, 45	216.20	216.30	3.22
24	C2Ar (t)/Matuyama-Gilbert	8R-1, 50	8R-1, 25	244.80	244.90	3.58
25	LO <i>R. pseudoubilicus</i>	8R-4, 17	8R-CC, 0	249.27	249.40	3.77
26	LO <i>Gr. margaritae</i>	7R-1, 125	8R-CC, 0-2	236.24	249.41	3.79
27	FO <i>D. tamalis</i>	9R-1, 8	9R-3, 81	254.18	257.91	4.01
28	C3n1n (t)/Cochiti (t)	10R-1, 145	—	265.10	—	4.18
29	C3n1n (o)/Cochiti (o)	10R-3, 95	—	267.70	—	4.29
30	LO <i>Amaurolithus</i> spp.	11R-3, 57	11R-CC, 0	276.97	279.88	4.39
31	LO <i>G. nepenthes</i>	10R-CC, 0-2	11R-CC, 0-2	267.69	279.89	4.63
32	C3n3n (t)/Sidjufall (t)	13R-3, 150	—	296.90	—	4.80
33	C3n3n (o)/Sidjufall (o)	13R-5, 65	—	299.40	—	4.89
34	C3n3n (t)/Thvera (t)	14R-1, 115	—	302.60	—	4.98
35	C3n3n (o)/Thvera (o)	14R-2, 125	15R-1, 15	305.20	312.30	5.23
36	LO <i>D. quinqueramus</i>	15R-2, 38	16R-2, 132	313.98	324.42	5.56
37	C3A.n1 (t)	17R-4, 115	17R-4, 125	336.70	336.90	5.87
38	LO <i>A. amplificus</i>	18R-1, 36	18R-3, 101	340.96	344.61	5.88
39	C3A.n1 (o)	20R-2, 95	20R-2, 105	362.30	362.40	6.12
40	FO <i>A. amplificus</i>	19R-1, 48	19R-1, 143	350.68	351.63	6.50
41	FO <i>Gr. margaritae</i>	16R-CC, 0-2	17R-CC, 0-2	326.06	338.77	6.64
42	FO <i>Gr. conomiozea</i>	20R-CC, 0-2	21R-CC, 0-2	367.29	377.22	6.70
43	FO <i>R. pseudoubilicus</i> (>7μm)	21R-2, 102	22R-5, 18	372.02	385.28	6.80
44	FO <i>Amaurolithus delicatus</i>	21R-2, 102	22R-5, 18	372.02	385.28	6.90
45	C3Bn (t)	21R-1, 75	21R-1, 115	370.20	370.60	6.92
46	C3Bn (o)	21R-3, 75	21R-3, 85	373.30	373.40	7.07
47	C4n.1n (t)	22R-2, 15	22R-2, 25	380.80	380.90	7.41
48	C4n.1n (o)	22R-2, 105	22R-2, 115	381.70	381.70	7.53
49	C4n.2n (t)	22R-2, 145	22R-3, 15	382.10	382.30	7.62
50	C4n.2n (o)	23R-5, 15	23R-5, 25	394.80	394.90	8.03
51	C4r.1n (t)	23R-6, 145	24R-1, 25	396.10	398.40	8.17
52	C4r.1n (o)	24R-3, 15	24R-3, 25	401.20	401.40	8.21
53	FO <i>D. quinqueramus</i>	24R-5, 4.5	25R-1, 32	404.15	408.02	8.40
54	C4An (t)	26R-2, 15	26R-2, 25	418.90	419.00	8.63
55	LO <i>R. pseudoubilicus</i> (>7μm)	28R-1, 41	28R-7, 25	437.01	442.85	8.80
56	FO <i>D. loeblichii</i>	28R-7, 40	29R-4, 54	443.00	451.24	8.80
57	C4An (o)	28R-1, 35	28R-1, 95	437.00	437.60	8.95
58	C4Ar.1n (t)	28R-4, 25	28R-4, 65	441.40	441.70	9.14
59	C4Ar.1n (o)	30R-1, 45	30R-1, 55	456.40	456.40	9.22
60	LO <i>D. hamatus</i>	32R-2, 86	32R-CC, 7	477.56	480.97	9.40
61	C4Ar.2n (t)	31R-4, 145	32R-2, 15	471.40	476.90	9.48
62	C4Ar.2n (o)	32R-3, 15	32R-3, 25	478.30	478.40	9.54
63	C5n.1n (t)	33R-1, 75	33R-2, 45	485.60	486.80	9.64
64	FO <i>Nq. acostaensis</i>	33R-4, 59-62	34R-6, 18-20	489.97	501.81	9.99
65	FO <i>D. hamatus</i>	34R-5, 50	35R-3, 5	500.62	506.93	10.40
66	FO <i>C. coalitus</i>	38R-4, 56	39R-2, 94	537.81	545.12	10.70
67	FO <i>G. nepenthes</i>	39R-6, 3.5	40R-3, 79-81	549.57	555.88	10.80
68	LO <i>C. miopelagicus</i>	39R-2, 94	39R-6, 95	545.12	550.50	10.80
69	C5n.2n (o)	39R-3, 105	39R-3, 115	546.50	546.60	10.84
70	C5r.1n (t)	39R-5, 95	39R-5, 105	549.20	549.30	10.94
71	C5r.1n (o)	39R-6, 135	40R-1, 55	550.90	553.00	10.99
72	LO <i>D. kugleri</i>	42R-1, 44	43R-1, 48	571.84	581.48	11.30
73	FO common <i>D. kugleri</i>	47R-4, 32	48R-6, 22	623.35	635.32	11.70
74	C5An.1n (t)	44R-1, 95	44R-2, 25	591.60	592.40	11.84
75	C5An.1n (o)	47R-4, 45	48R-1, 45	623.50	629.80	11.99
76	C5An.2n (t)	49R-3, 115	49R-3, 125	642.90	643.00	12.10
77	FO <i>Gr. languaensis</i>	55R-1, 33	56R-3, 3.4	696.82	708.89	12.30
78	C5An.2n (o)	51R-2, 115	51R-2, 125	660.40	660.50	12.32
79	LO <i>C. premacintyreii</i>	57R-5, 9	58R-5, 60	721.36	731.61	12.70
80	C5AAAn (t)	55R-2, 15	55R-3, 5	697.90	699.10	12.93
81	C5AAAn (o)	57R-2, 55	57R-2, 65	717.50	717.60	13.08
82	C5ABn (t)	58R-5, 75	58R-5, 105	731.80	732.10	13.25
83	C5ABn (o)	62R-3, 15	62R-4, 5	766.70	768.10	13.45
84	LO <i>S. heteromorphus</i>	63R-1, 1	64R-2, 8	773.11	784.34	13.60

Table 15 (continued).

	Event	Sample		Depth (mbsf)		Age (Ma)
		Top	Bottom	Top	Bottom	
85	C5ACn (t)	65R-1, 35	65R-1, 45	792.70	792.80	13.67
86	Base Mogan Formation	70R-3	—	843.50	—	14.00
87	LO <i>H. ampliaperta</i>	83R-1, 64	83R-2, 89	966.64	968.22	15.80
88	FO <i>H. premacintyreii</i>	83R-1, 64	83R-2, 89	966.64	968.22	17.40

Notes: Numbers in left column match numbers on Figure 63.

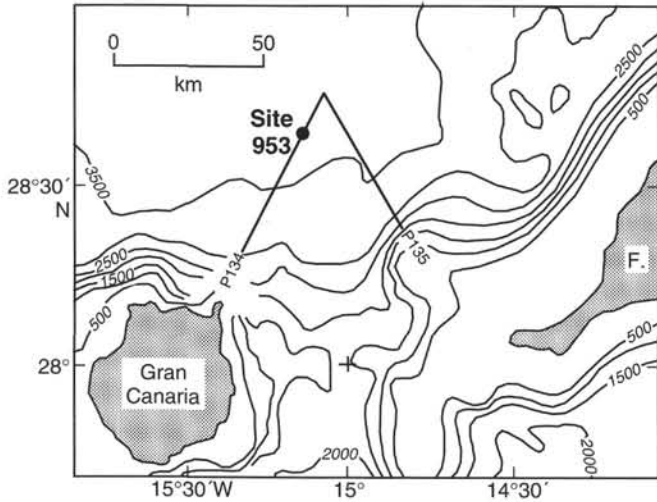


Figure 64. Location of Site 953 and reflection seismic Profiles P134 and P135. Depth contours in mbsf. F. = Fuerteventura.

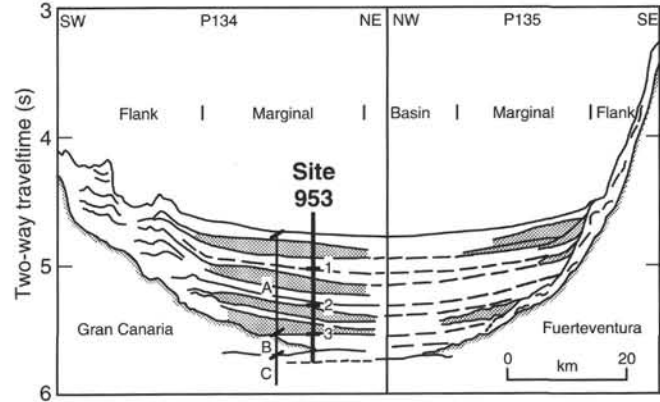


Figure 65. Simplified line drawing of main reflectors observed in the reflection seismic Profiles P134 and P135. Major seismic facies units are indicated and the wedge units and mounded sheets in the marginal basin facies are emphasized by stippling. Seismic stratigraphic Units A, B, and C and the prominent internal reflectors in Unit A are shown.

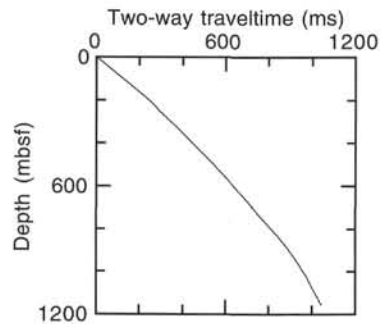


Figure 66. Two-way traveltimes vs. depth relationship derived from seismic velocity data from physical properties lab and from sonic log.

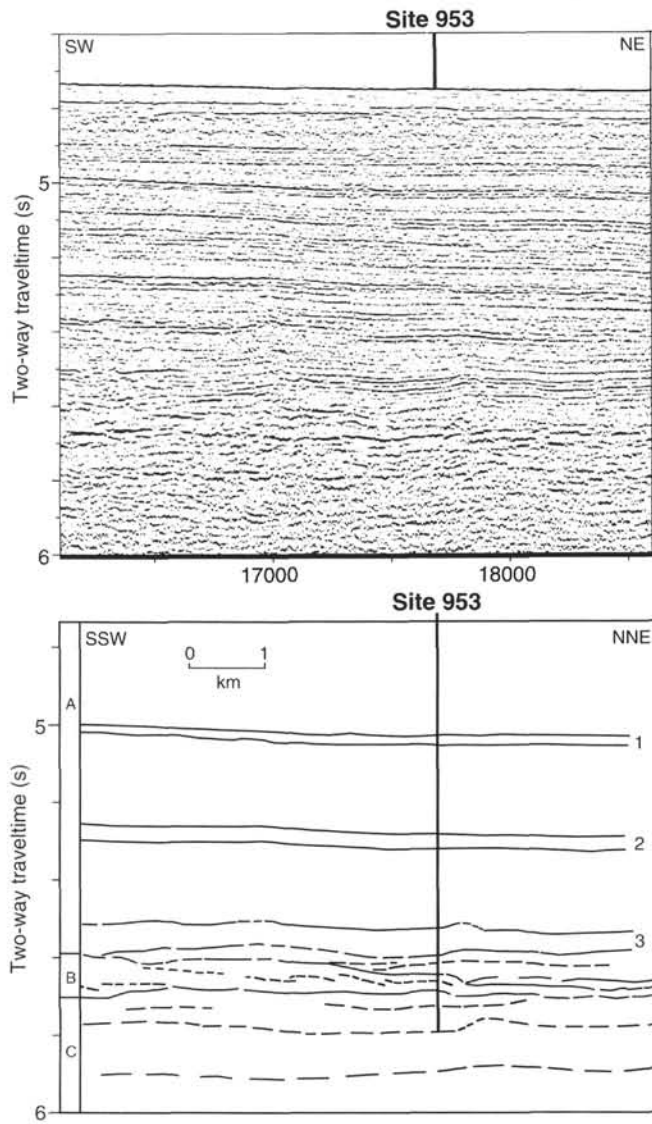


Figure 67. Seismic Profile P134 in the vicinity of Site 953. Seismic stratigraphic Units A, B, and C, and prominent reflector bands, 1-3, in Unit A, are indicated in the line drawing. Internal reflectors in Units B and C are indicated by thin, broken lines.

## SHORE-BASED LOG PROCESSING

## HOLE 953C

**Bottom felt:** 3588.9 mbrf  
**Total penetration:** 1158.7 mbsf  
**Total core recovered:** 556.53 m (48%)

## Logging Runs

**Logging string 1:** DIT/LSS/HLDT/CNTG/NGT

Wireline heave compensator was used to counter ship heave resulting from the mild sea conditions (0.2–1 m).

## Bottom-hole Assembly/Drill Pipe

The following bottom-hole assembly and drill pipe depths are as they appear on the logs after differential depth shift (see "Depth shift" section) and depth shift to the seafloor. As such, there might be a discrepancy with the original depths given by the drillers on board. Possible reasons for depth discrepancies are ship heave, use of wireline heave compensator, and drill string and/or wireline stretch.

DIT/LSS/HLDT/CNTG/NGT: Bottom-hole assembly at ~372 mbsf.

DIT/LSS/HLDT/CNTG/NGT: Drill pipe at ~287.5 mbsf.

## Processing

**Depth shift:** Reference runs for depth shift are the gamma ray and resistivity data from downlog. Due to hole obstructions, the data recorded uphole is locally stretched. The amount of stretch differs for each tool and therefore different amounts of depth shift have been applied in the attempt to account for the stretch. Two zones are particularly affected: from about 478 to 528 mbsf and from 908 mbsf to total depth. Therefore the data quality over these two intervals is very questionable. After interactive depth shift the logs have been shifted to the seafloor (–3591.5 m). This amount corresponds to the mud line as seen on the gamma ray log (uplog); it differs 2.6 m from the "bottom felt" depth (see above).

A list of the amount of differential depth shifts applied at this hole is available upon request.

**Gamma-ray processing:** NGT data have been processed to correct for borehole size and type of drilling fluid.

**Acoustic data processing:** The sonic logs have been processed to eliminate some of the noise and cycle skipping experienced during the recording.

## Quality Control

During the processing, quality control of the data is mainly performed by cross-correlation of all logging data. Large (>12 in.) and/or irregular borehole affects most recordings, particularly those that require eccentricization (CNTG, HLDT) and a good contact with the borehole wall.

The following is a list of the reliable logs from both uphole and downhole passes:

Resistivity (both downlog and uplog)

Sonic (uplog)

Gamma ray (downlog; uplog can be used as well, except in the intervals where the data is stretched; see "Depth shift" section)

Density and caliper (uplog)

Neutron (uplog)

Hole diameter was recorded by the hydraulic caliper on the HLDT tool (CALI); the caliper tool was closed several times during the uplog in attempt to reduce the severe overpull caused by hole caving.

Data recorded through pipe and bottom-hole assembly should be used qualitatively only because of the attenuation on the incoming signal.

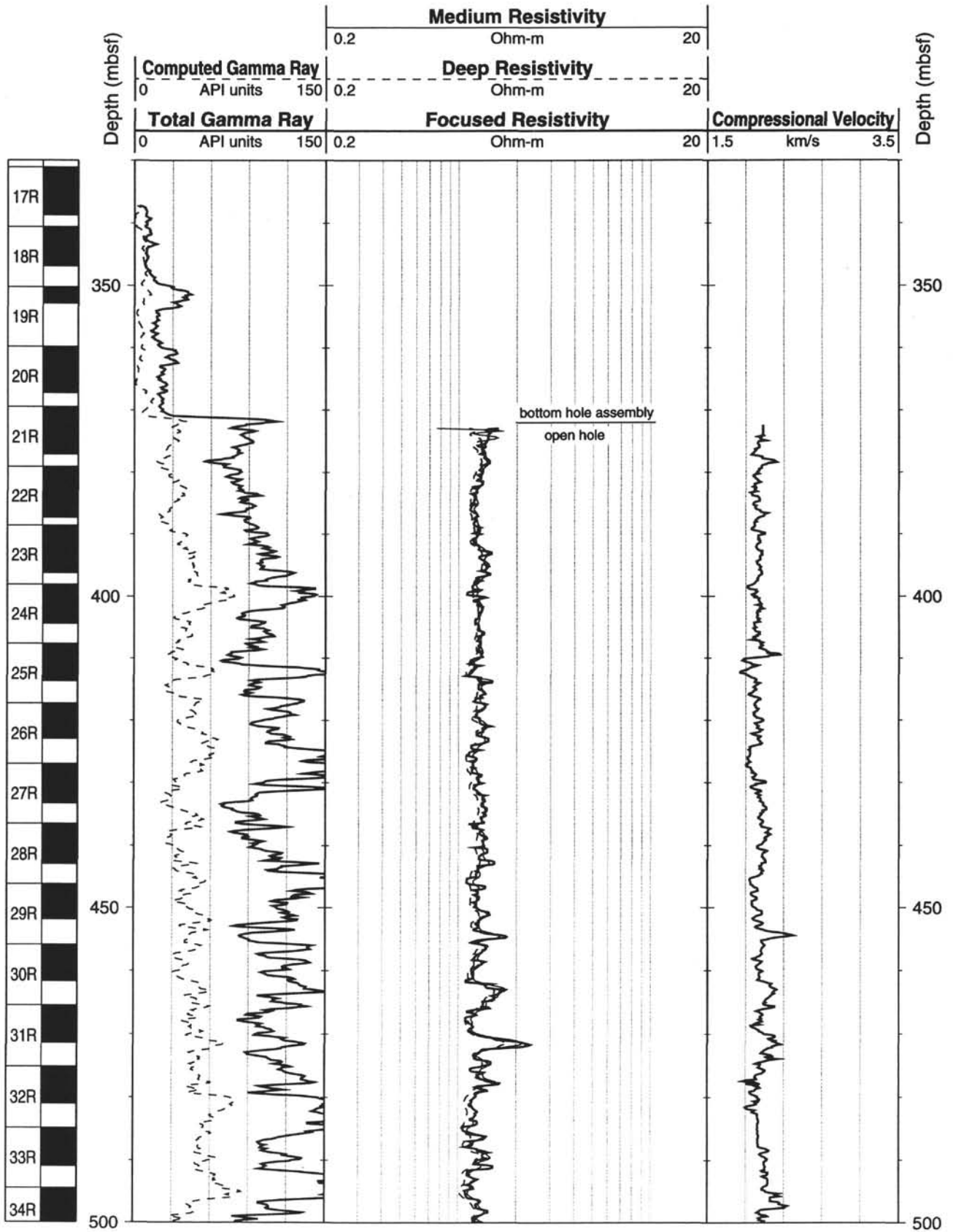
Hole diameter was recorded by the hydraulic caliper on the HLDT tool (CALI).

**Note:** Details of standard shore-based processing procedures are found in the "Explanatory Notes" chapter, this volume. For further information about the logs, please contact:

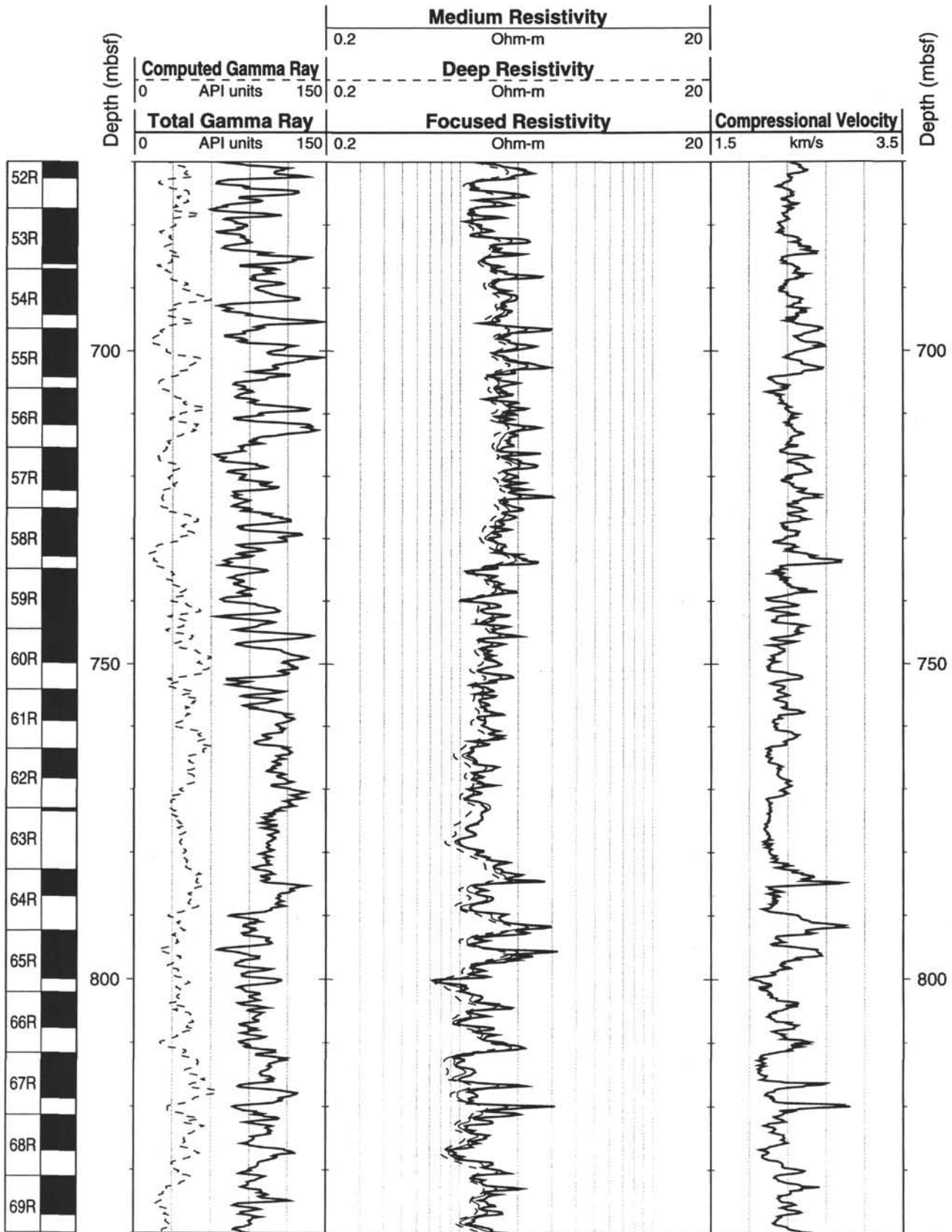
Cristina Broglia  
 Phone: 914-365-8343  
 Fax: 914-365-3182  
 E-mail: chris@ldeo.columbia.edu

Elizabeth Pratson  
 Phone: 914-365-8313  
 Fax: 914-365-3182  
 E-mail: beth@ldeo.columbia.edu

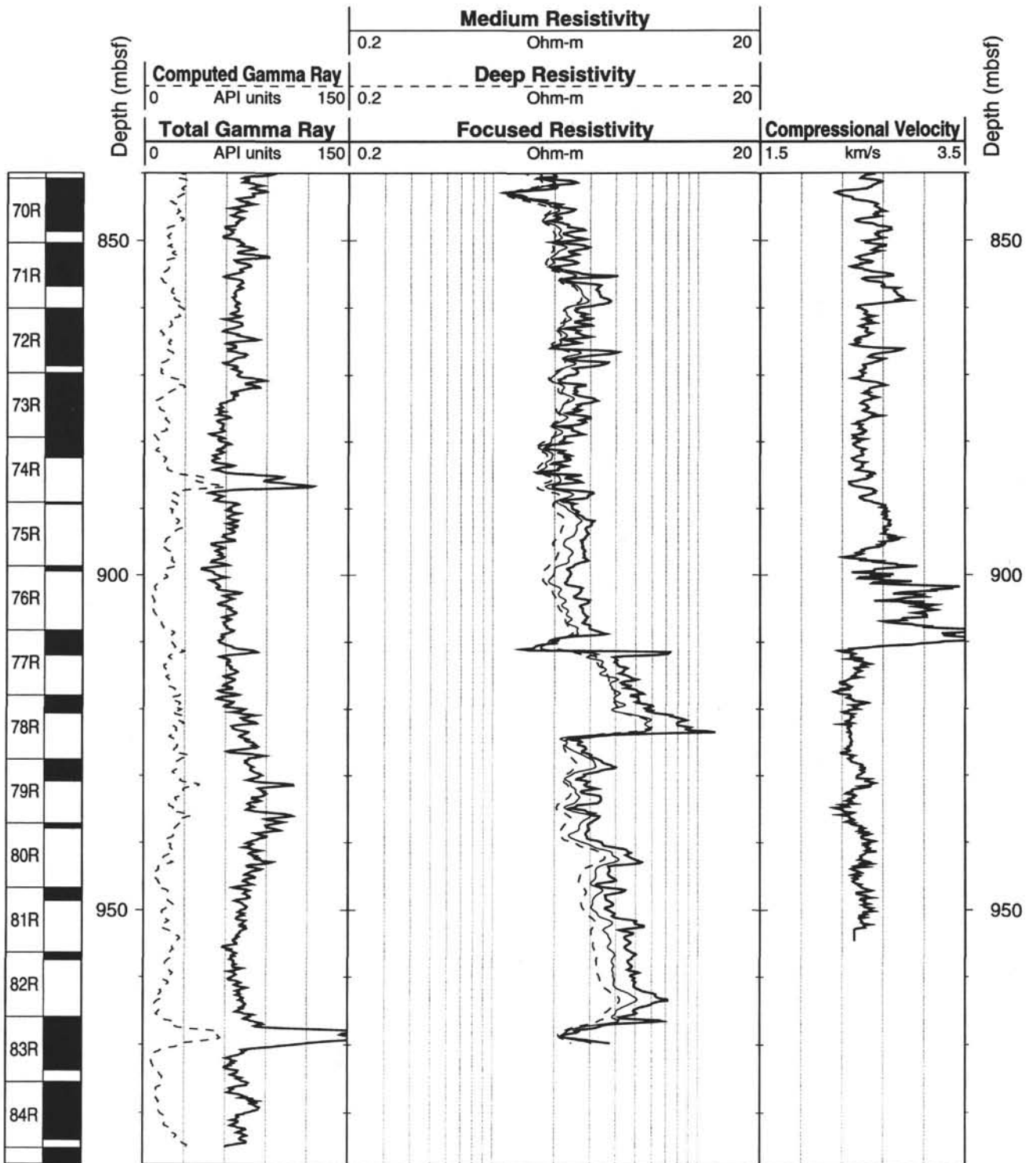
Hole 953C: Natural Gamma Ray-Resistivity-Sonic Logging Data



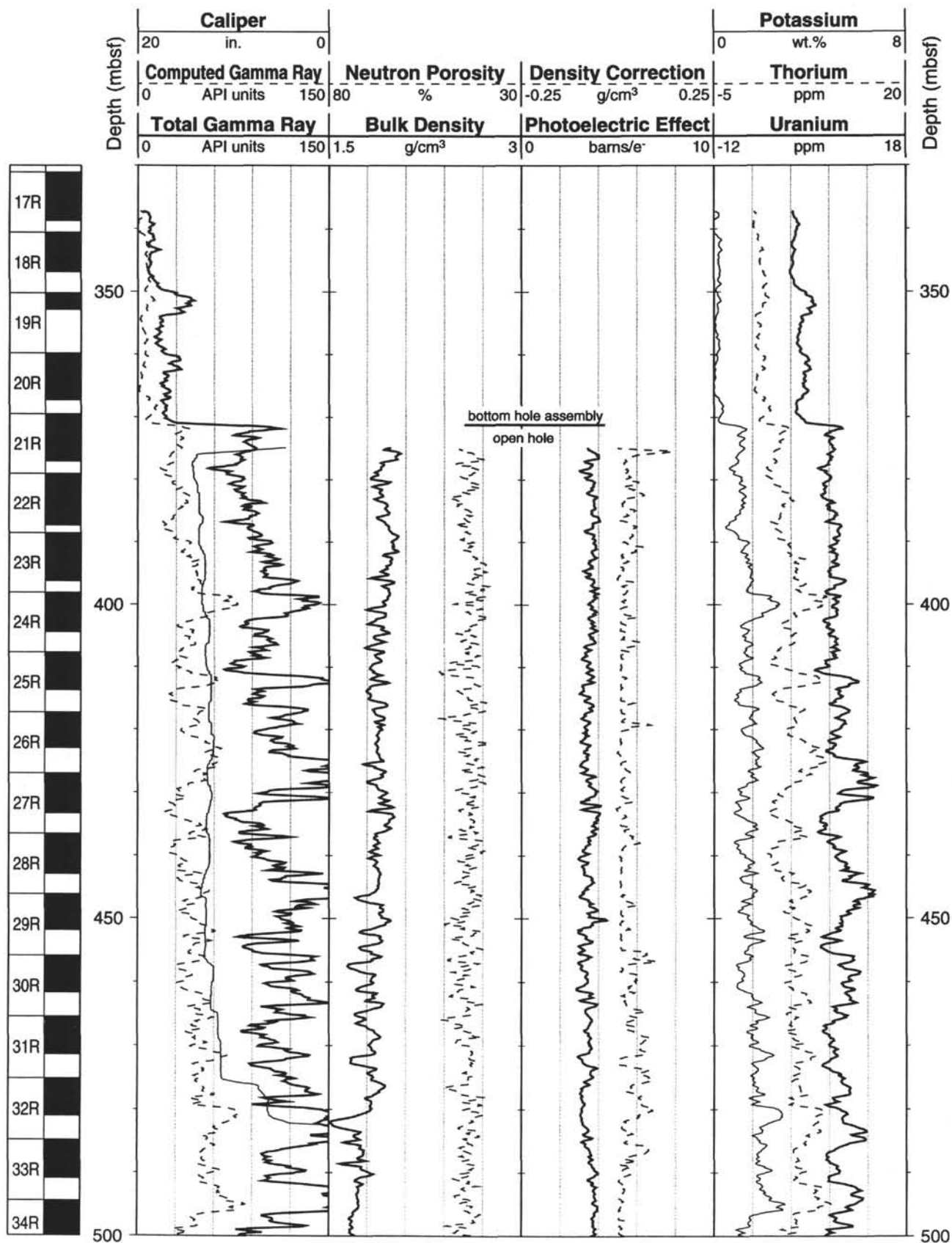
Hole 953C: Natural Gamma Ray-Resistivity-Sonic Logging Data (cont.)



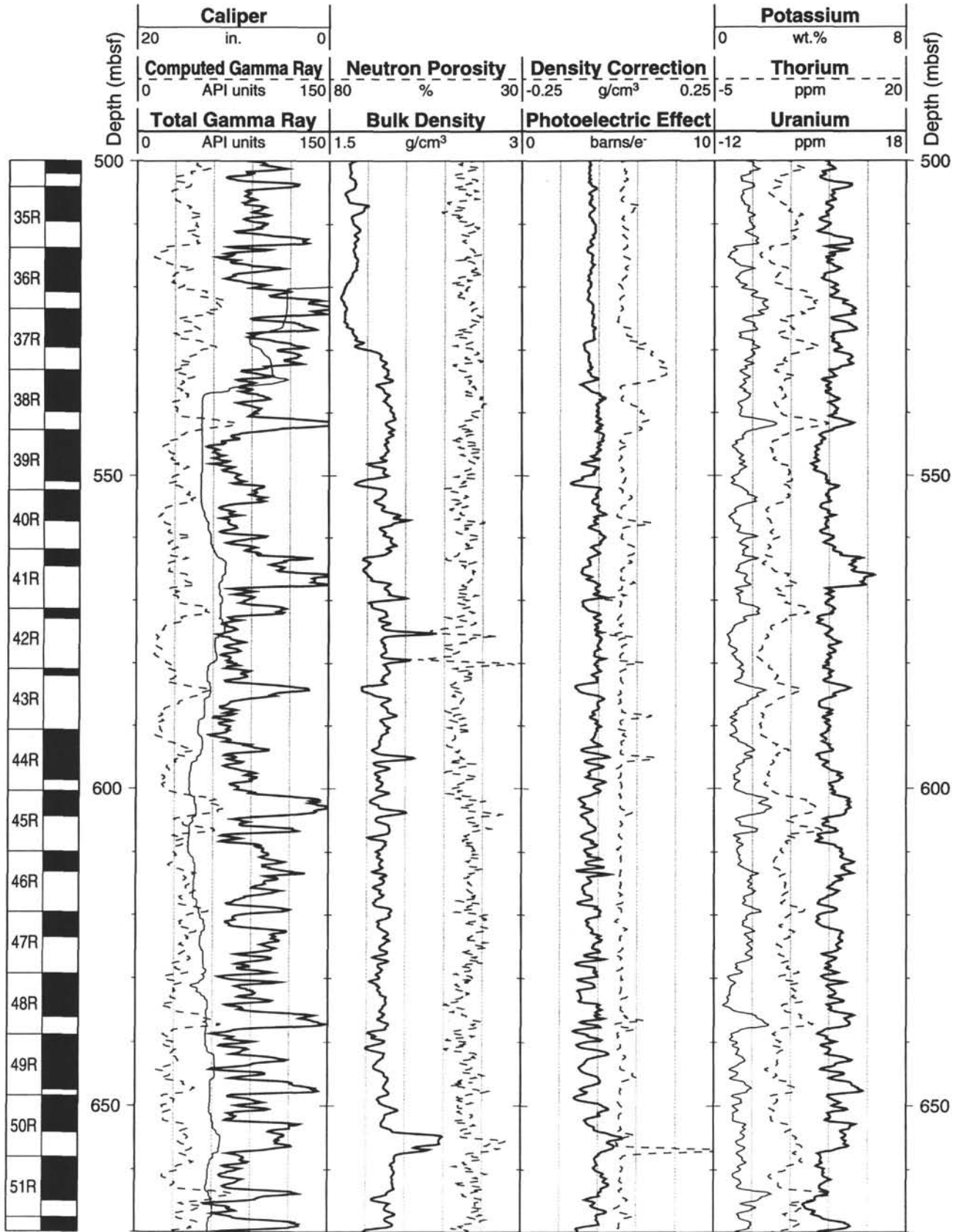
Hole 953C: Natural Gamma Ray-Resistivity-Sonic Logging Data (cont.)



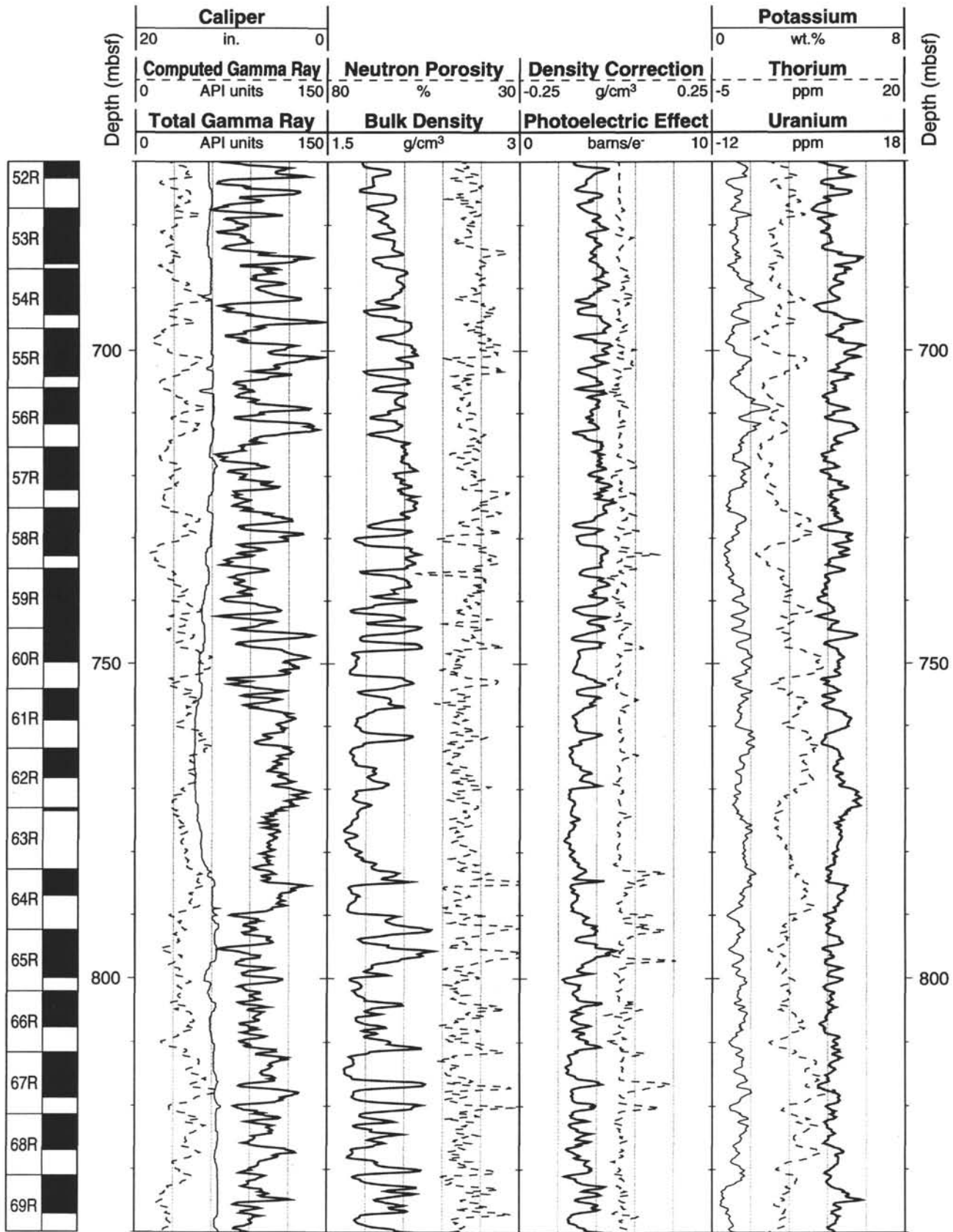
Hole 953C: Natural Gamma Ray-Density-Porosity Logging Data



Hole 953C: Natural Gamma Ray-Density-Porosity Logging Data (cont.)



Hole 953C: Natural Gamma Ray-Density-Porosity Logging Data (cont.)



Hole 953C: Natural Gamma Ray-Density-Porosity Logging Data (cont.)

